Modelling fibroblast dependent wound healing and scarring in the injured heart

Abbygail Mary Shaw

Thesis submitted for the degree of Doctor of Philosophy

Institute of Child Health, University College London

Centre for Mathematics and Physics in the Life Sciences and Experimental Biology, University College London

24 February 15

Disclaimer

I, Abbygail Shaw, confirm that the work presented in this thesis is my own. Where information has been derived from other sources, I confirm that this has been indicated in the thesis.

Signed ABBYGAIL MARY SHAW

Abstract

The most common cause of deaths worldwide is cardiovascular disease, including coronary heart disease (CHD) which is responsible for over 7 million deaths per year. CHD often leads to myocardial infarction (MI), more commonly referred to as a heart attack. MI restricts blood flow to the heart, causing death of a large number of muscle and blood vessel cells in the surrounding cardiac tissue. A collagen-rich scar is formed post-MI to patch up the area of injury and compensate for the lost tissue. However, the scarring can be excessive (a condition termed fibrosis), which can itself cause further complications such as ventricular remodelling and ultimately heart failure.

A relatable agent-based cardiac healing model was developed to improve the understanding of the complex cardiac healing process and predict the effects of pharmacological interventions on scarring. The model focuses on the interplay between fibroblast cells present in the cardiac tissue and the collagen matrix that constitutes the scar. The dynamics of these interactions dictate the remodelling outcomes post-MI. The model simulates a wide range of cell behaviours thought to play a role in cardiac remodelling, including migration, proliferation, apoptosis, and differentiation. Crucially, the implementation of these behaviours was informed by *in-vitro* experiments carried out using primary cardiac fibroblasts cells in a setting mimicking a cardiac wound.

Local collagen alignment, a property differentiating healthy and scar tissue, was systematically and quantitatively determined using a novel metric that could be applied to both simulation outcomes and fluorescence microscopy images of collagen in tissue sections from intact and post-MI murine hearts. This metric enabled the comparison between model predictions and *in-vivo* experimental data.

The model was used to simulate cardiac wound healing in a wide range of conditions, including those mimicking the administration of pharmacological compounds aiming at manipulating scarring by targeting various cell behaviours.

Abstract word count: 300

Table of Contents

Disclaimer 2
Abstract 3
Table of Contents 4
List of Figures 8
List of Tables 13
List of Abbreviations and Acronyms 14
Acknowledgements 15
1 Introduction 16
1.1 The structure of the healthy heart 16
1.1.1 Cellular composition 16
1.1.2 Extracellular matrix 18
1.2 Myocardial infarction and cardiac wound healing 19
1.3 Post myocardial infarction 19
1.3.1 The inflammatory phase 21
1.3.2 The proliferative phase 23
1.3.3 The maturation phase 28
1.3.4 Changes to non-infarct tissue 29
1.3.5 The collagen scar post-MI and its properties 29
1.4 Scarring optimisation through pharmacological interventions 30
1.5 Analysing the scar post-MI 34
1.5.1 Brightfield microscopy of stained samples 35
1.5.2 Polarized light microscopy 36
1.5.3 Second-harmonic imaging microscopy 36
1.5.4 Immunofluorescence microscopy 36
1.5.5 Whole-heart and *in-vivo* imaging 37
1.5.6 Quantitative analysis of collagen structures 38
1.6 Mathematical modelling of biological complexity 39
1.7 Mathematical modelling of the heart 41
1.8 Mathematical modelling of wound healing 41
1.9 Mathematical modelling of cardiac wound healing post-MI 46
1.10 Towards a predictive mathematical model of cardiac wound healing post-myocardial infarction 48
2 *In-vitro* experiments to inform model parameter values 50
2.1 Introduction 50

2.1 Aims 52
2.2 Experimental materials and methods 53
2.2.1 Primary cardiac fibroblast cell isolation from murine hearts 53
2.2.2 Primary skin fibroblast cell isolation from murine ears 54
2.2.3 Cell culture and maintenance 54
2.2.4 Induction and inhibition of specific cell responses 54
2.2.5 Pharmacological intervention 55
2.2.6 Scratch assay 55
2.2.7 Immunofluorescence 55
2.2.8 Flow cytometry cell cycle analysis 56
2.2.9 Masson's trichrome staining 57
2.2.10 Protein detection by western blot analysis 57
2.2.11 Genotyping 60
2.3 Analytical Methods 60
2.3.1 Cell migration speed 60
2.3.2 Dynamics of cell division 62
2.3.3 Cell differentiation 63
2.3.4 Cell Area 64
2.3.5 Statistical methods 65
2.4 Results 65
2.4.1 Primary cardiac fibroblasts as an experimental cell model 65
2.4.2 Cell migration 68
2.4.3 Cell proliferation 77
2.4.4 Cell differentiation 78
2.4.5 Cell area 83
2.5 Discussion 85
3 *In-vivo* cues for model refinement and validation 92
3.1 Introduction 92
3.2 Aims 94
3.3 Experimental methods 95
3.3.1 Myocardial infarction animal model and tissue section preparation 95
3.3.2 Tissue section immunochemistry and fluorescence imaging 96
3.4 Analytical methods 97
3.4.1 Visualisation of collagen I fibre bundles in heart sections 97
3.4.2 Automated processing and analysis of fluorescence heart sections images 97
3.4.3 Quantification of collagen fibre bundle orientation 98
3.5 Results 100
3.5.1 Heart tissue section imaging 100

3.5.2 Optimal parameters for the analysis image processing tool 103
3.5.3 Threshold parameter for local collagen alignment quantification 105
3.5.4 Quantification of the changes in collagen alignment post-injury 107
3.5.5 Estimation of model initial conditions from heart tissue section 111
3.6 Discussion 113
4 An *in-silico* model of cardiac wound healing 119
4.1 Motivation 119
4.2 Aims 119
4.3 An overview of the *in-silico* model 120
4.3.1 Agent-based modelling 120
4.3.2 Model organisation 121
4.4 Key model components and properties 124
4.4.1 Chemotactic gradient 124
4.4.2 Collagen fibrous matrix 126
4.4.3 Cells 128
4.5 Simulation outcome evaluation 146
4.5.1 Model visualisation 146
4.5.2 Quantitative analysis 147
4.5.3 Database for simulation results exports 148
4.6 Model implementation 149
4.7 Summary of the model simulation and parameter values 151
4.8 Illustration of cell behaviours in the model 154
4.8.1 Interactions between cells and the collagen matrix 154
4.8.2 Contact inhibition of locomotion 158
4.8.3 Contact inhibition of proliferation 158
4.8.4 Dynamic cell area changes in response to crowding 159
4.8.5 Typical output of the wound healing model 160
4.9 Evaluation of the impact of parameters on simulation outcomes 163
4.9.1 Cell population size and distribution 164
4.9.2 Cellular properties and functions 167
4.9.3 Interpolation functions 182
4.9.4 The model visualisation 185
4.9.5 Chemotactic gradient 186
4.9.6 Wound shape 189
4.9.7 Collagen content in the wounded region 190
4.9.8 Initial orientation of the collagen matrix 193
4.9.9 Initial wound dimensions 194
4.10 Discussion 195

5 Model validation and predictions of the effects of pharmacological interventions 204
5.1 Introduction 204
5.2 Comparison of simulation results with *in-vivo* experimental data 208
5.3 Potential model refinement 212
5.4 Model prediction of pharmacological intervention outcomes based on *in-vitro* experimental data 214
5.4.1 Transforming growth factor-beta 1 (TGFβ1) 214
5.4.2 Inhibition of activin receptor-like kinase 5 216
5.4.3 Inhibition of FGF receptor 1 219
5.5 Discussion 221
6 Future work 227
6.1 Further *in-vitro* investigation of cell behaviours and properties 227
6.1.1 Ability of the cells to alter the matrix 228
6.1.2 The relationship between cell velocity and collagen fibres properties 229
6.1.3 Effects of chemotaxis on the cell migratory speed and direction 230
6.1.4 Dose dependent response of cardiac fibroblasts to TGFβ1 231
6.1.5 Collagen matrix production and degradation by fibroblast cells 231
6.1.6 Effects of FGF-pathway manipulation 232
6.2 Cardiac wound healing model refinement 233
6.2.1 Mechanical stimuli 233
6.2.2 Additional cell types 234
6.2.3 Extending the experimental and mathematical models to three-dimensions 235
6.3 Further *in-vivo* analysis for mathematical model validation 239
6.3.1 Quantifying other scar properties 240
6.3.2 Generation of *in-vivo* data for pharmacological interventions 240
Bibliography 241
Annexes 260
A.1 Database organisation 260
A.2 3-dimensional cell culture experiments 262

List of Figures

Figure 1-1 Structure of rabbit ventricular myocardium at tissue and cellular scales. 17
Figure 1-2 Three-dimensional collagen fibre arrangement in the healthy canine heart..... 18
Figure 1-3 A comparison between the intact and infarcted heart. 19
Figure 1-4 Cardiac wound healing process post-MI. 20
Figure 1-5 Initiation of the inflammatory response. 21
Figure 1-6 Immune cell types that infiltrate the wounded region post-MI. 23
Figure 1-7 Cardiac fibroblast functions during cardiac wound healing. 24
Figure 1-8 The TGFβ signalling pathway. 32
Figure 1-9 Examples of different collagen imaging techniques. 35
Figure 2-1 Time-lapse phase contrast microscopy images of a scratch assay experiment at different time points (as indicated below each image). 61
Figure 2-2 Schematic representation of cell speed measurements from manual cell tracking. .. 62
Figure 2-3 Schematic representation of cell division. 63
Figure 2-4 Determination of the proportion of myofibroblasts during wound healing. 64
Figure 2-5 Determination of cell area using fluorescence images of co-cultures. 65
Figure 2-6 Comparison of three fibroblast experimental cell models. 66
Figure 2-7 Assessment of the expression of fibroblast and myofibroblast markers in cells isolated from murine hearts. 67
Figure 2-8 Visualisation of Collagen I production and deposition by cardiac fibroblasts. 67
Figure 2-9 Instantaneous cell speed as measured during *in-vitro* scratch assays. 69
Figure 2-10 Instantaneous cell speed as measured during *in-vitro* scratch assays. 70
Figure 2-11 Instantaneous cell speed as measured during *in-vitro* scratch assays on collagen-coated plates after addition of compounds mimicking a pharmacological intervention. 71
Figure 2-12 Analysis of cell migration patterns. 72
Figure 2-13 Effective cell speed as measured during *in-vitro* scratch assays. 73
Figure 2-14 Time-course visualisation of the instantaneous cell speed of a single migrating cells. 74
Figure 2-15 Changes in cell migration direction in response to contact with obstructing cells.. 75
Figure 2-16 Investigation of contact inhibition of locomotion *in-vitro*. 76
Figure 2-17 Cell behaviour immediately after division. 77
Figure 2-18 Changes in the proportion of cells at different phases of the cell cycle. 78
Figure 2-19 Detection of myofibroblast cells on immunofluorescence microscopy images. 79
Figure 2-20 Changes in the proportion of α-SMA positive cells (indicating a myofibroblast phenotype) in function of the time after scratch. 80
Figure 2-21 Effect of the addition of TGFβ1 on α-SMA expression by cells. 80

Figure 2-22 Effects of the addition of TGFβ1 and BSA (vehicle) to the culture medium on kinetics of changes in the fraction of cells highly expressing α-SMA. 81

Figure 2-23 Validation of the effect of the addition of TGFβ1 on known downstream target. 82

Figure 2-24 Evaluation of the effects of two pharmacological interventions on the fraction of α-SMA positive cells during the course of scratch assays using primary cardiac fibroblasts. 83

Figure 2-25 *In-vitro* cardiac fibroblast cells at the boundary of a scratch assay. 83

Figure 2-26 Visualisation of the data used for cell area determination. 84

Figure 2-27 Distribution of cell areas as measured *in-vitro* for cardiac fibroblast and myofibroblast cells. 85

Figure 3-1 Schematic of the angular difference ($\theta_{Difference}$) and threshold ($\theta_{Threshold}$) considered in the computation of fibre alignment. 99

Figure 3-2 Images of an intact heart section illustrating the cells and collagen I fibre bundles. 101

Figure 3-3 Highly variable collagen I structures in intact heart tissue sections. 101

Figure 3-4 Changes in collagen I fibre bundles patterns over time after injury. 102

Figure 3-5 Second-harmonic imaging microscopy (SHIM) for collagen visualisation on tissue sections from injured hearts 21 days post-MI. 103

Figure 3-6 Second-harmonic imaging microscopy (SHIM) for collagen visualisation on tissue sections from uninjured (control) hearts. 103

Figure 3-7 Automated characterisation of local collagen bundle orientation on heart section immunofluorescence images. 104

Figure 3-8 Evaluation of the cluster scoring approach for an intact sample. 105

Figure 3-9 Evaluation of the cluster scoring approach for an injured sample. 106

Figure 3-10 Evaluation of the number of clusters as a scoring metric for collagen fibre bundles alignment. 107

Figure 3-11 Quantitative analysis of collagen alignment on immunofluorescence microscopy images of heart tissue sections. 108

Figure 3-12 Changes in collagen angle distributions after MI. 110

Figure 3-13 Determination of residing fibroblast cell population size. 111

Figure 3-14 Estimation of the orientation of collagen fibres during early wound healing in the heart. 112

Figure 3-15 From heart tissue section to computational model. 112

Figure 3-16 Simulated tissue dimensions compared to that of a whole-heart. 113

Figure 4-1 Two-dimensional model approximation of the cardiac wound. 122

Figure 4-2 Images of intact heart tissue stained for cardiac fibroblast cells. 123

Figure 4-3 Overview of the mathematical model of cardiac wound healing. 123

Figure 4-4 Implementation of the chemotactic gradient. 126

Figure 4-5 Comparison of interpolation methods. 127

Figure 4-6 Relationship between the cell speed of fibroblast and myofibroblast cells and the collagen density. 129

Figure 4-7 Relationship between cell speed of a fibroblast cell and the chemotactic gradient for different densities of collagen. 129

Figure 4-8 Influence of the chemoattractant on cell direction. 131
Figure 4-9 Pseudopodia observed during the migration of cardiac fibroblasts..... 132
Figure 4-10 Illustration of the avoidance algorithm. 133
Figure 4-11 Estimation of differentiation probability. 135
Figure 4-12 Implementation of cell proliferation..... 137
Figure 4-13 Implementation of myofibroblast apoptosis. 139
Figure 4-14 Implementation of fibroblast apoptosis. 141
Figure 4-15 Wedge-shaped region of influence of a fibroblast (top row) and myofibroblast (bottom row) cell..... 143
Figure 4-16 Ability of a cell to re-orient collagen (κ) based on the density of the collagen matrix. 145
Figure 4-17 Different visual outputs from a model simulation (A) cells and collagen, (B) collagen only, and (C) chemotactic gradient. 147
Figure 4-18 Illustration of the cell class with the derived visual, fibroblast, and myofibroblast classes. 150
Figure 4-19 The model graphical user interface (GUI) allows the user to easily modify parameter values, to start a simulation run (2), and to visualise the outcome of the simulation (1). 151
Figure 4-20 Typical use of the model. 151
Figure 4-21 Typical model iteration. 152
Figure 4-22 Interactions between migrating cells and the collagen matrix in the case where all fibres were uniformly aligned horizontally. 155
Figure 4-23 Interactions between migrating cells and the collagen matrix in the case where all fibres were uniformly aligned vertically. 156
Figure 4-24 Interactions between migrating cells and the collagen matrix in the case where the orientation of the fibres was randomised. 156
Figure 4-25 Effect of collagen matrix densities on cell migration..... 157
Figure 4-26 Illustration of the avoidance algorithm. 158
Figure 4-27 Illustration of contact inhibition of proliferation. 159
Figure 4-28 Illustration of cell polarity changes following division..... 159
Figure 4-29 Illustration of the dynamic change in cell area in response to crowding. 160
Figure 4-30 Typical simulation including all functions and behaviours of the model..... 160
Figure 4-31 Typical simulation dynamics including all functions and behaviours of the model. 163
Figure 4-32 Impact of starting fibroblast population size on collagen matrix remodelling. 164
Figure 4-33 Impact of starting fibroblast population size on collagen matrix remodelling in the whole tissue..... 165
Figure 4-34 Initial cell distribution, using (A) randomly assigned locations (model default) and (B) uniformly distributed locations. 166
Figure 4-35 Effects of two different methods for initial cell distribution: randomly distributed tissue (model default) and evenly spaced within the healthy tissue..... 166
Figure 4-36 Effects of having myofibroblasts present at the start of a simulation on collagen matrix alignment. 167

Figure 4-37 Impact of cell proliferation on simulation visualisation. 168
Figure 4-38 Impact of cell proliferation on the cell population size and wound closure rate... 168
Figure 4-39 Impact of the minimum cell age requirement for division on simulation outcomes. 169
Figure 4-40 Impact of daughter cell behaviour implementation on local collagen alignment as quantified by the number of collagen clusters. 170
Figure 4-41 Impact on fibroblast cell migration baseline speed on simulation outcome..... 171
Figure 4-42 Impact of myofibroblast baseline cell speed on simulation outcome..... 171
Figure 4-43 Impact of polarisation parameter values on simulation outputs. 172
Figure 4-44 Impact of cell avoidance on simulation outcome. 173
Figure 4-45 Simulation visualisations of the collagen matrix with and without cell avoidance. 174
Figure 4-46 Sensitivity of the collagen alignment (as quantified by the number of collagen clusters) to the value of the distance threshold parameter. 175
Figure 4-47 Illustration of a square-based pyramid cell representation. 176
Figure 4-48 Illustration of a conical cell representation. 177
Figure 4-49 Illustration of a semi-circular base cone cell representation. 178
Figure 4-50 Illustration of an inverted square pyramid cell representation. 179
Figure 4-51 Impact of cell area of influence representations on collagen matrix properties.... 179
Figure 4-52 Impact of changes in parameter κ_{max} (ability of the cells to re-orient collagen fibres) on the collagen matrix alignment. 180
Figure 4-53 Alternative approach to the modelling of matrix re-orientation by migrating cells. 181
Figure 4-54 Impact of the differentiation of fibroblasts into myofibroblasts on the collagen density in the wounded region. 182
Figure 4-55 Effect of the interpolation method on collagen alignment. 184
Figure 4-56 Impact of the interpolation method on collagen matrix visualisation. 185
Figure 4-57 Model simulation output images of the collagen matrix at 800 time steps for (A) 15 (model default), (B) 5 and (C) 25 visual iterations. 186
Figure 4-58 Simulation visualisations of the collagen matrix, fibroblast (pink squares) and myofibroblast (red squares) cells with and without the chemotactic gradient. 186
Figure 4-59 Further investigating the impact of the chemotactic gradient on simulation components. 187
Figure 4-60 Chemotactic gradient manipulations. 188
Figure 4-61 Model simulation results from varying both the duration and production rate of the chemotactic gradient. 189
Figure 4-62 Implementation of a circular wounded region. 189
Figure 4-63 Effects of initial collagen density on matrix remodelling outcomes. 191
Figure 4-64 Effect of changes in initial collagen density in the wounded region on the number of collagen clusters thorough a simulation. 192
Figure 4-65 (A) Impact of the initial collagen arrangement in the healthy tissue on the number of collagen clusters during the course of simulations. 194

Figure 4-66 Impact of the wound size on the simulation outcome. 195
Figure 5-1 The TGFβ signalling pathway. 205
Figure 5-2 The FGF signalling pathway. 206
Figure 5-3 Representative images of the cells and collagen matrix from a simulation using all *in-vitro* and *in-vivo* estimated parameters. 209
Figure 5-4 Changes in local collagen alignment in model simulations and on heart tissue section images. 211
Figure 5-5 Comparison of global collagen alignment between model predictions and *in-vivo* data. 212
Figure 5-6 Altering the dynamics of collagen remodelling in the model. 213
Figure 5-7 Differentiation probability functions fitted to *in-vitro* differentiation data. 215
Figure 5-8 Model predictions of the effects of a TGFβ1 pharmacological intervention. 216
Figure 5-9 Differentiation probability functions fitted to *in-vitro* differentiation data. 217
Figure 5-10 Model predictions of the effects of ALK5 inhibitor pharmacological intervention. 219
Figure 5-11 Differentiation probability functions fitted to *in-vitro* differentiation data. 220
Figure 5-12 Model predictions of the effects of SU5402 pharmacological intervention. 221
Figure 6-1 Potential refinements of cell behaviours in the computational model. 228
Figure 6-2 Measuring the effects of local collagen orientation on cell migration direction. 230
Figure 6-3 Potential refinements and extensions to the mathematical model. 233
Figure 6-4 Chemotactic gradient formulation extended to 3D. 236
Figure 6-5 Potential visualisation scheme for a 3D model of cardiac wound healing. 237
Figure 6-6 3D primary cardiac fibroblast culture shortly after seeding. 238
Figure 6-7 3D primary cardiac fibroblast culture 20 hours after seeding. 239

List of Tables

Table 1 Composition of the resolving and stacking gels for western blot analysis 58

Table 2 Genotyping primers for Cre and R26R-EYFP. 60

Table 3 Model parameters for the fibroblast and myofibroblast cell based on *in-vitro* experiments and data from the current literature. 146

Table 4 Summary of the model parameter values relating to the tissue structure, chemoattractant, properties of the cell (e.g. migration, proliferation) and the simulation itself (e.g. time step duration). 153

Table 5 Details of the RUNS database table. The first columns (field) details the various fields of the table, while the second column shows the data type used to store said fields 260

Table 6 Details of the RESULTS database table. The first columns (field) details the various fields of the table, while the second column shows the data type used to store said fields 261

Table 7 Details of the RESULTS_RATES database table. The first columns (field) details the various fields of the table, while the second column shows the data type used to store said fields 261

List of Abbreviations and Acronyms

α-SMA	Alpha smooth muscle actin
ALK5	Activin receptor-like kinase 5
BSA	Bovine serum albumin
CHD	Coronary heart disease
DMSO	Dimethyl sulfoxide
FGF	Fibroblast growth factor
IL-1β	Interleukin-1 beta
MI	Myocardial infarction
MMP(s)	Matrix metalloproteinases
TGFβ	Transforming growth factor beta
TNF-α	Tumor necrosis factor alpha

Acknowledgements

I would firstly like to express my gratitude to my supervisors Professor Paul Riley and Professor Peter Hammond who have been supportive, enthusiastic, and have always offered constructive feedback and suggestions for my research. It has been a privilege to work with them both.

I wish to thank the following people for the technical support they have provided throughout my PhD. Firstly, Dr Mark Evans who has been both supportive and patient when guiding me through my early days of laboratory and cell culture work. Assistance provided by Dr Bertrand Vernay for microscopy techniques was greatly appreciated. I am grateful for the help provided by Dr Lewis Griffin for the development of the image processing software for tissue sample analysis. Thank you to the members of the Riley group who have been very supportive during my PhD and have provided me with the tissue samples used in my research.

A special thanks to everyone in the CoMPLEX department and the molecular medicine unit from the institute of child health who have made my PhD an enjoyable experience. In particular Donal, Mirna, and David who have always been full of encouragement.

I wish to thank my family Carol, Steve, Roberta, and Nicolas for their love and tremendous support throughout my PhD.

Finally, I would like to thank CoMPLEX and the British Heart Foundation who have provided me with financial support during my PhD.

Chapter 1

Introduction

1.1 The structure of the healthy heart

The heart is essentially a muscular pump, whose main function is to circulate blood throughout the body in order to supply organs and tissues with oxygen, nutrients and other molecules essential for their normal function while also removing metabolic waste (Katz, 2001). The pumping mechanism is made possible by the physical structure of the organ and its cellular composition. The mammalian heart is composed of four chambers: two atria and two ventricles. Contraction of the atria forces the blood into the heart (diastole) and contraction of the ventricles forces it out (systole). Atria tend to develop much lower pressures and have thinner walls when compared to ventricles. In particular, the wall of the left ventricle is much thicker in order to sustain the pressure necessary to push the blood through the systematic circulation (e.g. organs and extremities); as opposed to the right ventricle whose role is to pump blood to the lungs via the pulmonary circulation.

The outer surface of the heart is termed the epicardium and the inner surface of the atria and ventricles are covered with connective tissue also known as the endocardium. The ventricular muscle is sandwiched between the epicardium and endocardium and is formed of overlapping sheets of muscle bundles. These muscle fibres account for most of the wall thickness. The layer of epicardial cells that cover the surface of the heart lie on top of a network of fibroelastic connective tissue. Endocardial cells that line the atrial and ventricular cavities are positioned on top of layers of collagen, elastic fibers and smooth muscle cells (Katz, 2001).

1.1.1 Cellular composition

The mammalian heart is a highly organised structure made up of several different cell types that are supported by a macromolecular network of fibres (Camelliti et al, 2005; Jugdutt, 2003). The major cell types include cardiomyocytes and non-myocytes such as cardiac fibroblasts which form the skeleton of the heart, and vascular endothelial cells and smooth muscle cells which make up the coronary vessels (van den Borne et al., 2010). While the ratio of cardiomyocytes to non-myocytes varies between species, work in the 1970's revealed that the former makes up for about 25% of the adult rat left ventricle (Jugdutt, 2003; Souders et al., 2009; Zak, 1974). In comparison, subsequent research confirmed that cardiomyocytes in the adult mouse heart

accounted for approximately 56% of the total cardiac cell population (Banerjee et al, 2007). Together, cardiomyocytes generate the heart's pumping action by contracting in unison (Woodcock and Matkovich, 2005).

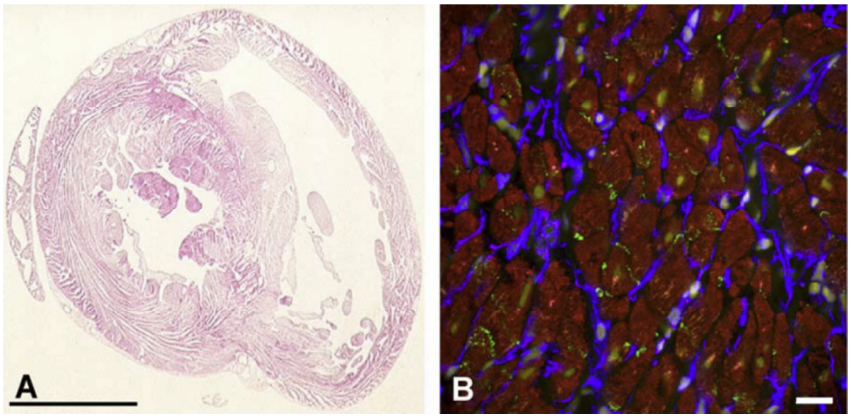

Figure 1-1 Structure of rabbit ventricular myocardium at tissue and cellular scales. (A) Transverse cross-section stained with Hematoxylin and Eosin, cardiac muscle cells (pink) exist in layers with gaps indicating unmarked regions that consist of nonmyocytes. (B) Immunofluorescence confocal microscopy image of a cross section of the tissue showing fibroblasts marked with anti-vimentin (blue) present in between myocytes marked with anti-myomesin (red), anti-connexin43 (bright green dots) and nuclei stained with DAPI (pale yellow-green patches). Scale bars represent A (5 mm) and B (20 μm). Adapted from (Camelliti et al., 2005a). Reproduced with permission.

The cellular architecture of the heart at the organ level is illustrated in Figure 1-1A, which shows a rabbit ventricular myocardium stained for cardiomyocytes. At the cellular level, fibroblast cells are typically layered between cardiomyocytes as shown in Figure 1-1B (Camelliti et al., 2005a). Fibroblast cells are estimated to represent 90-95% of the total nonmyocyte cell mass and are responsible for maintaining tissue homeostasis and preserving the structure and function of the heart (Jugdutt, 2003; Souders et al., 2009). The role of fibroblast cells is carried out through regulation of cell proliferation, cell-cell interactions with myocytes, cell-extracellular matrix (ECM) interactions, ECM degradation and synthesis (Souders et al., 2009). In general, fibroblast cells in the healthy adult heart are often described as quiescent cells which maintain the ECM (Chen and Frangogiannis, 2012). Fibroblast cells have a mesenchymal origin (Chen and Frangogiannis, 2012) and are characterised by key morphological attributes, including oval nuclei (Camelliti et al., 2005a), membrane projections known as pseudopodia (Abercrombie and Heaysman, 1953) and a flat spindle-like appearance (Camelliti et al., 2004). These morphological features are often used to distinguish fibroblasts from other cell types e.g. cardiomyocytes. However, it remains difficult to identify fibroblasts within a tissue with certainty in a non-destructive manner due to the lack of fibroblast-specific markers (Chen and Frangogiannis, 2012). Two markers routinely used to complement morphological features for fibroblast identification: vimentin (an intermediate filament protein) (Franke et al., 1979; Krenning et al., 2010) and fibroblast-specific protein (FSP)-1/S100A4 (Camelliti et al., 2004; Krenning et al., 2010; Strutz et al., 1995). However, both markers are not entirely specific to fibroblasts. Indeed, there is evidence to suggest that FSP-1 is also expressed by smooth muscle

cells, vascular endothelial cells, lymphocytes and monocytes/macrophages (Schneider et al., 2007; Strutz et al., 1995). Similarly, smooth muscle and vascular endothelial cells have also been shown to express vimentin (Franke et al., 1979; Mark et al., 1990).

1.1.2 Extracellular matrix

The ECM is a highly complex three-dimensional (3D) macromolecular network of fibres (Jugdutt, 2003). The composition of the ECM has a major impact on the structural and functional integrity of the myocardium (Jugdutt, 2003). The ECM is made up of several components, including interstitial collagens (types I, II, IV V and VI), cytokines, and growth factors (Souders et al., 2009). In the myocardium, more than 70% of the collagen content is of type I (van den Borne et al., 2010). The ECM provides a scaffold for the support of the heart and also acts as an adhesion substrate for cardiac cells (Souders et al., 2009). In healthy canine hearts, the 3D collagen structure has been described as both irregular and honeycomb-like (Figure 1-2)(Benedicto et al., 2011). The dimensions of collagen fibres from rat tail tendons has been analysed with atomic force microscopy (AFM). The width of collagen fibres has been estimated at 100 nm (Revenko et al., 1994).

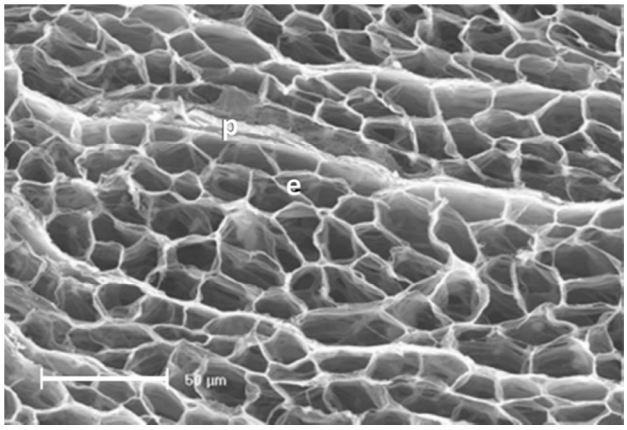

Figure 1-2 Three-dimensional collagen fibre arrangement in the healthy canine heart. A scanning electron microscopy image of the three dimensional arrangement of the collagen fibres within a healthy canine heart, post NaOH maceration. The fibrous structure may be likened to a honeycomb structure. The scale bar represents 50 µm. Adapted from (Benedicto et al., 2011). Reproduced with permission.

Cardiac fibroblasts migrate through the ECM and maintain its structure by producing and degrading its macromolecular components, including collagen (Jugdutt, 2003). The collagen content is degraded by matrix metalloproteinases (MMPs) (Souders et al., 2009). A tight regulation of MMPs expression and that of the tissue inhibitors of metalloproteinases (TIMPs) ensures a balance between ECM degradation and production in the healthy heart (Souders et al., 2009). Collagen synthesis by cardiac fibroblasts is influenced by many factors such as transforming growth factor-β_1 (TGF-β_1), an isoform of TGFβ reported to increase collagen synthesis. In addition, pro-inflammatory cytokines tumor necrosis factor-α (TNF-α) and interleukin-1 (IL-1) have been shown to have a detrimental effect on collagen synthesis (Jugdutt, 2003).

1.2 Myocardial infarction and cardiac wound healing

The primary cause of deaths worldwide is cardiovascular disease (World Health Organization, 2011), including coronary heart disease (CHD) which is responsible for over 7 million deaths per year (World Health Organization, 2011). In the United Kingdom (UK) CHD is estimated to cost the economy over £6.7 billion a year (Townsend et al., 2012). CHD is defined as the narrowing of blood vessels that supply the heart with the necessary oxygen and blood. This disease may often lead to myocardial infarction (MI) more commonly known as a heart attack. In 2010 the incidence of MI in England for the age group of 65 to 75 years old was 533 males and 237 females per 100,000. In 2010 the case fatality rates (proportion of deaths in the number of cases of MI) for MI were 10.6 and 15.1 for males and females, which means that 10.6 % of males and 15.1 % of females diagnosed with MI, died from this disease (Townsend et al., 2012).

MI is most commonly caused by coronary artery occlusion (an extreme form of vessel narrowing often due to atherosclerosis/plaque formation) resulting in a reduced blood and oxygen supply (ischemia) to the area of the heart directly downstream of the blockage, as depicted in Figure 1-3 (Frangogiannis et al, 2002). If the occlusion persists for a significant period of time, the ischemic environment promotes necrotic loss of resident cardiomyocytes (Frangogiannis et al., 2002; Sun et al., 2002).

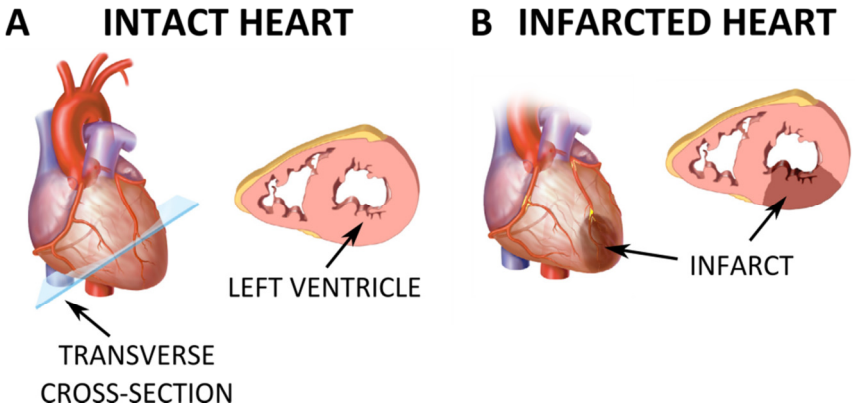

Figure 1-3 A comparison between the intact and infarcted heart. (A) The left ventricle of the intact heart has a thick muscular wall as shown by the transverse cross-section. (B) Infarcted heart post-MI, the infarct is located within the left ventricle. Adapted from (Goldthwaite, Charles A., 2006).

1.3 Post myocardial infarction

The necrotic loss of resident cardiomyocytes triggers a cascade of events (Weber, 1989) and initiates the healing process, which can be broken down into inflammatory, proliferative and maturation phases (Chen and Frangogiannis, 2012; Dobaczewski and Frangogiannis, 2011). These three phases are partially overlapping in time (Figure 1-4).

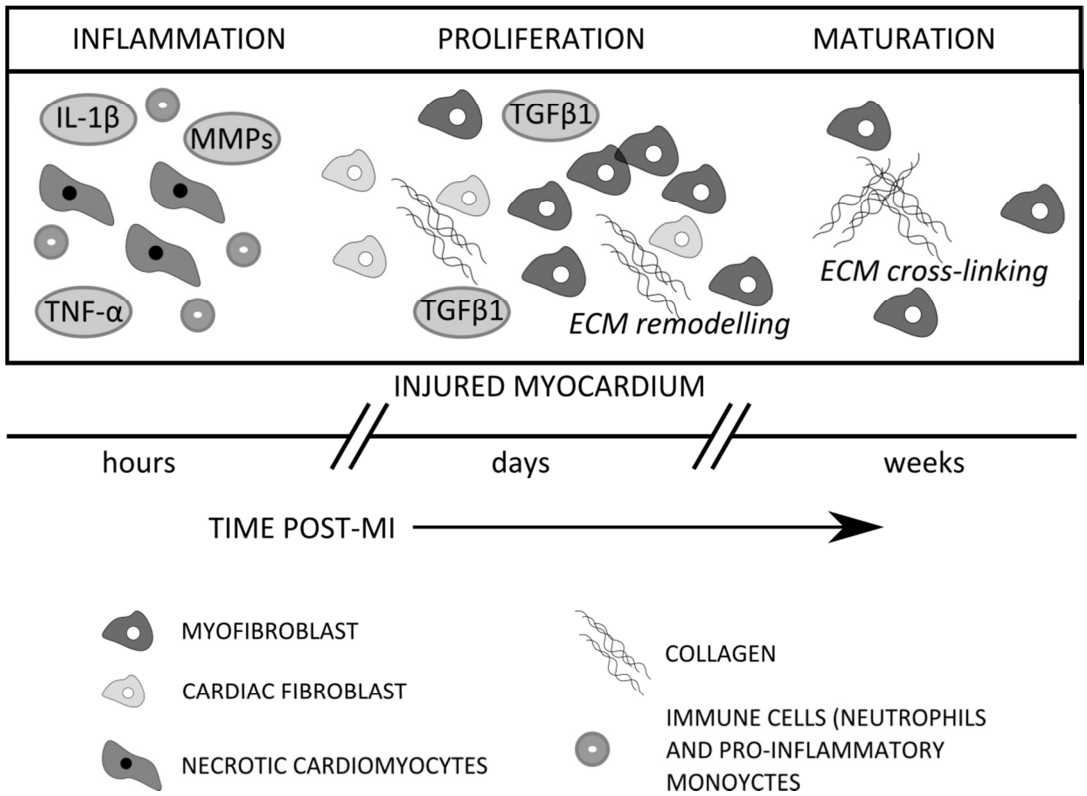

Figure 1-4 Cardiac wound healing process post-MI. Cardiac wound healing is defined by three overlapping phases: inflammation, proliferation and maturation. Myocardial necrosis triggers the initiation of the inflammatory response. Increased levels of pro-inflammatory cytokines (TNF-α and IL-1β) result in the recruitment of immune cells. Suppression of the inflammatory response is followed by proliferation. Fibroblast and myofibroblast (differentiated fibroblast) cells remodel the ECM. Fibroblast differentiation is promoted by TGFβ. ECM cross-linking occurs during the maturation phase. Figure adapted from (Nahrendorf et al., 2010; van Nieuwenhoven and Turner, 2013).

In summary, the inflammatory phase is triggered by myocardial necrosis, leading to an increase in pro-inflammatory mediators including tumour necrosis factor-alpha (TNF-α) and interleukin-1 beta (IL-1β), which are responsible for the recruitment of immune cells such as neutrophils and macrophages (Chen and Frangogiannis, 2012; Frantz et al., 2009). The damaged ECM and coronary vasculature are degraded by activated MMPs (Sun et al., 2002). In the mouse, the inflammatory phase starts shortly after MI (~1 hour) and lasts up to 5 days (Dobaczewski et al., 2010; Nahrendorf et al., 2010). The inflammatory response is suppressed with the polarisation of reparative macrophages which produce anti-inflammatory stimuli for example transforming growth factor beta (TGFβ) (Frangogiannis, 2008). During this time fibroblast cells begin to infiltrate the infarct and differentiate into myofibroblasts, which marks the start of the proliferative phase of cardiac healing (Chen and Frangogiannis, 2012; Willems et al., 1994). Fibroblast and myofibroblast cells produce collagen and contribute to the replacement of necrotic tissue by a fibrotic scar. In rodents, the proliferative phase is most prominent between 48 hours and 5 days post-MI (Dobaczewski et al., 2010). Over time the myocardial scar matures and a dense collagen-based infarct is formed as a result of extensive matrix cross-linking. During this maturation phase, a decrease in the numbers of myofibroblast cells have been

reported, possibly due to apoptosis (Frangogiannis et al., 2000). In rodents, a typical maturation phase starts 5 days post-MI and lasts up to 28 days (Dobaczewski et al., 2010).

1.3.1 The inflammatory phase

1.3.1.1 The initiation of the inflammatory response

Inflammation is triggered by the release of intracellular components into the local microenvironment following necrotic events. This release initiates these responses: complement cascade activation, reactive oxygen species (ROS) generation, and nuclear factor-κB (NF-κB) pathway activation (Figure 1-5). All these are thought to contribute to the upregulation of pro-inflammatory cytokine pathways, including TNF-α and IL-1β, both of which promoting the recruitment of immune cells originating from the systemic circulation to the wounded region (Frangogiannis et al., 1998; Frangogiannis et al., 2002).

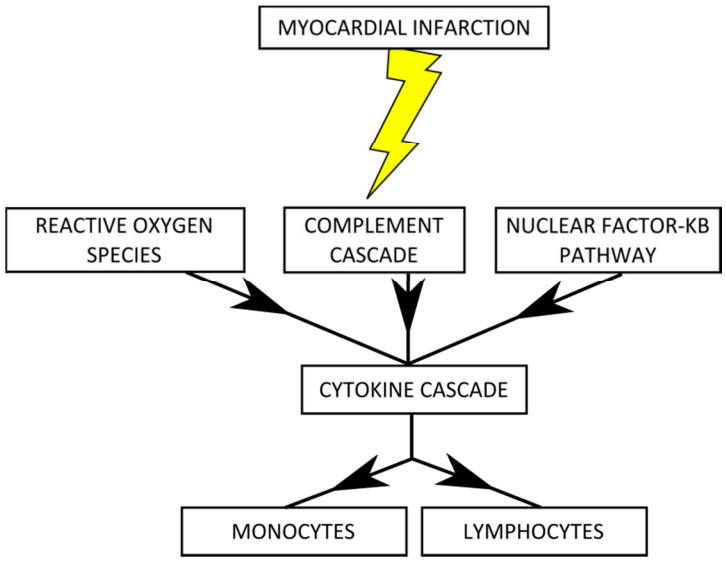

Figure 1-5 Initiation of the inflammatory response. Post-MI, the following responses are initiated: reactive oxygen species generation as well as complement cascade and nuclear factor-κB pathway activation. All of these attributes contribute to the initiation of the cytokine cascade, which promotes the recruitment of immune cells (e.g. monocytes and lymphocytes).

1.3.1.2 The infiltration of inflammatory cells into the injured region

Immune cells are recruited into the wounded region by pro-inflammatory cytokines (or chemokines) and aided by adhesion molecules (Dobaczewski et al., 2010). Cardiac mast cells located at the infarct border have been recognised as a source of the pro-inflammatory cytokine TNF-α (Frangogiannis et al., 1998). The recruited immune cells include neutrophils and monocytes/macrophages (Nahrendorf et al., 2010). The main role of these cells is to remove dead or injured tissue after MI. This is achieved through the release of ROS and proteolytic enzymes, both of which can potentially be harmful for any resident myocytes that may have survived the ischemic conditions. Immune cells also secrete pro-inflammatory cytokines such as TNF-α, IL-6, and IL-1 (Nahrendorf et al., 2010), thus resulting in a positive feedback loop.

Neutrophils were observed in the infarcted myocardium in rodents a few hours post-MI and their number peaks after approximately one day (Nahrendorf et al., 2010) (Figure 1-6). Monocytes, and their differentiated form macrophages, contribute to both inflammatory and proliferative stages of cardiac wound healing (Nahrendorf et al., 2010). Monocytes and macrophages were observed in the injured region one day and between one and two days post-MI, respectively (Nahrendorf et al., 2010; Sun and Weber, 2000) (Figure 1-6).

The immune cell migration into the infarct is facilitated by the proteolytic activity of secreted MMPs, which degrade the original collagen matrix thus allowing cells to move more freely (Nahrendorf et al., 2010; Sun et al., 2002). The level of MMP expression in healthy adult tissue is generally low, however upregulation is reported for specific pathological and physiological remodelling processes (Matsumura et al., 2005). MMP synthesis is stimulated by cytokines such as TGFβ, TNF-α, IL-1 and IL-6, along with growth factors such as epidermal growth factor (Creemers et al., 2001; Phatharajaree et al., 2007). The activity of MMPs within tissues is controlled by specific inhibitors such as TIMPs (Creemers et al., 2001; Visse and Nagase, 2003). Post-MI, the equilibrium between MMPs and TIMPs that normally regulates collagen turnover is disrupted causing changes to the collagen matrix in both the infarct and neighbouring tissues (Matsumura et al., 2005; Mukherjee et al., 2003; Phatharajaree et al., 2007).

The different members of the MMPs family have distinct functions. MMP-1, MMP-2 and MMP-9 in particular are reported to play a role in cardiac wound healing post-MI (Chen et al., 2005; Cleutjens et al., 1995a; Phatharajaree et al., 2007). MMP-1, MMP-2 and MMP-9 degrade collagen, basement membrane components and elastin (Chen et al., 2005; Cleutjens et al., 1995a; Phatharajaree et al., 2007). MMP-2 can digest collagens type I, II and III. The ability of some MMPs to degrade the ECM thus makes them an important player in myocardial matrix remodelling. The timing of activation of MMPs can vary depending on the type (1, 2 or 9) and the species considered, but increased levels are typically observed as early as 2 hours after injury while normal (i.e. pre-injury) levels are usually observed by 14 days post-MI (Chen et al., 2005; Cleutjens et al., 1995a; Cleutjens et al., 1995b; Herzog et al., 1998; Phatharajaree et al., 2007). MMP activation is thus a transient phenomenon. Similarly, TIMP mRNA levels were shown to increase after 6 hours and reach a maximum at 2 days post-MI in the infarcted region (Cleutjens et al., 1995a).

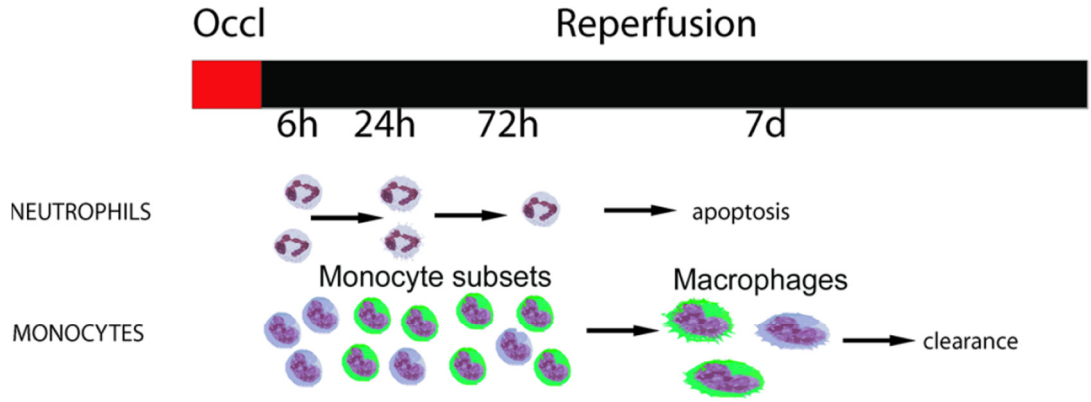

Figure 1-6 Immune cell types that infiltrate the wounded region post-MI. Neutrophils and monocytes are shown to be present in the wound by one day post-MI. Macrophages appear between one and two days post-MI. Adapted from (Frangogiannis, 2008). Reproduced with permission.

Within weeks post-MI, immune cells are depleted due to apoptosis and the lack of new cells to ensure a continuous turnover (Sun et al., 2002). Once the inflammatory stage is complete, the wound healing process moves onto the reparative stage, also commonly referred to as the proliferative phase (Frantz et al, 2009).

1.3.2 The proliferative phase

The transition from the inflammatory to the proliferative stages of wound healing is initiated by stop signals that suppress the inflammation (Frangogiannis, 2012). A different subset of monocytes (Ly-6C^{low}, as opposed to Ly-6C^{high} during the inflammatory phase) is recruited (Nahrendorf et al., 2010). The "reparative" monocytes secrete endothelial growth factor (VEGF), fibroblast growth factor (FGF) and TGFβ (Nahrendorf et al., 2010; Sun and Weber, 2000). Both VEGF and FGF are involved in the regulation of fibroblast migration and differentiation (Kaftan et al., 2012; Mohammadi et al., 1997; Murakami et al., 2008; Zhao et al., 2014). TGFβ is an anti-inflammatory cytokine that promotes fibroblast proliferation and differentiation to myofibroblasts (Frantz et al., 2009). Together, FGF and TGFβ stimulate the production and deposition of collagen by myofibroblasts (Nahrendorf et al., 2010). The proliferative phase is characterised by the formation of a scar, mostly by cardiac fibroblast cells. The following section details the role of these cells during wound healing (Daskalopoulos et al., 2012; Porter and Turner, 2009).

1.3.2.1 Cardiac fibroblasts and their role post myocardial infarction

Cardiac fibroblasts are widely distributed connective tissue cells whose main role in the healthy heart is to maintain the ECM, which provides both structural and functional support to the heart (Souders et al., 2009). In the adult myocardium, fibroblast cells constitute the majority of the interstitial cells (Camelliti et al., 2005a; Chen and Frangogiannis, 2012; Souders et al., 2009). Post-MI the fibroblast cells are key players in cardiac remodelling and the regulation of the cardiac function and geometry. As such although they exhibit different phenotypes and

functions at various stages of cardiac wound healing, fibroblast cells are most often associated with the proliferative phase (Chen and Frangogiannis, 2012).

Cardiac fibroblast cells present in the infarct originate from proliferating and migrating interstitial fibroblasts from the uninjured myocardium (Freed et al., 2005). Post-MI the fibroblast cells have many important functions which include: migration, proliferation, differentiation, degradation and secretion of the ECM, secretion of cytokines and growth factors (Figure 1-7).

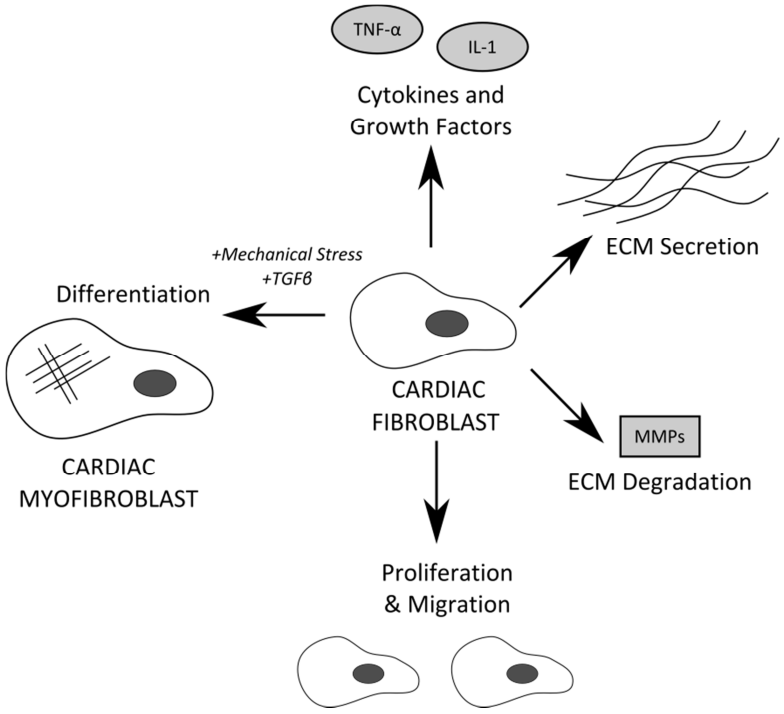

Figure 1-7 Cardiac fibroblast functions during cardiac wound healing. The cardiac fibroblast cell has the ability to proliferate, migrate, differentiate to myofibroblast cells, degrade and secrete ECM, and secrete cytokines and growth factors. In general cardiac fibroblasts differentiate into myofibroblast cells with the addition of mechanical stress and TGFβ. Figure adapted from (Chen and Frangogiannis, 2012; Souders et al., 2009) illustrating the various potentials of the fibroblast cell.

Migration of fibroblast cells through the ECM requires production of proteases for degrading the ECM, deposition of matricellular proteins and integrin activation on the cells surface (Murphy-ullrich, 2001). A mathematical model developed by DiMilla *et al* proposed that an intermediate ratio between the adhesive strength and cellular force was optimal for the greatest cell migration (DiMilla et al., 1991; Murphy-ullrich, 2001). Fibroblast migration may be controlled by both cytokines and growth factors which cause cardiac fibroblast gene expression changes that encourages fibroblasts to migrate towards the wound (Souders et al., 2009). Increased concentration levels of TNF-α and IL-1β have been reported to correlate with an increase in the migration of cardiac fibroblasts (Mitchell et al., 2007). Moreover, both TGFβ and fibroblast growth factors (FGFs) may also influence fibroblast migration (Chen and Frangogiannis, 2012). However, the molecular signals which are responsible for fibroblast migration are not well understood (Chen and Frangogiannis, 2012; Freed et al., 2005).

Fibroblasts secrete MMPs such as MMP-1, MMP-2 and MMP-9 in order to degrade the ECM and also produce varied components of the ECM in particular multiple collagens including collagen types I and III (Kanekar et al., 1998; Souders et al., 2009; Turner and Porter, 2012). In particular studies on rat adult cardiac fibroblasts in the presence of ROS such as H_2O_2 have shown an increase in MMP activity and a decrease in collagen production (Siwik et al., 2001). Conversely, under hypoxic conditions an increase in the production of TNF-α and collagen synthesis by cardiac fibroblast cells have also been described (Shivakumar et al., 2008; Tamamori et al., 1997).

Fibroblast cells are more resistant to oxidative stress compared to cardiomyocytes. Fibroblast cells exposed to hydrogen peroxide (H_20_2) have shown almost no DNA fragmentation (Zhang et al., 2001) which enables fibroblast cells to sense changes in the hearts microenvironment post-MI. Oxidative stress, hypoxia, reactive oxygen and high levels of cytokines all present at some point in the infarcted myocardium and have been shown to influence the function and phenotype of *in-vitro* cardiac fibroblast cells (Zhang et al., 2001).

Under specific stress conditions, such as injury, fibroblasts can be activated and start forming contractile stress fibres. This differentiated form is termed myofibroblast and can be identified by its high expression of alpha-smooth muscle actin (α-SMA) (Dobaczewski et al., 2012; Souders et al., 2009). Post-MI, the release of TGFβ was shown to promote cardiac fibroblast cell differentiation to myofibroblasts (Souders et al., 2009). In the earlier stages of wound healing, an intermediate form that does not express α-SMA but still produces cytoplasmic stress fibres has been observed and is referred to as a proto-myofibroblast (Hinz et al., 2007). In response to injury stimuli, initially quiescent (nonproliferating) cardiac fibroblast cells (G_0 phase of the cell cycle) may transition through the G_1-S phase cell cycle checkpoint (Pillai et al., 2011) and can thus actively proliferate.

The next three sections discuss the ability of the fibroblast to remodel the ECM and their proliferation and differentiation response post-MI.

1.3.2.2 Cardiac fibroblast proliferation

Unlike cardiomyocytes, the proliferative capacity of cardiac fibroblasts remains throughout adult life (Pillai et al., 2011). The proliferation rate of both fibroblast and myofibroblast cells increases after injury (van den Borne et al., 2010; Pillai et al., 2011), driven by factors such as ROS (Cheng et al., 2003), miRNA-21 (Thum et al., 2008), TNF-α (Jacobs et al., 1999), FGF-2 (Detillieux et al., 2003; Galzie et al., 1997) and TGFβ in mice (Squires et al., 2005). TGFβ1 has been shown to have antiproliferative effects on human subcutaneous fibroblast cells cultured *in-vitro* (Desmoulière et al., 1993). The signalling cascade Ras/Raf/MEK/ERK is responsible for regulating cellular processes such as proliferation in response to extracellular stimuli (Chambard et al., 2007; Porter and Turner, 2009). In particular, fibroblast proliferation has been shown to

require ERK activation. The activation of MAP kinase in fibroblast cells was inhibited by two methods which transiently expressed a non-phosphorylatable mutant of ERK1 and the entire ERK1 antisense RNA. Inhibition of MAP kinase led to a reduction in cell proliferation (Pagès et al., 1993).

1.3.2.3 Cardiac fibroblast differentiation to myofibroblast fate

Myofibroblast cells were first described in the early 1970's (Daskalopoulos et al., 2012; Gabbiani et al., 1972). Myofibroblasts exhibit features of both smooth muscle and cardiac fibroblast cells with their contractile stress fibers and well-developed, rough endoplasmic reticulum, respectively (Hinz, 2007). Unlike smooth muscle cells, myofibroblasts do not express smooth muscle myosin heavy chain, desmin and smoothelin (Chen and Frangogiannis, 2012; Dobaczewski et al., 2004; Frangogiannis et al., 2000; Tomasek et al., 2002; Willems et al., 1994). The presence of contractile stress fibres confers myofibroblast cells their contractile behaviour (Sun and Weber, 2000), and these fibres are produced by the cell in response to a mechanical stimulus (Chen and Frangogiannis, 2012; Hinz et al., 2001). The myofibroblast phenotype is also associated with increased levels of α-SMA, which has been described as a "mechanosensitive protein" capable of sensing changes in ECM stiffness such as those observed during wound healing (Hinz et al., 2007). Indeed, the levels of α-SMA expression in myofibroblasts cultured *in-vitro* increased with the stiffness of the culture substrate (Hinz, 2010). Increases in expression levels of collagen I and III were observed during repeated mechanical stretching (Daskalopoulos et al., 2012; Husse et al., 2007), thus suggesting myofibroblasts response to mechanical stimuli is an increase in ECM production and possibly degradation. In general, myofibroblasts secrete increased levels of collagen compared to fibroblast cells (van den Borne et al., 2010; Turner and Porter, 2013).

1.3.2.3.1 The sources of myofibroblast cells

The origin of myofibroblast cells observed in the infarcted myocardium is currently unclear. Three likely and non-mutually exclusive sources have been hypothesized: resident fibroblast cells in the myocardium (Yano et al., 2005), pericytes present within the outermost epithelial layer of blood vessels (Sun and Weber, 1996) and precursor cells originating from the bone marrow (Forbes et al., 2004; Yano et al., 2005). The current consensus appears to be that most of the myofibroblasts observed in the injured region are the result of the differentiation of a portion of the fibroblast population present in the intact surrounding tissue. This hypothesis was supported by a study during which GFP-tagged bone marrow was transplanted into nude rats (Yano et al., 2005).

1.3.2.3.2 The effects of TGFβ on myofibroblast differentiation

It has been shown that post-MI TGFβ expression at the infarct border is markedly increased (Bujak and Frangogiannis, 2007; Dean et al., 2005) compared to baseline conditions. Increased expression of p-Smad2, a downstream effector of TGFβ, was observed 24 to 72 hours after reperfusion in infarcted mouse hearts (Bujak et al., 2007). TGFβ is a growth factor that influences cell migration, proliferation, differentiation and apoptosis. In mammals three isoforms of TGFβ have been identified: TGFβ1, TGFβ2 and TGFβ3 (Schiller et al., 2004). TGFβ has been reported to contribute to both *in-vitro* and *in-vivo* fibroblast differentiation. TGFβ1 is the most abundant isoform (Bujak and Frangogiannis, 2007). MMP-2 and MMP-9 have been reported to activate TGFβ (Annes et al., 2003).

1.3.2.3.3 The role of myofibroblast cells in the healing infarct

In general, myofibroblasts are not present in the healthy adult heart, apart from within the heart valve leaflets (Daskalopoulos et al., 2012; Sun and Weber, 1996; Sun and Weber, 2000). Myofibroblast cells are observed in the injured region by day 3 post-MI in the rat and day 4 to 6 in humans, when they remain in large numbers for up to several months (Sun and Weber, 2000; Willems et al., 1994). Neovascularisation at the infarct site likely provides essential oxygen and nutrients to myofibroblast cells (Sun and Weber, 2000), however, this has yet to be fully elucidated. Myofibroblasts in the infarcted myocardium are observed in clumps and are generally aligned with the long axis of the collagen and the muscle fibres situated in the visceral pericardium (Sun and Weber, 1996).

Myofibroblast cells secrete increased levels of collagen and express increased levels of α-SMA compared to their undifferentiated counterparts, ultimately resulting in the formation of a scar. Myofibroblasts secrete collagen types I and III (van den Borne et al., 2010; Turner and Porter, 2013) and their stress fibres facilitate the contraction of the ECM (Hinz and Gabbiani, 2003). The myofibroblast contains focal adhesions which create attachments between the cell and ECM such that mechanical forces generated by the myofibroblast cell can be relayed to the ECM to facilitate contraction. α-SMA produced in myofibroblasts and increases the level of cellular contractility (Arora and McCulloch, 1994; Hinz et al., 2001) and enables the modification of mechanical properties of the local ECM to promote the closure of the wound (Souders et al., 2009). The level of α-SMA in cultured cells was quantified with single cell fluorimetry (Arora and McCulloch, 1994) and the relationship between the level and the level of gel contraction was shown to be linear. Moreover, the addition of α-SMA to fibroblast *in-vitro* cultures was shown to be positively correlated to the cells ability to contract stress-released collagen gels and deformable silicone substrates (Hinz et al., 2001). The force generated by these cells is promoted by serotonin, angiotensin-II and endothelin-1 (Tomasek et al.,). Chemokines and growth factors (e.g. IL-1β, IL-6 and TNF-α) diffusing from the site of injury promotes

myofibroblast proliferation, their migration towards the wound and the remodelling of the matrix via increased secretion of both collagen and MMPs (Baum et al, 2011; Souders et al., 2009). In turn, myofibroblasts also secrete soluble signals such as IL-1β, TNF-α and TGFβ thus resulting in an amplification of the inflammatory signals (Baum and Duffy, 2011).

1.3.3 The maturation phase

During the final phase of the cardiac wound healing process, the maturation phase, the levels of collagen continue to increase and the fibres become cross-linked, resulting in the formation of a mature scar (Chen and Frangogiannis, 2012; Dobaczewski et al., 2010; Shinde and Frangogiannis, 2014). Increasing levels of collagen were observed for up to 6 weeks post-MI in canine models (Jugdutt and Amy, 1986). At 6 weeks, the scar is mainly composed of collagen type I fibres (Whittaker et al., 1989). While myofibroblast cells have been described to persist in the injured region for some time after injury and are still observed in human myocardial scars 17 years post-MI (Turner and Porter, 2013; Willems et al., 1994), the size of the myofibroblast cell population was shown to decrease with time after MI (Frangogiannis et al., 2000). This reduction in the number of myofibroblast and vascular cells may occur through apoptosis or deactivation (Dobaczewski et al., 2010; Ren et al., 2002; Takemura et al., 1998; Turner and Porter, 2013; Zhao et al., 2004). TUNEL staining has been used as an indicator for apoptosis by detecting DNA fragmentation (Takemura et al., 1998). In the rabbit myocardium at 2 weeks post-MI there were approximately 2.5% TUNEL positive cells and around a third of these cells were myofibroblasts. At 4 weeks post-MI almost half of the TUNEL positive cells were fibroblast cells. The fate of a cell is dependent upon the ratio of the expression of two factors Bcl-2 and Bax which suppress and enhance apoptosis respectively (Zhao et al., 2004). Immediately after injury an increase in the expression of Bcl-2 is observed in humans (Misao et al., 1996). Myofibroblasts express Bax during the later stages of healing at approximately 28 days in the rat (Zhao et al., 2004). It is unknown whether the myofibroblast cells deactivate before becoming apoptotic (Dobaczewski et al., 2010). As the scar matures the collagen fibres become cross-linked. This new collagen structure has been suggested to shield resident myofibroblast cells from stress resulting in their deactivation. This is unlike dermal wound healing where no myofibroblasts were observed in the induced dermal wounds of rats 1 month after injury (Willems et al., 1994). In dermal wound healing, the disappearance of myofibroblasts is also mediated by apoptosis (Desmoulière et al., 1995).

The reparative response in cardiac wound healing can result in a complication whereby increased wall stress causes fibroblast cells to become permanently activated (i.e. myofibroblast cells), possibly contributing to ventricular dysfunction and chamber remodelling (Turner and Porter, 2013). Instead, ECM dysregulation mediated by myofibroblast cells may result in progressive left ventricular dilatation and systolic dysfunction (Opie et al., 2006).

1.3.4 Changes to non-infarct tissue

Post-MI, structural changes also take place in the non-infarcted myocardium, including an increase in interstitial collagen, hypertrophy of the resident cardiomyocytes and growth of the capillary network (Cleutjens et al., 1999; Litwin et al., 1991; Pelouch et al., 1993). By one week post-MI, the fraction of interstitial collagen in the non-infarcted myocardium of humans and rats more than doubled when compared to intact hearts (Cleutjens et al., 1999). In the right ventricle on day 7 increases in the expression of procollagen I and III mRNAs have been recorded. Additionally these mRNAs were also shown to increase in the noninfarcted interventricular septum on day 4 (Sun and Weber, 2000). However it is less when compared to the infarcted tissue (Volders et al., 1993).

1.3.5 The collagen scar post-MI and its properties

The main function of the scar produced during wound healing post-MI is to provide the injured region with the tensile strength necessary to prevent tissue deformation and myocardial rupture (Sun et al., 2002). Changes to the structure of the heart after injury often result in impaired cardiac function (Cleutjens et al., 1999).

Scar tissue is predominantly composed of type I and III fibrillar collagen (Cleutjens et al., 1995b; Sun and Weber, 2000; Whittaker et al., 1989). Hydroxyproline, used to directly measure collagen in canine infarct tissue, was shown to increase over the first 6 weeks following injury (Jugdutt et al., 1992; Jugdutt and Amy, 1986; Sun and Weber, 2000). Early after MI (~4 days), the levels of type I procollagen mRNA have also been shown to increase in the infarct region and remain at high levels for up to 3 months (Cleutjens et al., 1995b; Sun and Weber, 2000). The balance between collagen synthesis and degradation dictates the severity of fibrosis (over-scarring).

The stiffness of myocardial scar tissue was shown to peak at 1 to 2 weeks post-MI (Holmes et al., 1997), while as mentioned above, density increases were measured over a much longer time frame (Jugdutt and Amy, 1986). This implies that increased myocardial stiffness might be attributable to other factors, such as the architecture and arrangement of collagen fibres (Holmes et al., 1997). Differences are observed in the collagen fibre arrangement between intact and scar tissue. In healthy tissue, the orientation of collagen is described as random and isotropic (no directional dependency) (Whittaker et al., 1989) with fibres surrounding resident cardiomyocytes and adopting a structure often described as having a honeycomb-like appearance (Benedicto et al., 2011). In contrast, the collagen fibre architecture in scar tissue is highly anisotropic (directionally dependent) and fibres are arranged in striated bundles (Whittaker et al., 1989). Mechanical testing of scar tissue displays a greater resistance to deformation in some directions (Holmes et al., 1997; Przyklenk et al., 1987). The increased stiffness of the scar tissue can be detrimental post-MI, as additional strains are imposed on the

surrounding healthy myocardium. This may lead to complications such as wall thinning, cardiac dysfunction, adverse ventricular remodelling, dilatation and eventually heart failure (van den Borne et al., 2010; Dean et al., 2005; Opie et al., 2006; Weisman and Healy, 1987).

1.3.5.1 Cellular composition of the infarct

Scar tissue post-MI was once thought to be an inert and cell-free tissue solely composed of fibrillar (Kenneth Mallory et al., 1939; Lodge-Patch, 1951; Sun and Weber, 2000), it is now viewed as a vascularised, metabolically active, cell-containing, contractile tissue (Cleutjens et al., 1999; Sun and Weber, 2000). Both perivascular (pericyte or smooth muscle) cells and myofibroblast cells have been observed in the infarct (Dobaczewski et al., 2010; Ren et al., 2002). Angiogenesis is a major component of tissue repair and was shown to begin in the infarct tissue 3 days post-MI, and by 2 weeks the vascular network is clearly established. The injured myocardium can remain vascularised for 8 weeks (Cleutjens et al., 1995b) and this vasculature is essential to support the myofibroblast cells that populate the infarct scar tissue during this time (Willems et al., 1994).

1.3.5.2 The infarct expansion

Infarct expansion defined as the disproportionate thinning and dilatation of the infarct region, can occur as early as 24 hours post-MI (Weisman and Healy, 1987). The thinning of the infarct post-MI is likely to be caused by contraction forces generated by resident myofibroblast cells (Sun and Weber, 2000). Substances such as AngII and endothelin-I stimulate the contraction of fibrous tissue (Sun and Weber, 2000). Studies of canine hearts post-MI showed increased infarct contraction and thinning between 4 and 6 weeks after injury (Jugdutt et al., 1992; Jugdutt and Amy, 1986). Infarct expansion contributes to post-MI complications, such as diastolic dysfunction and abnormal ventricular chamber stiffness.

1.4 Scarring optimisation through pharmacological interventions

Following MI, a certain level of scarring is necessary to replace the injured tissue and prevent structural rupture of the heart. However, there is a threshold above which scarring becomes detrimental to the wound healing process. Excessive scar production and remodelling of both the infarct and surrounding uninjured tissues have been linked to a reduction in cardiac function, which subsequently leads to increases in the incidence of heart failure and cardiac arrhythmias, and thus higher mortality rates (Frangogiannis, 2008; Phatharajaree et al., 2007; White et al., 1987). In particular, left ventricular dilation resulting from infarct expansion was identified as a major risk factor for sudden cardiac death (White et al., 1987). Reducing the incidence of these conditions post-MI, may be achievable by manipulation of the cardiac wound healing process through pharmacological intervention with the aim of optimising the level of scarring and minimising pathological remodelling.

Wound healing is a very complex process and interventions can potentially target any number of components, at the molecular level (e.g. modulation of gene expression by addition of effectors), through to the cellular level (e.g. cell therapy), and even the organ proper through structural reinforcements using scaffolds. Determining which component to target, and when to start the intervention, is challenging, given the dynamic nature of the healing heart. Devising a therapeutic strategy that would be efficient across a wide range of patients is confounded by variables such as infarct size, gender, and age (Frantz et al., 2009). A Personalised Medicine approach will almost certainly be needed to successfully manipulate scarring post-MI. Accurate and predictive computational models of scarring and wound healing could thus be invaluable tools to assist with the design of therapeutic targets.

Myofibroblasts have been identified as a potential target for interventions due to their role in the production and remodelling of the collagen-based scar (Chen and Frangogiannis, 2012; Turner and Porter, 2013). Altering myofibroblast function is challenging, as reducing the level of fibroblast activity to the point where the low collagen content leads to the formation of defective scars with low tensile strength, could worsen the prognosis of a patient. The number of myofibroblast cells and their function can be manipulated by altering the levels of TGFβ in the infarct area. A computational model of dermal wound healing predicted that early (e.g. within 7 days) suppression of TGFβ, for example by the way of anti-TGFβ monoclonal antibodies, would significantly reduce the risk of developing hypertrophic wounds (Murphy et al., 2012b). This outcome is consistent with experimental data that showed that the early administration of anti-TGFβ1,2 antibodies was required to induce healing without scarring (i.e. regeneration) of the skin of rodent models (Shah et al., 1994). In general, during dermal wound healing, TGFβ1 and TGFβ2 were found to promote the formation of fibrotic scars in animals and humans, while TGFβ3 appears to induce a regenerative (scar-free) response (Ferguson and O'Kane, 2004).

Activin receptor-like kinase 5 (ALK5) inhibitor is an inhibitor of TGFβ signalling (Figure 1-8) (Inman et al., 2002; Tan et al., 2010). Inhibition of TGFβ1 by gene therapy in the murine heart within 10 days of MI resulted in a significant decrease in the mortality rate and reduced ventricular dilatation, as well as improved heart function (Okada et al., 2005). These improvements were also accompanied by a decrease in the level of fibrosis, possibly because of a decreased number of myofibroblasts within the infarct tissue. The timing of the treatment was critical, as TGFβ1 was shown to be cardioprotective during the acute phase and consequently, early inhibition would result in detrimental effects. Another study showed that inhibiting TGFβ1 seven days prior to MI in mice led to worsened contractile dysfunction at day 1 post-MI, potentially due to an increased number of neutrophils present in the infarcted tissue (Ikeuchi et al., 2004) . When TGFβ1 was inhibited on day 0 and day 7, the collagen volume fraction in the infarct tissue was significantly decreased 28 days post-MI, indicating reduced fibrosis and remodelling.

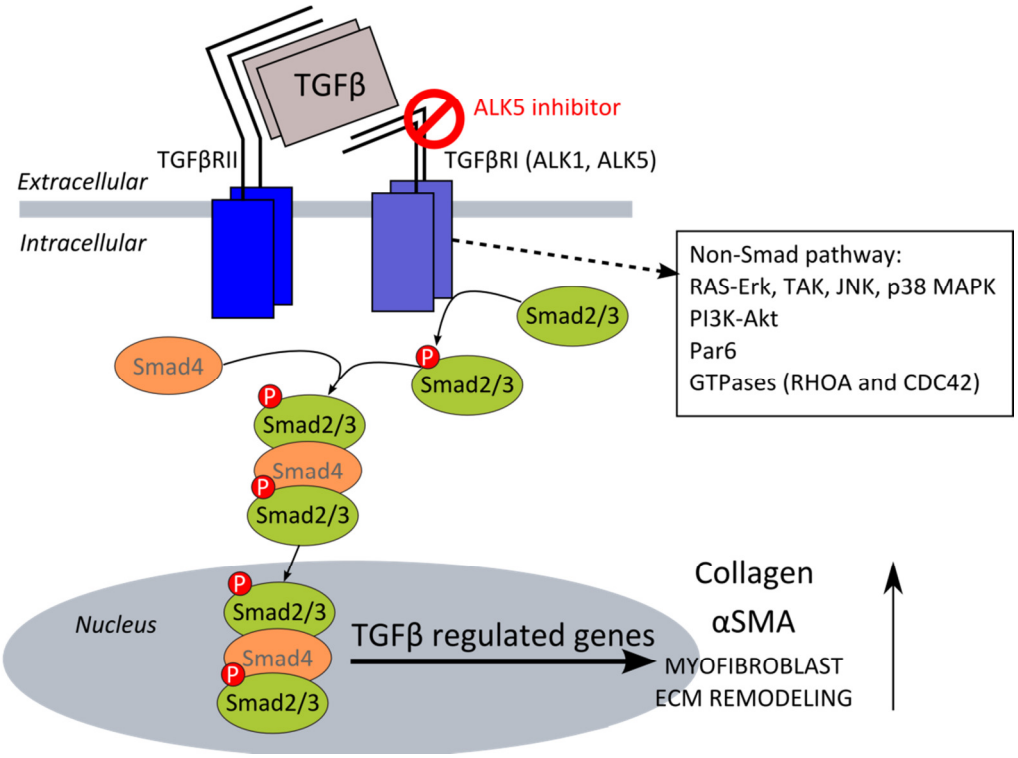

Figure 1-8 The TGFβ signalling pathway. TGFβ can bind with receptors TGFβRII and TGFβRI (ALK5) located at the cell membrane. TGFβRI activates and phosphorylates (P) Smad2/3 which binds and forms a complex with Smad4. In the nucleus this complex regulates TGFβ related gene expression. A non-Smad pathway which includes RAS-Erk, JNK and p38 MAPK can also be activated by TGFβ. An inhibitor activin receptor-like kinase 5 (ALK5) can be used to block TGFβ binding with TGFβRI. This figure has been adapted from (Buijs et al., 2012; Leask, 2010).

Based on the above studies, TGFβ1 is potentially a viable target for pharmacological interventions with the aim of optimising scarring. However, it is necessary to gain a better understanding of its different functions in order to devise the precise window of treatment that would preserve initial cardioprotective effects while minimising longer-term fibrotic effects.

Another candidate for scarring manipulation, related to TGFβ1, is the protein cathepsin S (CatS), whose expression and activity increase significantly post-MI in mice (Chen et al., 2013). CatS is thought to participate in the formation of the scar and the maintenance of left ventricular function post-MI through its role in the TGFβ1 pathway, fibroblast differentiation, and ECM synthesis. Administration of a non-selective CatS inhibitor led to an increase in cytokine expression and to the accumulation of inflammatory cells in the infarct border. The collagen content for treated mice was significantly lower at day 28, coincident with a significant decrease in the number of myofibroblasts within the infarct at day 7. Overall, the heart function was impaired at day 7 and 28 post-MI following inhibition of CatS when compared to controls; however an improved understanding of the timeline of effects associated with CatS mode of action is required to realise any therapeutic potential.

MMPs are potential candidates for the manipulation of the scarring process during cardiac wound healing. Administration of selective or broad-spectrum MMP-inhibitors post-MI in

animal models did not significantly impact the collagen content but attenuated adverse left ventricular remodelling (Lindsey et al., 2002; Rohde et al., 1999). A study that used selective MMPs inhibitors, that spared MMP-1 and MMP-7, to treat pigs revealed decreased collagen content when compared to control conditions (Yarbrough et al., 2003). Similarly, a study showed that the administration of the broad-spectrum MMP inhibitor Illomastat (Witte et al., 1998) also led to a significant decrease in collagen deposition (Creemers et al., 2001). This counter-intuitive result, given that MMPs are proteolytic enzymes and their inhibition should thus lead to an increase in collagen content, was explained by a delayed migration of myofibroblasts into the wound and the interaction of MMPs with inflammatory pathways (e.g. TGFβ). A similar outcome was observed in post-MI murine hearts after administration of an MMP-2 inhibitor, which led to an increased resistance to cardiac rupture and inhibition of macrophage migration towards the infarct zone (Matsumura et al., 2005). The latter suggested MMP-2 activity in the infarcted myocardium generated a chemotactic signal responsible for the recruitment of macrophages. The results of aforementioned studies based on animal models were contradicted by a clinical trial during which long-term administration (>90 days) of an MMP inhibitor with high affinity for all MMPs besides MMP-1 and MMP-7 failed to improve the clinical outcome of patients post-MI (Hudson et al., 2006).

Evidence suggests that FGF-1 and FGF-2, are cardioprotective and could be targeted for scarring manipulation post-MI (Detillieux et al., 2003; Jiang et al., 2002; Palmen et al., 2004). Deletion of FGF-2 in mice led to reduced collagen deposition and fibroblast proliferation post-MI, while overexpression had the opposite effect with increased collagen deposition and fibroblast proliferation (Virag et al., 2007). Similarly, the administration of SU5402, a pan FGF inhibitor, to zebrafish significantly impaired caudal fin regeneration capability (Poss et al., 2000). SU5402 acts by blocking the proliferation of fibroblast-like cells involved in the formation of the blastemal for fin outgrowth. Left ventricular function was preserved in mice overexpressing FGF-2, but was deteriorated in mice where FGF-2 was not expressed. Likewise, overexpression of FGF-1 in mice improved functional recovery post-MI and attenuated cell necrosis induced by reperfusion (Palmen et al., 2004). Administration of FGF-2 before or during ischemic injury in mouse and rat models was also shown to result in increased cardiomyocytes survival and reduced infarct size (Detillieux et al., 2003). Equally administration of FGF-2 during reperfusion following an MI protected against ischemia-reperfusion injury and thus could potentially improve clinical outcome (Jiang et al., 2002).

Up until this point, the various interventions mentioned involved the administration of molecules or the manipulation of gene expression by the way of gene therapy. Another approach, is to use cell therapy, whereby cells are transplanted into the site of injury and either contribute directly to wound healing or indirectly via secretion of growth factors. Transplantation of vascular smooth muscle cells (VSMCs) in rat hearts 4 weeks post-MI was

shown to improve contractile function (Li et al., 1999). In another study, VSMCs were transplanted into rat hearts 2 weeks post-MI, resulting in a decrease in the number of myofibroblasts (thought to be linked to increased levels of bFGF, a known inhibitor of TGFβ-dependant differentiation) and a reduction in pathological remodelling due to improved collagen homeostasis (Fedak et al., 2012).

Many of the potential modulators of fibrosis described in this section reveal a potential for optimisation and manipulation of scarring post-MI. However, all these studies highlight the need to fully understand the very complex cardiac wound healing process in order to determine which molecular and cellular component to target, when to initiate and stop a treatment, and how to make sure that the potential detrimental side-effects remain as minimal as possible. Isolated experiments are not enough to gain an understanding of the intricate interactions between all these different components. There is also a need for suitable computational tools that can be used to integrate the vast amount of experimental data available and for subsequent exploration.

1.5 Analysing the scar post-MI

The ability to image the scar post-MI is critical to gain a better understanding of its formation and maintenance, and also to evaluate the effects of any pharmacological intervention(s). A number of techniques can be used to image the scar, and constituent collagen, in tissue sections with different resolutions and specificity (i.e. ability to differentiate collagen from other structures on an image). Examples of such techniques include brightfield microscopy, polarized light microscopy, immunofluorescence microscopy, and second-harmonic imaging microscopy (Figure 1-9). Ideally, the image produced would be high contrast, in the sense that collagen fibres should be easily distinguishable from the background and other cellular structures, to facilitate interpretation and automated image processing.

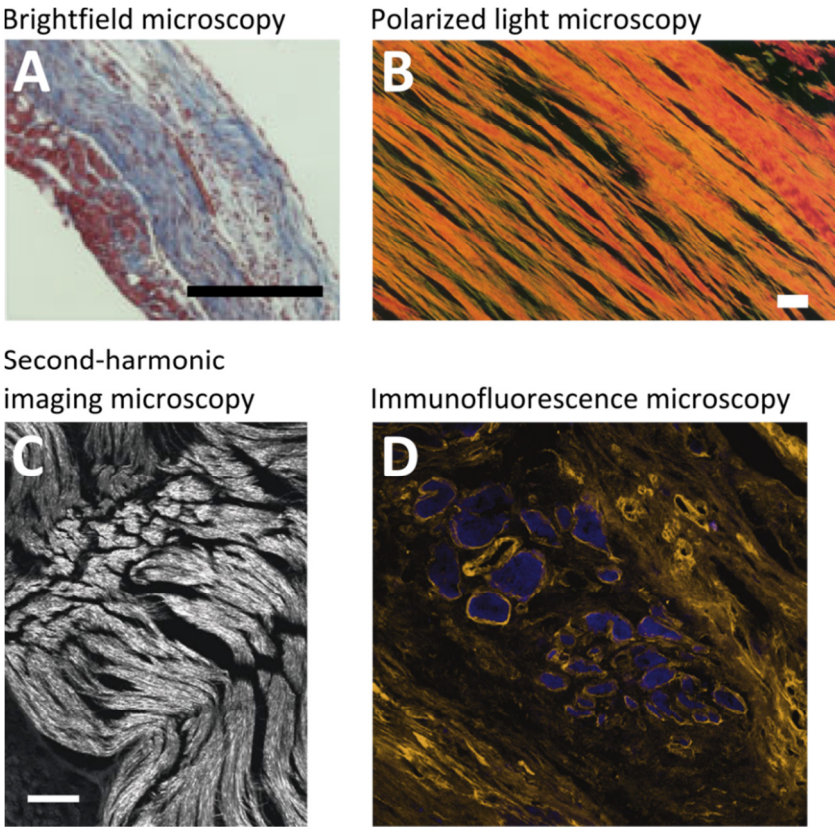

Figure 1-9 Examples of different collagen imaging techniques. (A) Murine heart section 28 days post-MI stained with Masson's trichrome imaged with brightfield microscopy. Collagen stained light blue and scale bar represents 250 µm. Image adapted from (Strijkers et al., 2009). (B) Canine heart sections 6 weeks post-MI stained with picrosirius red imaged with polarized light microscopy. Scale bars represent 20 µm. Image adapted from (Whittaker et al., 1989). (C) Histological section of a kangaroo-tail tendon embedded in a paravertebral muscle of a rat imaged with second-harmonic imaging microscopy. Scale bar represents 50 µm. Image adapted from (Cox et al., 2003). (D) Rat heart section post-MI stained with anti-collagen (orange) and DAPI (blue). Image adapted from (Mewhort et al., 2014). Reproduced with permission.

1.5.1 Brightfield microscopy of stained samples

Brightfield microscopy is routinely used for the imaging of histological tissue sections. This method is not specific to collagen and all structures present in a section will have similar contrast relative to background. In order to image specific structures in tissue sections using light microscopy, it is thus necessary to use histological stains to identify the structures of interest. Masson's trichrome is frequently used for scar tissue imaging as it allows the discrimination between collagen (dyed light blue) and cells (nuclei and cytoplasm dyed in dark brown and light red, respectively). This method was successfully employed to image the scar in tissue sections of post-MI murine hearts (Strijkers et al., 2009). The intensity and extent of the light blue dye can be loosely correlated with the amount of collagen present. The resulting images can still be relatively noisy, making their interpretation challenging (Figure 1-9A). In addition, a light microscopy assessment of samples stained with Masson's trichrome might systematically underestimate the collagen content in a histological section due to the inability to

detect thin fibres, which were easily observable using polarized light microscopy (Whittaker et al., 1994).

1.5.2 Polarized light microscopy

Specificity and contrast can be improved using a variant of light microscopy termed polarized light microscopy. Whereas unpolarized light vibrates in all planes perpendicular to the direction of wave propagation, polarized light vibrates within one of those planes (Changoor et al., 2011). Polarized light can interact with birefringent materials, a property that arises from structural anisotropy, which collagen possesses. As a result, collagen appears brighter than isotropic structures when imaged using polarized light microscopy. The contrast between collagen and background can be further improved by staining with picrosirius red prior to analysis (Figure 1-9 B) as the latter increases the birefringent properties of collagen fibres (Whittaker et al., 1994). Polarized light microscopy can be used to detect changes in fibre packing, thickness, and orientation (Whittaker et al., 1994). The method was applied to the monitoring of changes in collagen structure post-MI in dogs, where increase in mean intensity were related to increases in collagen content (Whittaker et al., 1989), however polarized light microscopy cannot readily differentiate between different collagen types (Rich and Whittaker, 2005).

1.5.3 Second-harmonic imaging microscopy

Another alternative to conventional light microscopy is second-harmonic imaging microscopy (SHIM). As for polarized light microscopy, SHIM does not require prior sample preparation (e.g. stains), instead, SHIM is based on the interaction of high intensity light (usually a laser derived) with non-centrosymmetric structures, which results in the emission of second-harmonic light at half the excitation wavelength (Campagnola et al., 2001; Cox and Kable, 2006). SHIM can be used to analyse the density of collagen, orientation, and morphology based on its non-centrosymmetric properties (Figure 1-9 C). SHIM cannot readily distinguish between different collagen types, and its lack of specificity (i.e. it detects any non-centrosymmetric structure) might lead to the detection of other structures, such as myosin filaments in cardiomyocytes (Cleutjens et al., 1995b; Liu et al., 2013). Discrimination between types collagen type I and III can potentially be achieved based on intensity differences (Cox et al., 2003).

1.5.4 Immunofluorescence microscopy

Immunofluorescence microscopy enables the imaging of biological structures with a very high specificity based on antibody-antigen binding using a fluorescently tagged antibody (the probe)(Odell and Cook, 2013). The most common approach is to use a primary antibody, to bind to the target molecule in the sample. The primary antibody should be raised in a different species to the species of the sample to prevent any possibly cross-reactivity which could occur between the secondary anti-immunoglobulin antibody. The secondary antibody, which is

conjugated to a fluorescent molecule, binds to the primary antibody. The secondary antibody should be raised against the species of the primary antibody. This indirect labelling method results in an amplified signal as multiple fluorescently-tagged secondary antibody molecules can bind to each of the primary antibody molecules. This is in contrast with direct labelling, a one-step protocol where the primary antibody is itself conjugated with the fluorescent molecule, and thus while simpler to carry out, results in lower signal intensities.

Fluorescence occurs when a molecule excited to a higher quantum state after absorption of a photon relaxes down to a ground state, resulting in the emission of a photon of lower energy (i.e. higher wavelength) than the exciting photon (Lakowicz, 2006). As excitation and emission wavelengths are different, it is possible to obtain high contrast images where most of the signal originates from the structure of interest. In immunofluorescence microscopy, the fluorescent molecules usually conjugated to antibodies include fluorescein derivatives such as fluorescein isothiocyanate (FITC) or alexa fluorophores (Panchuk-Voloshina et al., 1999). By carefully choosing the combination of antibody and fluorescent molecules employed, it is possible to image multiple structures simultaneously. In wide-field fluorescence, the entire field of view is excited uniformly, even structures that are out of focus. In contrast, confocal microscopy uses a point illumination (usually a laser) to limit the excitation and emission to a very small volume, significantly increasing the spatial resolution compared to wide-field fluorescence methods (Wilson, 2011). Moreover, by scanning in a plane and along the z-axis, it is possible to reconstruct 3-dimensional (3D) representations of the specimen imaged.

Immunofluorescence microscopy enables characterisation of both the connective and cellular components of the scar post-MI. Antibodies specific for the different types of collagens are readily available (de Jong et al., 2012; Mewhort et al., 2014). Collagen types which have been identified in the rat cardiac ECM are I, III, IV and VI (Bashey et al., 1992). Immunofluorescence microscopy can thus be used to generate high contrast images of collagen in heart tissue sections (Figure 1-9D). Cell type-specific markers can then be employed to identify the active cellular constituents; for example, fibroblast and myofibroblast can be distinguished as the latter express α-SMA (see section 1.3.2.3).

1.5.5 Whole-heart and *in-vivo* imaging

The methods described so far are focused on imaging the scar in histological sections. This requires careful sample preparation. As an alternative, methods for whole-heart *ex-vivo* imaging have been described. Diffusion tensor imaging (DTI) is a method related to magnetic resonance imaging (MRI) and maps the diffusion of molecules in the structure imaged. Instead of only being assigned a contrast value like in standard MRI, voxels in DTI are also associated with diffusion directions and rates. This was employed to non-destructively estimate the alignment of collagen fibres in infarct tissue (Chen et al., 2003; Strijkers et al., 2009).

Non-invasive measurements of collagen *in-vivo* would enable time course studies on a single specimen instead of relying on multiple animals scarified at various time points post-injury. A few methods have been proposed, though none achieves the versatility and resolution of the approaches suitable for histology section imaging. In most cases, *in-vivo* methods enable localization of collagen and estimation of its density but do not enable the characterisation of its structure (e.g. fibre orientation). One such method consists in imaging a novel collagen-specific probes using scintigraphy (isotopic imaging) (Muzard et al., 2009).

1.5.6 Quantitative analysis of collagen structures

The images acquired or generated using the methods described above can be visually inspected in order to gain information about the properties of the scar. However, the data collected is subjective and qualitative, and thus unsuitable for experimental outcome assessment or the establishment of a baseline for comparison with the computational model to be developed in this study.

Quantitative measurements can be carried out using image processing and analysis methods, and in general, two types of measurements represent the major datasets as relevant to this study: collagen content (i.e. density) and morphology (e.g. orientation, patterns). With respect to collagen content, fibrotic areas in liver fibrotic sections were detected by applying an intensity threshold to the mean projection of SHIM optical sections (Guilbert et al., 2010); based on these area measurements, the authors proposed a standardized metric termed the Fibrosis-SHG index, which can be used to compare the degree of fibrosis of various types of biopsies, regardless of their size. Additional information can be gained by morphometric analysis of collagen images. The thickness and spacing of collagen bundles in immunofluorescence images of skin biopsies were automatically measured using standard image processing techniques such as intensity thresholding, skeletenization, and distance map computation (Verhaegen et al., 2012). The thickness and spacing measurements obtained using this approach were significantly different for healthy and scar tissue. Collagen organisation can also be assessed using a first order power plot resulting from the fast Fourier transform (FFT) of immunofluorescence images of collagen bundles (de Vries et al., 2000). The Fourier transform converts an image from the spatial domain to the frequency domain. The collagen forms patterns with an intrinsic frequency, which is made evident in the frequency domain. The order of these patterns was quantified by taking the ratio of the width of the power spectrum resulting from the FFT to its height (Verhaegen et al., 2012).

Another approach based on machine learning (i.e. algorithms capable of learning from data) used intensity distribution statistics (e.g. mean, skewness, kurtosis) and gray level co-occurrence matrix (GLCM, a representation of image texture) to classify SHIM images of collagen into one of five categories: curled, high density, disoriented and dense, random distribution, and straight

(Mostaço-Guidolin et al., 2013). A classification accuracy (as assessed by comparison with classification by human experts) >90% was achieved, but it did not provide a mean to directly quantify morphological attributes such as orientation, which was necessary for this work.

1.6 Mathematical modelling of biological complexity

Over recent years, mathematical modelling and computational methods in biology have become increasingly popular (Noble, 2002). These numerical tools are now routinely used to complement experimental and empirical approaches when tackling complex biological processes. This rapid uptake was made possible by multiple factors. First, advances in experimental techniques and methods enable the generation of previously unattainable quantitative data that is suitable for abstracted representations of biological systems (Gavaghan et al., 2006). In parallel to these advances, the computational power readily available to researchers has increased at an exponential rate (Moore and Fellow, 1998) and now enables development of models with fewer compromises, thus resulting in more accurate approximations of biological complexity. A system-wide approach to biological modelling, for example by simulating each individual component of a physiological system, is often overly complex and impractical. Instead focusing on the few key elements of the system is preferable (Noble, 2002) since increasing the complexity may be detrimental to the ability of the model to accurately mimic the biology or be subsequently validated.

Agent based modelling has been used to simulate a wide range of biological processes, from cell migration (Groh and Wagner, 2011) to the dynamics of the immune response (Chavali et al., 2008). Agent based modelling involves simulation of a collection of entities which can be people (Graw et al., 2012), animals (Pratt et al., 2005) or even molecules (Pogson et al., 2006). For biological models, agents often represent individual cells. Each agent has properties (e.g. size) and behaviours (e.g. proliferation, migration). A typical property is the location of the agent, which allows the development of spatial models (Groh and Wagner, 2011). This spatial component often greatly simplifies visualisation and interpretation of the simulation results. In many cases, behaviours that are not explicitly included in a model can emerge due to the interactions between agents. Agent based models are usually hybrid, combining stochastic elements with more conventional approaches, such as ordinary differential equations (ODEs) or partial differential equations (PDEs). Differential equations describe how the rate of change of a variable (i.e. its derivate) relates to another variable. ODEs contain a single independent variable (and its derivatives), whereas PDEs contain multiple variables (and their derivatives). As such, multiple scales can potentially be combined in agent-based models, for example gene expression modelled with ODEs could dictate the value of one of the agent properties (e.g. expression of a gene impacting on proliferation rates of cells). Another advantage of agent based models is that the parameters used tend to correspond to measurable quantities, instead of

more abstract and artificial parameters used in other types of models. While potentially powerful, these models can be computationally demanding.

Spatial behaviours involving multiple cells have been extensively modelled using agent based approaches. A typical example is cell migration, in particular systems where the cells interact with their environment (e.g. ECM) or with each other. A model to investigate the effects of ECM properties (e.g. density, anisotropy, stiffness) on cell migration (Schlüter et al., 2012) predicted that cells tend to remain in or migrate towards regions of high stiffness. Moreover, the model accurately predicted the biphasic relationship between cell speed and ECM density, which is in agreement with experimental results (Palecek et al., 1997). Rules for cell-cell interactions included a simple implementation of contact inhibition of locomotion, whereby cell direction is altered to avoid a cell-cell collision. A similar approach was taken when developing a three dimensional model of cell migration biased by a chemotactic cue such as migration along ECM fibres such as collagen (Groh and Wagner, 2011); here the model predicted that both chemotaxis and contact guidance were required for desmoplasia (growth of dense connective tissue around tumors caused by migration and proliferation of fibroblasts).

The immune response involves multiple cell types and interactions between cells and their environment (e.g. cytokines), which is challenging to investigate experimentally. Agent based modelling lends itself well to this system as it can accommodate different cellular and molecular scales to simulate cell-cell interactions and influence of molecular cues (Chavali et al., 2008). For example, the binding dynamics between T-cell receptors (TCRs) and major histocompatibility complex (MHC) molecules, a key step of the immune response, was studied in a model where the agents represented molecules subject to Brownian motion (Casal et al., 2005). Another agent based model was used to study the formation of granulomas (collection of macrophages spatially surrounding and isolating infectious organisms) following an infection of the lungs by bacteria (Segovia-Juarez et al., 2004). The key cell players, T cells and macrophages, were the agents in the model while bacteria and a chemoattractant were represented as continuous variables. The environment is a collection of micro-compartments similar to a cellular automaton model. After exploration of the model parameter space, three stable simulation outcomes relatable to known pathological scenarios were identified: clearance (elimination of the infection), containment, and dissemination (failure to contain or eliminate infection).

These types of models have been applied to many areas of biology and physiology. The next section will focus on their application to the heart.

1.7 Mathematical modelling of the heart

Early models of the heart tended to focus on its electrophysiology. For example, the action potential of cardiac muscle cells was simulated based on the Hodgkin and Huxley model, a set of non-linear differential equations describing how electric current propagates through excitable cells based on membrane properties (Noble, 1960). Even though the equations were originally devised for neuronal activity, it was possible to adjust the model parameters to recreate an unstable system that resulted in pacemaker activity (diastole depolarization) typical of cardiac cells. This work led to the establishment of cardiac modelling software such as Oxsoft, which is still in use today (Hilgemann and Noble, 1987). This approach, for example, was employed to investigate how selectively blocking specific ion channels could minimise the risk of developing cardiac arrhythmias (Noble and Noble, 2000). Electrophysiology models were successfully extended from the simulation of a single or small group of cells to heterogeneous tissues containing multiple cells types (ten Tusscher et al., 2004) and to the whole heart (Trayanova, 2011).

Models have also attempted to combine electrophysiology with other key aspects underlying heart structure and function. For instance, an electromechanics model was developed by coupling the aforementioned model by Noble with the Hunter-McCulloch-ter Keurs model which describes the mechanical properties of contracting cardiac muscle cells (Hunter et al., 1998; Nickerson et al., 2001; Noble et al., 1998). This hybrid model was used to relate changes in the length of cardiac muscle fibres with changes in both the intracellular calcium concentration and associated action potential. Another model took into account the specific structure and morphology of ventricular myocytes, whose plasma membrane forms invaginated structures known as T-tubules (Pásek et al., 2006). The model showed that T-tubules contributed significantly to calcium transport and homeostasis in ventricular cardiomyocytes. Blood flow in the heart has been another aspect of cardiac function that attracted much attention from a modelling standpoint. These models, often based on finite difference and element methods (numerical methods to approximate solutions of differential equations), can accommodate vastly different scales including epicardial vessels, intramural vessels and microcirculation (Lee and Smith, 2012; Smith et al., 2002).

The following section discusses models of wound healing in general, before presenting approaches proposed for modelling the response of the heart to injury.

1.8 Mathematical modelling of wound healing

A large proportion of wound healing models, described in the literature, focus on the skin. A likely reason for this is the relative ease with which experimental data can be acquired. In contrast, wound healing in other organs, such as the heart, is much more challenging to

characterise. Key factors in dermal wound healing are generic to most organ systems, including the heart, namely cell migration, chemotaxis, cell proliferation, cell differentiation and cell mediated scar formation (Sherratt and Dallon, 2002). Different methods have been applied to the modelling of dermal wound healing (Geris et al., 2010), including differential equation (Menon et al., 2012; Tranquillo and Murray, 1992), level sets (Javierre et al., 2009), and agent-based (Dallon et al., 1999) models. A few examples of applications of these methods are discussed below.

Early models applied differential equations to simulate wound healing. In these instances, all components (e.g. ECM, cells) were represented by their density or concentration, which varied with time according to rate constants and the density of components they interacted with. For example the rate of change in the collagen density might be based on the local density of fibroblast cells. One such model simulated cellular, biochemical, and biomechanical phenomena during the wound healing process in a one-dimensional framework (Tranquillo and Murray, 1992). The migration of fibroblast cells was modelled as a diffusion process (i.e. passive transport, here representing random migration) with a convective element (i.e. active transport, here representing biased migration) depending on the ECM, and was influenced by cytokine gradients (i.e. chemotaxis). Cell proliferation was modelled using the logistic growth equation (formulation approximating the lag, exponential, and stationary phases of cell growth), and was also affected by cytokine gradients. The ECM was considered a homogeneous compressible solid subject to traction forces exerted by migrating cells, as well as reaction forces due to the attachment of the ECM to subdermal tissue. The two types of forces (traction and reaction) drove the contraction of the wound with time. The model was used to understand the conditions under which wound contraction could result from changes in fibroblast properties, as induced by inflammatory cytokines gradients (Tranquillo and Murray, 1992). This model was further extended by taking into account both the differentiation of fibroblast cells into myofibroblasts and the effect of changes in tissue elasticity as a result of ECM accumulation (Murphy et al., 2012a). Myofibroblast differentiation was mediated by TGFβ and elastic stress; the latter being proportional to the density of the collagen matrix. The model also included fibroblast and myofibroblast-synthesised collagenases, which activated TGFβ and degraded the ECM. Qualitative comparisons of model predictions with experimental datasets were in agreement and the model successfully recapitulated the main phases of dermal wound healing. Another model based on similar principles was developed with the aim of better understanding the ECM remodelling as induced by cell migration as well as contact guidance, whereby ECM orientation influences the direction of cell migration (Taylor et al., 1998). As the model did not include chemotaxis, cell migration was dictated by a combination of random locomotion and contact guidance, with the cells continuously moving towards the wound. For both forms of movement, the cell speed was affected by the ECM density: cells were assumed not to migrate in absence of

ECM and, conversely, to be impeded by highly dense matrices. The ECM fibres were either horizontal or vertical, and could switch between the two during the simulations due to cell-mediated realignment. Ultimately this model, predicted faster healing tends to be associated with higher degrees of ECM alignment and increased scarring.

The presence of pathogens and changes in oxygen levels are likely to be important determinants of dermal wound healing. These factors were included in a model using a system of ODEs that represented the damage as inversely proportional to the degree of healing, pathogens, inflammation, and number of fibroblasts (Menke et al., 2009). The pathogens rate of proliferation was assumed to be increased in low level oxygen conditions (O_2), such as those found in wound healing in diabetic patients (Falanga, 2005). Inflammation resulted in decreased levels of pathogen's, but at the risk of increased damage. The recruitment and proliferation of fibroblasts were modulated by the degree of damage and inflammation and in-turn, the injury decreased proportionally with the number of fibroblasts present. The model predicted that wound dimensions above a certain threshold would not heal within two weeks after injury, which was in agreement with clinical outcomes of large acute wounds. It also showed that high levels of oxygenation are usually optimal, whereas decreased levels might lead to impaired wound healing and, in extreme cases, to chronic infections. Based on their results, the authors suggested that pharmacological intervention to increase fibroblast recruitment could potentially lead to faster healing rates.

The modelling approaches discussed above relied on systems of differential equations to describe the time course of the wound healing process and how its different components changed overtime. The rapid increase in computational power, accompanied by programming paradigms such as object-oriented programming, enabled the development of models whereby units of a process can be simulated individually, rather than as a collection (e.g. density of cells in ODE models). This agent-based approach is particularly suited for wound healing processes that are mainly steered by the interactions between cells (i.e. the agents) and their environment (e.g. ECM, chemotactic gradient, other cells).

The framework that inspired a large number of agent-based models of wound healing was devised by Dallon and colleagues in the late nineties (Dallon et al., 1999). The model mainly focused on the interactions between fibroblast cells and collagen fibres in the skin. The tissue was simulated as a 2-dimensional (2D) Cartesian coordinate system. The fibroblast cells were setup as the agents (discrete objects), and were assigned a set of behaviours (migration, ECM remodelling capability) and properties (e.g. position, velocity, area of influence). The collagen ECM was modelled as a continuum, which was sampled at equally spaced grid points as vectors whose magnitude and direction represented ECM density and dominant orientation, respectively. The velocity of the cells was computed at each time step based on their previous

motion (i.e. momentum) and the local collagen dominant orientation, thus approximating contact guidance. Cell migration also induced the remodelling of the local ECM whereby the collagen continuum was altered based on the collective velocity, area of influence, and proximity of the migrating cells. The model predicted that the ECM degree of alignment increased with cell speed. Moreover, having the direction of cell migration mainly influenced by its momentum led to increased alignment when compared to the case where local ECM orientation was the main influence on cell velocity.

This model of fibroblast and ECM interaction was then extended to scenarios that can be related to wound healing (Dallon et al., 1999). Firstly, two types of ECM were then considered: collagen (initially only in healthy tissue) and fibrin (blood clot). The initial state of the simulated tissue contained two non-overlapping regions representing healthy tissue surrounding a blood clot, solely composed of collagen and fibrin, respectively. The healing process was carried out by fibroblasts that could deposit collagen as well as degrade both collagen and fibrin. Cell speed was also influenced by local ECM density, whereby increasing collagen density impeded cell speed while fibrin had a beneficial effect.

A later iteration of the model was used to better understand the effects of TGFβ on the dynamics of dermal wound healing (Dallon et al., 2000; Dallon et al., 2001). TGFβ was modelled as having a uniform concentration throughout the wounded region. Its concentration was varied with time based on experimental data, with a steep increase around 48 hours, which corresponded to the initial infiltration of the wound by fibroblast cells. The concentration of TGFβ at a given time influenced motility (cell speed and flux of cells into the wound decrease with increasing TGFβ concentration), proliferation (growth rate increases with TGFβ concentration), and ECM remodelling capabilities (collagen production and degradation increase and decrease with TGFβ concentration, respectively). The combined effects of an increase in TGFβ concentration resulted in net increase in ECM alignment. This extended model was thus a useful tool to study how varying chemical cues (in this case TGFβ) can drastically alter simulation outcomes and thus inform potential therapeutic strategies.

Spatial concentration gradients (e.g. difference in concentration between two extremities of a cell) enable the introduction of directional biases in otherwise random processes. A typical example is chemotaxis during which cells tend to migrate in the direction corresponding to the largest change in the concentration of a chemoattractant. Whereas the previous model implemented chemical cues as step changes in concentration, a further extension included chemical gradients (McDougall et al., 2006). A single generic chemotactic gradient was generated within the wounded region and diffused outwards. The chemoattractant concentration was thus maximal in the wounded region and gradually decreased with the distance from the centre of the wound due to diffusion and a decay term. The gradient represented the collection

of cues that lead to infiltration of the wound by fibroblast cells. The equation dictating cell velocity was modified accordingly to take into account not only the concentration but also the local gradient of the chemoattractant. The model predicted that without chemotaxis (e.g. random locomotion and contact guidance only), very little healing would occur over the period of time considered. In addition, a higher rate of diffusion led to increased alignment in both the healthy and injured tissue. Such an outcome is indicative of detrimental scarring.

Another agent-based dermal wound healing model adopted a different representation for the ECM continuum. It was suggested that the vector-based representation originally proposed by Dallon had two main drawbacks: ambiguities due to the bi-directional nature of the vectors and the fact that it did not provide information about local ECM isotropy (Cumming et al., 2010). As an alternative, a tensor-based representation of ECM orientation was proposed. At each sampled point, the orientation tensor is computed based on the orientation and density of individual ECM fibres at that point. The tensor can then be decomposed into the sum of its orthogonal eigenvalues and eigenvectors, which in turn inform on the degree of isotropy and alignment of fibres at that position. As was the case in the Dallon modelling framework, cells and chemicals were modelled as agents and continua, respectively. The model included other refinements such as the way cells responded to cytokines by taking into account binding kinetics of cytokines to cell receptors instead of assuming an instantaneous response. Moreover, cells had a finite number of receptors so that pharmacological interventions involving the blocking of receptors could be evaluated. The model also included a form of contact inhibition of locomotion by not allowing cells to overlap. The model predicted that overall ECM alignment would decrease when the proportion of receptors available for TGFβ binding was reduced, which was in agreement with the results obtained with the Dallon model despite significant differences in the modelling approaches employed. The direct availability of the alignment and isotropy information also facilitated the interpretation of simulation outcomes.

During dermal wound healing, mechanical properties of the tissue are thought to be a key factor for wound contraction and the alignment of ECM fibres. The residing tension field resulting from wound contraction was taken into account in a biomechanical model of dermal wound healing (Yang et al., 2013). This was achieved through the concept of fibre-reinforced soft tissue whose mechanical properties depended on the structural properties of the embedded ECM fibres, in particular their anisotropy. When large deformation of this soft tissue occurred, for example through wound contraction, collagen fibres realigned along the resulting tension lines. This phenomenon, in conjunction with the aforementioned cell-mediated ECM remodelling, was thought to explain the formation of hypertrophic scars comprised of highly aligned ECM fibres. The contractions patterns produced by the model for different wound geometries were in good agreement with experimental data.

1.9 Mathematical modelling of cardiac wound healing post-MI

In contrast to the extensive dermal wound healing modelling literature, only a few studies have investigated cardiac wound healing and documented effects post-MI.

Abnormal strain due to changes in structure and material properties in the aftermath of MI might lead to heart failure and cardiac dysfunction such as arrhythmias. This was investigated using a model that simulated the effects of strains resulting from MI on the electrophysiology of the left ventricle during a single heartbeat (Wall et al., 2012). The hybrid model includes continuum mechanics, electrical diffusion, and cellular dynamics components. The simulated domain (left ventricle) was defined by a 3D mesh built from MRI images, which was split into three regions: healthy tissue, border zone, and infarct zone. Tissue mechanics was described by a passive term that represented its intrinsic properties (e.g. deformability, elasticity) and an active term influenced by the forces exerted by cardiomyocytes contraction in response to changes in transmembrane voltage. ECM fibres orientation was derived from diffusion tensor imaging of an explanted heart. The infarct was acellular, had no contractile activity, had impeded electrical diffusion, and was very stiff. The infarct border was an intermediate domain with some degree of active contraction that was less than that of the healthy tissue. Based on these components, cardiac cycle corresponding to a heartbeat could be simulated. The model provided a reasonable fit to experimentally observed heart function. It also highlighted how changes in cellular and extracellular connectivity could lead to abnormal action potentials and thus arrhythmias.

A partial differential equation model was developed to simulate the left ventricle remodelling following MI (Jin et al., 2011). Gene expression analysis of infarct tissue and plasma components profiling were used to identify key biomarkers of left ventricle remodelling. This experimental data informed the design of the mathematical model with regards to the cell types (i.e. monocytes, macrophages, and cardiac fibroblasts) and key molecules (i.e. TGFβ1 and MMP-9). Monocytes infiltrated the wound, where they differentiated into macrophages that secreted both MMP-9 (responsible for collagen degradation) and TGFβ (promotes monocyte recruitment, inhibited MMP-9 activity, and stimulated fibroblast proliferation). Finally, fibroblast cells were modelled as responsible for the production of collagen. Myofibroblasts were not explicitly modelled but their phenotype was approximated by production of TGFβ to increase the rate of collagen deposition by fibroblast cells. Contact inhibition of proliferation was included in the model in the form of a crowding effect, whereby fibroblast proliferation was inversely proportional to the total cell density. The degradation of the collagen matrix by MMP-9 was subject to binding of the activated form of the latter with collagen fibres, and modelled using simple enzymatic reaction kinetics where a reversible binding reaction took place between activated MMP-9 and collagen, resulting in a binding between a MMP-9 and collagen complex.

This was followed by an irreversible reaction whose products were fragmented collagen peptides and the released MMP-9 enzyme. Extensive simulations revealed that the balance between ECM deposition and degradation was a key determinant of scar formation and thus that its manipulation could represent a viable therapeutic strategy to modulate scarring.

As with other types of wound healing, agent-based models are well suited for the simulation of cardiac wound healing post-MI. In particular, it allows the integration of processes taking place at different scales (e.g. molecular, cellular, tissue scales) and the combination of stochastic modelling of objects with analytical approaches such as ODEs and PDEs. An agent-based approach was taken for the simulation of cardiac wound healing by incorporating mechanical, structural, and chemical cues into a model of the formation of a scar post injury (Rouillard and Holmes, 2012) largely inspired by the dermal wound healing model (Dallon et al., 1999; McDougall et al., 2006). The proposed mathematical model was informed and compared to *in-vivo* experimental data produced using a cryoinfarction model of MI where a circular wound is induced by selectively freezing part of the left ventricle. Consequently, the wound in the mathematical model was represented by a circular region surrounded by a rectangular area of healthy tissue. Fibroblast cells were the agents, which could migrate, proliferate, undergo apoptosis and interact with the ECM through its deposition, degradation, and re-orientation. The chemical cues were represented as a generic chemokine gradient modelled based on a steady state reaction-diffusion equation with generation limited to the infarct region. Migratory, proliferative, and ECM remodelling behaviours of the cells were activated proportionally to the local chemokine concentration. Cell migration trajectories were dictated by the chemokine gradient direction, as well as their momentum, the local ECM orientation (contact guidance), and mechanical strain. The latter was modelled as a cumulative normal distribution centred at the infarct border, which was mostly flat at the exception of the region corresponding to the infarct border. The simulation results suggested that the mechanical guidance cue was necessary to achieve the expected long-term ECM remodelling leading to the high tissue anisotropy (high alignment) usually observed experimentally. Different wound shapes, and thus different chemical guidance cues profiles, resulted in similar long-term alignment patterns, which was in agreement with data from cryoinfarction experiments. The initialization state of the ECM matrix (e.g. aligned and unaligned) was found to only have short-term effects as different simulations tended to eventually converge.

Although the model proposed by Rouillard and Holmes shares many points with the mathematical model of cardiac wound healing presented in this work, they differ on several fundamental aspects. While this model focuses on cell-mediated changes in local collagen structures as measured by a bespoke metric of local alignment, the main outputs of their model were tissue-wide measurements such as collagen orientation histograms and mean collagen angle. The implementation of the inflammatory cues was also different, where their model

assumed continuous production within the wound whereas the chemotactic gradient in the model presented here is activated and subsequently allowed to decay in agreement with previously reported experimental findings. The behaviours of the cells also differed significantly between the two models. Rouillard and Holmes' model approximated contact inhibition of locomotion by stopping the migration of a cell if its destination was already occupied by another cell. In contrast, the model presented in this work simulates cell avoidance; a cell attempts to alter its migration direction when encountering an obstacle in its path. The main differentiator between the two studies is the type of experiments carried out with the respective models. While Rouillard and Holmes mainly focused on developing a model capable of recapitulating their previous experimental findings, this study will attempt to predict the effects of pharmacological interventions on the scarring process post-MI.

The Rouillard and Holmes model was later extended by replacing the cumulative normal distribution representation of the strain field by a finite-element model (FEM), which enabled the direct use of experimental data (Rouillard and Holmes, 2014). The domain of the agent-based model was a 20 by 20 array of patches, directly linked to a mesh of 20 by 20 elements in the FEM. The FEM informed the remodelling of the collagen matrix by mechanical strain in the various patches of the agent-based model. Simulations showed that it was necessary to let mechanical stresses increase over time (related to infarct thinning) in order to match measured strain experimentally.

1.10 Towards a predictive mathematical model of cardiac wound healing post-myocardial infarction

Cardiac wound healing post-MI is a complex process involving the interaction between a large number of components across multiple time and length scales. Although the contributions of individual parts have been extensively studied, it remains challenging to gain a thorough understanding of how their interactions influence the clinical outcome of the healing process. In particular, the sequence of events leading to detrimental scarring needs to be fully characterised in order to devise therapeutic strategies for its modulation to strike a balance between effective wound healing and tissue regeneration versus excessive fibrosis and pathological remodelling of the injured heart. For instance, it might be necessary to promote scarring during the acute phase of healing to ensure that the heart's structural integrity is maintained while minimising the risks of fibrosis and adverse remodelling in the longer term.

In-vitro experiments are unlikely to provide insights into a cardiac wound healing model that can be directly applied in a clinical context. Although the gold standard remains *in-vivo* studies, dynamic processes taking place at a molecular and cellular scale cannot easily be observed and quantified non-invasively in animal models. Instead, the information available is generally limited to discrete snapshots from which an approximate time course is extrapolated. The

throughput of *in-vivo* studies is also generally low, thus limiting the range of investigations that can be reasonably carried out. In the related field of dermal wound healing, mathematical models have been used extensively to integrate experimental data into a knowledge-based framework that enabled simulations whose outcome were in good agreement with clinical data. The aim of this project was to devise such a predictive model for cardiac wound healing post-MI focusing extensively on fibroblast-mediated collagen scar production and remodelling.

In order to achieve this aim, individual cell behaviours relevant to scar formation and remodelling were quantified *in-vitro* (Chapter 2). The experiments were designed so that the information gained could be applied directly in the mathematical model. Behaviours of interest included fibroblast cell migration, proliferation, and differentiation. A series of scratch assay experiments were carried out using low passage number primary cardiac cells isolated from murine hearts. The effects on cell behaviour of various treatments mimicking potential pharmacological interventions were also investigated.

In-vivo experimental data was collated to determine suitable initial conditions for the mathematical model (e.g. number of cells, wound size, collagen arrangement) and to provide a baseline against which the model output could be validated (Chapter 3). The information was derived from immunofluorescence microscopy images of histological section from healthy and injured murine hearts. An automated image processing algorithm was employed to detect and analyse collagen bundles on heart sections and a novel metric was developed to quantify local and global collagen alignment patterns from the output of the image processing algorithm.

A mathematical agent-based model of cardiac wound healing whose design was informed by *in-vitro* and *in-vivo* experimental data was developed (Chapter 4). The model was inspired by a dermal wound healing modelling framework (Dallon et al., 1999; McDougall et al., 2006). The time period simulated by the model was initiated at the later stage of the inflammatory phase (~48 hours post-MI), at which point fibroblast cells are beginning to infiltrate the wound (Frangogiannis et al., 2000; Sun et al., 2000). The cells were modelled as agents which migrate, proliferate, undergo apoptosis, differentiate, and interact with the ECM to bring about its deposition, degradation, and re-orientation. The outcomes of simulations were evaluated in terms of collagen alignment, collagen content, and cell numbers. The various components of the models were tested and their effects on simulation outcomes assessed.

The model outputs were then compared with *in-vivo* experimental data (Chapter 5). Discrepancies were identified and discussed. The model was also used to predict the effects of potential pharmacological interventions on the scarring process based on the corresponding *in-vitro* experimental data. The testing of equivalent pharmacological interventions in a murine model of MI to subsequently validate model predictions represents a key area of further study.

Chapter 2

In-vitro experiments to inform model parameter values

2.1 Introduction

Cardiac wound healing post myocardial infarction (MI) is a highly complex process, which is often described as consisting of three partially overlapping phases: inflammatory; proliferative and maturation (Chen and Frangogiannis, 2012). During the inflammatory phase, immune cells such as neutrophils and monocytes infiltrate the wound to remove necrotic cells and debris resulting from MI (Chen and Frangogiannis, 2012; Frantz et al., 2009). Indeed, the hypoxic environment established as a result of coronary artery occlusion contributes to the death of cells within the cardiac tissue, including cardiomyocytes that are essential for normal heart function (Frangogiannis et al., 2002). Directed migration (chemotaxis) and proliferation of the immune cells are promoted by pro-inflammatory factors such as tumor necrosis factor alpha (TNF-α) and Interleukin-1 beta (IL-1β) (Frangogiannis et al., 2002; Frantz et al., 2009; Nahrendorf et al., 2010). The proliferative phase is characterised by the production of a scar by cardiac fibroblast cells to replace the damaged tissue (Chen and Frangogiannis, 2012). Finally, during the maturation phase the collagen matrix undergoes cross-linking, induced by cross-linking enzymes. Cross-linking of the collagen is a feature of scar maturation and enhances the tensile strength of the infarct. Moreover this process can contribute to diastolic dysfunction and cause increased passive stiffness (Dobaczewski et al., 2010).

The migration, proliferation, and differentiation of cardiac fibroblasts into myofibroblasts are thought to play important roles during cardiac wound healing in general, and during the proliferative phase in particular (Souders et al., 2009). The migration of fibroblasts from neighbouring healthy tissue towards the site of injury and their subsequent proliferation ensure that a sufficient number of cells reach the infarct for tissue reparation and scar formation. Following infiltration, fibroblast cells produce and secrete collagen type I, one of the main constituent of the fibrotic scar tissue (van den Borne et al., 2010). Fibroblast cells can differentiate to myofibroblast cells, an activated phenotype that produce increased levels of collagen types I and III (Souders et al., 2009), contract using alpha-smooth muscle actin (α-SMA) and myosin bundles (Hinz et al., 2001; Hinz, 2010; Sun and Weber, 2000; Willems et al.,

1994), and possess dimensions larger than those of inactivated fibroblasts (Masur et al., 1996; Masur et al., 1999). In addition to their ability to lay down collagen, both fibroblast and myofibroblast cells can re-arrange the collagen matrix through interactions during migration, myofibroblasts having the additional ability to pull fibre bundles together through cell contractions (Petroll et al., 2003). The cell area partially dictates the organisation within tissues and also determines the extent of the contact between the cell and the extra-cellular matrix (ECM). This might in-turn influence the impact a cell will have on its surrounding ECM and to what degree it will remodel the ECM during migration and contractions.

The function and phenotype of *in-vitro* cardiac fibroblast cells were shown to be influenced by the biochemical and physicochemical environment of the injured heart, including low oxygen levels (oxidative stress) and cytokines concentrations (Zhang et al., 2001). Hydrogen peroxide (H_2O_2) a reactive oxygen species (ROS) has been shown to increase the matrix metalloproteinase (MMP) activity of adult rat cardiac fibroblasts (Siwik et al., 2001). Fibroblast differentiation to myofibroblasts is promoted by the pro-inflammatory stimulus transforming growth factor beta (TGFβ) (Chen and Frangogiannis, 2012). The inhibition of the TGFβ pathway through administration of an ALK5 inhibitor (targeting TGFβ receptor 1) in rats post-MI reduced the expression α-SMA (i.e. lower number of myofibroblast cells) and production of collagen I in the non-infarct regions (Tan et al., 2010).

Likewise, the vascular endothelial growth factor (VEGF) and fibroblast growth factor (FGF) signalling pathways play a role in myofibroblast differentiation but also in the proliferation and collagen production behaviours of fibroblast cells (Kaftan et al., 2012; Murakami et al., 2008; Zhao et al., 2014). Conversely, deletion of FGF-2 in mice led to reduced levels of collagen deposition and fibroblast proliferation post injury (Virag et al., 2007). The administration of a pan FGF inhibitor such as SU5402 could in principle be used to manipulate FGF signalling and thus the outcome of scarring post-MI (Palmen et al., 2004).

The computational model presented in this work focuses on the proliferative phase of the wound healing process and as such, relies on the availability of quantitative information regarding the migration, proliferation, and differentiation behaviours of cardiac fibroblast cells in the context of an injury. A common approach was to derive this information from the published literature. However, this can be challenging for two main reasons. First, the experimental setup and conditions of published studies might not match the model requirements. For example, particular behaviours of interest might have been thoroughly tested and documented but with a different cell type than the one considered in the model. However, this data would still be considered acceptable in cases where there are fewer better alternatives. The second challenge with using published studies as a basis for parameter value estimation is related to how the experimental results are presented and communicated. It is not uncommon for high quality and

relevant publications to omit readily usable quantitative data. Sometimes for example cellular parameters (i.e. numbers, area) can be estimated from microscopy images provided in a publication but again, this is far from being ideal. The modelling approach taken for this work (agent-based modelling) has an advantage over most other types of models in that they can often accommodate semi-quantitative and observational data.

Experiments were carried out in order to obtain the information required for the establishment of a biologically relevant, and ideally predictive, cardiac wound healing model. Due to the dynamic nature of cardiac wound healing, evaluating the contribution of fibroblast-specific properties and behaviours (e.g. migration, proliferation) to the scarring process *in-vivo* is extremely difficult. As an alternative, an injury can be mimicked *in-vitro* by growing cells to a confluent monolayer before mechanically dissociating a portion of the cells, resulting in a synthetic wound, also known as a scratch assay (Liang et al., 2007). Conventional analytical approaches such as molecular biology and microscopy can then be employed to quantify cell behaviours and properties (e.g. area) with defined biochemical and physicochemical environments (e.g. by adding a signalling molecule to the culture medium). The hearts ECM and the fibrotic scar tissue can also be approximated by coating the growth surface with collagen I prior to seeding.

This simple scratch assay experimental model is useful to study individual cell behaviours and properties. This experimental setup could not possibly re-create the complex and dynamic environment of the cardiac tissue during wound healing. The measurements obtained from these *in-vitro* experiments, together with cues from *in-vivo* studies (see chapter 3), represented a baseline for building the computational model of cardiac wound healing. The complex events expected to occur during cardiac wound healing could possibly emerge as a result of the interactions between individual cells and their environment during model simulations. As such, the computational model served as an intermediary that could potentially improve the understanding of the effects of changes measured *in-vitro* in the context of *in-vivo* cardiac wound healing. This approach enabled tailoring of the experiments for requirements of the model and conversely, to develop the model knowing the limitations and constraints of the experimental systems used.

2.1 Aims

The computational model required a number of parameters whose value could potentially be determined using *in-vitro* scratch assay experiments. The aims of this section were thus the following:

- Determine the most appropriate cell model for cell behaviour assessment, either a cell line such as NIH 3T3 cells or primary cells isolated from heart or skin tissues.

- Devise a simple *in-vitro* experimental setup that closely mimics the *in-vivo* setting and the different stages of the wound healing process such as inflammatory response and hypoxia.
- Measure cell behaviour and properties such as migration speed, contact inhibition of locomotion, cell area, proliferation, and differentiation rates.
- Assess the effects of pharmacological interventions to target three signalling pathways with a known involvement in cardiac wound healing: TGFβ, FGF and VEGF. ALK5-inhibitor is a known inhibitor of the effects of TGFβ1 (Inman et al., 2002; Laping et al., 2002). Moreover, SU5402 was previously shown to have inhibitory effects on vascular endothelial growth factor and fibroblast growth factor receptors (VEGFR and FGFR, respectively), both of which are involved in the regulation of fibroblast differentiation and migration behaviours (Kaftan et al., 2012; Mohammadi et al., 1997; Murakami et al., 2008; Zhao et al., 2014).

Another important part of these investigations was the identification of cell behaviours and properties that are relevant to cardiac wound healing and that should therefore be implemented in the model.

2.2 Experimental materials and methods

All procedures involving animal models were performed in accordance with the Animals (Scientific Procedures) Act 1986, (Home Office, UK).

2.2.1 Primary cardiac fibroblast cell isolation from murine hearts

The protocol for primary cardiac fibroblast isolation was adapted from (Kuruvilla and Kartha, 2009). Heart tissue was harvested from either wild type C57BL/6 or β-actin cre and yfp positive transgenic adult (8-12 weeks old) mice and dissected into pieces (<1mm^3). Cardiac tissue was then digested using a 0.25% (v/v) Trypsin solution (Life Technologies, 25050014) supplemented with 1 mg ml^{-1} Collagenase D (Roche, 11088866001), and 200 μg ml^{-1} bovine pancreas DNase I (Roche, 11284932001). The digestion was done in cycles whereby the tissue was put in contact with the digestion solution and incubated at 37 °C for 10 minutes before triturating the resulting mixture for ~2 minutes. After decantation, the supernatant was collected and mixed with 1 ml of foetal bovine serum (FBS, Invitrogen, 10270) for inactivation of the digestive enzymes. This suspension contained isolated cells and was kept on ice while the cycle was repeated with the remaining tissue until the digestion was complete (usually 4 to 5 cycles were needed). The cell suspension was then centrifuged (400 g, room temperature), the supernatant was discarded and the pellet was re-suspended in culture medium and cultured as outlined below (section 2.2.3). After 16 hours of plating the cells were washed twice in PBS (Invitrogen, 14190).

2.2.2 Primary skin fibroblast cell isolation from murine ears

Ear tissue was harvested from wild type C57BL/6 adult (8-12 weeks old) mice. The tissue was immersed in 70% ethanol for 10 minutes. The tissue was then dissected into pieces (<1mm^3). Ear tissue was then digested using a 0.25% (v/v) Trypsin solution (Life Technologies, 25050014) supplemented with 1 mg ml^{-1} Collagenase D (Roche, 11088866001), and 200 µg ml^{-1} bovine pancreas DNase I (Roche, 11284932001) and incubated at 37 °C for 1 hour. The tissue pieces were collected and washed once in culture medium. The tissue was then re-suspended in culture medium and plated under 25 mm glass coverslips (VWR, 631-0693) in 6-well culture dishes. The primary skin fibroblast cells were then cultured as outlined below (section 2.2.3). After 16 hours of plating the cells were washed twice in PBS (Invitrogen, 14190).

2.2.3 Cell culture and maintenance

Cells were grown in disposable tissue culture vessels (Corning) that were pre-coated by incubation with either a 10 µg cm^{-2} Collagen I solution (Sigma, C9791) for at least 3 hours and washed once with PBS (Invitrogen, 14190) or 0.1% gelatin (Sigma, G9391) in PBS (Invitrogen, 14190) at 37 °C for 15 minutes. The culture medium was DMEM medium (Invitrogen, 61965) supplemented with 10% FBS (Invitrogen, 10270) and 1% Penicillin Streptomycin (Invitrogen, 15140-122). Cells were kept in a humidified cell culture incubator at 37 °C with a 5% CO_2 gas atmosphere.

Cultures were passaged when reaching ~80% confluency. In brief, spent culture medium was discarded, cells were washed twice with PBS (Invitrogen, 14190) and incubated with a 0.05% Trypsin-EDTA solution (Invitrogen, 25300096) for 3 minutes at 37°C. After gentle mixing, the cell suspension was centrifuged at 400 g for 5 minutes. The supernatant was discarded and the pellet re-suspended in fresh culture medium. New cultures were seeded with a split ratio of 1:2 or 1:3 depending on the original culture confluency and the passage number. The culture medium was exchanged every 2 days.

For experiments with primary cardiac fibroblast cells, passage number was kept at a maximum of 3 after isolation.

2.2.4 Induction and inhibition of specific cell responses

The effects of anti- and pro-inflammatory signals on the cells were assessed by the addition of small molecules to the culture medium. Transforming growth factor beta 1 (TGFβ1, R&D Systems, 240-B-002) was added at a concentration of 2 ng ml^{-1} to study the impact of pro-inflammatory signals. Similarly, response of the cells to anti-inflammatory signals was assessed by adding a cocktail of 100 ng ml^{-1} tumor necrosis factor-alpha (TNF-α, R&D Systems, 410-MT) and 10 ng ml^{-1} interleukin-1 beta (IL-1β, R&D Systems, 401-ML-005/CF). In all cases, bovine serum albumin (BSA, Sigma, A4503) was used as vehicle and negative control.

Hypoxic conditions were mimicked by the addition of cobalt chloride ($CoCl_2$, Sigma, C8661) at a concentration of 200 μM in the culture medium. $CoCl_2$ is an oxygen scavenger that leads to the up-regulation of the hypoxia inducible factor-1 (HIF1-α). Deionised water (dH_2O) was used as negative control.

2.2.5 Pharmacological intervention

Cell response to two pharmacological interventions was also studied. SU5402 (Calbiochem, 572630), an inhibitor of tyrosine kinase activity of the fibroblast growth factor receptor 1 (FGFR1) was added at a concentration of 2 nM. ALK5 inhibitor (also referred as SB431542 from Stemolecule, Miltenyi Biotec 04-0010), an inhibitor of the TGFβ1 activin receptor-like kinases (ALKs) was added at a concentration of 10 μM.

2.2.6 Scratch assay

Scratch assays were used as simple model for tissue injury, whereby mechanical dissociation of a defined cell area promoted migration of the surrounding cells (Liang et al., 2007). Cells were first cultured and grown in 6 or 12-well plates to confluent monolayer as outlined in section 2.2.3. The culture medium was exchanged about 16 hours before the experiment. A pipette tip (p200) was then used to mechanically remove the cells along a line spanning the diameter. Hereafter, this line will be referenced as a scratch. After scratching, the cells were placed back into the incubator for 6 hours.

The cultures were then imaged using time lapse phase contrast microscopy. A Zeiss Axiovert 135 microscope was used together with the Velocity image acquisition and processing software. For each culture, a single field of view was imaged every 5 minutes in a central area of the well in order to avoid edge and meniscus effects. A 10× objective was used for all experiments (corresponding to a field of view of ~1.46 mm^2). During acquisition, the cells were kept at 37°C and 5% CO_2 using an on-stage incubator. Imaging was carried out until complete closure of the scratch.

2.2.7 Immunofluorescence

For immunofluorescence experiments, cells were grown on glass microscopy coverslips loosely placed in individual circular culture dishes. Spent culture medium was discarded and the cells were fixed by incubation with a 4% (v/v) formaldehyde solution (Sigma, F1635) for 20 minutes at room temperature. Cell were then permeabilised by incubation with 0.5% Triton X-100 (Sigma, T8787) for 5 minutes at room temperature. A blocking solution made up of 10% (v/v) goat serum (Sigma, G9023), 0.1% (v/), BSA (Sigma, A4503), and PBS (Sigma, P4417) was applied for an hour at room temperature. The cells were then incubator with the primary antibody appropriately diluted in the blocking solution for 16 hours at 4°C. Cells were then washed three times with 0.1% triton X-100 (Sigma, T8787) for 5 minutes each time. Cells were

incubated with the secondary antibodies appropriately diluted in blocking solution for an hour protected from light. Finally, the coverslips were washed as previously described and mounted on a microscopy slides in a 50% (v/v) glycerol in PBS solution. Coverslips were sealed using clear nail varnish. A Zeiss image z1 microscope was used for imaging.

The primary antibodies used to carry out immunofluorescence were monoclonal anti-α smooth muscle actin clone 1A4 (Sigma, A2547) used at 1:200 dilution. This marker was used to stain for myofibroblast cells (Gabbiani et al., 1972; Gabbiani, 1993; Gabbiani, 1996; Sun and Weber, 2000). Anti-fibroblast activation protein alpha (Abcam, ab53066) used at a 1:50 dilution, (Krenning et al., 2010; Ramirez-Montagut et al., 2004; Rettig et al., 1993). Anti-vimentin (Abcam, ab54939) used at a 1:200 dilution was used as a fibroblast cell marker (Camelliti et al., 2005a; Krenning et al., 2010). Anti-fibroblast specific protein 1 (S100A4, Merck Millipore, ABF32) was also used as a fibroblast cell marker at a dilution of 1:500 (Krenning et al., 2010; Strutz et al., 1995). Polyclonal anti-GFP (Abcam, ab13970) used at a 1:1000 dilution was used to detect YFP (Hao et al., 2013). DAPI (4',6-diamidino-2-phenylindole, Cell Signalling Technologies, 4083S) was used at a dilution of 1 μg ml^{-1} for the visualisation of cell nuclei (Kapuscinski, 1995).

The secondary antibodies used were Alexa Fluor 488 goat anti rabbit lgG (H+L) antibody ($\lambda_{emission}$ = 488m, Life Technologies, A-11008), Alexa Fluor goat anti mouse lgG (H+L) antibody ($\lambda_{emission}$ = 594, Life Technologies, A-11005) and Alexa Fluor 488 goat anti chicken lgG (H+L) antibody ($\lambda_{emission}$ = 488, Life Technologies, A-11039). Unless otherwise specified, all secondary antibodies were used at a 1:1000 dilution. Unless specified each staining experiment included secondary controls and no signal was detected.

2.2.8 Flow cytometry cell cycle analysis

In-vitro cardiac fibroblast cells were synchronized by placing them in serum-free media for 24 hours prior to the experiment. This ensures that all cells are in the G0 phase, which enables us to observe a proliferative change caused by the wound alone. Suspensions of cardiac fibroblast cells harvested at 18 and 24 hours after scratching were washed once with PBS and fixed by addition of 1 ml of cold 70% (v/v/) ethanol added drop wise to the cell pellet whilst continuously vortexing to minimise clumping. Cells were incubated with the ethanol for 30 minutes on ice. Cells were then centrifuged at 13,000 rpm for 5 minutes. The supernatant was discarded and the cells washed using PBS before being centrifuged again. This was repeated twice to make sure the cells were thoroughly washed. The supernatant was discarded and 50 μl ribonuclease A (100 μg ml^{-1}) (RNase A, Qiagen, 19101) and 400 μl propidium iodide (50 μg ml^{-1}) (PI, Sigma, P4170) solution per million cells were added to the pellet. After thorough mixing using a micropipette, the cells were incubated for 16 hours while continuously mixing gently by end-over-end rotation.

Samples analysed by flow cytometry LSRII analyser in PI/RNaseA solution in 75mm polystyrene tubes (Fisher Scientific, 14-959-1A). The samples were analysed using FlowJo (Tree Star Inc.) and analysed at a low flow rate of less than 400 events per second. For each sample, single cells were identified by measuring the forward and side scatters. Cell doublets and clumps were excluded from the analysis by using the pulse area versus the pulse width. A histogram of PI was produced and used to determine the percentage cells in each of the three cell cycle phases G0/G1, S and G2/M.

2.2.9 Masson's trichrome staining

Masson's trichrome staining (all solutions from the kit HT15-1KT, Sigma-Aldrich, UK) was used for the visualisation of collagen. Cultures of cardiac fibroblast cells were washed once with PBS and fixed by incubation with a 4% (v/v) formaldehyde for 20 minutes at room temperature. Cells were then washed with PBS and mordanted in heated Bouin's solution (Sigma, HT10132) solution for 15 minutes at 56°C. The wells were then cooled down by gently running water over them until the yellow colour disappeared. Cells were then incubated with Weigert's iron hematoxylin solution (Sigma, HT1079) for 5 minutes. Cells were washed under running water for 5 minutes and rinsed in deionised water. Cells were then incubated with Biebrich Scarlet-Acid Fucshin solution for 5 minutes and rinsed in deionised water. The cells were incubated with phosphotungstic/phosphomolybdic acid solution for 5 minutes followed by another incubation in aniline blue solution for a further 5 minutes, and finally in 1% (v/v) acetic acid for 2 minutes. Cells were then rinsed with deionised water and dehydrated through alcohol (50%, 80%, 90% and 100% ethanol), cleared in xylene and mounted in DPX mountant (44581, Sigma Aldrich, UK). Samples were imaged using a Nikon TE2000 inverted microscope and Vision Assistant (National Instruments, US).

2.2.10 Protein detection by western blot analysis

2.2.10.1 Cell lysis and protein extraction

Cells cultured in disposable culture vessels were washed twice with PBS before lysis by addition of ice-cold RIPA buffer (89900, Thermo Fischer), 1 mM dithiothreitol (DTT, Sigma, D9779), protease inhibitors and 0.01 M phenylmethylsulfonyl fluoride (PMSF, Sigma, P7626). The cells were scraped and re-suspended. A syringe was used to pass the viscous lysate through a 21 g needle 2 to 3 times in order to shear the DNA. The resulting lysate solution was incubated for 15 to 30 minutes at 4 ºC while continuously mixed by end-over-end rotation. The lysate was then centrifuged at 15,000 g at 4ºC for 20 minutes. The supernatant containing the extracted proteins was then collected, aliquoted and stored at -20ºC until further analysis.

2.2.10.2 Total protein concentration determination using a Bradford assay

A Bradford assay was carried out to determine the total protein concentration of each sample. A standard curve was prepared using a serial dilution of 1 µg μl^{-1}, 3 µg μl^{-1}, 5 µg μl^{-1} and 10 µg μl^{-1} of Bovine Serum Albumin prepared in Bradford reagent (Sigma, B6916). For each sample 2 µl ml^{-1} of the lysate was prepared in Bradford reagent (Sigma, B6916). A blank sample was created with 2 µl ml^{-1} of RIPA buffer in Bradford reagent (Sigma, B6916). All of the solutions were incubated at room temperature for 30 minutes. The absorbance was measured at 595 nm with a Multiskan FC (Thermo Scientific) and recorded with Skanlt for Multiskan FC version 2.5.1 software.

2.2.10.3 Gel preparation

The gel casting plates were cleaned with 70% Ethanol and set up into the casting stand (Biorad). A 10% resolving gel and a 5% resolving gel were prepared as shown in Table 1. The resolving gel was poured between the plates and topped up with isobutanol (VWR, IB05120). The gel was incubated at room temperature for 30 minutes. Once set, the isobutanol was removed and the top of the gel was washed twice with deionised water. The stacking gel was poured on top of the set resolving gel and a comb was inserted. The gel was incubated at room temperature for 20 minutes or until set. The comb was removed and the top of the gel was washed with deionised water. The gel was then placed in the electrophoresis instrument and submerged in running buffer whose composition was 25 mM Tris (Sigma, T5030), 192 mM Glycine (Sigma, G8898), and 0.1% SDS (Sigma, 862010). 10 µg of each sample was mixed with an equal volume of loading buffer, whose composition was 250 mM Tris-Cl pH 6.8 (Sigma, T5030), 4% SDS (Sigma, 862010), 25% glycerol (Sigma, G5516), 0.1% bromophenol blue (Sigma, 114405), and 5% beta mercaptoethanol (Sigma, M3148). The sample mix was boiled for 5-10 minutes in a heat block before being loaded into the gel. The gel was run at 100 to 140 V for 1 to 1.5 hours. A 100 base pair DNA ladder (New England Biolaboratory, N3231L) was loaded into the first well of each gel.

Table 1 Composition of the resolving and stacking gels for western blot analysis

Reagent	Stock concentration	10 % Resolving gel	5% Stacking gel
Acrylamide (Sigma, A3699)	30% (w/v)	3.33 ml	830 µl
Sodium dodecyl sulphate (SDS, Sigma, 862010)	10% (w/v)	100 µl	50 µl
Tetramethylethylenediamine (Temed,Sigma, T22500)	99% (v/v)	3.3 µl	5 µl
Ammonium persulfate (AMPS. A3678)	20% (w/v)	50 µl	25 µl
Tris pH 6.8 (Sigma, T5030)	1 M	-	625 µl
Tris pH 8.8 (Sigma, T5030)	1 M	3.75 ml	-
Deionised water	-	2.82 ml	3.48 ml

2.2.10.4 Western blotting and immunodetection

The western transfer was assembled by placing the gel and a polyvinylidene fluoride (PVDF, Sigma, Z613835) membrane in-between 3MM gel blot paper (Sigma, Z270857), and again sandwiched between blotting pads. The tank transfer apparatus was filled with transfer buffer whose composition was 25 mM Tris (Sigma, T5030), 190 mM glycine (Sigma, G8898), and 20% (v/v) methanol (VWR, BDH1135). The western transfer was carried out overnight at 30 to 50 mA at 4 ºC. The transfer was then dissembled and the membrane rinsed in tris-buffered saline (TBS). The membrane was blocked with a blocking buffer whose composition was 5% non-fat milk in TBS with 0.05% Triton X-100 (Sigma, T8787). The membrane was incubated with said blocking buffer for either 1 to 2 hours at room temperature or overnight at 4 ºC with agitation. The membrane was then briefly washed in a solution of TBS with 0.05% Triton X-100 (Sigma, T8787). Primary antibodies were diluted to the appropriate concentration in the blocking buffer and incubated with the membrane for 1 to 2 hours at room temperature or overnight at 4 ºC with agitation. The membrane was washed by incubation with a washing buffer made up of 0.5% Triton X-100 (Sigma, T8787) in TBS for 10 minutes. This was repeated 6 times. The membrane was then incubated with the appropriate HRP-linked secondary antibody diluted in blocking buffer for an hour at room temperature with agitation. The membrane was washed as described previously. Finally, it was washed twice for 5 minutes with TBS alone. A one to one mix of ECL components (GE Healthcare Life sciences, RPN2209) was added to the membrane. After one minute any excess ECL solution was removed and the membrane was covered in saran wrap. The membrane was then exposed to an Amersham Hyperfilm ECL (GE Healthcare Life sciences, 28906837) for 16 hours for anti-Smad3 and 20 minutes for GADPH before developing. The protein bands were quantified using densitometry in ImageJ software.

The primary antibodies used were anti-Smad3 (phosphor S423 + S425) [EP823Y] (Abcam, ab52903) at 1:2000 and anti-GAPDH (Millipore, MAB374) at 1:1000. The secondary antibodies used were donkey anti-rabbit lgG H&L HRP (Abcam, ab16284) at 1:5000 and goat anti-mouse lgG H&L HRP (Abcam, ab6789) at 1:5000.

2.2.10.5 Membrane stripping and re-probing

Membrane was incubated at 50 ºC for 10 minutes in an oven under gentle agitation with a stripping buffer whose composition was 100 mM beta mercaptoethanol (Sigma, M3148), 2% SDS (Sigma, 862010), 62.5 mM Tris-HCL pH 6.7 (Sigma, T5030). The membrane was then washed twice for 10 minutes with washing buffer (as previously described in section 2.2.10.4). The membrane was blocked with the blocking buffer (as previously described in section 2.2.10.4) for 1 hour at room temperature and the immunodetection protocol repeated.

2.2.11 Genotyping

Some experiments relied on the crossing of R26R-EYFP mice with β-actin cre mice. These crosses were genotyped using primers for Cre and R26R-EYFP as shown in Table 2.

Table 2 Genotyping primers for Cre and R26R-EYFP.

	Cre	**R26R-EYFP**
Forward	GTTCGCAAGAACCTGATGGACA	AAGTCGCTCTGAGTTGTTAT
Reverse 1	CTAGAGCCTGTTTTGCACGTTC	GCGAAGAGTTTGTCCTCAACC
Reverse 2	-	GGAGCGGGAGAAATGGATATG

Ear punch samples were prepared by adding 500µl of tail lysis buffer whose composition was 100 mM Tris-HCl pH8.5, 200 mM NaCl, 5 mM EDTA pH8.0 (Sigma, ED2SS) and 0.2% SDS with 50 mg ml^{-1} Proteinase K (Sigma, p2308) and incubated overnight at 55 ºC. The samples were then incubated with 500 µl of isopropanol for 20 minutes at room temperature, before being centrifuged at 16060 g at 4ºC for 15 minutes. The supernatant was discarded and 300µl of 70% ethanol was added to each sample. Samples were then mixed using a vortex and centrifuged at 16060 g at 4ºC for 5 minutes. The supernatant was discarded, the pellet was re-suspended with 65µl of TE buffer (10 mM Tris-HCl pH8.0 and 1 mM EDTA pH8.0) and thoroughly mixed using a vortex.

For each sample, 2 µl of DNA was prepared with 22 µl of deionised water and 1 µl of each primer required. Positive controls used 2 µl of DNA from either heterozygous R26R-EYFP or positive cre mice. The negative control used 2 µl of TE instead of 2 µl of DNA. In each case this was added to a PCR bead (Fisher, 27-9557-02). The samples were run on a PCR machine (Applied biosystems Veriti 96 well thermal cycler). The method involved three stages. Stage 1 heated the sample at 94ºC for 2 minutes and 55ºC for 1 minute. Stage 2 was repeated 32 times and was a cycle of 72ºC for 45 seconds, 94ºC for 30 seconds and either 55ºC (R26R-EYFP) or 58ºC (Cre) for 45 seconds. The final stage was 72ºC for 3 minutes.

Each sample was run on a 1.5% agarose gel with 0.5 µg ml^{-1} ethidium bromide (Sigma, E1510) at 140V for approximately 40 minutes. The gel was then visualised with ultra violet light.

2.3 Analytical Methods

This section gives an overview of the analytical and computational methods applied for the generation of the results discussed later in the chapter.

2.3.1 Cell migration speed

Cardiac fibroblast cells were manually tracked on time-lapse phase contrast images acquired during scratch assay experiments. The ImageJ plugin ‘Manual Tracking’ was used to facilitate the generation of multiple tracks per experiment (Figure 2-1). To ensure that the speed measured was that of unobstructed migration (e.g. by other cells), cells to be tracked were chosen at random along the edge of the scratch. Cells were tracked until their migration was

obstructed, for example by a cell migrating from the opposite site of the scratch. Tracking was restricted to cells that did not divide during the time lapse period.

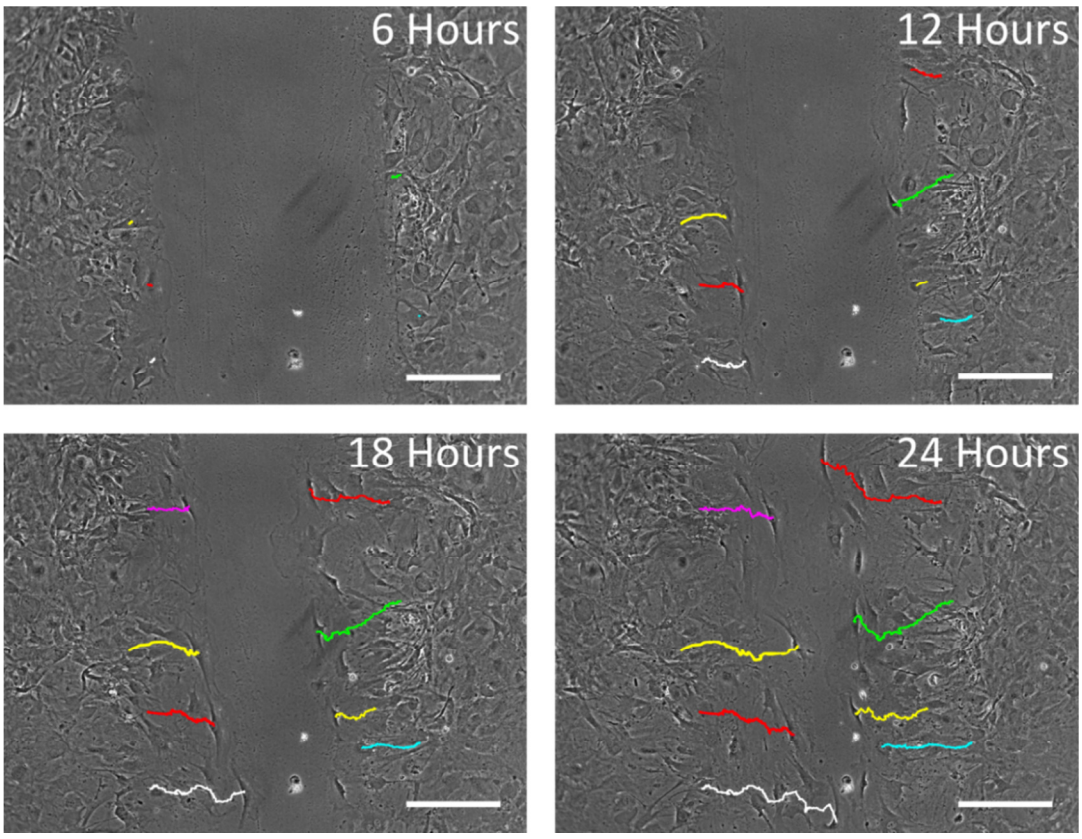

Figure 2-1 Time-lapse phase contrast microscopy images of a scratch assay experiment at different time points (as indicated below each image). Coloured lines represent the manually determined migration tracks of individual cells. Images represent different time points after injury 6, 12, 18 and 24 hours. Scale bar represents 250 µm.

For an individual cell, the position (x_i) was recorded for each movie frame. Frames were acquired at an interval (Δt) of 5 minutes. The instantaneous cell speed s_i between each frame was computed from the change in cell position (displacement) as shown in Equation 2.1 and Figure 2-2.

$$s_i = \frac{\|x_i - x_{i+1}\|}{\Delta t} \qquad 2.1$$

The approximate migration speed was then computed by averaging the instantaneous cell speed for each frame considered during tracking. This was compared to an alternative method where the cell speed was computed based on the initial and final cell positions (total displacement), termed effective (or displacement) cell speed (Figure 2-2).

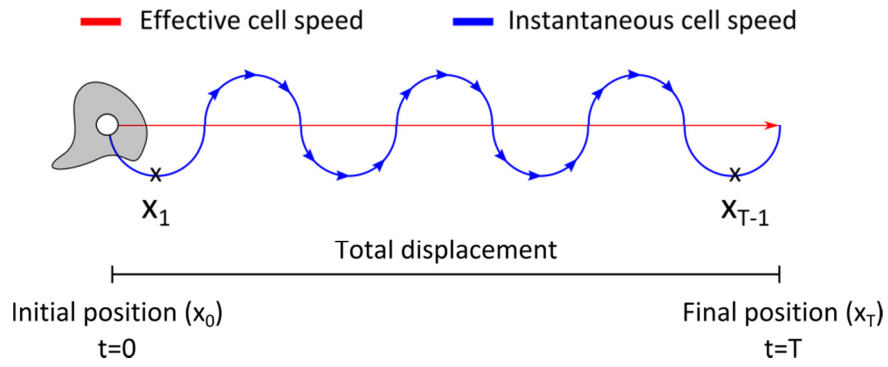

Figure 2-2 Schematic representation of cell speed measurements from manual cell tracking. Effective cell speed (red) was computed based on the total displacement. Instantaneous cell speed (blue) was computed between each frame and averaged over all of the frames for each.

The level of movement directionality of the cells was also assessed by computing the displacement effectiveness (E) measurement (Arboleda-Estudillo et al., 2010; Deforet et al., 2012). This measurement was computed by dividing the distance of the trajectory between the initial (x_0) and final (x_T) cell position by the total displacement of a cell as shown in Equation 2.2 (Arboleda-Estudillo et al., 2010).

$$E = \frac{\left|x_T - x_0\right|}{\sum_{i=0}^{i=T-1} \left|x_{i+1} - x_i\right|} \qquad 2.2$$

The value of the displacement effectiveness varied between 0 and 1. A measure of 1 indicated that the cells travelled along a straight trajectory and did not deviate at all from their paths.

2.3.2 Dynamics of cell division

The dynamics of cell division were analysed from time-lapse phase contrast images. In particular, the distance and angle between the two daughter cells immediately after division were measured. The positions of the cells were manually tracked with the 'Manual Tracking' plugin for ImageJ. The last location of the mother cell (x_O, y_O) was used as the reference point for the rest of the measurements, and was determined as the midpoint between the two newly forming nuclei on the last frame before their separation (Figure 2-3). As such, this reference point was approximately between the anaphase and telophase stages of the cell cycle. This was only an approximation due to the 5 minutes time interval between frames. However this measurement interval remained well under the doubling time reported for cardiac fibroblasts, which generally ranged between 24 and 36 hours (Agocha et al., 1997). In subsequent frames, the daughter cells were tracked individually.

The angle between the two daughter cells following division was determined based on two different angles (Figure 2-3). The first (θ_1) was defined as the angle between the reference point (x_O, y_O) and the initial positions of both daughter cells. The second (θ_2) was the angle between the midpoint of the initial daughter cell positions (M) and the daughter cell positions at the next

frame (Figure 2-3). The angle between the daughter cell was then calculated by averaging θ_1 and θ_2. Similarly, the distance between the nuclei of the two daughter cells after division was calculated by taking the average of the distance d_0, d_1, and d_2 measured at nuclei separation, after 5 minutes, and after 10 minutes, respectively (Figure 2-3).

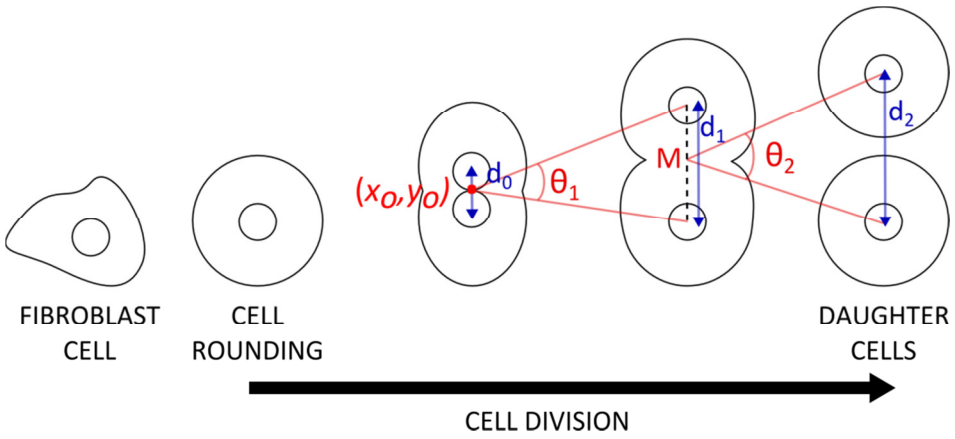

Figure 2-3 Schematic representation of cell division. The distances (d_i, blue) and angular measurements (θ_i, red) between the daughter cells. The distances (d_i) represent the separation of two daughter cell nuclei measured from a single image. The angle (θ_i) is measured between the daughter cell positions at one time point. The origin is taken as the midpoint (M) between the two daughter cells from the previous image time point. The distances d_0, d_1, and d_2 were measured between the nuclei of the daughter cells directly after separation, after 5 minutes, and after 10 minutes respectively. The angle between the daughter cells was computed as shown by θ_1 and θ_2.

2.3.3 Cell differentiation

In order to determine the proportion of myofibroblast during wound healing, primary cardiac cells were fixed at time 0h, 3h, 6h, 10h, and 16h after the initial scratch. The cells were stained for α-SMA, a myofibroblast marker, while DAPI was used to visualise cell nuclei. Images were acquired along the edge of the scratch (Figure 2-4A). The two fluorescence channels used were merged prior to analysis (Figure 2-4B). An intensity threshold was used to produce a binary representation of the images (Figure 2-4C). The value for the threshold was adjusted empirically to maximise the contrast between fibroblast and myofibroblast cells. The latter were identified based on the intensity of the α-SMA signal and on the presence of clearly visible myofilaments (Hinz et al., 2007; Souders et al., 2009). Counting both cell types was facilitated by the use of the cell counter plugin in ImageJ. The region considered for counting was delimited on one side by the edge of the scratch and extended ~400 µm away from the wound (i.e. into the region with cells). While optimal image quality would be obtained as a 20× magnification, images were acquired using a 10× objective to minimise the risks of photo bleaching and signal attenuation.

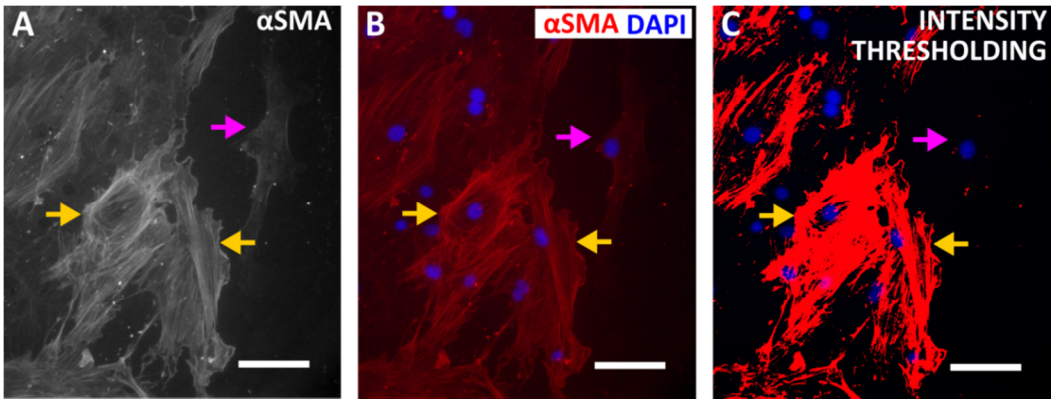

Figure 2-4 Determination of the proportion of myofibroblasts during wound healing. (A) Cells in culture stained for α-SMA, myofibroblast cells are identified by their expression of α-SMA and the presence of myofilaments. (B) Composite image of the α-SMA and DAPI (nucleus marker). (C) The α-SMA image was binarised using an intensity threshold. The yellow and pink arrows indicate fibroblast and myofibroblast cells, respectively. All scale bars represent 100µm.

2.3.4 Cell Area

Cell area is typically difficult to determine as cell boundaries are often indistinct when cells are grown in a monolayer at relatively high density. In order to alleviate this issue, wild type and YFP-expressing primary cardiac fibroblast cells were co-cultured at an approximate 5:1 ratio. The ratio was chosen empirically after preliminary tests as it resulted in a sufficient number of YFP-positive cells to produce statistically significant measurements while minimising the probability of said cells being neighbours and thus preventing the determination of their area. A normal scratch experiment was carried out and the cells were fixed after 16 hours. Using immunofluorescence, the cells were stained for YFP and α-SMA (a myofibroblast phenotype marker) while DAPI was used for nuclei visualisation. It was necessary to stain for YFP using a GFP-labelled antibody in order to amplify the signal so the entire cell area could be determined from the images using ImageJ (Figure 2-5A). The fluorescence image was first binarised (converted to a black and white image) using an intensity threshold, whose value was determined empirically (Figure 2-5B). The wand (tracing) tool in ImageJ could then be used to automatically trace around the cells (Figure 2-5C and D). The signal from the α-SMA marker enabled the discrimination between fibroblasts and myofibroblasts cell area measurements applying the same approach used for the determination of myofibroblast proportions (see section 2.3.3).

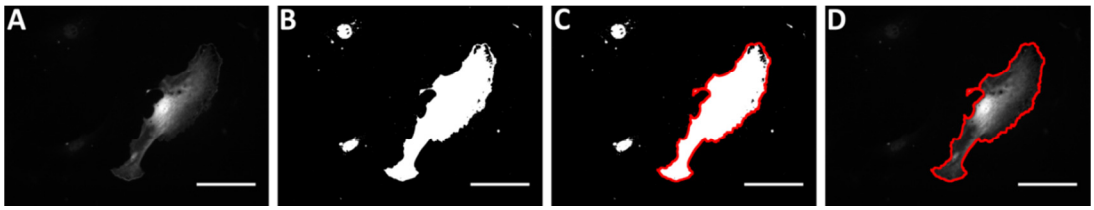

Figure 2-5 Determination of cell area using fluorescence images of co-cultures. (A) YFP-expressing cell stained using a GFP-labelled antibody. (B) Binary image obtained using intensity thresholding. (C) Cell outline automatically determined using ImageJ's wand tool. (D) Overlay of the image in A with the outline determined in C. The scale bars represent 100μm.

2.3.5 Statistical methods

Unless otherwise specified, all experiments were performed in biological triplicates. Results are generally presented as mean ± standard deviation. Independent t-tests were used to determine whether two means were significantly different. A p-value of either less than 0.05(*) or 0.01(**) was interpreted as the mean being significantly different. All data was assumed to be normally distributed.

2.4 Results

This section outlines the results obtained for the various experimental *in-vitro* cell behaviour investigations carried out. A 2-dimensional (2D) cell culture system was considered with the following additions inflammatory stimuli, hypoxia and pharmacological interventions. In general, primary cardiac cells were used as the cell model and scratch assays were employed to study cell behaviours in response to injury.

2.4.1 Primary cardiac fibroblasts as an experimental cell model

Scratch assay experiments were carried out with three different cell types and phase contrast microscopy images were acquired so that their morphological features could be compared (Figure 2-6). Both NIH 3T3 cells (Figure 2-6 A) and primary dermal fibroblasts (Figure 2-6 B) had significantly different morphological features when compared to primary cardiac fibroblasts (Figure 2-6 C). NIH 3T3 cells had a spindle-shaped morphology, similar to that of the cardiac fibroblasts but much narrower. In contrast, primary dermal fibroblasts had a cobble stone appearance that differed drastically from the other two. Because morphological features were key for this work (e.g. cell shape, area), the two alternative models were found to be unsuitable.

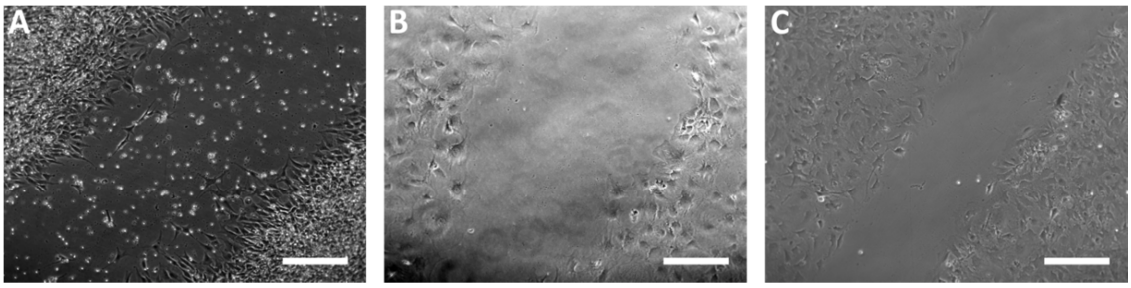

Figure 2-6 Comparison of three fibroblast experimental cell models. Phase contrast microscopy images of scratch assay experiments using (A) NIH 3T3 cells, (B) primary skin fibroblast cell (derived from murine ear tissue), and (C) primary cardiac fibroblast cells (derived from murine heart tissue). Scale bars represent 250μm.

In addition to morphological differences, it was previously shown that the gene expression profiles of fibroblast cells derived from different tissues can also differ significantly (Chang et al., 2002). Primary cardiac fibroblasts were thus employed as the experimental cell model for the rest of this work.

Further characterisation work was carried out to validate the protocols used for the isolation of primary cardiac fibroblast from adult murine hearts. Immunofluorescence techniques were employed to assess the expression of well-documented markers for cardiac fibroblast cells (Figure 2-7). Both fibroblast specific protein (Fsp1, Figure 2-7 B) (Krenning et al., 2010; Strutz et al., 1995) and vimentin (Figure 2-7 C) (Franke et al., 1979; Krenning et al., 2010) were strongly expressed by the cells. Along with these markers, cultured fibroblasts were also shown to express fibroblast activation protein 1 alpha (Fap1α, Figure 2-7 A), often observed in activated fibroblast cells in wound healing and have been noted to express this marker in culture (Krenning et al., 2010; Ramirez-Montagut et al., 2004; Rettig et al., 1993). In addition, a fraction of the isolated cells also expressed the myofibroblast cell marker alpha-smooth muscle actin (α-SMA, Figure 2-7 A-C) (Gabbiani, 1996; Hinz et al., 2007). These results demonstrated that the gene expression of the cells derived from mice heart was consistent with what would be expected from cardiac fibroblast and myofibroblast cells.

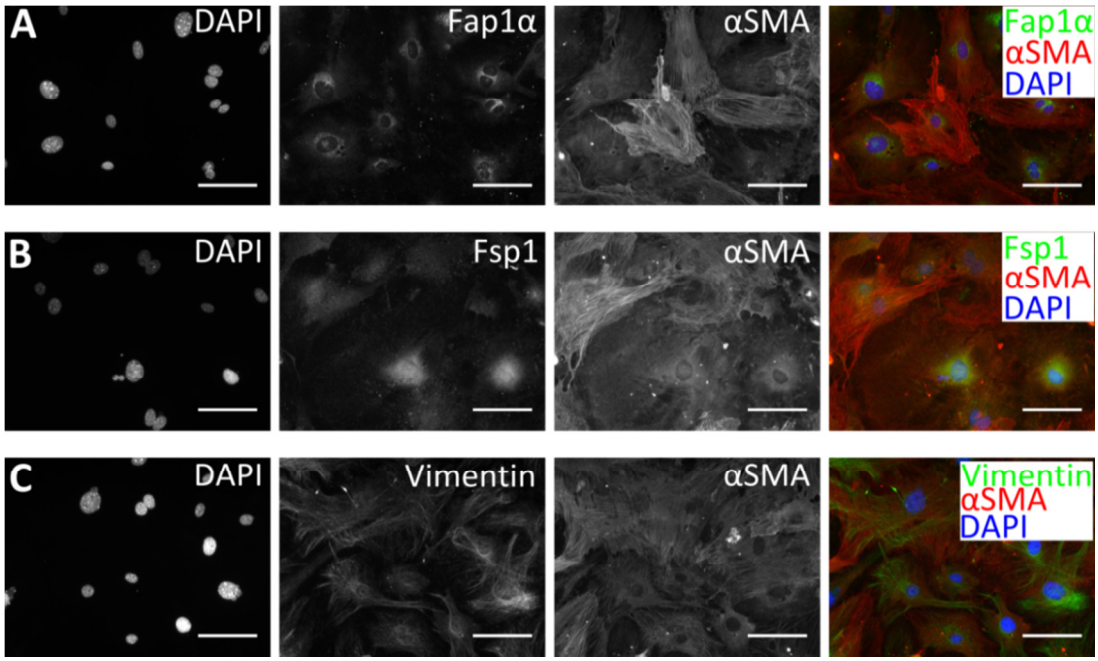

Figure 2-7 Assessment of the expression of fibroblast and myofibroblast markers in cells isolated from murine hearts. Each row corresponds to a different set of cells analysed using DAPI (nucleus marker, first column, blue), general fibroblast markers (Fsp1 and Vimentin, green), and myofibroblast-specific markers (Fap1α and α-SMA) indicated with green and red respectively. All scale bars represent 100μm.

Another key property of cardiac fibroblast cells is their ability to produce and deposit collagen. This was assessed by carrying out a conventional scratch assay where cells were grown on gelatin pre-coated plates instead of collagen-coated plates as used in the rest of this work. The cells were fixed after 16 hours and stained using the Masson's trichrome protocol. Collagen fibres were stained in blue and thus could be imaged using conventional phase contrast microscopy and a colour camera (Figure 2-8A). These experiments showed the presence of collagen fibres near the edge of the scratches, which indicated that the cells actively produced and deposited collagen, as expected for cardiac fibroblasts. The primary cardiac fibroblast cells also stained positive for collagen I (Figure 2-8B).

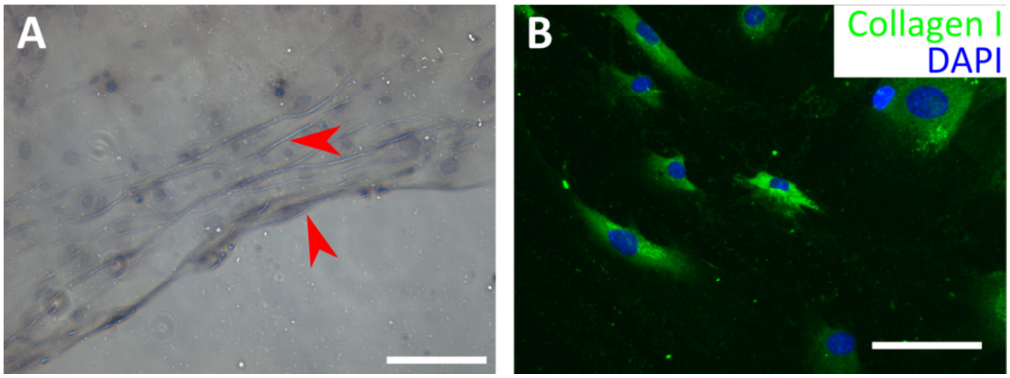

Figure 2-8 Visualisation of Collagen I production and deposition by cardiac fibroblasts. Cells were fixed 16 hours into a scratch assay experiment. (A) Cells grown on gelatin-coated plates were stained using the Masson's trichrome protocol. Images were acquired using a phase contrast microscope equipped with a colour camera. The blue lines show collagen fibres (red arrows). (B) Immunofluorescence staining for collagen I (green) and a nucleus marker DAPI (blue) of cells grown on collagen coated plates. Images acquired using a fluorescent microscope. All scale bars represent 100μm.

Cells consistent with gene expression profiles and behaviours expected from cardiac fibroblast (and myofibroblast) were routinely isolated from murine hearts and used as the basis for the experimental investigations to follow.

2.4.2 Cell migration

Migration is a key cell behaviour during cardiac wound healing. Cell migration is a combination of directionality and speed, which can be assessed by a number of different parameters. In general, cells will modify both their direction and speed during migration. Firstly, the instantaneous cell speed (see Section 2.3.1) was analysed, this measure provided an estimate for the average cell migratory speed. This measure was not sensitive to any directional changes made by the cell. The effects of two factors were studied: the pre-coating of the growth area with collagen I and the addition of cytokines to the culture medium (Figure 2-9). The pre-coating of plates with collagen was expected to better mimic the ECM and the attachment substrate of the cells during cardiac wound healing. Similarly, cytokines were used as an approximation of the inflammatory response. A cocktail of tumor necrosis factor (TNF-α) and interleukin-1 beta (IL-1β) was used as a pro-inflammatory signal. Likewise, transforming growth factor beta-1 (TGFβ1) was added to the culture medium as an anti-inflammatory stimulus. It was thus of interest to determine whether pre-coating of the growth substrate with collagen or the addition of signalling molecules would impact cell migratory speed measured during *in-vitro* scratch assays.

An increase in the instantaneous cell speed was measured across all conditions when pre-coating the culture substrate with collagen I. The instantaneous speeds were significantly higher in the presence of collagen I for both the cocktail of pro-inflammatory cytokines (p-value=0.005) and anti-inflammatory stimuli TGFβ1 (p-value=0.03) cases. The average instantaneous cell speed for the vehicle control (BSA) was 25 and 28 $\mu m\ hr^{-1}$ on non-coated and collagen I coated vessels, respectively. The addition of TGFβ1 to the culture medium resulted in significantly lower instantaneous speeds when compared to the control condition, both for non-coated vessels (p-value = 0.021) and collagen I coated vessels (p-value = 0.013). Likewise, the cultures with TGFβ1 also had migratory speeds significantly lower than those in culture medium supplemented with pro-inflammatory cytokines, both in non-coated vessels (p-value = 0.029) and collagen I-coated vessels (p-value = 0.001). The cocktail of pro-inflammatory cytokines was found not to significantly impact the migration speed of cells when compared to vehicle control, both in non-coated and collagen I coated culture vessels.

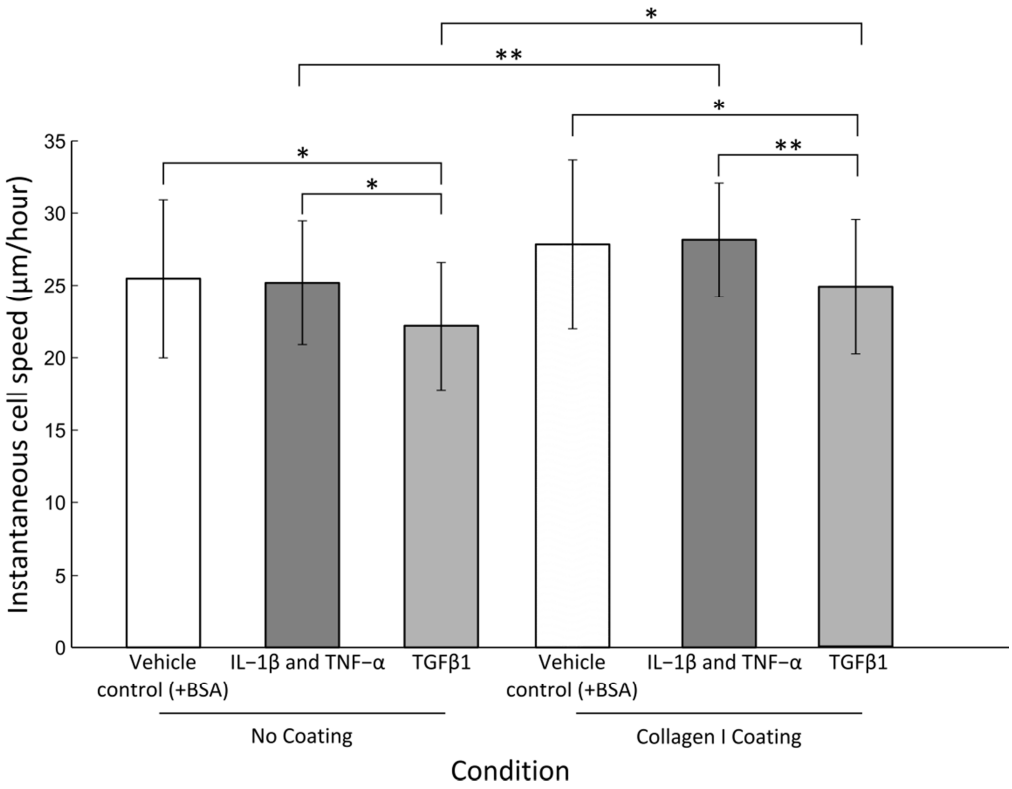

Figure 2-9 Instantaneous cell speed as measured during *in-vitro* scratch assays. The growth substrate was either uncoated (tissue culture polystyrene) or pre-coated with collagen I. Scratch assay was carried out in regular cell culture medium (control with the vehicle BSA), culture medium supplemented with pro-inflammatory cytokines IL-1β and TNF-α, and culture medium supplemented with anti-inflammatory cytokine TGFβ1. Measurements shown as mean instantaneous cell speed ± standard deviation across three biological replicates (i.e. separate primary cardiac fibroblast isolations). Significance of results was assessed using an independent t-test and indicated as * (p-value < 0.05) and ** (p-value < 0.01).

The effect of hypoxic conditions on migration was also investigated. Hypoxic conditions were mimicked in *in-vitro* scratch assays by the addition of cobalt chloride ($CoCl_2$) an oxygen scavenger (Figure 2-10). The influence from the addition of cobalt chloride on the instantaneous cell speed showed non-significant decreases when compared to the vehicle control (dH_2O) in both the non-coated and collagen I coated culture vessels.

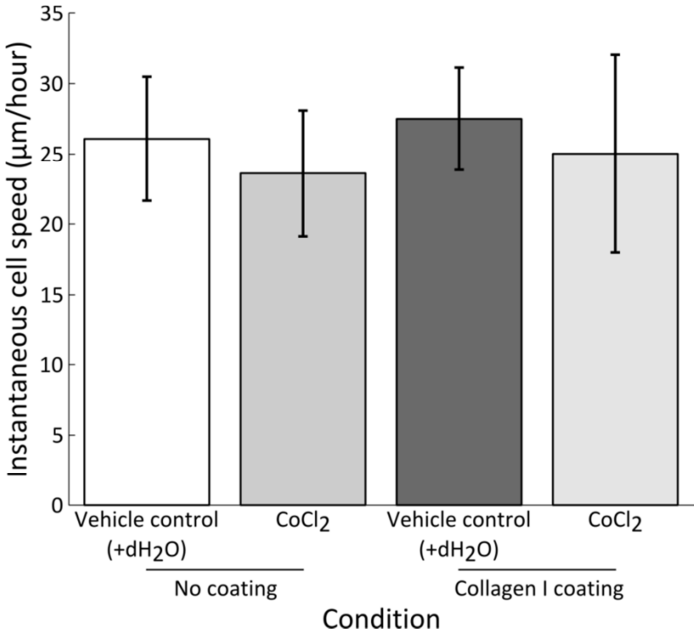

Figure 2-10 Instantaneous cell speed as measured during *in-vitro* scratch assays. The growth substrate was either uncoated (tissue culture polystyrene) or pre-coated with collagen I. Cardiac fibroblast cells were treated with $CoCl_2$ at a concentration of 200 µM to mimic hypoxic conditions. For the control culture, the vehicle (dH_2O) was added at a concentration of 0.2%. $CoCl_2$ is an oxygen scavenger that leads to the up-regulation of the hypoxia inducible factor-1 (HIF1-α). Measurements shown as mean instantaneous cell speed ± standard deviation across two biological replicates (i.e. separate primary cardiac fibroblast isolations). An average of 19 cells was tracked for each case.

In addition to pro- and anti-inflammatory cues, it was of interest to determine whether compounds that might be used as part of a pharmacological intervention had an effect on the migration speed of primary cardiac fibroblasts during scratch assay experiments. The pharmacological interventions analysed in this study were ALK5 inhibitor and SU5402 both compared to vehicle control (DMSO). A notable result was that the vehicle control (DMSO) for those conditions (Figure 2-11) differed significantly (p-value = $5x10^{-7}$) from the vehicle control (BSA) shown for the collagen coated vessels previously (Figure 2-9). The addition of this vehicle (DMSO) on its own thus had a detrimental effect on the instantaneous cell speed measured. When ALK5 inhibitor was added to the culture medium, the measured speed was slightly higher than the vehicle control (DMSO, Figure 2-11) and also similar to the instantaneous speed measured for the previous vehicle control (BSA, Figure 2-9), though in both cases there was no significant difference. In the case of SU5402, a slight decrease in average instantaneous cell speed was measured when compared to the vehicle control (DMSO) but again, this was not significant (Figure 2-11). However, there was a significant decrease when compared to vehicle control (BSA) used for the pro- and anti-inflammatory stimuli (p-value = $1.864x10^{-9}$).

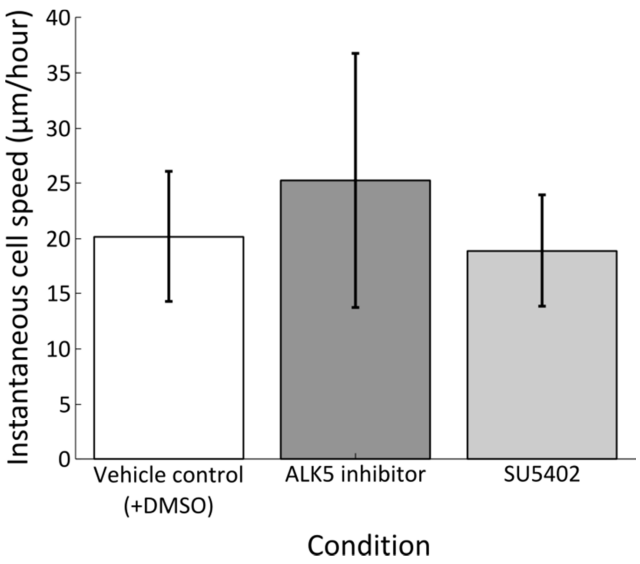

Figure 2-11 Instantaneous cell speed as measured during *in-vitro* scratch assays on collagen-coated plates after addition of compounds mimicking a pharmacological intervention. For the control culture, the vehicle (DMSO) was added at a concentration of 1%. ALK5 inhibitor is a known inhibitor of the effects of TGFβ1 while SU5402 was reported to have inhibitory effects on both VEGFR and FGFR pathways. Measurements shown as mean instantaneous cell speed ± standard deviation across three biological replicates (i.e. separate primary cardiac fibroblast isolations). In all cases, 24 cells were tracked.

In order to gain an understanding on the motion of individual cells during migration, the individual manually generated cell tracks were visualised. The cell migratory tracks were visualised by translating their starting point so that it corresponded to the origin of a Cartesian coordinate system (Figure 2-12 A). The origin, therefore, represented the edge of the wound, thus tracks moving towards either the right or the left in this visualisation indicated cells migrating towards the wound. In a first instance, most cells migrated directly towards the wound as shown by horizontal tracks. In some cases, however, the cell trajectories were not straight lines but instead changed direction once or more during the course of their migration.

The level of movement directionality of the cells for different conditions was assessed with displacement effectiveness measurement in the range [0,1] (Section 2.3.1 and Equation 2.2) (Arboleda-Estudillo et al., 2010; Deforet et al., 2012). A score of 1 indicated that the cells travelled along a straight trajectory and did not deviate at all from their paths. This measure was compared for migrating cells in a scratch assay which had been seeded on collagen pre-coated plates and/or had the media supplemented with inflammatory stimuli (Figure 2-12B). Pre-coating the culture vessels with collagen I resulted in a significant increase in the displacement effectiveness compared to no coating ($p=0.005$). A significant increase was also observed in the pro-inflammatory stimuli (IL-1β and TNF-α) no pre-coating case ($p=0.047$). These results show that the cells which are present in media stimulated with pro-inflammatory cytokines have an increased direction of motion compared with the addition of a vehicle on culture vessels with no coating. For collagen pre-coated culture plates the addition of anti-inflammatory stimulus

lowered the displacement effectiveness compared to both the addition of control vehicle (p=0.005) and pro-inflammatory stimuli (p=0.03).

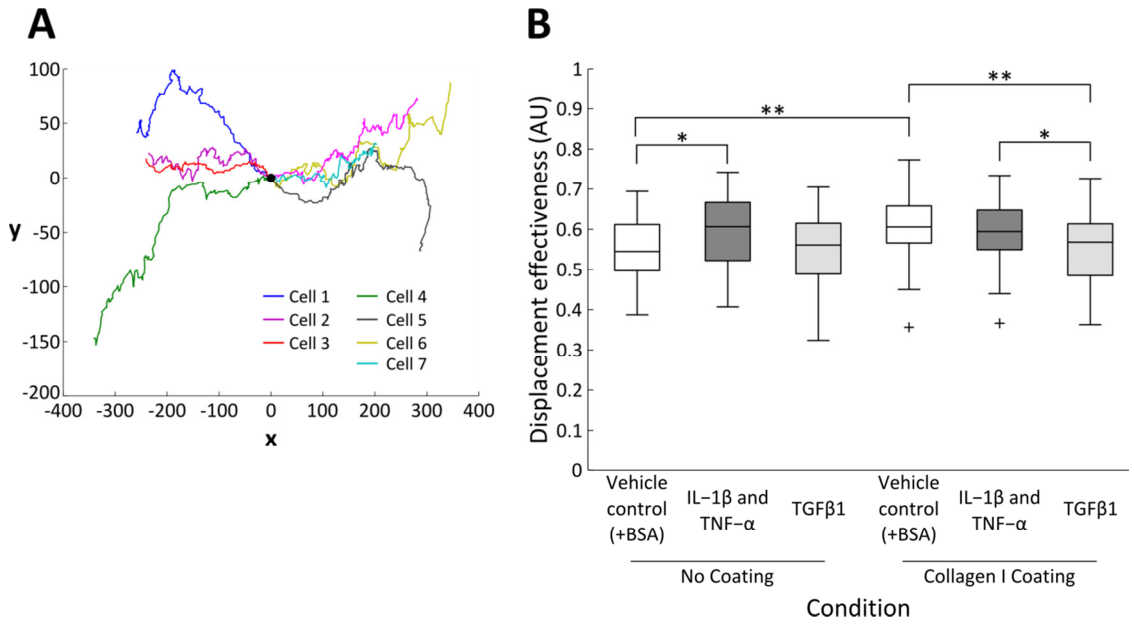

Figure 2-12 Analysis of cell migration patterns. (A) Visualisation of cell migration trajectories. Each coloured line represent cell migration track. Each tracked was translated so that their starting point corresponded to the origin of the Cartesian coordinate system (0,0). (B) Boxplots of the displacement effectiveness as measured during *in-vitro* scratch assays. The horizontal line is the median of the distribution, the edges of the boxes are the 25th and 75th percentiles and the whiskers extend to the most extreme data points not considering outliers. Outliers are plotted with a single cross. The growth substrate was either uncoated (tissue culture polystyrene) or pre-coated with collagen I. Scratch assay was carried out in regular cell culture medium (control with the vehicle BSA), culture medium supplemented with pro-inflammatory cytokines IL-1β and TNF-α, and culture medium supplemented with anti-inflammatory cytokine TGFβ1. Significance of results was assessed using an independent t-test and indicated as * (p-value < 0.05) and ** (p-value < 0.01).

The impact of changes in migratory direction were assessed by measuring the effective cell speed (also known as displacement speed) by only taking into consideration the effective displacement between the start and end position of a cell (Figure 2-13). The measured cell speeds were markedly lower than those determined for average instantaneous speed, highlighting the effect of changes in direction over the migration patterns of the cells. Interestingly, the differences between the different conditions contrasted with those observed for the instantaneous speed. Pre-coating of the vessel with collagen resulted in a significant increase in the average effective cell speed for the control (p=0.004), pro-inflammatory stimuli (p=0.01) and anti-inflammatory stimulus (p=0.04). For non-coated vessels, supplementation of the culture medium with TGFβ1 led to an average effective cell speed significantly lower than the control cultures (p-value=0.04) and cultures with pro-inflammatory cytokines added (p-value=0.0002). Likewise for collagen-coated vessels, addition of TGFβ1 also resulted in decreased average effective cell speed when compared to control cultures (p-value=0.0002) and cultures supplemented with pro-inflammatory cytokines (p-value=0.0001).

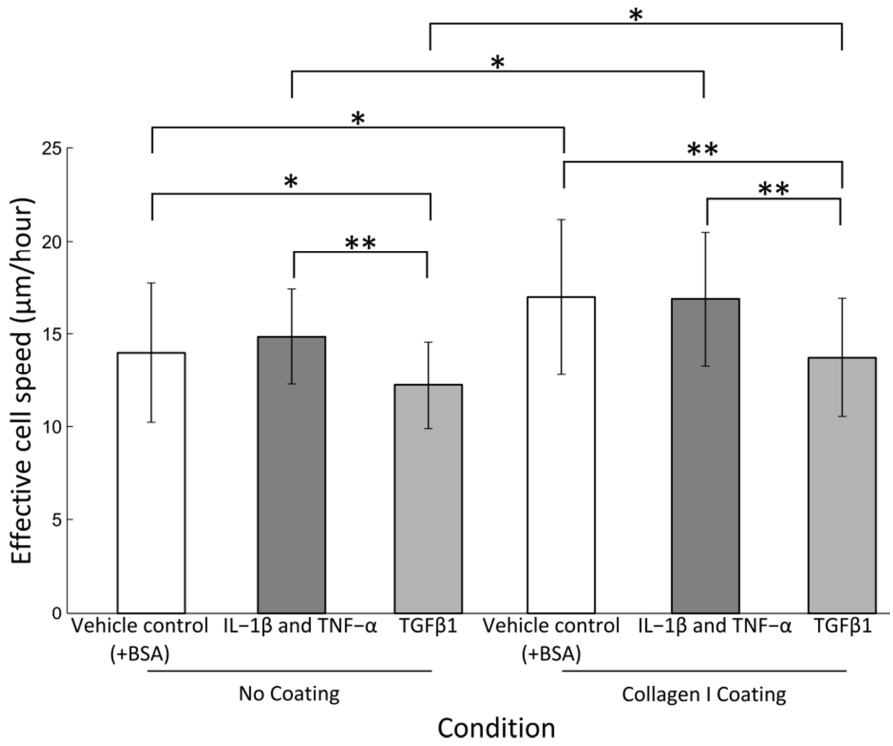

Figure 2-13 Effective cell speed as measured during *in-vitro* scratch assays. The growth substrate was either left as is (tissue culture polystyrene) or pre-coated with collagen I. Scratch assay was carried out in regular cell culture medium (control), culture medium supplemented with pro-inflammatory cytokines IL-1β and TNF-α, and culture medium supplemented with anti-inflammatory cytokine TGFβ1. Measurements shown as mean effective cell speed ± standard deviation across three biological replicates (i.e. separate primary cardiac fibroblast isolations). Significance of results was assessed using an independent t-test and indicated as * (p-value < 0.05) and ** (p-value < 0.01).

The differences observed between instantaneous and effective cell speed showed that changes in direction did impact how cells migrated. Cell migration is an important part of cardiac wound healing as fibroblast cells often situated in the surrounding healthy myocardium are required at the site of injury for reparation (production of a scar). Cell migration is likely to have an influence on the rate of scarring post-MI. Therefore, it is important to gain a further understanding of the stability and variability of cell speed during migration. The variability of cell migration was visualised by measuring the changes in instantaneous cell speed over a period of ~22 hours (Figure 2-14). Instantaneous cell speed appeared to fluctuate greatly overtime. When combined with the changes in direction shown in Figure 2-12A, it appeared that cell locomotion followed an intrinsically discrete pattern whereby the cells sensed their environment, changed direction, and moved.

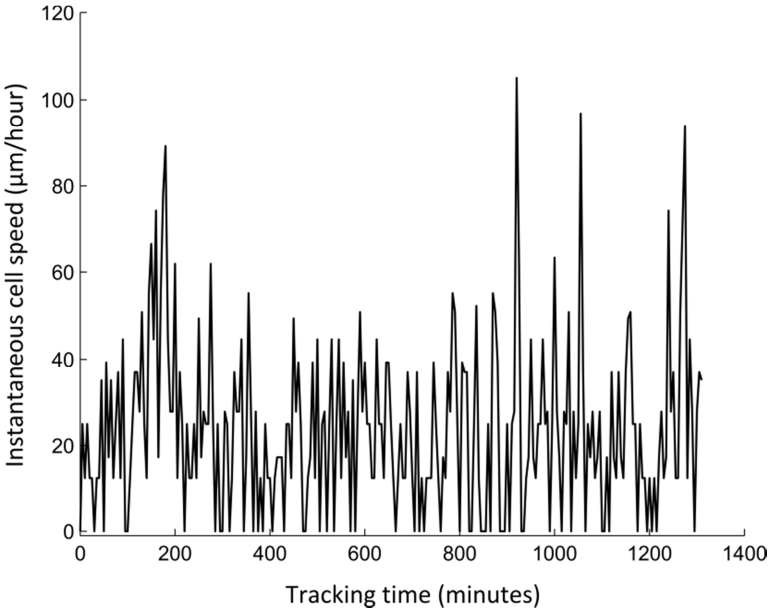

Figure 2-14 Time-course visualisation of the instantaneous cell speed of a single migrating cells.

Further analysis of the cell migration trajectories on time lapse microscopy movies suggested that the presence of obstructing cells often contributed to changes in migration direction (Figure 2-15). Cells tended to migrate in straight lines towards the centre of the wound until obstructing cells forced changes in direction towards an unoccupied region.

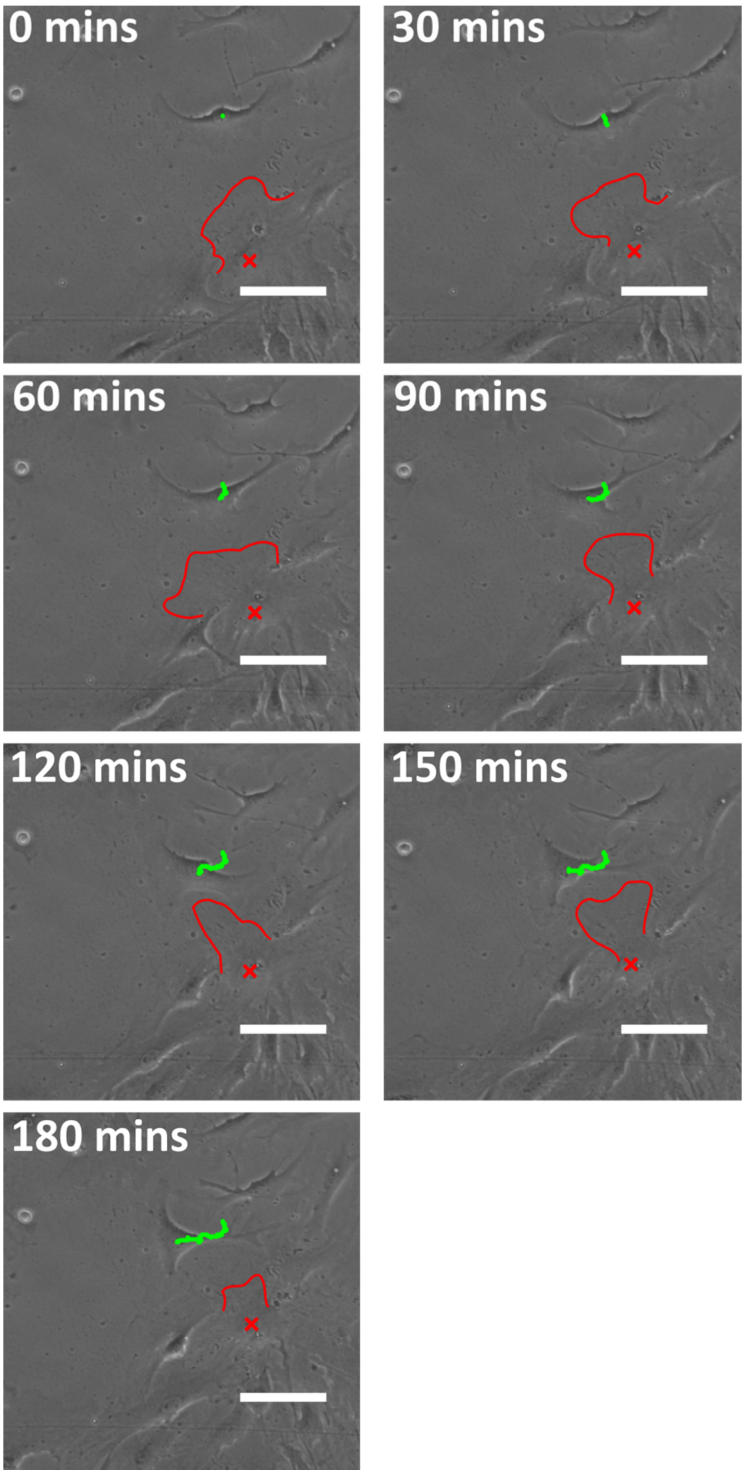

Figure 2-15 Changes in cell migration direction in response to contact with obstructing cells. A cell was tracked (green tracking line) over 180 minutes across the frames of a time-lapse phase contrast microscopy movie. The tracked cell changed direction in response to contact with a neighbouring cell (protrusions outlined in red, nucleus indicated by a red cross). The scale bars represent 100 μm.

Contact inhibition of locomotion is a mechanism arising from cell-cell interactions that affects the trajectory of migration. As it was likely to alter the rate at which fibroblast cells migrate into the wounded region, quantification of this behaviour was thus necessary to inform its implementation in the mathematical model. Contact inhibition of locomotion of primary cardiac fibroblasts during the course of a scratch assay was investigated.

Firstly, the frequency of various responses of cells when encountering obstructing cells along their migratory trajectory was determined. The responses considered included stopping, alteration of migratory direction to move towards unoccupied regions, overlapping (i.e. climbing over the obstructing cells), and alteration of the obstructing cell migratory direction (Figure 2-16A). In the vast majority of cases (78.6%), the migration direction of cells changed to move into unoccupied regions. The other two most frequent responses were the tracked cell stopping in place (9.5%) and having the obstructing cell move so that the tracked cell could continue on an unaltered trajectory (11.9%). For the case where a cell stopped, it was always due to the lack of readily accessible free space. Moreover, cells were never observed climbing on-top each other, and instead remained in a 2D monolayer.

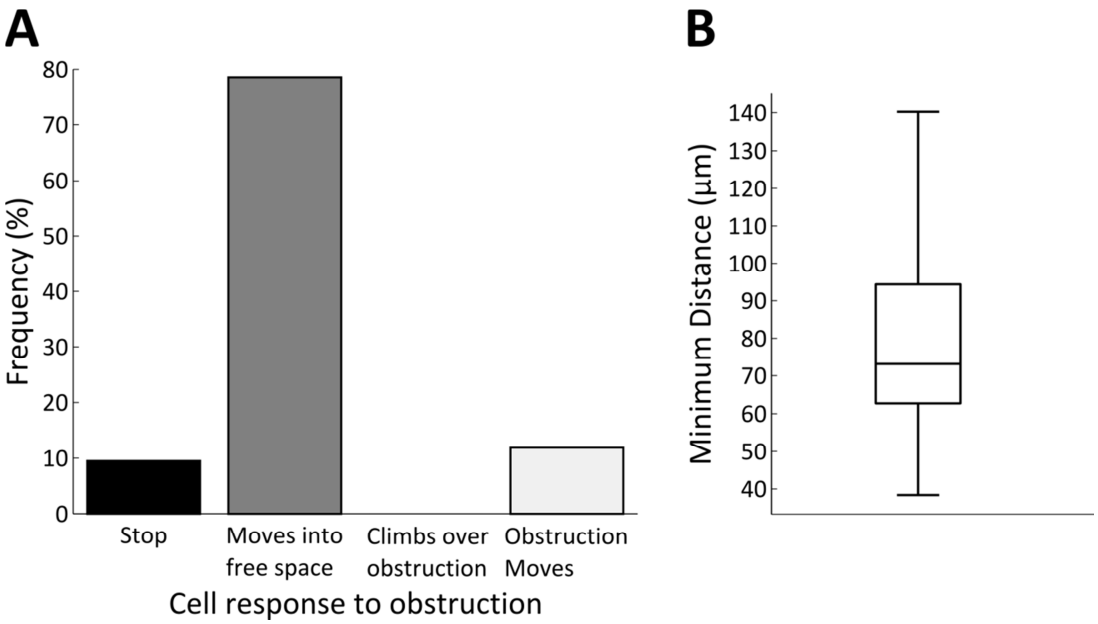

Figure 2-16 Investigation of contact inhibition of locomotion *in-vitro*. (A) Cell response to the presence of other cells in its migration trajectory. (B) Boxplot of the minimum distances between two cells before at least one of the two altered its migration direction. The horizontal line is the median of the distribution, the edges of the boxes are the 25th and 75th percentiles and the whiskers extend to the most extreme data points. 42 primary cardiac fibroblast cells were tracked across three independent experiments (separate isolations).

Based on the same data, it was also possible to determine the distance at which cells tended to react to the presence of an obstruction on their migration trajectory (Figure 2-16B). This distance was defined as the distance between the cell nuclei in the frame preceding the first observable cell response to the obstruction. The mean and median reaction distance were found to be 78.9 μm and 73.1 μm respectively, with a range of measured values spanning just under 102 μm and a standard deviation of 25.5 μm. This high variability in distance measurements might be due to the wide range of cell areas observed, which could potentially relate to variations in their capacity to sense their surroundings.

2.4.3 Cell proliferation

Cell proliferation is an important cell behaviour in the context of cardiac wound healing. One such phenomenon was the position dynamics of migration immediately following division (Figure 2-17). First, the angle between two cells after division was tracked overtime (Figure 2-17A and B). As soon as 5 minutes after division, the cells migrated away from one another at an average angle of about 170°, which was maintained for at least 45 minutes. In other words, the cells tended to migrate away in almost opposite directions, given that their trajectory was unobstructed. It was also investigated how far apart two daughter cells were positioned shortly after division (mean distance within 15 minutes or 3 time points). This distance is likely to be close to the diameter of a rounded cell. Indeed, the distance between the two daughter cells was found to be on average 3.09 µm with a standard deviation of 0.67 µm (Figure 2-17C).

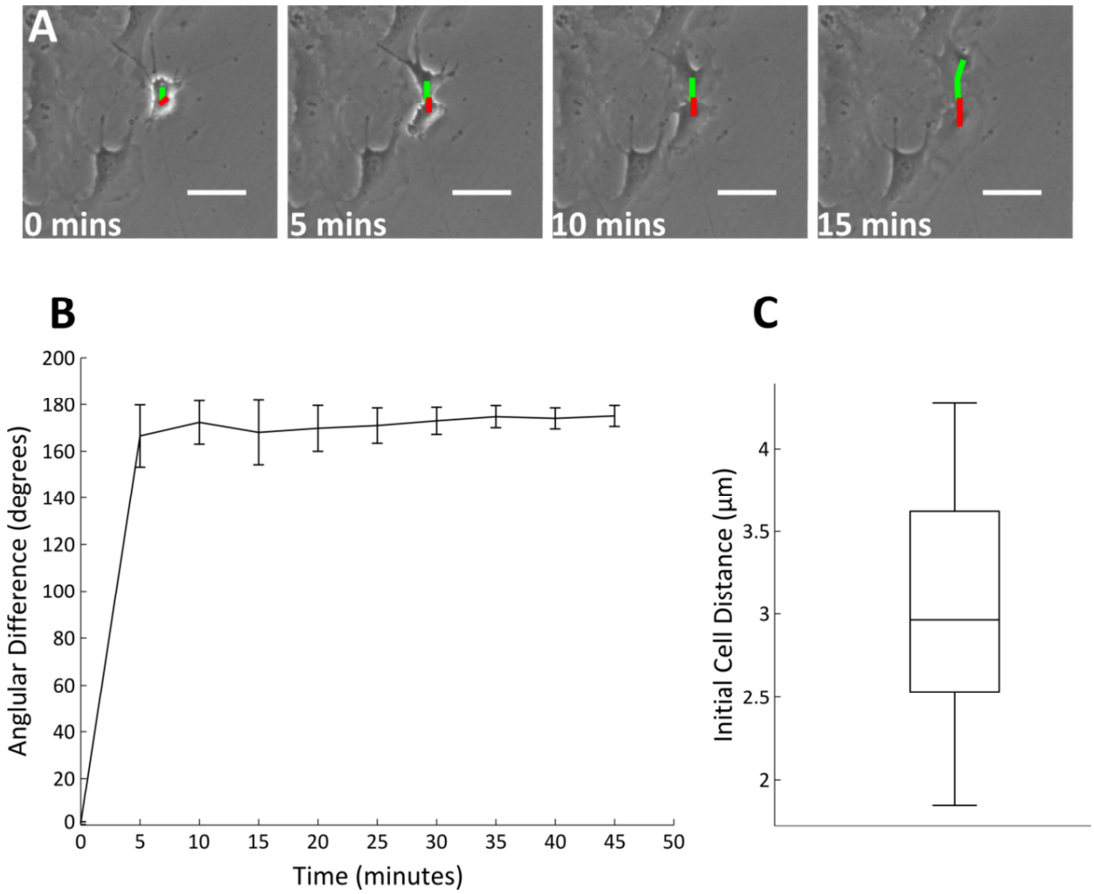

Figure 2-17 Cell behaviour immediately after division. (A) Two cells after division are tracked over the first 4 frames (20 minutes) of a time-lapse phase contrast microscopy movie. The scale bars represent 50 µm. (B) Angular difference in function of time and (C) average distance between two daughter cells up to 15 minutes after division. The horizontal line is the median of the distribution, the edges of the boxes are the 25th and 75th percentiles and the whiskers extend to the most extreme data points. In both cases, a total of 21 pairs of primary cardiac cells were analysed from three independent experiments (separate isolations).

The effects of wounding on the rate of proliferation at a population level were studied. Changes in the proportion of synchronized cells in the three phases of the cell cycle G1 (G_1 checkpoint), S (synthesis) and G2/M (G_2 checkpoint/mitosis) at different time points after wounding were

compared with the distribution at the same time points without a scratch (no wound control condition). Figure 2-18, shows the difference in the +/-scratch cases after 24 hours, 53.8% of cells in the scratched case (Figure 2-18 A) are in the cell cycle compared with only 42.3% in the unscratched cells (Figure 2-18 B). These results revealed no significance as they represent a single experiment but the trends suggested that wounding increases the probability for progression through the cell cycle.

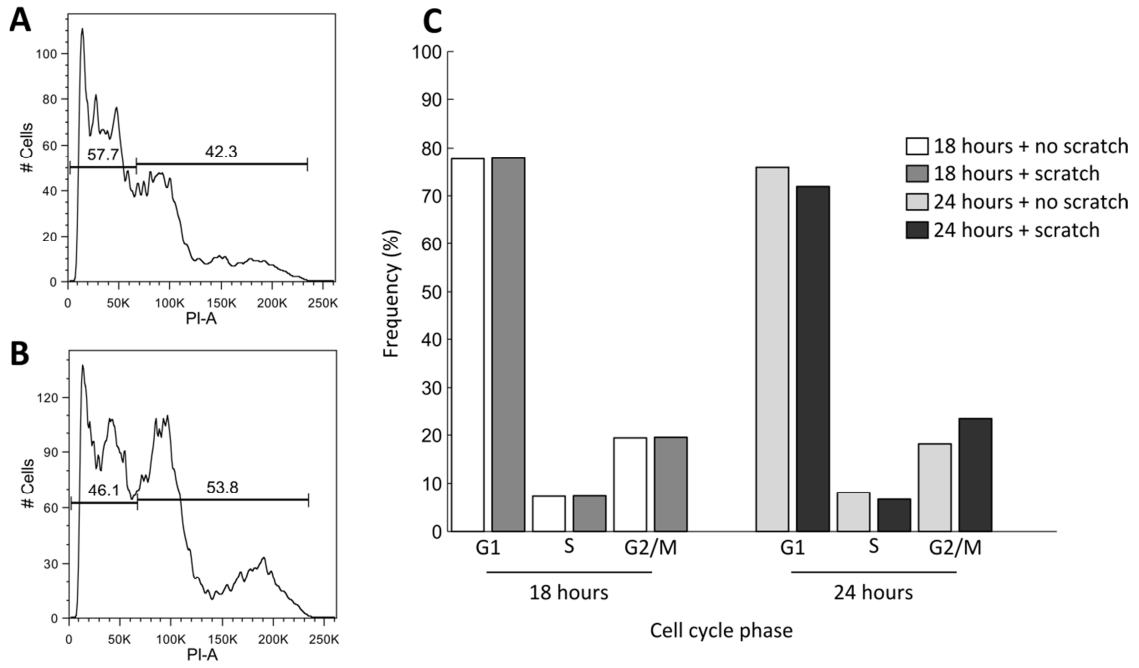

Figure 2-18 Changes in the proportion of cells at different phases of the cell cycle. (A-B) Illustrates the percentage cells (%) in the sub G1 phase and in the cell cycle (G1, S, and G2/M) after 24 hours with (A) and without (B) a scratch. (C) Percentage of synchronized cells in each cell cycle phase (G1, S and G2/M), at 18 and 24 hours with and without a scratch in both cases. The cells were fixed at the time point after wounding. There is no statistical significance as n=1.

Analysing this data more closely, the distribution of cells in each phase of the cell cycle (G1, S and G2/M) at 18 and 24 hours are shown in Figure 2-18C). Figure 2-18C shows a 5.2% increase in the proportion of scratched cells in G2/M compared with the control after 24 hours. However, these represent preliminary data and are not statistically significant, so the findings are inconclusive.

2.4.4 Cell differentiation

Expression of the myofibroblast marker α-SMA was used as a basis for the discrimination between fibroblasts and myofibroblasts on fluorescence microscopy images (Figure 2-19).

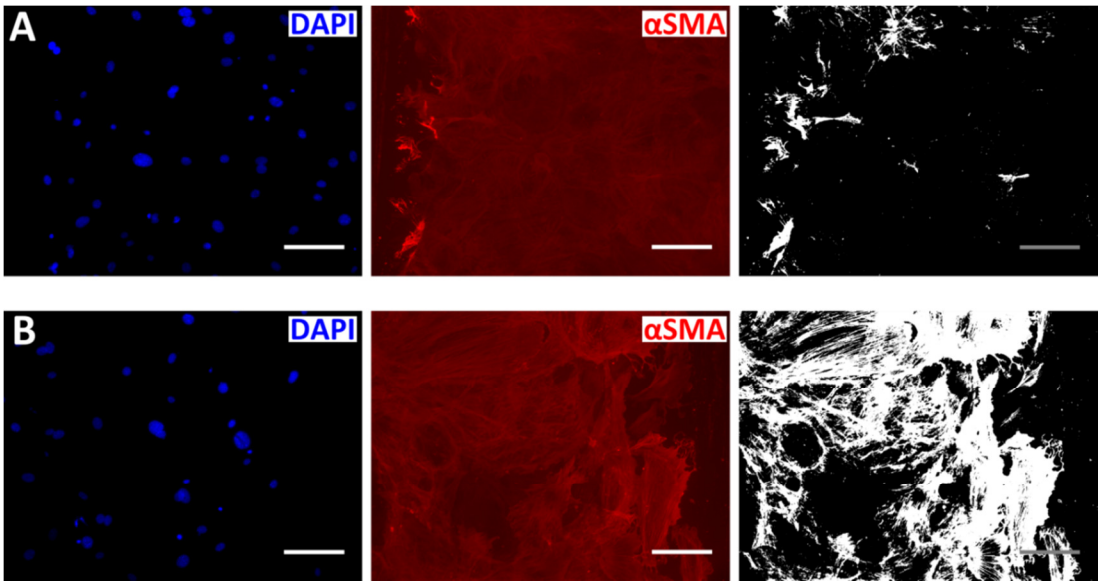

Figure 2-19 Detection of myofibroblast cells on immunofluorescence microscopy images. Images acquired just after scratch (A) and after 10 hours (B). Both DAPI (nucleus marker) and α-SMA (myofibroblast marker) were imaged. The brightness and contrast have been enhanced for clarity. Binary mask obtained after thresholding of α-SMA. The threshold value was the same for both (A) and (B). All scale bars represent 150µm.

First, changes in phenotype were measured in serial scratch assays whereby a large number of cultures were seeded and subsequently analysed at various time points. This allowed the determination of differentiation kinetics (Figure 2-20). Just after a scratch, about 30% of the cell population stained highly positive for the myofibroblast marker. Thereafter, the fraction of the cells testing positive for the myofibroblast marker increased with time. The first significant increase when compared to the initial proportion was observed 6 hours after the scratch (p-value=0.0191) when ~55% of the cells were positive. This proportion further increased up to the 10h time point where the cell population comprised of about 75% of cells positive for α-SMA, a significant increase compared to the initial proportion (p-value=0.0004). After 16 hours, the fraction of positive cells had decreased from the 10 hour time point, but was still significantly higher than the proportion measured initially after scratching (p=value=0.005).

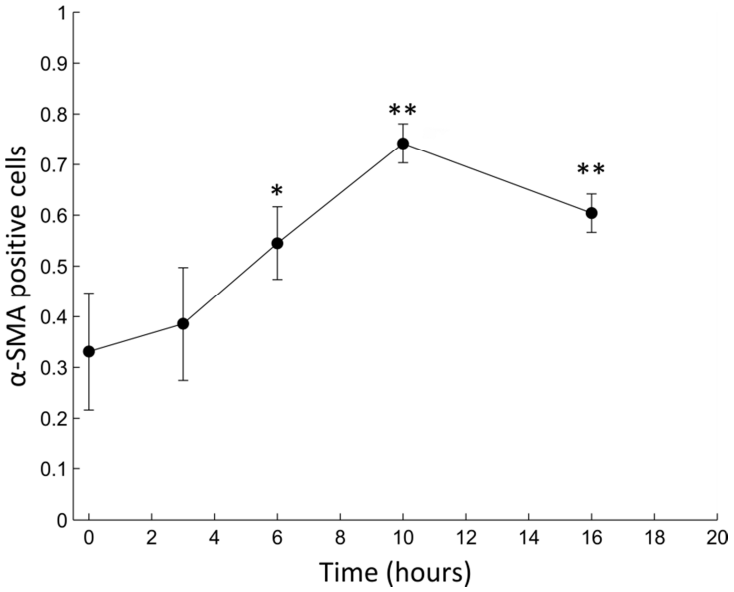

Figure 2-20 Changes in the proportion of α-SMA positive cells (indicating a myofibroblast phenotype) in function of the time after scratch. Immunofluorescence was used to count the myofibroblast and fibroblasts cells just after scratch and subsequently at 3h, 6h, 10h, and 16 hours after scratch. Each time point is shown as mean ± standard deviation across three independent cultures. Significance in comparison to initial proportion after scratch as * (p-value < 0.05) and ** (p-value < 0.01). On average, 454 cells were counted along the edge for a given replicate.

It is likely that external stimuli promote the differentiation of cardiac fibroblasts towards myofibroblast lineages during cardiac wound healing. It is thought that TGFβ1 might be one such signal (Frantz et al., 2009). Experiments were therefore carried out where TGFβ1 was added to the culture medium directly after the scratch was performed. The control experiment was carried out by adding the vehicle in which the TGFβ1 was dissolved, BSA, to the culture medium instead (Figure 2-21).

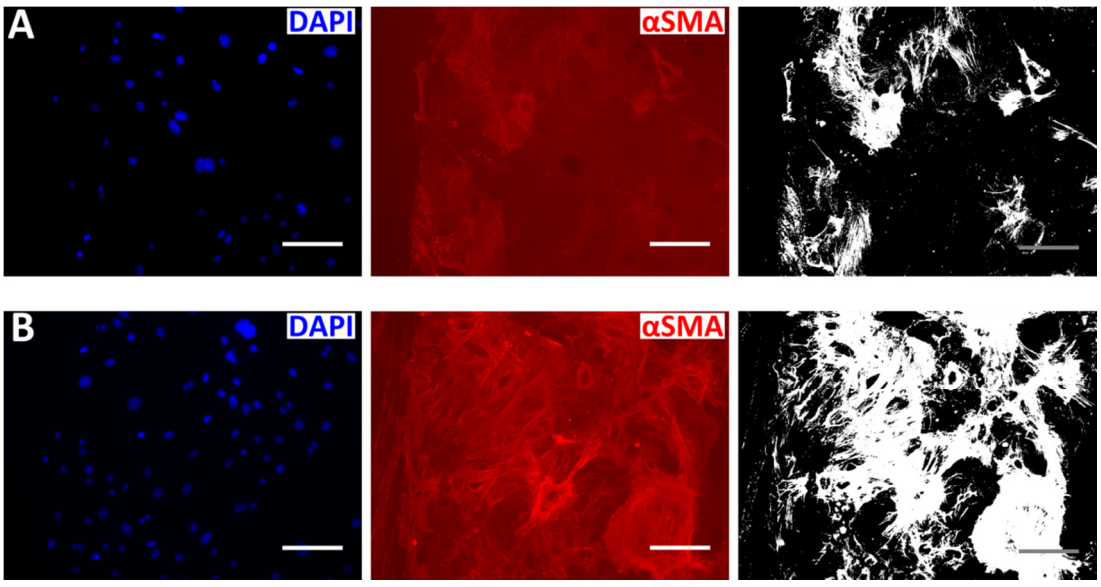

Figure 2-21 Effect of the addition of TGFβ1 on α-SMA expression by cells. Representative images from cultures with medium supplemented with (A) BSA and (B) TGFβ1. Both DAPI (nucleus marker) and α-SMA (myofibroblast marker) were imaged using immunofluorescence microscopy. The brightness and contrast have been enhanced for clarity. Binary mask obtained after thresholding of α-SMA. The threshold value was the same for both (A) and (B). All scale bars represent 150µm.

The proportion of α-SMA positive cells was then determined at multiple time points during the course of scratch assay experiments (Figure 2-22). The proportion at each time point was averaged across three independent experiments, where on average ~400 cells were counted for each experiment. Both conditions (TGFβ1 and BSA) had starting proportions identical to the case without any addition to the culture medium. However, 3 hours after the scratch the profiles started to differ from what was previously measured (without the addition of a vehicle control or TGFβ1, Figure 2-20). Both the vehicle control (BSA) and TGFβ1 attained proportions of ~55% of α-SMA positive cells (Figure 2-22), whereas that fraction was less than 40% in the case without any supplementation to the medium (Figure 2-20). The proportion of positive cells in the vehicle control (BSA) then remained stable at about 55% until the last time point recorded. In contrast, the cultures with TGFβ1 added to the medium reached 70% at 6 hours and then remained constant. Thus at time points 6, 10, and 16 hours, the fraction of cells positive for the α-SMA marker was significantly higher in presence of TGFβ1 than in the case where BSA was added (p-values of 0.006, 0.003, and 0.001 respectively). Surprisingly, the addition of the vehicle control (BSA) also had a marked effect on the proportion of α-SMA positive cells measured when compared to the case with no addition to the culture medium.

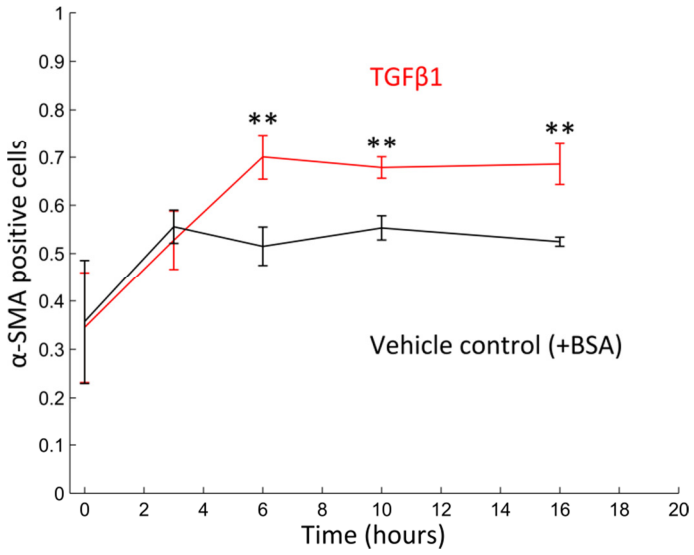

Figure 2-22 Effects of the addition of TGFβ1 and BSA (vehicle) to the culture medium on kinetics of changes in the fraction of cells highly expressing α-SMA. Immunofluorescence was used to count the myofibroblast and fibroblasts cells just after scratch and subsequently at 3h, 6h, 10h, and 16 hours after scratch for cultures in medium supplemented with 0.001 % BSA (black) and TGFβ1 (red). Each time point is shown as mean ± standard deviation across three independent cultures. Significance of the results between the two conditions was assessed using an independent t-test and indicated as ** (p-value < 0.01).

It was important to confirm that the addition of TGFβ1 to the culture medium had the expected effects on pathways it was known to interact with. This was done by analysing the protein content of cells during a scratch assay using western blot analysis. In particular, the concentration of pSmad3, a known downstream target of TGFβ1 (Sato et al., 2003), was assessed 30, 60, and 120 minutes after initiation of the scratch in the cases where either TGFβ1

or BSA were added to the culture medium (Figure 2-23). The pSmad3 content in the cells appeared to peak at around 60 minutes after the scratch in TGFβ1-supplemented medium, and the measured levels were markedly higher than those observed in the case where BSA was added to the culture medium. These results confirmed that TGFβ1 had the intended effects on the cells, and thus that the responses measured during these experiments could potentially be a direct effect of its addition.

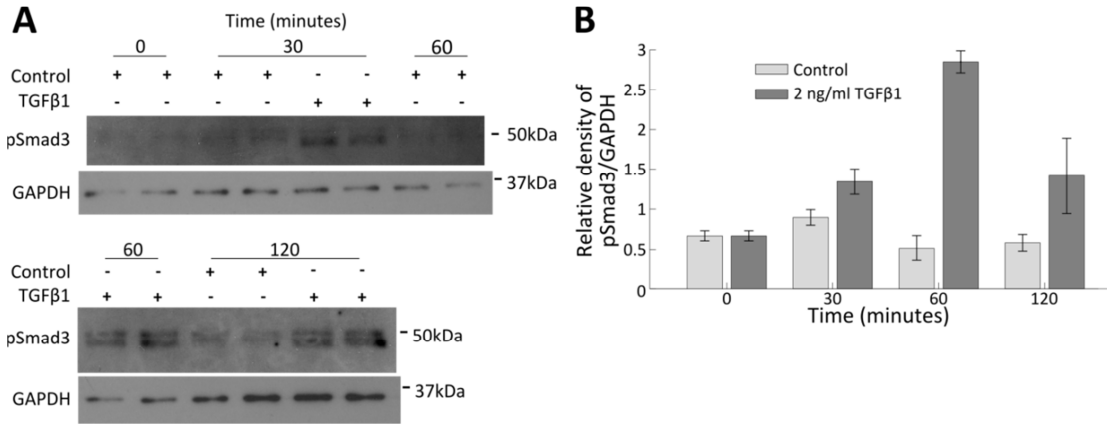

Figure 2-23 Validation of the effect of the addition of TGFβ1 on known downstream target. Determination of the phospho-Smad 3 (pSmad3) content in primary cardiac fibroblasts during a wound healing assay after stimulation with 2ng/ml TGFβ1. In the control case, the vehicle (BSA) was added. (A) Photographs of the gels. (B) Relative density of pSmad3 to GAPDH estimated with the densitometry plugin for ImageJ. The error bars represent standard deviation across a duplicate.

Experiments were also performed to determine the effects of two other compounds that would mimic pharmacological interventions. The first one was ALK5 inhibitor, which shown to effectively block the effects of TGFβ1 (Inman et al., 2002). The addition of ALK5 inhibitor resulted in a marked decrease in the proportion of cells staining positive for α-SMA, with a significant difference (p-value of 0.03) measured at 10 hours after the start of the scratch compared to vehicle control (DMSO) (Figure 2-24 A). Whereas the fraction of positive cells stabilised at around 70% when TGFβ1 was added to the culture medium, the proportion of positive cells stayed relatively constant at ~50% when ALK5 inhibitor was added. The other compound evaluated was SU5402, a known inhibitor of vascular endothelial growth factor receptor (VEGFR) and fibroblast growth factor receptor (FGFR) (Kaftan et al., 2012; Mohammadi et al., 1997). Its addition to the culture medium resulted in a slightly slower increase in the proportion of cells expressing α-SMA but the difference was not found to be significant (Figure 2-24 B).

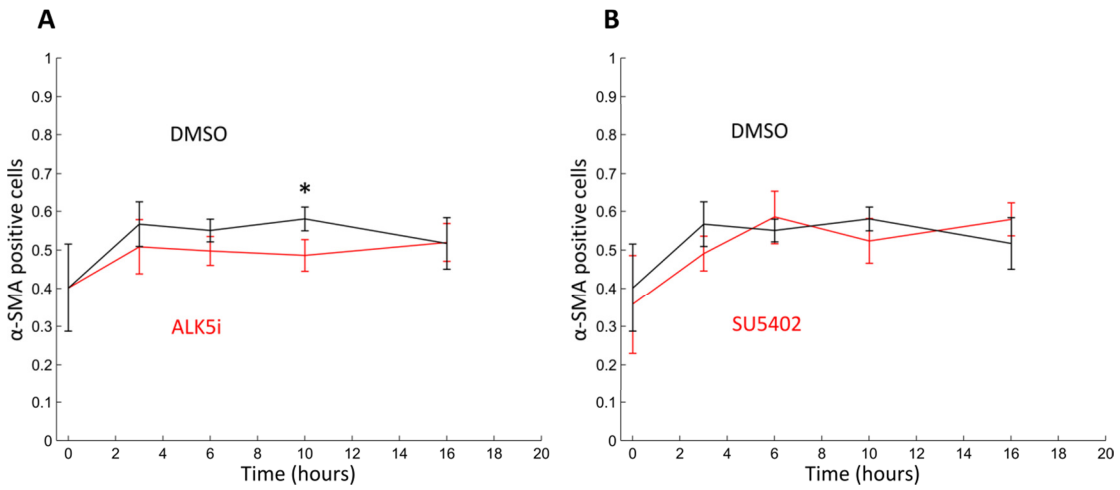

Figure 2-24 Evaluation of the effects of two pharmacological interventions on the fraction of α-SMA positive cells during the course of scratch assays using primary cardiac fibroblasts. (A) Activin-like kinase inhibitor (ALK5, a TGFβ1 inhibitor) at a 10 μM concentration or (B) SU5402 (VEGFR and FGFR inhibitor) at a 2 nM concentration was added to the culture medium. In both cases, the control was the vehicle (DMSO at 1% concentration). Immunofluorescence was used to count the myofibroblast and fibroblasts cells just after scratch and subsequently at 3h, 6h, 10h, and 16 hours after scratch Each time point is shown as mean ± standard deviation across three independent isolation (i.e. biological triplicates). Significance of the results between the two conditions was assessed using an independent t-test and indicated and indicated as * (p-value < 0.05).

2.4.5 Cell area

The population of cells used for these experiments was a mixture of wild type primary cardiac fibroblasts and cardiac fibroblasts that expressed a yellow fluorescence protein (YFP) marker. This approach made it easier to distinguish individual cells and allowed for their perimeter to be traced automatically using a software package such as ImageJ (Figure 2-25). As the difference in cell area distributions between fibroblast and myofibroblast cells was also of importance for the model, cells were also co-stained for α-SMA (a myofibroblast marker) so that the analysis could be further refined by associating a given measurement with the corresponding cell type.

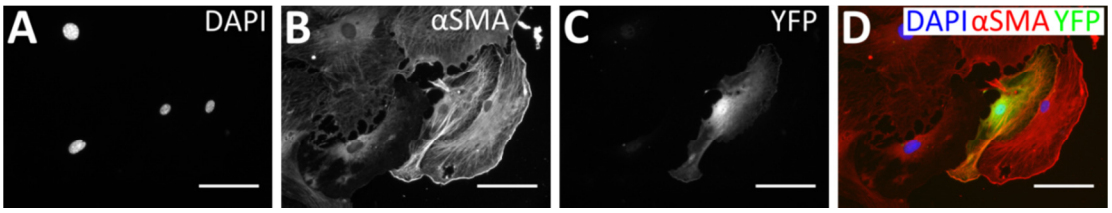

Figure 2-25 *In-vitro* cardiac fibroblast cells at the boundary of a scratch assay. Immunofluorescence used to stain for (A) DAPI (nucleus marker), (B) α-SMA (myofibroblast marker) and (C) YFP. (D) Composite image of all 3 fluorescence channels. Scale bars represent 100 μm.

At 16 hours after a scratch assay was initiated, cells were fixed and stained with the markers for α-SMA and YFP. The whole length of the scratch was imaged and, after establishing a composite of individual field of views, could be represented in a single continuous image (Figure 2-26 B). Cells were sampled within a region restricted to one side of the wound edge and spanning ~1000 μm towards the bulk of the cells. A cell was deemed suitable for analysis if its cell outline could be clearly identified, with no visible overlap between neighbouring cells

(Figure 2-26 B). All cells in the region that met these requirements were counted. This was repeated for three scratch experiments carried out using primary cardiac fibroblasts from independent isolations. Interestingly, the cells closer to the scratch edge were not necessarily the largest ones (Figure 2-26 A). There did not appear to be any correlation between the distance from the wound and the size of the cells.

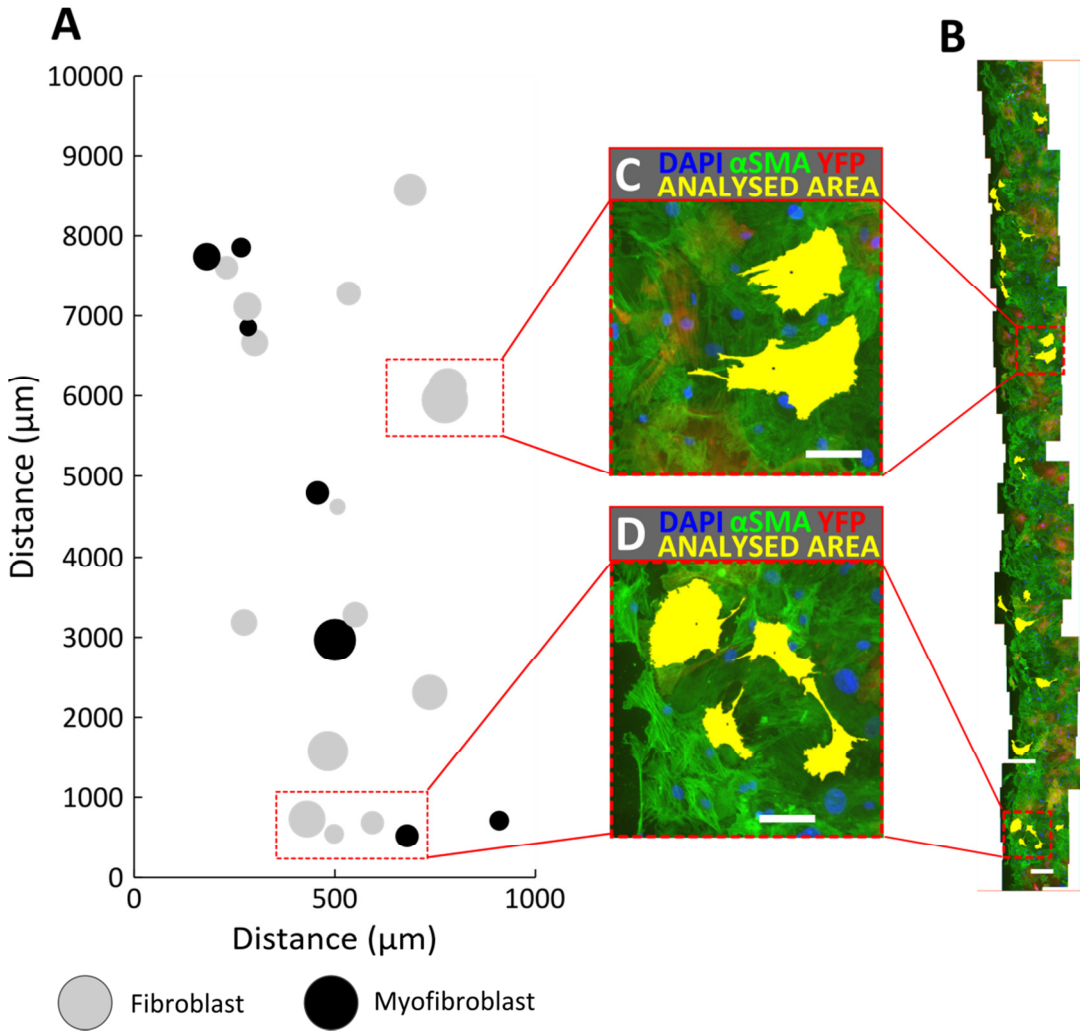

Figure 2-26 Visualisation of the data used for cell area determination. (A) Abstract representation of the position of the analysed cells in respect to the edge of the scratch. Cells are represented as circles whose radius was scaled according to their area. Fibroblasts and myofibroblast were represented as grey and black circles, respectively. (B) Whole scratch imaged 16 hours into a scratch assay experiment. Composite of fluorescence channels: DAPI (blue), α-SMA (green), YFP (red) and analysed cell areas (yellow). In addition, cells whose area was measured are filled in yellow. Scale bar represents 250 µm. (C-D) High magnifications of some regions of interest from (B), regions indicated on (A). Scale bars represent 100 µm.

The areas of myofibroblast cells were found to be significantly larger than those of fibroblasts (one-tailed independent t-test, p-value = 0.039), with median areas of 7149 μm^2 and 5414 μm^2, respectively (Figure 2-27). Interestingly, the distribution of areas for myofibroblast cells was found to be very broad, markedly more so than that of fibroblast cell areas.

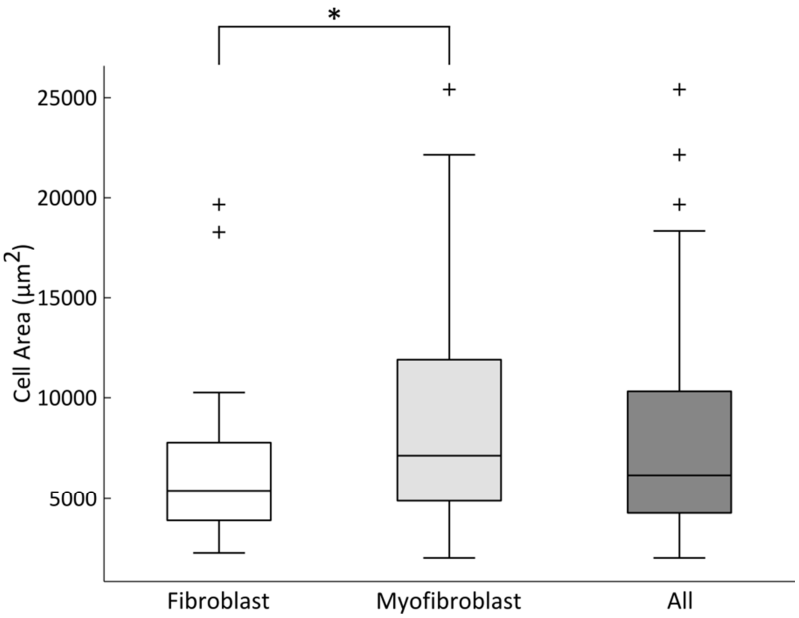

Figure 2-27 Distribution of cell areas as measured *in-vitro* for cardiac fibroblast and myofibroblast cells. Boxplot of the cell areas of the fibroblast cells, myofibroblast cells and all cells together. The horizontal line is the median of the distribution, the edges of the boxes are the 25th and 75th percentiles and the whiskers extend to the most extreme data points. In total, 65 cells (including 40 myofibroblasts) across three independent experiments (i.e. separate isolations) were analysed. The significance shown was assessed using a one-tailed independent t-test.

2.5 Discussion

In this study, the migration, proliferation, differentiation and area of *in-vitro* primary cardiac fibroblast cells isolated from murine hearts were analysed in the setting of a wound (scratch assay). Cell behaviours measured during *in-vitro* experiments were used to directly inform model parameter in the model. Therefore, it was important to devise a cell model that would mimic as closely as possible the cells involved in the wound healing process *in-vivo*. Three potential fibroblast cell models were initially considered: NIH 3T3 cells (immortalised mouse embryonic fibroblasts), primary dermal fibroblast cells (isolated from murine ear tissue), and primary cardiac fibroblast cells (isolated from murine hearts). NIH 3T3 cells were the most attractive model from a convenience point of view, as large numbers of cells could be generated without the need to maintain mice colonies. Both primary dermal and cardiac cells required isolation from an animal. The former was more attainable due to ease of access to the tissue the cells were derived from. Primary cardiac fibroblasts were the gold standard for such experiment but their isolation was challenging and time consuming. The morphologies of these three cell types: NIH 3T3, primary dermal fibroblasts and primary cardiac fibroblasts were shown to be very different. In addition to the morphological differences, it was previously shown that the gene expression profiles of fibroblast cells derived from different tissues can also differ significantly (Chang et al., 2002).

The migratory speed of *in-vitro* cardiac fibroblasts was identified as an important behaviour of cells during cardiac wound healing post-MI. Indeed, resident cells from the healthy tissue

migrate towards the site of injury so that the damaged tissue can be replaced with a scar. The dynamics of this infiltration of the wounded tissue by cells are dictated by the migration speed of individual cells, as well as their trajectories. Both these cellular behaviours were investigated *in-vitro* by analysing the motion of primary cardiac fibroblast cells during scratch assay experiments. The migratory speed of cardiac fibroblast cells was analysed with the addition of pro-inflammatory stimuli TNF-α and IL-1β. *In-vivo*, TNF-α and IL-1β are present during the inflammatory phase of wound healing and act as a chemoattractant steering the cells to promote infiltration of the wound (Frangogiannis et al., 2002; Frantz et al., 2009; Nahrendorf et al., 2010). The migratory speed was not affected by the addition of these two cytokines together. This is in contrast with a previously published study where Boyden chamber assays were used to measure the population migration speed of primary cardiac fibroblasts (Brown et al., 2007). Indeed, it reported a significant increase in migration speed when TNF-α and IL-1β were added to the culture medium. However, the experimental setup was different, as Boyden assays do not usually allow tracking of individual adherent cells and are instead used to determine the number of cells in suspension migrating a set distance at each time point and the cells were pre-stimulated for 24 hours with the pro-inflammatory cytokines (Mitchell et al., 2007). In addition, a gradient of TNF-α and IL-1β was formed, instead of having them homogeneously mixed at all locations of the culture.

One of the main functions during the inflammatory phase is the removal of dead cardiomyocytes, which have become apoptotic as a result of the hypoxic environment which is established as a result of coronary artery occlusion (Frangogiannis et al., 2002). Cardiomyocytes are more sensitive to damage by hydrogen peroxide (H_2O_2, used to initiate oxidative stress) than cardiac fibroblasts, comparing their respective survival rates (Zhang et al., 2001). Moreover the function and phenotype of *in-vitro* cardiac fibroblast cells have been influenced by hypoxia. Cardiac fibroblast cells were observed to have a reduced percentage of survival with increasing concentrations of H_2O_2 (Zhang et al., 2001). It was important however, to determine whether a hypoxic environment had an impact on fibroblast migration. Prolonged hypoxia could lead to a reduction in the number of fibroblast cells reaching the infarct region for repair. Cardiac fibroblast cells stimulated with $CoCl_2$ (an oxygen scavenger) were observed to migrate at lower speeds although, this was not statistically significant. $CoCl_2$ has been shown to induce cell death in a different fibroblast cell type (Vengellur and LaPres, 2004). The decrease in migration speed could be linked to an increase in cell death. A larger decrease in migratory speed may occur for higher concentrations of $CoCl_2$.

The proliferative phase of wound healing is associated with the production of a collagen I based scar by fibroblast cells and their differentiated counterparts myofibroblast cells. TGFβ1 is expressed at the site of injury during the regenerative phase of cardiac wound healing and is a known promoter of fibroblast differentiation (Chen and Frangogiannis, 2012; Souders et al.,

2009; Walker et al., 2004). The addition of TGFβ1 to the culture medium led to a decrease of both instantaneous and effective cell speed in all cases tested. TGFβ1 has been shown to inhibit pro-migratory matrix metalloproteinase-2 (MMP-2) normally expressed in fibroblast cells which could explain the decrease observed in the migratory speed of cardiac fibroblasts (Howard et al., 2012). Cell speed was determined for cells cultured in either non-coated culture vessels (i.e. cells were attached directly to tissue culture treated polystyrene) or vessels pre-coated with collagen I. The latter was included as a more accurate representation of the *in-vivo* extracellular matrix. Pre-coating led to a statistically significant increase in the effective cell speed and in the instantaneous cell speed for the pro-inflammatory and anti-inflammatory conditions. Cell speeds measured in the control case (BSA and collagen I-coated vessels) and those obtained after addition of TGFβ1 (in collagen I-coated vessels) were used as the baseline cell speeds for fibroblast and myofibroblast cells in the computational model, respectively.

The effective cell speed was approximated as cell migration was not continuously imaged and an image was captured every 5 minutes during an experiment. Ideally, continuous imaging of the cell culture would be preferred but due to experimental limitations, this was deemed an acceptable compromise. Cell tracking on time-lapse phase contrast microscopy movies also improved understanding of the cell avoidance response when encountering obstructing neighbours. In almost four out of five cases, a cell would change its migration direction towards an unoccupied region. In the absence of free space, the cell would usually stop. This phenomenon is referred to as contact inhibition of cell locomotion and was first demonstrated *in-vitro* by Abercrombie in the 1950's (Abercrombie and Heaysman, 1953). More recently, selective contact inhibition of locomotion was shown to occur both *in-vitro* and *in-vivo* during the migration of neural crest cells (Carmona-Fontaine et al., 2008). *In-vitro* cardiac fibroblast cells were never observed to move over one another. One mechanism by which cells can sense their environment is through the use of long, thin and elongated protrusions called pseudopodia (Abercrombie and Heaysman, 1953). Such processes are assumed to sense the local environment and influence cell behaviour. The minimum distance between two cells on a colliding course before one, or both, altered direction of migration was measured and found to be approximately 75 μm. However, this distance varied significantly between measurements, indicating that other factors might affect it, such as the respective areas of the cells, their migration speed or ability to produce sensing protrusions. These findings and measurements informed the avoidance algorithm in the computational model. It is still unclear whether contact inhibition of locomotion occurs during cardiac wound healing, and if so, to what degree. This phenomenon could potentially play a major role in dictating cell migration trajectories during wound infiltration by neighbouring cells, impacting both collagen deposition and re-orientation and thus the characteristics of the resulting scar tissue.

The proliferation of cardiac fibroblast cells during cardiac wound healing is important. Indeed, together with migration, it could potentially be key to ensure that a sufficient number of cells reach the injured tissue for reparation and scar formation. Similarly to migration, scratch assays carried out using primary cardiac fibroblasts were used as the experimental setup. The goal was to study proliferation at a cellular level (i.e. dynamics of division) and the population level. At the level of an individual cell, it was important to determine whether the daughter cells' resulting from a division had an effect on each other's migratory direction. It was found that both daughter cells tended to migrate away from one another in almost perfectly opposite direction. This could possibly be an effect of the aforementioned contact inhibition of locomotion as the cells were extremely close to one another at that stage.

The influence of the wound (scratch assay) on the fibroblast cell proliferation at a population level was also studied. Flow cytometry was used to analyse the proportion of cells at each stage in the cell cycle from the initial phases G0/G1 and S to the mitotic phase G2/M for a given cell population. *In-vitro* cardiac fibroblast cell populations were compared with and without a scratch at both 18 and 24 hours. Preliminary results showed a small increase in the proportion of cells in the G2/M cell cycle phase at 24 hours in a scratched environment. *In-vitro* cardiac fibroblast cells have a doubling time of roughly 24 hours (Agocha et al., 1997). Any increase in the proportion of cells in the G2/M phase in the wounded setting may only be evident after 24 hours. It generally took approximately 24 hours for the scratch to close. If measurements were obtained after the closure of the scratch (>24 hours), they may not have been representative of a wound healing setting. Another possible limitation of this experimental setup is that the whole population in the dish was analysed. This will include cells far away from the scratched region. It is likely that any change in the proliferation rate of cells close to the scratch could be diluted by the cells far away from the wound. This problem may have been solved by just analysing cells close to the edge of the wound or creating multiple wounds in the culture dish. This would have reduced the number of cells for analysis, reducing the reliability of the results.

In general myofibroblast cells are not present in the healthy myocardium but emerge in the damaged myocardium through differentiation (Daskalopoulos et al., 2012; Sun and Weber, 1996; Sun and Weber, 2000). Myofibroblast cells can be identified by the presence of contractile stress fibres (α-SMA), which are usually absent in undifferentiated cardiac fibroblasts. Immunofluorescence microscopy was employed to determine the fraction of cells that highly expressed α-SMA along the edge of a scratch, up to 16 hours after the start of an experiment. It was found that between 30% and 40% of the cell population was α-SMA positive directly after the scratch. This was consistent with previously reported findings that cells in culture tend to show some degree of spontaneous differentiation, which depended on their passage number and plating density (Masur et al., 1996; Petrov et al., 2002). The fraction of positive cells then increased and peaked at around 10 hours with 70% of the population staining

positive for α-SMA before declining. The *in-vitro* wound is initiated by scratching away cells from a cultured monolayer. This may increase the level of mechanical stress on the cells either side of the wound. Moreover, the rise in the proportion of myofibroblast cells after wounding could be linked to an increase in mechanical stress.

Cultures stimulated with TGFβ1 had a significantly higher proportion of α-SMA cells after 6 hours when compared to BSA vehicle control cultures (both were stable at around 70% and 55%, respectively). The positively correlated relationship between TGFβ1 and fibroblast differentiation has been previously reported (Desmoulière et al., 1993). This data agrees with these findings, while also providing a good understanding of the kinetics of this process *in-vitro*. Differences were observed between BSA the vehicle control and the case where the media was not supplemented with any molecule or compound. In the case where the media was not supplemented the proportion of myofibroblast cells peaked at 70% after 10 hours whereas, the cultures with BSA initially increased to 55% after 6 hours and then remained constant. There were experimental differences between these two cases such as a mixing step which was required when adding BSA. This process involved pipetting a small volume of BSA in each culture followed by gentle agitation to ensure thorough mixing. These two steps were absent from the protocol used for the experiments without any addition, and could thus be detrimental to cell function. In particular, the mixing could have disrupted the cells through flow-induced shear stress. Moreover, the results obtained using the standard cell culture medium and scratch assay protocol had very low variability between the biological triplicates, further highlighting their reliability. It was thus decided to use the profile of changes in α-SMA positive cells as a basis for the generation of the probability function used for the control of the differentiation process in the computational model.

The cell area is an important cell characteristic in any biological process in general, and in cardiac wound healing in particular. Indeed, the size of a cell partially dictates the organisation within tissues and also determines the extent of the contact between the cell and the ECM. This might in-turn influence the impact a cell will have on its surrounding ECM and to what degree it will remodel it during migration. It was also a very important parameter in the model developed in this work, and it was thus investigated *in-vitro* in the context of a scratch assay using primary cardiac cells. Myofibroblast cells were observed to be almost 1.5 times greater in area than fibroblast cells. This was consistent with previous reports where myofibroblasts were often described as a larger cell type when compared to non-activated cardiac fibroblast cells (Masur et al., 1996; Masur et al., 1999). The area of the myofibroblasts varied over a much greater range in comparison to the area of the fibroblast cells. These variations could be due to the cells being at different stages of differentiation. Likewise, it is possible that the specific local arrangement of cells also dictated the cell area and should therefore account for some of this variation. These values were used as the maximum cell area cells could take in the computational model, as it

was assumed that organisation within tissue would prevents cells from attaining this area *in-vivo*.

The *in-vitro* experiments with cardiac fibroblast were also partly extended to include two pharmacological interventions ALK5 inhibitor and SU5402. ALK5 inhibitor is a known inhibitor of the effects of TGFβ1 (Inman et al., 2002). TGFβ1 is a known promoter of fibroblast differentiation and its inhibition post-MI has been correlated with decreased levels of scarring and was shown to have a beneficial impact on cardiac function (Okada et al., 2005). Post-MI rats treated with ALK5 inhibitor have shown delayed systolic dysfunction (Tan et al., 2010). Experiments investigated the effects of this inhibitor on the migratory speed and differentiation of *in-vitro* cardiac fibroblasts. ALK5 inhibitor did not produce significant differences in cell speed however it did lead to an overall decrease in the fraction of α-SMA positive cells. This decrease in the proportion of α-SMA positive cells was significant 10 hours into the experiment where it stabilised at around 50% in comparison to approximately 57% for the DMSO vehicle control. Rats post-MI treated with an ALK5 inhibitor have shown a reduced expression of both α-SMA (a myofibroblast marker) and collagen I in the non-infarct zones of the myocardium (Tan et al., 2010). The addition of ALK5 inhibitor may have had a greater impact on differentiation at regions further away from the wound.

In-vitro experiments investigated the effects of SU5402 on the migratory speed and differentiation of cardiac fibroblasts. SU5402 is a known inhibitor of vascular endothelial growth factor receptor (VEGFR) and fibroblast growth factor receptor (FGFR), both of which have been shown to play a role in myofibroblast differentiation, proliferation and collagen production behaviours (Kaftan et al., 2012; Murakami et al., 2008; Zhao et al., 2014). SU5402 did not significantly impact cell speed or differentiation when compared to the vehicle control (DMSO). Contradictory results were obtained when using different vehicle controls (addition of BSA or DMSO to the culture medium). For instance, a reduction in the cell migratory speed was observed for the vehicle control DMSO compared to the vehicle control BSA. This could potentially be explained by the widely reported cytotoxic effects of DMSO (Cao et al., 2007). ALK5 inhibitor and SU5402 did not produce significant differences in cell speed, as any differences were most likely hidden by the detrimental impact of the vehicle control DMSO.

The properties of cardiac fibroblast cells quantified in this chapter were undertaken in a two-dimensional (2D) culture system, as it was not possible to live image dynamics of the fibroblast behaviour. This is a clear limitation and only an estimation of the three-dimensional setting *in-vivo*. Three-dimensional cell cultures could be adapted to incorporate the 2D experiments carried out in this study. The advantages of the 2D setting is that individual cellular behaviours are more easily observed and quantified individually and there is a greater control over the experimental conditions. The individual cellular behaviours quantified in this chapter are

valuable data inputs for a computational model of cardiac wound healing, discussed further in chapter 4. In terms of quantifying the scarring process post-MI, a 2D culture system would not be a good enough approximation. The scarring process is inherently 3D and composed of a complex series of events. Moreover, quantification of the infarct may be more reliably analysed *in-vivo* (see chapter 3).

Chapter 3

In-vivo cues for model refinement and validation

3.1 Introduction

Some aspects of the cardiac wound healing process could not be captured by the *in-vitro* cell culture experiments carried out to measure cell properties and behaviours (see Chapter 2). In particular, changes in the extracellular matrix (ECM) and cell arrangements in the cardiac tissue post injury can only be accurately characterised by analysis of tissue sections from animal models. Such measurements are critical in order to ensure the biological relevance of the computational model developed in this work, which aims at simulating the interactions between fibroblast cells and the surrounding ECM in the formation of a scar post myocardial infarction (MI).

The ECM in the heart is a highly complex 3-dimensional (3D) structure that both provides a scaffold for the various cardiac cell populations and defines the mechanical properties of the cardiac tissue (Souders et al., 2009). The ECM composition includes cytokines, growth factors, proteoglycans, and interstitial collagens (Souders et al., 2009). In the myocardium, the most predominant collagen is type I, which accounts for more than 70% of the total collagen content (van den Borne et al., 2010). The alignment and composition of the ECM are drastically impacted by the events following MI. Indeed, due to the heart's limited ability to regenerate, a scar is produced to replace the damaged tissue and provide support to the injured region in order to prevent excessive deformation and rupture of the cardiac tissue (Sun et al., 2002).

Collagen accumulation in the infarct tissue at least doubles by seven days post-MI while a highly organised arrangement of fibres, which constitutes the scar tissue, is evident by day 14 (Sun and Weber, 2000). The main components of the scar tissue are type I and III collagen fibres. Type III collagen production peaks early on post-MI, while type I collagen content increases more slowly over the course of the healing process (Cleutjens et al., 1999), constituting the predominant component of the scar in canine models six weeks post-MI (Whittaker et al., 1989). Type I collagen provides tensile strength to the scar as it gets progressively cross-linked, which plays a critical role in ensuring the maintenance of the heart's structural integrity (Weber, 1989). However, accumulation of cross-linked type I collagen at the

infarct site and at its periphery leads to increased tissue stiffness and can eventually adversely impact cardiac function (van den Borne et al., 2010; Cleutjens et al., 1999). The stiffness of myocardial scar tissue has been shown to peak after one to two weeks post-MI (Holmes et al., 1997), while the increase in collagen content and its subsequent cross-linking occurs over a longer time frame, up to 6 weeks post-MI (Jugdutt and Amy, 1986). This timing suggests that others factors, such as changes in the structure of the collagen fibre network (Holmes et al., 1997), might lead to the observed increase in cardiac tissue stiffness. Indeed, whereas arrangement of collagen fibres in the healthy heart is mostly isotropic (i.e. uniform in all orientations), fibres in the scar tissue form highly anisotropic structures (i.e. with a dominant direction) (Whittaker et al, 1989). Myocardial scar tissue which is highly anisotropic (directionally dependent) has shown greater resistance to deformation in some directions when mechanical tested (Holmes et al., 1997; Przyklenk et al., 1987).

Changes in collagen content and structure post-MI are mediated by cardiac fibroblasts and their activated form, myofibroblasts. Myofibroblast cells, which are generally not present in the healthy heart apart from valve leaflets (Porter and Turner, 2009), can be observed at the site of injury at 3 days post-MI in murine models (Cleutjens et al., 1999; Daskalopoulos et al., 2012; Frangogiannis et al., 2000; Sun et al., 2000; Sun and Weber, 1996; Sun and Weber, 2000) and have been shown to persist in a human myocardial scar for as long as 17 years post-MI (Willems et al., 1994).

In order to gain a thorough understanding of the cardiac wound healing process, it is therefore necessary to carry out *in-vivo* measurements of key cellular properties and characterise changes in the collagen matrix with time post-injury. Given that the acquisition of time-course data with the required resolution from live animal models is extremely challenging, these analyses are often carried out *ex-vivo* on tissue sections of hearts at various stages of the healing process. Two methods commonly used to create myocardial ischemia in a murine model of MI are cryoinfarction. This method involves the application of a nitrogen-cooled cryoprobe to the surface of the heart (Katz et al., 2011; Kolk et al., 2009). This technique is inaccurate as it is not guaranteed it will lead to ischemia and it may not always cause a transmural MI (Katz et al., 2011; Kolk et al., 2009). The second method which will be used in this study is permanent ligation of the left anterior descending artery (LAD) in mice to induce MI (Smart et al., 2011). Serial transverse sections from murine hearts post-MI can be analysed. A number of different imaging techniques can be used to image collagen fibres in histological sections and three-dimensional *in-vitro* cell cultures, including second-harmonic generation (SHG) microscopy (Guilbert et al., 2010; Mega et al., 2012; Mostaço-Guidolin et al., 2013), polarized light microscopy (Whittaker et al., 1989; Whittaker et al., 1994) and immunofluorescence confocal microscopy (Mewhort et al., 2014). SHG has the main advantage of enable imaging of unlabelled collagen fibres, thus minimising the amount of tissue preparation required (de Jong

et al., 2012). Immunofluorescence confocal microscopy is specific and allows imaging of a particular structure (e.g. type I collagen fibre) (Mewhort et al., 2014).

Regardless of the imaging modality chosen, further analysis of the images acquired is necessary to derive useful measurements. These analyses are carried out either manually (e.g. annotation of images by an expert) or automatically (e.g. using image processing and machine vision techniques). The features of interest include the orientation, angular dispersion, bundle thickness and spacing of collagen within the myocardium (Reznikov et al., 2013; Verhaegen et al., 2012; Whittaker et al., 1994). By combining texture analysis with machine learning approaches, it was possible to classify SHG images into different categories depending on the collagen structure and density (Mostaço-Guidolin et al., 2013). The angular dispersion of collagen fibrils has been investigated in the circumferential lamellar bone from rat tibiae. This metric has been used to provide information about the level of anisotropy (directional dependence) of the collagen fibres within a sample from a microscopy image (Reznikov et al., 2013). Such measurements allow the assessment of structural changes of the collagen matrix with time after injury or in response to treatments.

Imaging of cells in tissue sections can be carried out using immunofluorescence microscopy methods similar to those employed for *in-vitro* culture experiments. However, there is the additional challenge posed by the thickness of the samples. Whereas conventional wide-field fluorescence microscopy could be used with cell monolayers, the imaging of sections is usually done using confocal microscopy, which enables optical sectioning of thick samples (Nwaneshiudu et al., 2012).

3.2 Aims

The collagen matrix structure and cellular arrangement in both the healthy and uninjured (intact) myocardium will be characterised experimentally from tissue sections of murine hearts to inform the design and parameters of the cardiac healing computational model. Moreover, it will provide a baseline for the evaluation of the simulation outcomes. As such, the aims for the work described in this chapter are:

- Evaluation of different approaches for the imaging of collagen fibre bundles within the scar tissue post-MI.
- Analysis of microscopy images of intact hearts to estimate the size of the resident cardiac fibroblast population and determine appropriate dimensions for the tissue simulated in the computational model.
- Establish an image-processing workflow for the determination of collagen fibre bundle orientation on microscopy images.

- Develop a quantitative metric of the collagen fibre alignment which can be universally applied to both processed microscopy images of heart tissue sections and model simulations outputs. Such a metric is essential for the assessment of the model prediction capabilities.
- Using these tools, characterise collagen fibres orientation of intact hearts and injured hearts at different time points post-MI. This will constitute the dataset used for evaluation and validation of the computational model.

3.3 Experimental methods

3.3.1 Myocardial infarction animal model and tissue section preparation

Surgical induction of myocardial infarction and heart tissue section preparation were carried out by Nicola Smart, Karina Dube, Sveva Bollini and Gemma Balmer (Institute of Child Health, University College London).

Mice were housed and maintained in a controlled environment. All surgical and pharmacological procedures were performed in accordance with the Animals (Scientific Procedures) Act 1986, (Home Office, UK). The injury model of MI was induced by permanent left anterior descending artery (LAD) ligation. Permanent occlusion of the LAD prevents further blood flow in that area, forming an ischemia (Kolk et al., 2009). MI surgery was performed in isofluorane-anaesthetized adult mice weighing approximately 20 to 25 g (Smart et al., 2011). The injured hearts were harvested at various time points post ligation (7, 14 and 21 days) and fixed in 4% paraformaldehyde for two hours on ice. The time points 7 and 14 days post-MI correspond to the times at which there is a peak in the myocardial stiffness (Holmes et al., 1997). The increased myocardial stiffness has been associated with collagen anisotropy (directionally dependent) (Holmes et al., 1997; Przyklenk et al., 1987). In general, by 21 days post-MI there is substantial thinning of the infarct region (infarct expansion) (Mukherjee et al., 2003). Any changes in the collagen architecture will be investigated at this later stage (21 days post-MI).

After rinsing in PBS, hearts were transferred to a 30% sucrose solution in PBS (VWR) to equilibrate overnight at 4ºC. Hearts were then incubated for 30 minutes at room temperature in a 1:1 (v/v) mix of a 30% sucrose solution in PBS (VWR) and OCT embedding compound (Thermo Scientific) under continuous rotation. The OCT-embedded heart samples were then frozen at -80ºC and subsequently sectioned at a thickness of 20 μm using a Bright Model OTF cryostat with 5040 Microtome (Bright Instruments). Sections were then collected on SuperFrost Plus slides (VWR) and were stored at -80ºC until analysis.

In total, 13 hearts were analysed for this investigation. Six hearts for the intact case (17 images acquired), three hearts for day 7 (16 images acquired), two hearts for day 14 (8 images acquired), and two hearts for day 21 (13 images acquired).

3.3.2 Tissue section immunochemistry and fluorescence imaging

The frozen heart tissue sections were thawed at room temperature for 10 minutes and rinsed twice with PBS. Sections were then permeabilised by incubation in 0.5% triton X-100 for 5 minutes before being rinsed twice with PBS. Sections were incubated in blocking solution (1% BSA, 10% goat/donkey serum, 0.1% Triton X-100 in PBS) for 1 hour at room temperature. Sections were then incubated with primary antibodies diluted to the appropriate concentration in blocking solution for 16 hours at 4°C. Alternatively control sections were incubated with just the blocking solution for 16 hours at 4°C. After 5 washes with 0.1% Triton X-100 for 10 minutes each and two rinses in PBS, heart sections were incubated with secondary antibodies diluted in block solution for 1 hour at room temperature. Sections were then washed 3 times with 0.1% Triton X-100 for 10 minutes and incubated with DAPI at room temperature for 5 minutes. Two final washes were done, one with 0.1% Triton X-100 and the other with PBS, both for a duration of 10 minutes. The slides were mounted in a 50% (v/v) glycerol solution in PBS and sealed using clear nail vanish.

Primary antibodies used were anti-collagen I (abcam, ab34710) raised in rabbit used at 1:50 dilution. This marker was used to stain collagen type I fibres (Mewhort et al., 2014). Cy3 conjugated anti α-smooth muscle actin (Sigma, C6198) raised in mouse at 1:400 dilution stained for myofibroblast cells (Gabbiani et al., 1972; Gabbiani, 1993; Gabbiani, 1996; Sun and Weber, 2000). Expression of this marker is also associated with smooth muscle cells (Azuma et al., 2009; Krenning et al., 2010). Anti-vimentin (Abcam, ab54939) raised in rabbit used at 1:200 dilution was used as a fibroblast cell marker (Camelliti et al., 2005a; Krenning et al., 2010). Although smooth muscle and vascular endothelial cells have also been shown to express vimentin (Franke et al., 1979; Mark et al., 1990). DAPI (4',6-diamidino-2-phenylindole, Cell Signalling Technologies, 4083S) was used at a dilution of 1 $\mu g\ ml^{-1}$ for the visualisation of cell nuclei (Kapuscinski, 1995).

The secondary antibodies used was Alexa Fluor 488 anti-rabbit lgG (H+L) antibody raised in goat ($\lambda_{emission}$ = 488) (life technologies, A-11008).

Heart tissue sections were imaged with an inverted Zeiss LSM 710 confocal microscope. Excitation wavelengths used were 405nm (DAPI), 488 nm (Alex Fluor 488) and 594 nm (Cy3). In addition, slides were also imaged using two photon microscopy. Images were obtained with a Leica SP8 confocal microscope with a Coherent Vision II Multi-photon laser. The excitation wavelengths used were 488 nm (Alexa Fluor 488) and 880 nm (multi-photon). The second harmonic generation signal for collagen was collected in the transmission detector with a 430 to 450 band-pass filter.

3.4 Analytical methods

3.4.1 Visualisation of collagen I fibre bundles in heart sections

Collagen type I fibres are one of the main components of the scar that form post-MI (Whittaker et al., 1989). As collagen I is not readily observable using light microscopy, it is necessary to either stain it (using Masson's trichrome protocol, see section 2.2.9) or use a high contrast and specificity method such as immunofluorescence. The latter was used to image collagen I fibres bundles in hearts section using an anti-collagen I antibody. Heart sections from mice at 7, 14, and 21 days post-MI were imaged. As a control, images from heart sections of uninjured mice (intact hearts) were also acquired. Approximately the same locations corresponding to the site of injury were imaged for both injured and control samples.

3.4.2 Automated processing and analysis of fluorescence heart sections images

The main aim was to quantify the difference in collagen I fibre bundles organisation between the injured and control cases. In order to do so, automated image tools were employed to ensure consistent and reliable measurements of fibre bundles orientations. In addition, it produced a representation of the *in-vivo* data that could be directly compared to computational model outputs.

3.4.2.1 Collagen I fibre bundles detection based on local image gradients

The directionality Fiji plugin created by Jean-Yves Tinevez[1] was used to characterise the angular dispersion of the collagen fibre orientations from confocal images of heart sections. The plugin uses a 5×5 Sobel filter to compute the gradient of an image. The assumption is made that the image gradient should capture the orientation of the collagen I fibre bundles as they are the only structures present on the images. A Gaussian function (bell shaped curve) is fitted to the highest peak of the histogram. The standard deviation of this Gaussian is termed angular dispersion, a measure of order (Reznikov et al., 2013).

3.4.2.2 Collagen I fibre bundles detection based on texture analysis

The texture analysis software used was originally written by Dr Lewis Griffin (Computer Science, University College London) in Mathematica. The method detected the dominant orientation of the collagen I fibres at regularly spaced intervals on an image from the intensity of each pixel. The spacing distance was defined by the user and remained constant for all the images processed. The texture analysis software is based on the computation of basic image features (BIFs), whereby each pixel of an image is classified as one of seven categories (e.g. lines, blobs, gradients) based on local symmetries and structures (Crosier and Griffin, 2010). The computation of BIFs is dictated by two main parameters. First, a threshold parameter (ε)

[1] http://pacific.mpi-cbg.de/wiki/index.php/Directionality (last accessed February 2014)

dictates whether the neighbourhood of a pixel should be considered flat (i.e. no specific structure or structure). The second parameter (σ), determines the scales of the structures that will be detected by the algorithm as well as the size of local neighbourhood considered for the classification of each pixel. The output of the algorithm was a grid of uniformly spaced vectors of unit length and whose direction corresponded to the dominant orientation of the collagen I fibre bundles at that location.

3.4.3 Quantification of collagen fibre bundle orientation

It was critical to devise quantification methods for collagen fibre bundle orientation that could be used interchangeably between the heart section data and the computational simulation outcomes. Two approaches were considered for analysing the collagen fibre alignment: a global collagen alignment histogram and a local collagen fibre alignment score. The global collagen alignment histogram provided information about the level of anisotropy at the tissue scale. The local collagen fibre alignment score was used to quantify the level of local alignment most likely generated by cell-matrix interactions post-MI. A highly aligned collagen matrix can result in a reduced cardiac function post-MI (Fomovsky et al., 2011). Currently it is unclear about whether the effect on cardiac function is influenced by local and/or global alignments.

3.4.3.1 Global alignment histogram

Histograms of collagen orientations could be computed from the vector field obtained from either image analysis or computational model outputs. Flat histograms indicate isotropy (no preferred directionality) while the presence of peaks is associated with anisotropy (preferred orientation). As a single histogram was produced for the entire image, it provided a global numerical representation of collagen bundle orientations.

3.4.3.2 Local collagen fibre alignment scoring

Local collagen fibre alignment was scored by a clustering method, which determined regions where the collagen fibres within a region had a similar orientation. The total number of regions for an image represented the level of local alignment. For instance a large number of regions meant that the local alignment of collagen fibres was low. The clustering method was developed to provide a convenient metric characterising the local alignment of collagen I fibre bundles. The main input of the algorithm was an evenly spaced vector field that corresponded to the collagen fibre bundles orientations as outputted by the computational model or computed from the processed immunofluorescence images of heart sections stained for collagen I. A vector describes the dominant orientation of the collagen fibres at a specified location. The collagen fibres had an orientation but were assumed to not have a direction therefore, the vectors used to represent the dominant collagen fibre orientation were assumed to be bi-directional. Because vectors were considered bi-directional, only acute angles (<90°) were taken into account when calculating the angular difference ($\theta_{difference}$) between two vectors.

The cosine of the angular difference between two neighbouring vectors (dominant collagen fibre directions) was used as a measure of the similarity in orientation between two vectors (dominant collagen fibres). This measure ($cos\theta_{difference}$) gave an output in the numerical range [0, 1] and was computed as shown in equation 3.1 where $\boldsymbol{v_1}$ and $\boldsymbol{v_2}$ are the two vectors (dominant fibres) being compared. For $cos\theta_{difference}$ equal to one, two neighbouring collagen fibres (vectors) would be perfectly aligned.

$$\cos\theta_{Difference} = \frac{|v_1 \cdot v_2|}{\|v_1\|\|v_2\|} > T_\theta \qquad 3.1$$

Two vectors were considered of similar orientation and clustered together if the result of this computation was greater than a threshold value T_θ (Figure 3-1). The threshold value (T_θ) was used to define the level of similarity in the orientation of two collagen fibres required for them to be considered aligned.

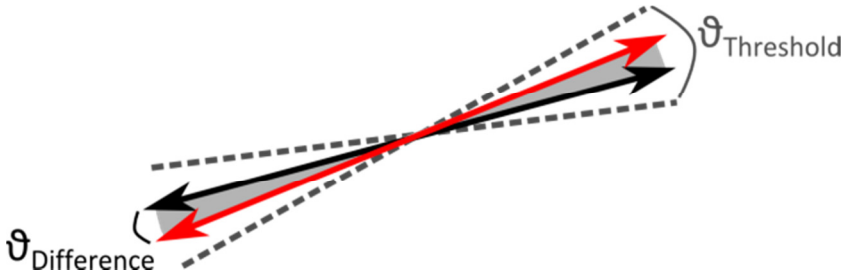

Figure 3-1 Schematic of the angular difference ($\theta_{Difference}$) and threshold ($\theta_{Threshold}$) considered in the computation of fibre alignment. The vectors are considered bi-directional and only acute angles (<90º) are used in the computation.

The algorithm clusters vectors (dominant collagen fibres) together based on their orientation by sequentially scanning the vector field, from left to right and top to bottom, eventually visiting all the vectors of the vector field. The vector field corresponds to the collagen fibre bundles orientations as outputted by the computational model or computed from the processed immunofluorescence images of heart sections stained for collagen I. A cluster represents a region of the tissue (vector field) where the dominant orientations of collagen fibres are similar. Clusters are represented by integer valued labels. Upon creation of a new cluster, the latter will be assigned a label equal to number of clusters already created incremented by one.

When a new vector is visited during the scanning, its angular distance with all 8-connected neighbours (north, north-east, east, etc…) was computed. The algorithm will then cluster the vectors (cluster regions where the dominant orientations of collagen fibres are similar) based on the following rules:

- If none of the neighbours (neighbouring collagen fibres) were found to be of similar orientation to the central vector (collagen fibre), the latter was assigned to a new cluster and the neighbours were unchanged.

- If at least one of the neighbours were found to be of similar orientation to the central vector, and were already previously assigned to a cluster, the cluster (or clusters) were merged by assigning the similar neighbour vectors and the central vector to a cluster whose label was given by the smallest cluster label amongst the similar neighbours.
- If at least one of the neighbours were found to be of similar orientation to the central vector, and none was previously assigned to a cluster, the central vector and similar neighbours were assigned to a new cluster.

The choice for the value of the threshold parameter (T_θ) dictated how similar vector orientations had to be in order to be clustered together. In terms of the scar, this threshold parameter defines how similar the orientations of two collagen fibre bundles must be in order for them to be defined as aligned. In absence of a method for the determination of an optimal value, the outputs obtained by varying T_θ need to be visually assessed based on the agreement with how humans would intuitively cluster the different vectors.

3.4.3.3 Identification of fibroblast cells from intact heart sections

Intact hearts were fixed, sectioned and stained for vimentin, α-SMA and DAPI (Section 3.3.1 and 3.3.2). Single z-stacks from confocal images of these sections were used for analysis (n=3 hearts). Fibroblast cells were identified by their expression of vimentin (Camelliti et al., 2005a; Krenning et al., 2010) and morphology. In general, fibroblast cells have multiple extensions known as pseudopodia (Abercrombie and Heaysman, 1953), lack a basement membrane and have an oval nucleus (Camelliti et al., 2005a).

3.5 Results

3.5.1 Heart tissue section imaging

The ability to generate biologically relevant yet tractable and easily interpretable data of the cardiac wound healing process was a key aspect of this work. *In-vitro*, this was achieved using robust and well understood scratch assays (Liang et al., 2007). Access to murine heart tissue sections from a murine MI model provided a unique opportunity to devise an experimental workflow that would allow the visualisations, and subsequent quantification, of the dynamics of *in-vivo* cardiac wound healing. Two imaging methods were evaluated: confocal immunofluorescence microscopy and second-harmonic imaging microscopy.

3.5.1.1 Confocal immunofluorescence microscopy

Both collagen fibre bundles and cells could be visualised in heart tissue sections using immunofluorescence techniques (Figure 3-2, Section 3.3.2). Due to the thickness (~20 μm) of the sample, it was necessary to use confocal microscopy instead of wide-field microscopy in order to obtain images of sufficient resolution for subsequent analysis.

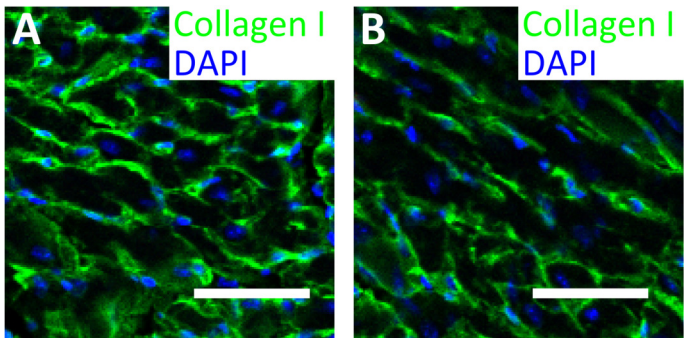

Figure 3-2 Images of an intact heart section illustrating the cells and collagen I fibre bundles. Both are confocal immunofluorescence microscopy images with heart sections stained for collagen I (green) and DAPI (blue). (A) Honeycomb structures and (B) stretched honeycomb structures. The scale bars represent 50 μm.

Confocal microscopy images of heart sections from intact hearts revealed recurring patterns. The collagen I architecture resembled a honeycomb-like structure which was prevalent in most of the samples imaged (n=6 hearts, Figure 3-3). Variations on these structures were also routinely observed, included a stretched honeycomb-like arrangement that might be due to variations in the plane of the heart section (Figure 3-3B).

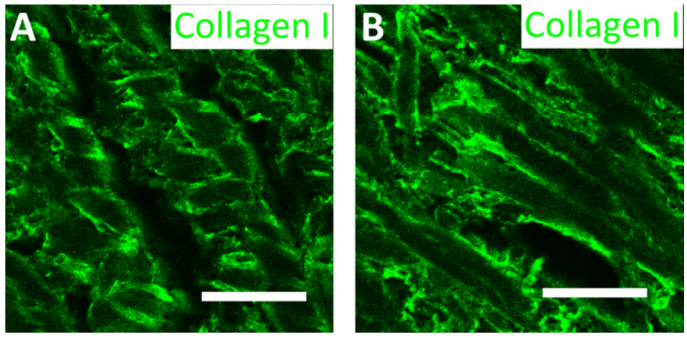

Figure 3-3 Highly variable collagen I structures in intact heart tissue sections. Both are confocal immunofluorescence microscopy images with heart sections stained for collagen I (green). (A) Honeycomb structures and (B) stretched honeycomb structures. The error bars represent 50 μm.

There was also a significant difference in visual appearances between intact hearts and that of hearts following MI (Figure 3-4). At day 7 post-MI the collagen showed a higher degree of alignment compared to intact hearts (Figure 3-4 A and B). This alignment was maintained after 14 days post-MI (Figure 3-4 C). After 21 days, the collagen I fibre bundles still showed a relatively high degree of alignment (Figure 3-4 D) but appeared to be much more densely packed compared to intact hearts and at 7 and 14 days post-MI (Figure 3-4 A-C).

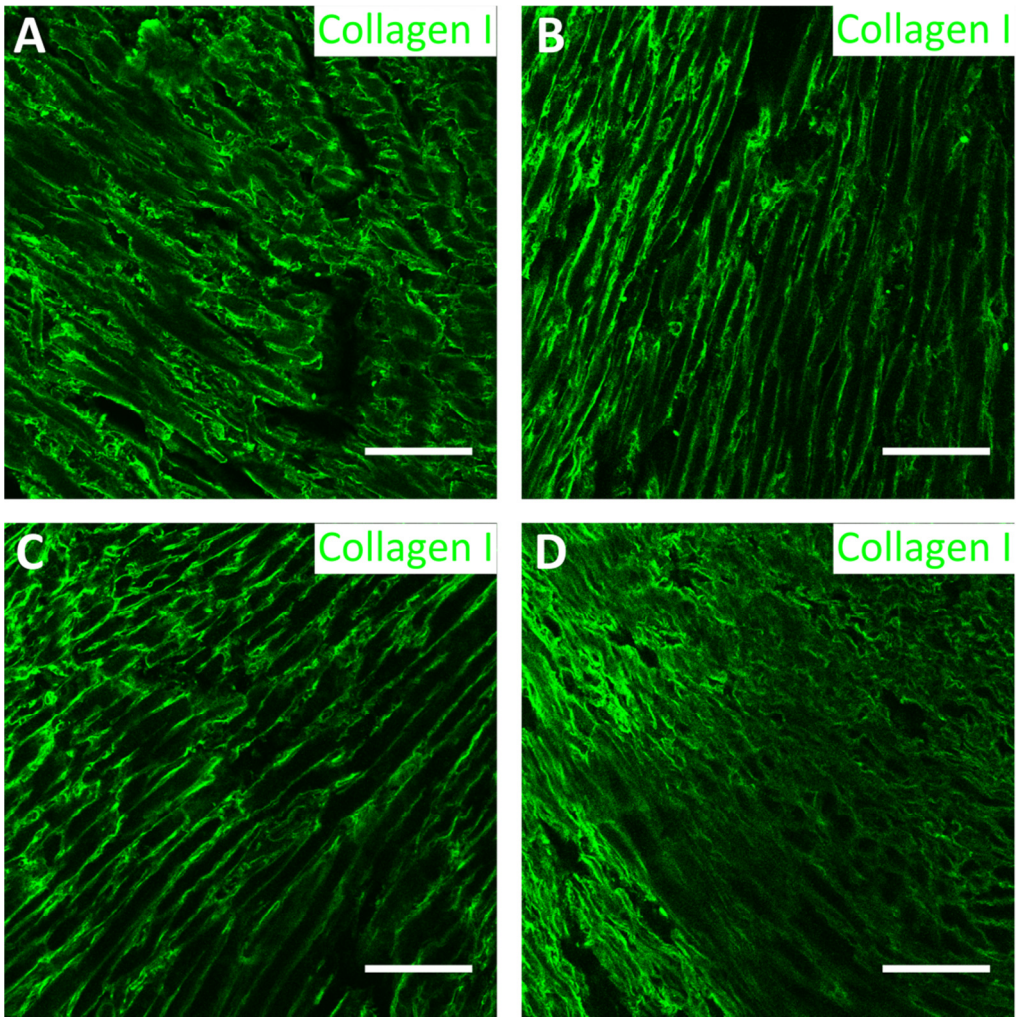

Figure 3-4 Changes in collagen I fibre bundles patterns over time after injury. Confocal immunofluorescence images of heart tissue sections stained for collagen I. (A) Intact heart tissue section (B-D) Heart tissue section of inured specimen 7 (B), 14 (C) and 21 (D) days post-surgery. All scale bars represent 100µm.

Immunofluorescence confocal microscopy proved to be a suitable imaging method for the visualisation of collagen I fibres on heart tissue sections. The high selectivity of collagen I, made it possible to produce high contrast images where the fibres were easily distinguishable.

3.5.1.2 Second-harmonic imaging microscopy

Collagen has a highly crystalline structure and is a non-centrosymmetric biological material, making it effective at producing second harmonics (Cox and Kable, 2006). As such, collagen does not require staining before imaging. Tissue sections from hearts 21 days after MI were imaged using SHIM (Figure 3-5A). The collagen fibre bundles were successfully detected with good agreement (Figure 3-5C) with confocal immunofluorescence images of the same fields of view (Figure 3-5B).

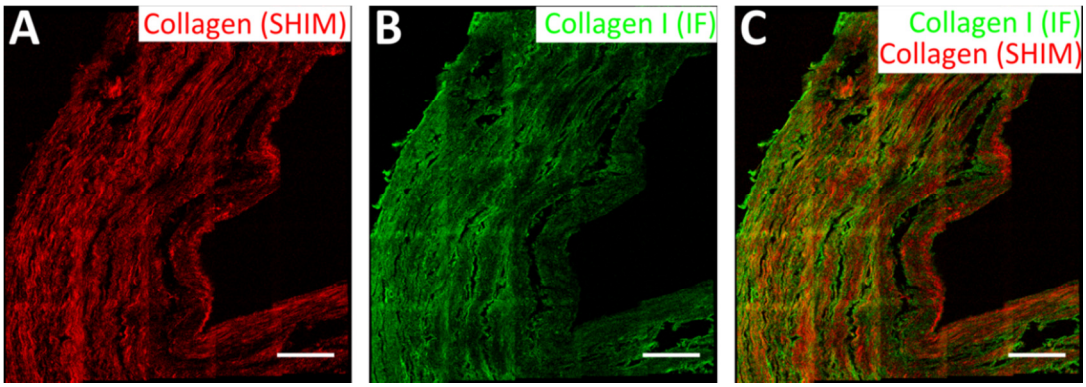

Figure 3-5 Second-harmonic imaging microscopy (SHIM) for collagen visualisation on tissue sections from injured hearts 21 days post-MI. (A) SHIM images of collagen fibres (red). (B) Immunofluorescence (IF) confocal microscopy image of the same field of view seen in (A) stained for collagen I (green). (C) Merged images from (A) and (B). All the scale bars represent 100 µm. The brightness and contrast have been enhanced for clarity.

The same imaging approach was taken with tissue sections from intact hearts (Figure 3-6). In this case, the SHIM images (Figure 3-6A) were different from immunofluorescence confocal microscopy images (Figure 3-6B). The latter showed the typical honeycomb-like structure that was previously mentioned (Section 3.5.1.1). The SHIM images showed highly striated structures (Figure 3-6A). There appeared to be little co-localisation between these two methods (Figure 3-6C). These striations were not as prevalent on SHIM images of sections of injured hearts (Figure 3-5A).

While SHIM offered a better insight into the structural composition of the wound and scar *in-vivo*, the resulting images were unsuitable for the characterisation of the collagen alignment due to the lack of specificity of the method.

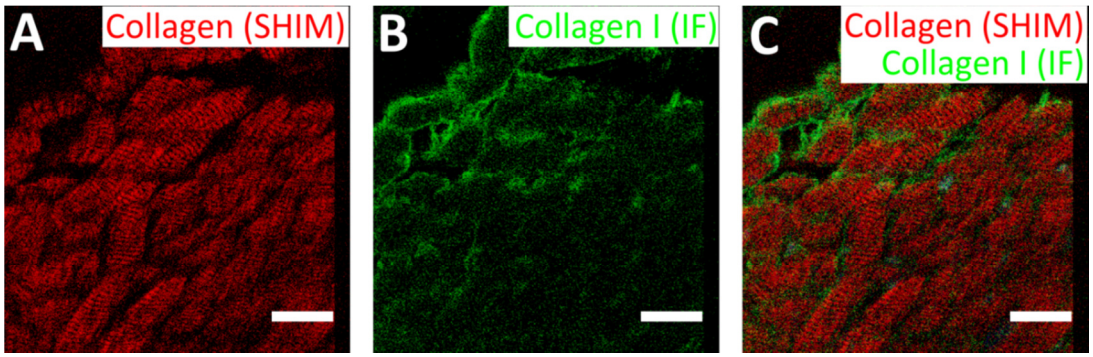

Figure 3-6 Second-harmonic imaging microscopy (SHIM) for collagen visualisation on tissue sections from uninjured (control) hearts. (A) SHIM images of collagen fibres (red). (B) Immunofluorescence confocal microscopy image of the same field of view seen in (A) stained for collagen I (green). (C) Merged images from (A) and (B). All the scale bars represent 25 µm. The brightness and contrast have been enhanced for clarity.

3.5.2 Optimal parameters for the analysis image processing tool

The texture-based analysis method was used to produce a vector field which corresponded to the dominant collagen fibre bundle orientation (Section 3.4.2.2). This method required two parameters: a threshold parameter (ε) and a filter scale parameter (σ). The threshold parameter

dictated whether the neighbourhood of a pixel should be considered flat (i.e. no specific structure or structure). The scale parameter (σ) determined the scales of the structures that would be detected by the algorithm as well as the size of local neighbourhood considered for the classification of each pixel. A value for the threshold parameter (ε) was approximated from previous studies which used this particular texture-based analysis method successfully (Newell and Griffin, 2011). The threshold parameter (ε) was set to 0.01. The optimal value for the scale parameter σ was determined empirically by visually inspecting the collagen orientation vector fields computed with the texture-based analysis tool for the scale (σ) varied between 3 and 48 (Figure 3-7). For larger scale values such as 24 and 48 (Figure 3-7 E and F) the texture-based method did not accurately capture the direction of the collagen bundles as the scale of the collagen was well below these values. Conversely, using a scale value of 3 resulted in a vector field that was sensitive to very small image structures and thus to noise. Again, the texture-based analysis tool with the scale value set to 3 did not capture the bundle direction appropriately (Figure 3-7 B). Intermediate scale values of 6 and 12 produced vector fields that appeared to correlate well with the local collagen bundle structures (Figure 3-7 C and D). From a visual inspection of the results obtained with multiple images, a value of 6 for the scale parameter was found to produce the most consistent results.

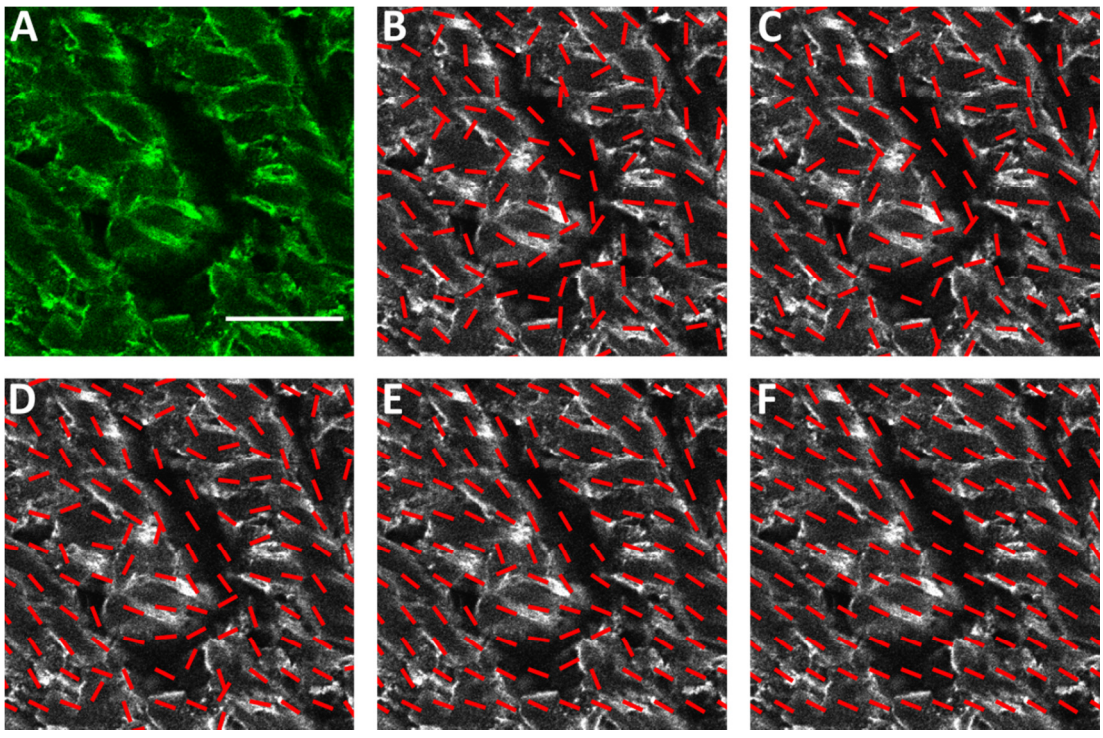

Figure 3-7 Automated characterisation of local collagen bundle orientation on heart section immunofluorescence images. (A) Raw confocal image of a section from an uninjured heart stained for collagen I (green). Scale bar represents 50 µm. (B-F) Image shown in (A) overlaid with a vector field sampled every 24 pixels indicating the orientation of local collagen bundles as determined using an algorithm based on Basic Image Features. The images were generated using different values for the scale parameter (σ): 3 (B), 6 (C), 12 (D), 24 (E) and 48 (F). The threshold parameter (ε) was kept constant at 0.01.

3.5.3 Threshold parameter for local collagen alignment quantification

The local collagen alignment from heart sections was quantified with a clustering method (Section 3.4.3.2). The clustering method classified regions of the tissue (vector field) which contained similar dominant collagen fibre orientations. The difference in orientation between two collagen fibre bundles was defined between 0 and 1, where 0 represented two unaligned (perpendicular) fibres and 1 represented two perfectly aligned (parallel) fibres. Due to errors which may have originated from the image processing method, the similarity of two collagen orientations was set by a threshold value (T_θ). The threshold value was defined by visually inspecting the clusters produced for threshold values of 0.99, 0.995 and 0.999. The three different threshold values were assessed by evaluating the effect on the local collagen alignment of the collagen vector field approximated by the texture-based analysis tool (Section 3.4.2.2). Firstly, the local collagen alignment of an intact heart was assessed (Figure 3-8).

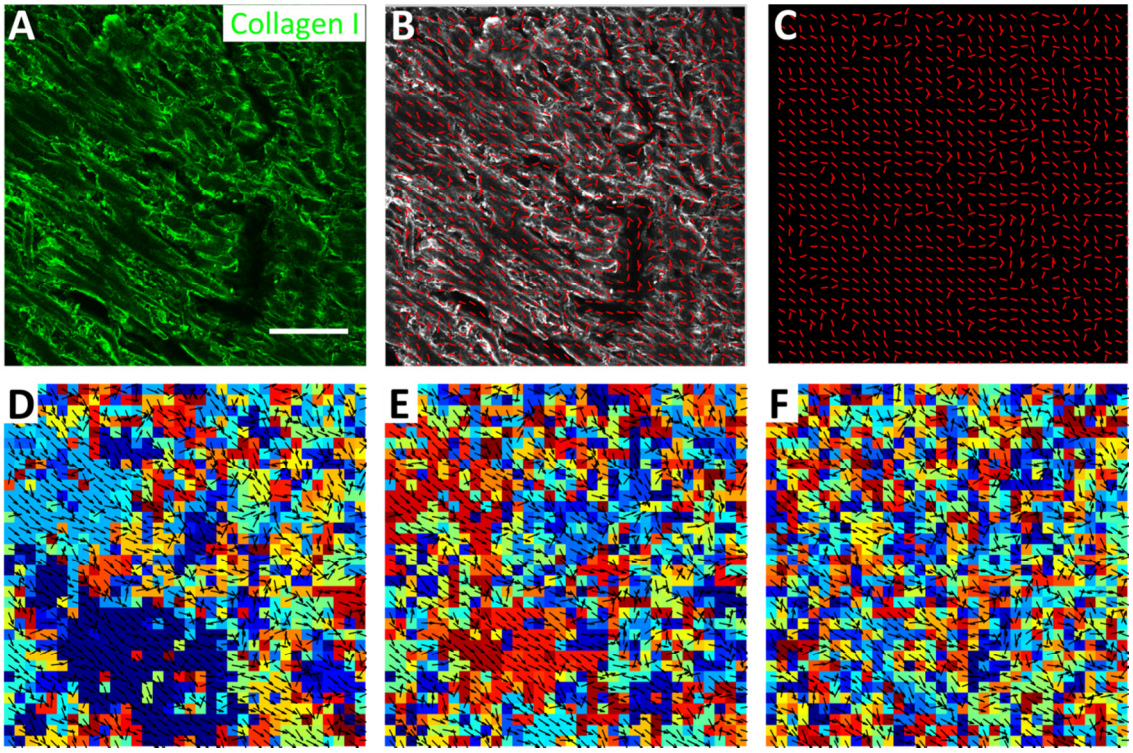

Figure 3-8 Evaluation of the cluster scoring approach for an intact sample. (A) Confocal immunofluorescence image of a section from a control intact heart stained for collagen I (green). The scale bar represents 100 µm. (B) Image shown in (A) overlaid with the vector field generated using the texture analysis tool with σ = 6 and ε = 0.01. (C) Vector field as shown in (B). (D-F) Visualisation of the output of the clustering algorithm for the vector field showed in (C). The T_θ parameter values considered were 0.990 (D), 0.995 (E), and 0.999 (F). Each cluster is represented by a different colour.

The section from an intact heart clearly showed low alignment of the collagen fibre bundles (Figure 3-8A). When visualising the output of the clustering algorithm with a value of 0.990 for the T_θ parameter (Figure 3-8D), it appeared that vectors whose orientations were visibly different were clustered together. Conversely, a value of 0.999 (Figure 3-8F) resulted in a very high number of clusters that did not accurately capture local collagen alignment patterns. An

intermediate value of 0.995 resulted in a clustering output that was in good agreement with visual evaluation of the alignment (Figure 3-8E). The same parameter values were used to evaluate the method for a confocal immunofluorescence image of a section from an injured heart (7 days post-MI). The collagen on the image was clearly more aligned that in the control case (Figure 3-9A). Again, a value of 0.990 for the threshold parameter resulted in a large number of clusters, with a large portion of the vector field assigned to the same cluster (Figure 3-9D). Conversely, a value of 0.999 resulted in a large number of clusters, which did not capture the aligned nature of the collagen fibre bundles on the image considered (Figure 3-9F). Similar to control cases, a value of 0.995 for T_θ resulted in a clustering that best captured the local collagen orientation in the image (Figure 3-9E). Unless otherwise specified, this value was used as the default throughout.

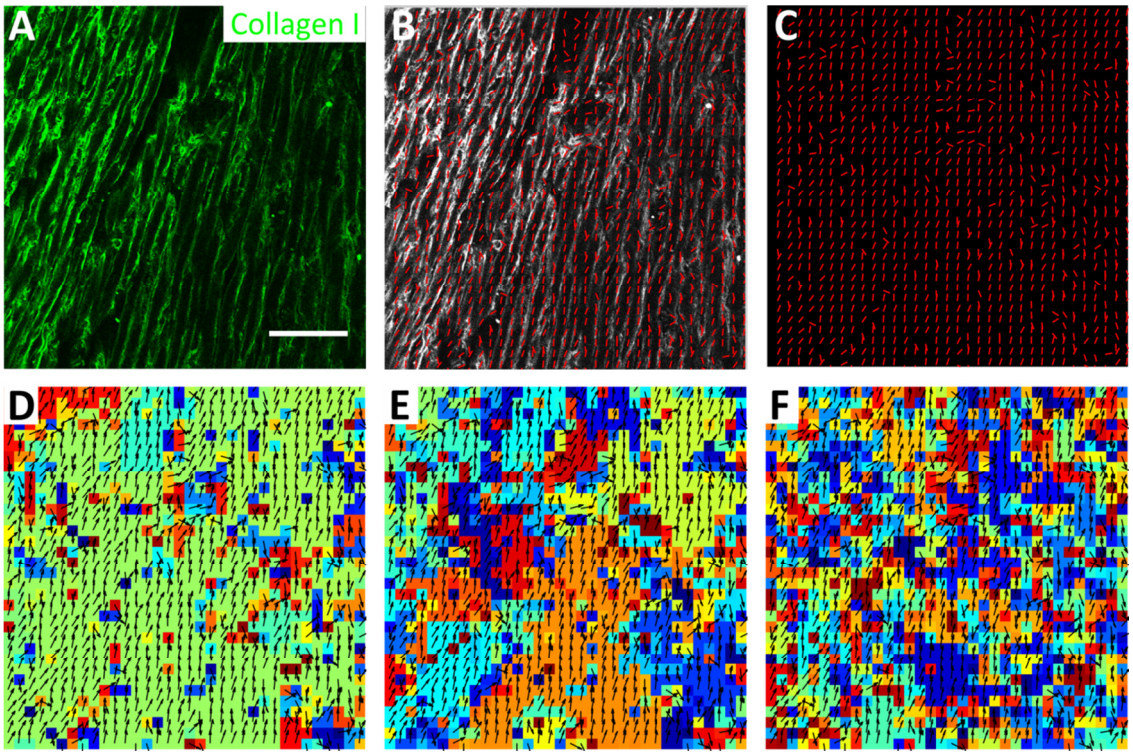

Figure 3-9 Evaluation of the cluster scoring approach for an injured sample. (A) Confocal immunofluorescence image of a section from an injured heart (7 days post ligation) stained for collagen I (green). The scale bar represents 100 µm. (B) Image shown in (A) overlaid with the vector field generated using the texture analysis tool with σ = 6 and ε = 0.01. (C) Vector field as shown in (B). (D-F) Visualisation of the output of the clustering algorithm for the vector field showed in (C). The T_θ parameter values considered were 0.990 (D), 0.995 (E), and 0.999 (F). Each cluster is represented by a different colour.

The number of clusters obtained from the clustering algorithm was applied as a simple metric for the scoring of collagen alignment. This was tested using an artificial example where the orientation of each collagen vector could be controlled as necessary. Initially, the whole vector field was perfectly aligned. At each iteration, one vector was assigned a random direction and the new vector field was analysed using the clustering algorithm. This was repeated until all vectors had been reoriented once. At each iteration, the number of clusters detected was stored

(Figure 3-10). As more vectors were randomly orientated, the number of clusters increased linearly. The relationship between alignment and the number of clusters remained linear until a low number of aligned vectors were left, at which point the number of clusters increased at a slower rate. This non-linear portion was due to vectors getting aligned by chance when randomly re-orientated, a behaviour which was dependent on the T_θ threshold parameter. For a lower threshold (T_θ=0.99) there was a lower number of clusters for unaligned vector fields when compared to higher thresholds.

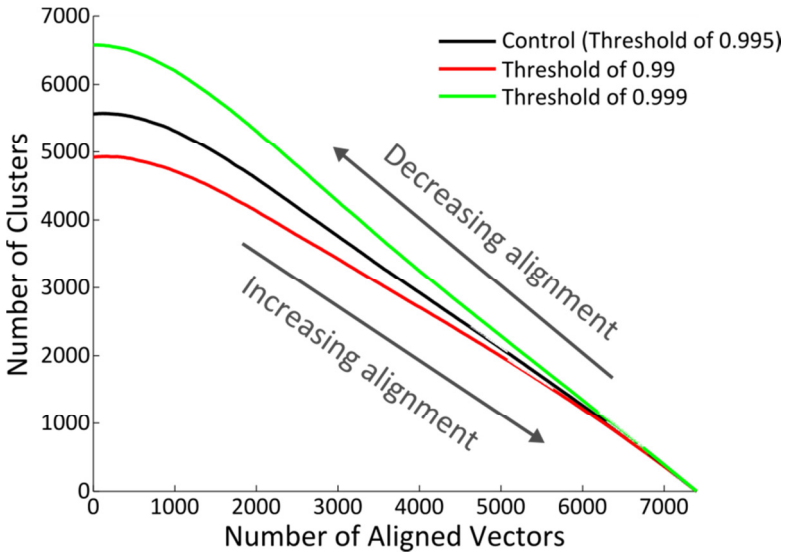

Figure 3-10 Evaluation of the number of clusters as a scoring metric for collagen fibre bundles alignment. Synthetic examples initiated with all vectors aligned. Subsequently, a vector gets assigned a random direction at each iteration, eventually leading to all the vectors being randomly orientated. The threshold parameters (T_θ) were set to 0.99 (red), 0.995 (control, black) and 0.999 (green). This process was repeated ten times for each case and results shown as the average number of clusters.

The number of clusters was thus shown to be a reasonable scoring metric for local collagen fibre bundles alignment. Having a single, easily interpretable metric greatly facilitated the analysis of both *in-vivo* heart sections and the collagen vector fields produced from model simulations. Moreover, this metric enabled the direct comparison between the *in-vivo* and *in-silico* analysis.

3.5.4 Quantification of the changes in collagen alignment post-injury

Collagen alignment on heart sections was quantified using two independent approaches. The first employed texture analysis (image processing method, Section 3.4.2.2) to produce a vector field that represented the dominant collagen direction at evenly spaced locations across the image. The resulting vector field was then analysed using a clustering algorithm (Section 3.4.3.2) whereby neighbouring vectors were grouped together if found to be of similar orientation (i.e. angular difference below a given threshold). The number of clusters was inversely proportional to the local collagen alignment, with low and high cluster numbers corresponding to high and low degrees of alignment, respectively. The second approach used the local image gradients of collagen I (image processing method, Section 3.4.2.1) to determine the direction of the collagen at each pixel of the image. The local image gradients of collagen I

were analysed from immunofluorescence images of heart sections stained for collagen I (Section 3.4.1). From the collagen gradients, histograms of orientations were constructed and the largest peak was fitted to a Gaussian function. The standard deviation of this Gaussian function is termed dispersion and describes the level of angular spread of collagen throughout an image (Section 3.4.2.1). A high dispersion (high standard deviation) would imply that the collagen fibres are more evenly distributed so indicating a low level of alignment. The angular dispersion is inversely proportional to the degree of collagen alignment (Reznikov et al., 2013).

The number of clusters and the dispersion were used both to characterise collagen alignment on tissue sections from intact hearts and that from injured hearts 7, 14, and 21 days post-MI (Figure 3-11). The mean number of clusters measured for intact hearts was 937 ± 94 (analysed from serial heart sections n=17 images ± SD). At 7 days after injury, the average number of clusters decreased to 837 ± 183 (n=16 images), when compared to the control (intact hearts) but this difference was not significant due to high inter-sample variations (Figure 3-11 A). The number of clusters continued to decrease at 14 days to 801 ± 127 clusters (n=8 images), this time was significant (Student's *t*-test) when compared to intact hearts (p=0.006). At day 21, the number of clusters significantly increased (937 ± 117, n=13 images) compared to day 14 (p=0.02), reaching levels close to those of the tissue sections from uninjured hearts. These results suggested that the degree of collagen alignment increased after injury, reaching a maximum at around day 14, before decreasing again after 21 days.

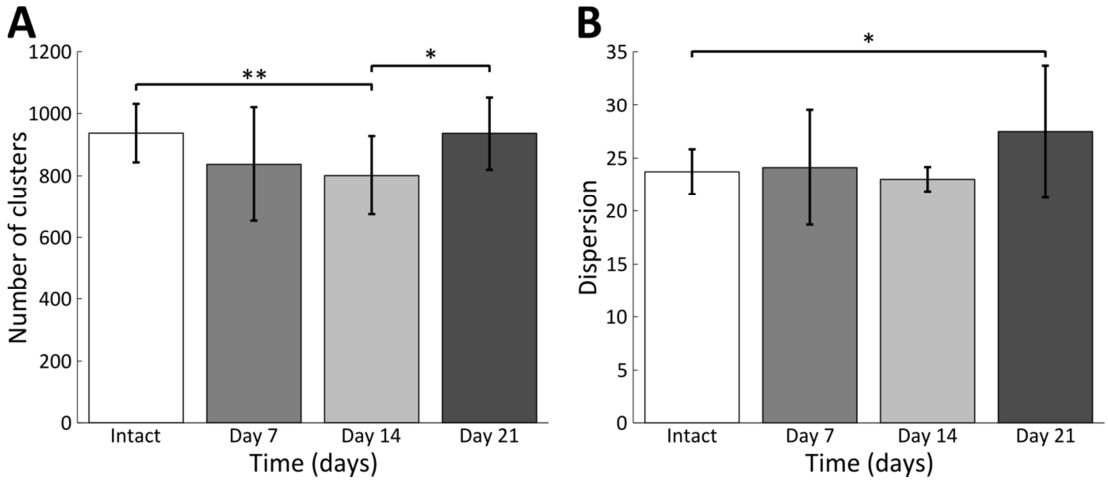

Figure 3-11 Quantitative analysis of collagen alignment on immunofluorescence microscopy images of heart tissue sections. The control was sections from uninjured hearts and three time points post-myocardial infarction were considered: 7, 14, and 21 days. In total, 54 images were analysed from 13 different hearts. (A) Number of clusters determined from the output of the texture analysis-based image processing tool (Section 3.4.2.2). The vector field was sampled every 24 pixels. (B) Dispersion as computed using Fiji's directionality plugin (Section 3.4.2.1). Student's t-test used to calculate P values, significance is indicated as * (p-value < 0.05) and ** (p-value < 0.01). Error bars represent mean ± SD.

A similar analysis was carried out based on the dispersion metric computed for the different images of heart tissue sections (Figure 3-11 B). The dispersion value was found to remain relatively constant up to 14 days after MI. The dispersion at day 14 post-MI was 23 ± 1.1 (n=8

images). At day 21, the average dispersion increased to 27.5 ± 6.2 (n=13 images), when compared to intact hearts (p=0.027). The dispersion profile over 21 days post-MI was markedly different than that for the number of clusters. The cluster number profile over 21 days post-MI was consistent with the qualitative image assessment (see section 3.5.1.1).

An alternative analysis of collagen alignment used orientation histograms based on the vector field resulting from the texture analysis-based image processing method (Section 3.4.3.1 and Figure 3-12). The collagen fibre bundles were assumed to be bi-directional as the collagen fibres had an orientation and not a direction. The collagen fibre orientation varied between -90° and 90°. The histograms had 18 bins, each bin corresponding to 5° intervals. Two types of patterns could be observed. For images of tissue sections from intact hearts and hearts 21 days post-MI (Figure 3-12A and D), the orientation was clearly multimodal (histogram contained multiple peaks) with maximum relative frequencies of ~0.08 (maximum angular peak) in both cases, indicating a high degree of angular spread and thus low alignment. Conversely, tissue sections from hearts 7 and 14 days post-MI (Figure 3-12 B and C) were characterised by a main peak at a collagen orientation of approximately -70° and -45º, respectively. Both these peaks had a high relative frequencies (~0.14), compared with the results in the intact case and 21 days post-MI. These results at 7 and 14 days post-MI suggested a very narrow angular spread and thus a high degree of collagen alignment. These results were consistent with those obtained for the number of clusters as they showed low degrees of collagen alignment in the intact case and 21 days after MI, while intermediate time points of 7 and 14 days post-MI were characterised by a higher degree of collagen alignment (Figure 3-11 A).

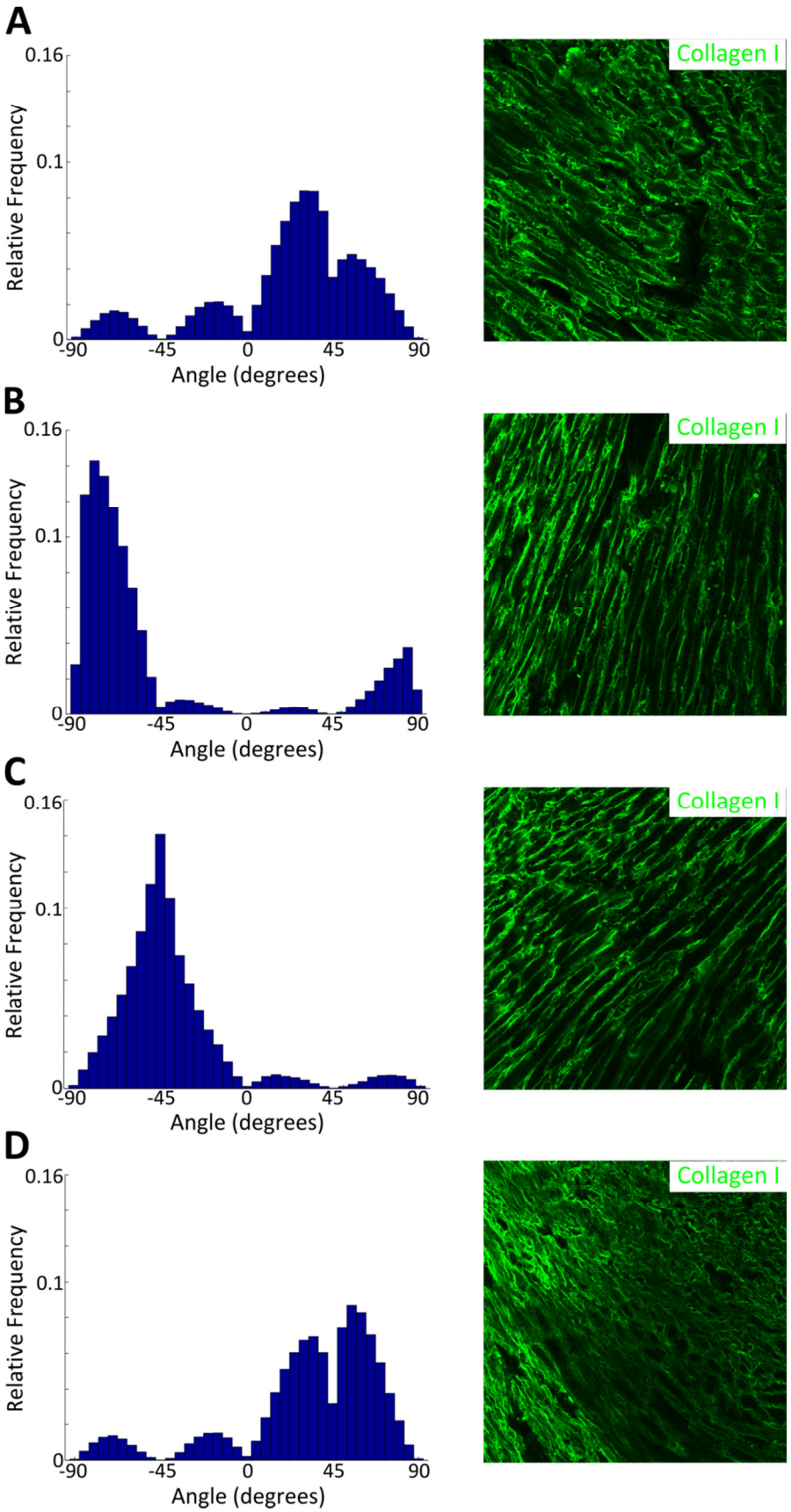

Figure 3-12 Changes in collagen angle distributions after MI. Normalised collagen angle histograms computed from the vector field as obtained from the texture based image processing method. Representative confocal immunofluorescence images of tissue section from (A) an intact heart and hearts (B) 7, (C) 14, and (D) 21 days post-MI stained with collagen I were analysed.

3.5.5 Estimation of model initial conditions from heart tissue section

In chapter 2, parameters related to cell behaviours and properties were estimated directly from *in-vitro* results. However, some aspects of the wound healing process could only be determined directly from *in-vivo* measurements. Analysis of immunostaining of intact hearts was used as a basis for the estimation of the size of the fibroblast cell population residing in the healthy tissue surrounding the wound (Section 3.4.3.3), the orientation of the collagen matrix (Section 3.4.2.2), and the dimensions of the tissue simulation, including those of the wounded region.

3.5.5.1 Size of the residing fibroblast population

Tissue sections of intact hearts were stained for vimentin, α-SMA and DAPI, and imaged using confocal microscopy (Figure 3-13). Fibroblasts were counted using an exclusion method based on the high expression of vimentin and morphology (Camelliti et al., 2005a) (Section 3.4.3.3).

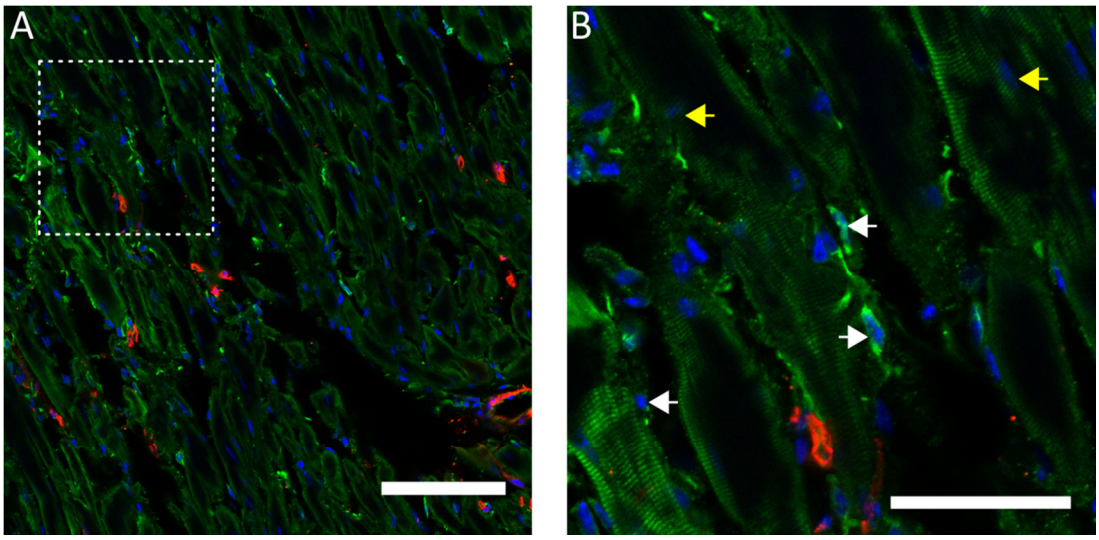

Figure 3-13 Determination of residing fibroblast cell population size. (A) Immunofluorescence confocal microscopy image of a tissue section from an intact heart stained for vimentin (green), smooth muscle actin (red), and DAPI (blue). Scale bar represents 100 µm. (B) Magnified region delimited by dashed square in (A). Fibroblast cells as determined using the exclusion method are shown in white, while other cell types are shown in yellow. The scale bar represents 50 µm.

The number of fibroblasts counted across intact heart sections were normalised to the area corresponding to the healthy tissue in the computational model (3.57×10^5 µm^2, Section 3.4.3.3). The average number of fibroblast cells in an area of 3.57×10^5 µm^2 was determined to be 301 ± 53 (mean ± SD, n=3 hearts) where a factor of 843 cells per square millimetre was used. Interestingly, a very low number were found to have a strong α-SMA signal. Indeed, most of the stained regions corresponded to blood vessels walls (Figure 3-13). This indicated there were very few myofibroblasts present in the intact heart, although additional experiments would be required to quantify these observations.

3.5.5.2 Orientation of the collagen matrix

In order to estimate collagen orientation during early stages of the wound healing process *in-vivo*, immunofluorescence microscopy images of intact heart were processed using the texture-based image processing tool previously discussed (see section 3.4.2.1). The result of this analysis was an evenly spaced vector field representing the orientation of the collagen at various positions throughout the image. The latter had a favoured direction as shown by the presence of a main peak in the orientation histograms, whereas a randomly orientated (synthetic example) resulted in a very flat and directionally independent histogram (Figure 3-14).

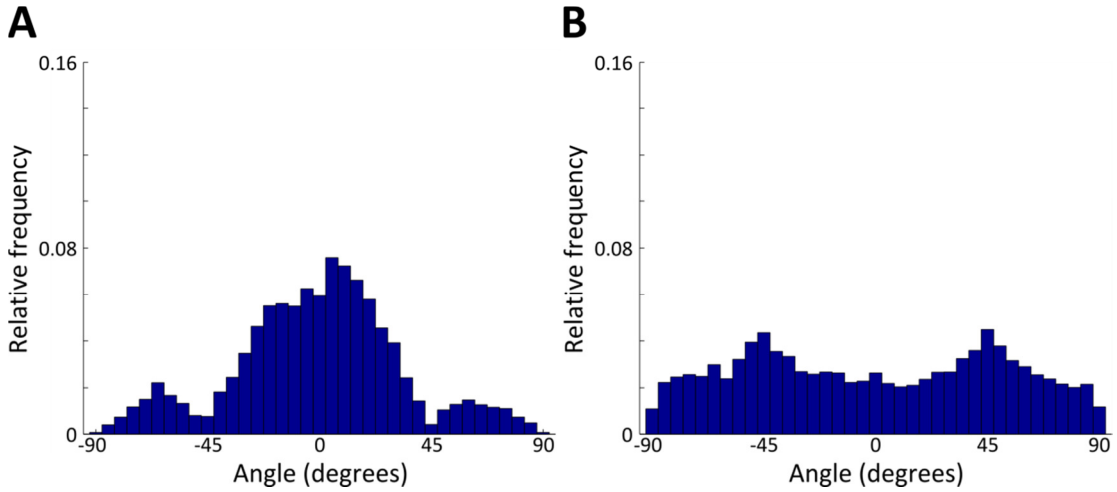

Figure 3-14 Estimation of the orientation of collagen fibres during early wound healing in the heart. (A) Collagen orientation as determined based on the processing of a representative immunofluorescence microscopy image of a tissue section from a healthy heart using the texture-based tool. (B) Randomly generated collagen field.

The texture-based analysis tool (Section 3.4.2.2) enabled extrapolation from an immunofluorescence image of a tissue section from an intact heart (Figure 4-17A) to a vector field corresponding to the orientation of the collagen (Figure 4-17B), and implementation into the computational model (Figure 4-17C). This provided a biologically realistic prediction of collagen fibre arrangement at the start of a model simulation.

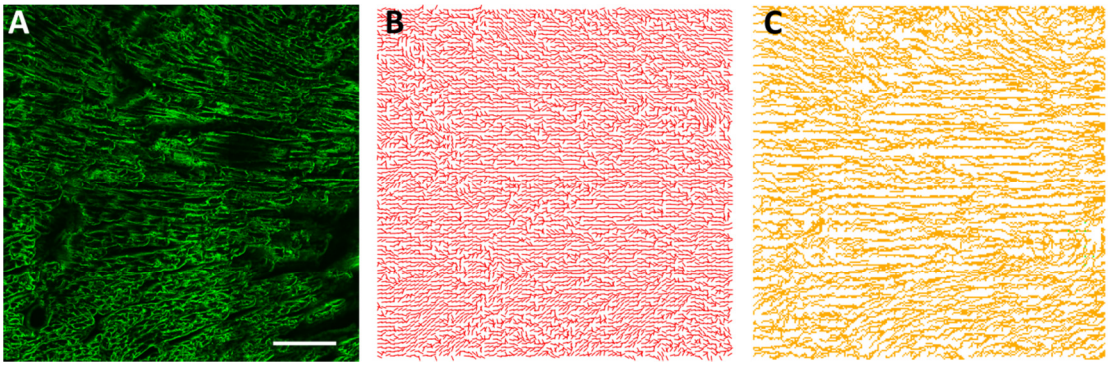

Figure 3-15 From heart tissue section to computational model. (A) Immunofluorescence microscopy image of a tissue section from an intact heart stained for collagen I (green). The scale bar represents 150 µm. (B) The vector field obtained from (A) using the texture-based image processing tool. (C) The collagen arrangement as visualised in the computational model.

3.5.5.3 Simulated tissue dimensions and location

The choice of dimensions for the wounded region to be modelled was an important parameter in the computational model. The size had to relate to the *in-vivo* process (the injury site) while allowing for reasonable computational complexity (i.e. tractable simulation times). The size of the tissue simulated (850×850 µm, including a 430×850 µm central wound) was determined by the field of view of a typical tissue section (425×425 µm) as captured at the MI injury site and it was important to allow direct comparison between these images and the model visualisations. In the heart post-MI, the size of the surviving healthy tissue is often large compared to that of the injured region (Moon et al., 2003). The simulated tissue could be related to an area situated within the left ventricle where the infarct is generally located (Figure 3-16).

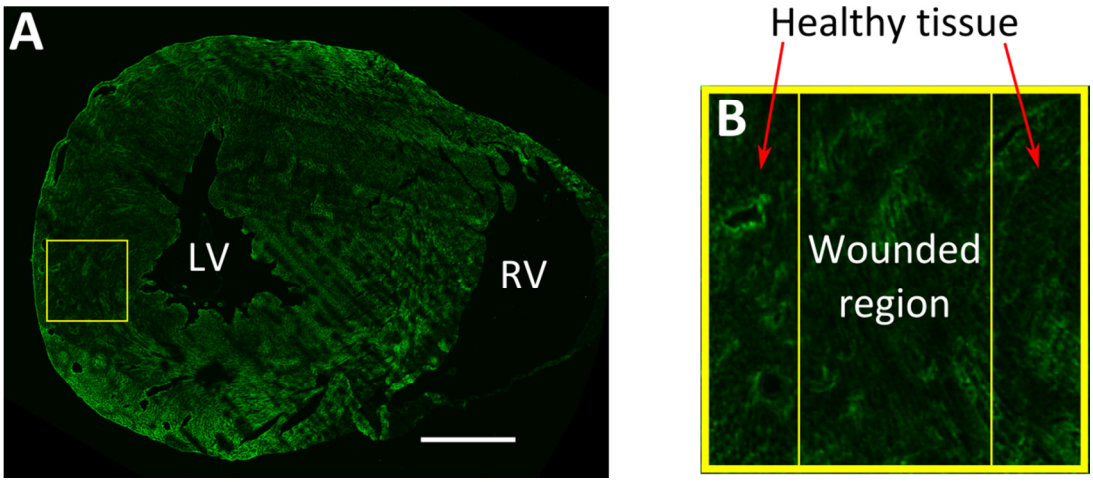

Figure 3-16 Simulated tissue dimensions compared to that of a whole-heart. (A) Tissue section from an intact heart stained for collagen I. LV and RV indicate the left and right ventricles, respectively. The yellow squared box indicates the dimensions (850×850 µm) of the simulated tissue as well as an approximate location it can be related to. (B) Magnified region highlighted in (A), indicating the model healthy tissue flanking the wounded region.

3.6 Discussion

The heart has an inability to regenerate post-MI in general a fibrotic scar is formed at the site of injury. Scar tissue has a different composition to the healthy myocardial tissue it replaced. Highly anisotropic (directionally dependent) myocardial scar tissue has shown a greater resistance to mechanical deformation (Holmes et al., 1997; Przyklenk et al., 1987). The presence of a fibrotic scar can have detrimental effects on the condition of the heart post-MI as it promotes myocardial stiffness, cardiac dysfunction, adverse ventricular remodelling and ultimately heart failure (van den Borne et al., 2010; Dean et al., 2005). Increasing levels of collagen and the later cross-linking of the collagen fibres within the scar have been shown to continue for up to 6 weeks post-MI (Jugdutt and Amy, 1986). Type I collagen provides tensile strength to the scar as it gets progressively cross-linked (Weber, 1989). Whereas, myocardial scar tissue stiffness has been shown to peak after one to two weeks post-MI (Holmes et al., 1997). Increased cardiac tissue stiffness may be related to the structure of the collagen fibres

within the scar as opposed to the amount (Holmes et al., 1997). This study investigated changes in the alignment of the collagen fibre bundles within the infarct at 7, 14 and 21 days post-MI.

Capturing the production of the scar post-MI by fibroblast cells is experimentally challenging. The behaviour of fibroblast cells or collagen deposition cannot be imaged in real time. The scarring process can be assessed by analysing heart tissue sections at discrete time points post-MI. Moreover, the behaviour of fibroblast cells in the context of an injury can be investigated with *in-vitro* scratch assays with time lapse microscopy (see Chapter 2).

There are a number of different imaging methods which can be used to visualise collagen within the scar post-MI. These methods include immunofluorescence confocal microscopy (Mewhort et al., 2014), SHIM (Guilbert et al., 2010; Mega et al., 2012; Mostaço-Guidolin et al., 2013), Masson trichrome (Virag and Murry, 2003) and polarized light microscopy (Whittaker et al., 1989; Whittaker et al., 1994). SHIM is often a preferred choice as this imaging method is less invasive as it requires no prior tissue staining preparation (Cox and Kable, 2006; de Jong et al., 2012; Mostaço-Guidolin et al., 2013). Instead, it uses the intrinsic property of non-centrosymmetric and crystalline structures to generate second-harmonic light. In biological samples, few structures including collagen fibres meet the criteria (Cox and Kable, 2006). In this study both intact hearts and hearts 21 days post-MI were imaged with SHIM. While it produced images suitable for further analysis, two disadvantages were identified, both related to its lack of specificity. Firstly, the imaging setup used could not discriminate between Collagen type I and III (Cox et al., 2003), the two main constituent of the scar post-MI (Cleutjens et al., 1995b; Sun and Weber, 2000). Secondly, The SHIM images showed highly striated structures that potentially corresponded to myosin and actin arrangements (sarcomeres) typically found in cardiomyocytes, which were previously shown to generate second harmonics (Plotnikov et al., 2006). Interestingly, these structures were only visible in the tissue sections from intact hearts and not in those 21 days post-MI. This discrepancy might be due to higher levels of collagen I and III 21 days after injury when compared to intact hearts (Cleutjens et al., 1995b). Therefore, the SHG signal from the collagens type I and III present within the scar at day 21 post-MI is likely to be higher than that from the intact heart. Moreover, there is an adverse impact of MI, which causes massive cell death of resident cardiomyocytes, thus making them more sparse and difficult to image 21 days post-injury (Frangogiannis, 2008). At day 21 post-MI the collagen type I and III present in the scar may produce a higher signal than any resident cardiomyocytes. In comparison to intact hearts the SHG signal from resident cardiomyocytes appeared to override the signal from collagen I and III in the ECM.

The second imaging method considered was immunofluorescence confocal microscopy, which made use of antibodies in order to specifically image structures of interest, in this case collagen I fibre bundles and resident cardiac cell populations. Unlike the *in-vitro* analyses, it was not

possible to use wide-field microscopy due to the thickness of the tissue sections instead, confocal microscopy was adopted, enabling the performance of optical sectioning and the production of images with a very high contrast between the labelled structures and background (Nwaneshiudu et al., 2012). This was critical to facilitate subsequent processing and analysis of the images. The sample preparation followed standardised protocols of tissue fixation and antibody staining, producing consistent results between sections. Collagen immunofluorescence images were inspected visually to estimate how fibre organisation changed over time. However, this approach yielded results that were both qualitative and subjective. Methods were required to both detect the orientation of collagen I from images and quantitatively analyse the collagen I alignment.

A texture-based image processing tool originally developed by Dr Lewis Griffin (Department of Computer Science, University College London) allowed the automatic determination of the dominant collagen orientation at each pixel. This image acquisition produced a uniformly spaced vector field, an output identical to that of the computational model. This was key so that both could be directly compared using the same analytical approach. Previous studies have manually detected the orientation of collagen fibres from images (Whittaker et al., 1989). Other methods have used texture based analysis to reliably classify SHG collagen images by extracting features associated with biochemical and structural changes of the tissue collagen matrix (Mostaço-Guidolin et al., 2013).

Quantitative analysis of the collagen I alignment of both intact hearts and at 7, 14 and 21 days post-MI is required for evaluating differences between samples, different time points post-MI and outputs from the computational model. A second tool, used to analyse these vector fields, is a custom-developed clustering method that detected local patches of collagen vectors with similar orientations. The number of clusters provided a single measure that described the degree of local alignment of collagen. The orientation of collagen fibres has previously been measured using a four-axis universal stage, which allows the 3D orientation to be assessed. The overall alignment was analysed with 2D Lambert projections which are more commonly used in geology (Whittaker et al., 1989). Each collagen orientation measured in 3D was represented by a point on the Lambert projection. This method was used for qualitatively assessing the orientation of collagen fibres. The alignment of collagen has been quantitatively measured by calculating the length of the major axis of each collagen fibre bundle (Noorlander et al., 2002). An average of the 10 longest lengths was computed and defined as the collagen alignment index (Noorlander et al., 2002). In this study the collagen fibre bundles from both intact hearts and hearts post-MI appear continuous. Therefore, this method would be difficult to employ as the collagen fibre bundles need to defined and analysed as separate entities. The angular dispersion has previously been used to measure the level of anisotropy of collagen fibres in the circumferential lamellar bone from rat tibiae (Reznikov et al., 2013). This metric can be used to

assess the structure of the collagen matrix in terms of the global fibre angular distribution. A complete experimental workflow was thus established for the generation of *in-vivo* data. Tissue sections of hearts were imaged using immunofluorescence confocal microscopy. An imaging processing tool then produced a vector field of dominant collagen orientations, which was then analysed using a clustering algorithm. Both the detection and quantification methods were used to produce quantitative, unbiased measures.

Visual inspection of collagen images and the quantitative metrics resulting from the automated processing were comparable. Intact hearts and those analysed at 21 days post-MI were generally found to be associated with lower collagen alignment when compared to hearts at 7 and 14 days after MI. Collagen type I fibres in intact tissue tended to adopt a honeycomb-like conformation which was consistent with previous descriptions of collagen I patterns in the heart (Benedicto et al., 2011; Engelmayr et al., 2008; Macchiarelli et al., 2002). The collagen architecture could be linked to presence of cardiomyocytes (Benedicto et al., 2011). Collagen type I is a dominant component of the connective tissue which supports and assists the resident cardiomyocytes, so they can be supported as a continuous and complex mass (Anderson et al., 2005; Benedicto et al., 2011). This honeycomb-like structure was associated with a large number of clusters (i.e. low degree of alignment) and a multi-modal (i.e. with multiple peaks) histogram of collagen orientation. By day 7 and up to day 14 post-MI, the honeycomb arrangement appeared to be completely lost, replaced by highly aligned collagen structures. This was confirmed by both lower numbers of collagen clusters when compared to intact heart tissue sections and the histogram of collagen orientation that was almost unimodal (i.e. most fibres orientated in a single dominant direction). The drastic change in collagen organisation was likely to be the result of multiple processes. In ischemic conditions, a large fraction of the resident cardiomyocytes undergo apoptosis or necrosis, thus disrupting the aforementioned honeycomb-like arrangement (Frangogiannis, 2008). Moreover, by 7 days post-MI the inflammatory response has been completed which involved the degradation and removal of both dead and dying tissue after MI (Nahrendorf et al., 2010). By 3 days post-MI myofibroblasts have been located in the wounded region. The role of these cells is the production, degradation and remodelling of the ECM (Baum and Duffy, 2011; Souders et al., 2009). These events contribute to the structural changes observed in the collagen matrix architecture.

At day 21 post-MI, another marked change in collagen organisation was observed. Both the number of clusters and the shape of the orientation histograms were equivalent to that of the intact case. The collagen fibres also appeared visibly more densely packed and abundant. This dense collagen structure is associated with fibrosis of the heart post-injury (Dean et al., 2005). At 21 days post-MI it is likely that the collagen fibre bundles would appear more compact when compared to the analysis at days 7 and 14 post-MI. During the maturation phase of cardiac wound healing cross-linking of the collagen fibres occurs, whereby a dense collagen-based scar

is formed (Dobaczewski et al., 2010; Frangogiannis et al., 2000). The cross-linking of collagen fibres could result in a decrease in the level of collagen alignment, which has been recorded in this study. The level of dispersion measured for intact hearts and hearts 14 days post-MI was similar. Whereas, the numbers of clusters measured for these two cases was significantly different, at 14 days post-MI there was a lower number of clusters compared to intact hearts. The differences observed between these two measures may be because the dispersion measured the angular spread based on the highest peak in the histogram of orientations detected from the image intensity gradient. It thus cannot take into account angular spread as a result of multimodality (presence of multiple peaks in the orientations histogram). Therefore, cluster number appeared to be a more suitable metric for collagen alignment characterisation of the immunostaining data, consistent with the qualitative image assessment (see section 3.5.1.1).

The experimental workflow provided *in-vivo* data for comparison with the output of the model in terms of alterations in the collagen alignment during cardiac wound healing. This enabled the quantification of the simulation outcomes with respect to the model initial conditions. These initial conditions included the number of resident fibroblasts, the initial collagen arrangement, and the dimensions of the wound site. Images used for the estimations of these properties were acquired in a region corresponding to wounded area in injured murine hearts (within the left ventricle). The size of the tissue simulated (850×850 μm, including a 430×850 μm central wound) was determined by the field of view of a typical tissue section as captured at the MI injury site. In the heart post-MI, the size of the surviving healthy tissue is often large compared to that of the injury region. In order to ensure moderate computation times, a comparatively small region of healthy tissue flanking the wounded region was assessed. The use of reflective boundary conditions in the model would partly alleviate the effects of this compromise. However, an important caveat is that the potential reservoir of cells from surrounding tissue is much larger in reality relative to the one which will be simulated in the model. The absolute number of fibroblast cells residing in the adult mouse heart is essentially unknown (Krenning et al., 2010). Studies of cells isolated from 12 week mouse hearts using fluorescence-activated cell sorting (FACS) determined the relative frequency of different cell types (Banerjee et al., 2007): cardiac fibroblasts (~27%), myocytes (~56%), vascular smooth muscle cells (~10%) and endothelial cells (~7%). These numbers, however, do not directly address the absolute size of each sub-population. In order to obtain an estimate for the number of cardiac fibroblasts, the number of cardiac fibroblast cells was counted from intact heart sections. Cardiac fibroblast cells were categorised as cardiac fibroblasts based on their expression of vimentin (Camelliti et al., 2005b; Krenning et al., 2010) and morphological attributes. Fibroblasts lack a basement membrane, have an oval nucleus (Camelliti et al., 2005b) and have multiple extensions known as pseudopodia (Abercrombie and Heaysman, 1953). There were approximately 843 ± 148 (mean ± SD, n=3 hearts) cardiac fibroblast cells per square millimetre in the region of interest.

This was used as an estimate for the initial size of the cardiac fibroblast cell population that resides in the healthy tissue surrounding the wounded region after injury. It is important to note, however, that this number is likely to be an overestimation due to the typical thickness of the tissue sections used in this study, which is approximately 20 μm. Cells present within multiple planes might have been included in the reported cell counts. It would therefore be of interest to devise improved methodologies for the enumeration of cells such as flow sorting based on fibroblast cell surface markers.

Finally, the initial collagen arrangement in the healthy tissue surrounding the wounded region was determined. Collagen fibres are often initialised using a random orientation (Dallon et al., 1999; McDougall et al., 2006; Rouillard and Holmes, 2012). However, results presented in this chapter showed that the collagen I arrangement in the healthy tissue was not completely isotropic (directionally independent) and structured. If the collagen I fibre bundles within the healthy were assumed to be random this would be representative of an isotropic (no directional dependence) structure. The honeycomb-like collagen structure visualised within intact hearts sometimes appeared distorted or stretched. These alignment features could be related to variations in the plane of the heart section. The tissue regions where the honeycomb-like structure appeared stretched could have been measured as more aligned resulting in an overestimation of the level of collagen alignment (Figure 3-3). In order to capture this structure in a usable form for the computational model, immunofluorescence confocal microscopy images of a tissue section from a healthy heart were processed using the texture-based tool previously discussed. The resulting vector field could be directly imported into the model and used to dictate the orientation of the collagen in the healthy tissue at the start of a simulation.

In summary, a suitable experimental workflow was established for the generation of quantitative data related to the wound healing process *in-vivo*. This data provided a better understanding of the changes in collagen organisation throughout this very dynamic process. It also enabled the determination of biologically relevant initial simulation conditions: the number of cardiac fibroblast cells, structure of the collagen matrix and appropriate dimensions for the wounded region. In chapter 4, the effect of these initial conditions on simulation outcomes will be further investigated. The ability of the model to predict what was observed *in-vivo* will be evaluated in chapter 5.

Chapter 4

An *in-silico* model of cardiac wound healing

4.1 Motivation

Cardiac wound healing is an intricate biological process, which consists of three sequential, yet overlapping phases: inflammation, reparation and granulation. During each of these phases, there exist interactions that occur simultaneously over time.

Cardiac injury occurs as a result of myocardial infarction (MI), which is caused by a dramatic reduction in blood supply to the myocardial tissue and eventually leads to the loss of cardiomyocytes, and coronary blood vessels as major cellular constituents of the adult heart. The heart has a limited ability to regenerate after such an injury (Frangogiannis, 2008). The necrotic tissue is replaced by a scar, the composition of which differs from that of the healthy myocardial tissue it has replaced. Scar tissue is often much stiffer and characterised by dense, closely aligned collagen I fibres. As a result, excessive scarring, a condition termed fibrosis, has a detrimental effect on the efficiency of heart muscle contraction which often results in pathological remodelling such as chamber dilatation and wall thinning which in turn ultimately results in heart failure.

Controlling the level of scarring during cardiac wound healing would, therefore, be greatly beneficial from a clinical perspective. This could be achieved through improved understanding of the underlying molecular and cellular processes that lead to fibrosis and their subsequent therapeutic manipulation.

4.2 Aims

The aim of this study was to gain insights into the scarring process post-MI using computational models based on relevant experimental data from wet lab experimentation.

Improving our understanding of the highly complex scarring process *in-vivo* is challenging. One of the major difficulties with *in-vivo* studies is the high variability between surgical animal models and their response to cardiac injury (Frangogiannis et al., 2002). A common approach involves breaking down the complexity of scarring into constituent parts e.g. contributory cell types, ECM, growth factors, cytokines, etc. This can be done to a certain extent using *in-vitro* experiments but it is then difficult to assess the effect of the interaction between the individual

components. Such limitations can be alleviated by combining into an *in-silico* model and integrating the findings from *in-vitro* experimental approaches.

A model not only offers a way of breaking down complexity into individual parts in a way that is not experimentally feasible, it also enables the simulation of collective behaviours and thus provides insight into interacting behaviours influencing cardiac scarring. A model can accommodate a large number of simulations for different conditions in a short space of time, compared with time-consuming *in-vitro* and *in-vivo* experimental protocols. A model is thus a very powerful tool with the potential to test different hypothesises or at least reduce the number or range of experiments needed to verify a hypothesis. However, a model is only clinically relevant and scientifically valid if it is grounded on a sound experimental basis and is predictive of outcomes.

This study was focused on the development and implementation of a predictive model of cardiac wound healing post-MI. The model focuses on the processes involved in the formation of a scar through cell-cell and cell-collagen matrix interactions. The cell types to consider are cardiac fibroblast cells and their activated form, myofibroblasts. Both cell types are thought to be responsible for the formation of the scar through collagen matrix deposition, degradation, and remodelling (Camelliti et al., 2005a; Chen and Frangogiannis, 2012; Sun et al., 2002; Sun and Weber, 2000). By investigating the behaviours of both fibroblast and myofibroblast cells (e.g. proliferation, differentiation, migration, apoptosis), it could improve our understanding of the scarring process at the cellular level and allow exploration of a wide range of individual and collective contributions. Model parameters will be informed by *in-vitro* and *in-vivo* experimental data. Similarly, this data will also be used as a basis for the assessment of the predictive capabilities of the model. The main simulation outputs are the degree of alignment and density of the collagen scar. Both of these scar properties are key determinants of the prognosis following MI (Dean et al., 2005; Fomovsky et al., 2011). Furthermore, analysis of the model outputs will be used as a basis for the understanding of scarring dynamics.

4.3 An overview of the *in-silico* model

4.3.1 Agent-based modelling

Agent based modelling is a well-suited approach for the simulation of physiological events at a cellular level. In brief, this method simulates the behaviour of individual entities (also known as agents), that are part of a system. Each agent is associated with a set of properties and rules. As a simulation progresses, the interactions between the agents and their environment lead to the emergence of complex behaviours (Amigoni and Schiaffonati, 2007). In this study, agents were used to model fibroblast and myofibroblast cells, whose collective behaviours and interactions with their environment could inform on the outcome of the wound healing process. Individual

properties of the cells could be directly derived from experimental investigations. The addition of further properties or rules were easily implemented and enabled a gradual increase in the complexity of the simulation (e.g. by adding new cellular behaviour). Moreover, because cells were modelled as individual objects with a size and defined position, it was possible to visualise each step of the simulation. This was particularly relevant for the comparison of the cell patterns and behaviours with *in-vitro* or *in-vivo* microscopy images.

The agent-based model was mainly designed to support complex simulations of experiments that cannot be readily investigated with traditional laboratory methods. But it could also be used to output simple cell behaviours that could be easily validated experimentally.

4.3.2 Model organisation

The two-dimensional stochastic agent-based model of cardiac wound healing described here captured the contribution of fibroblast cells and their interaction with the collagen matrix during the remodelling of a scar post-MI. This model was inspired by a previously described dermal wound healing model (Dallon et al., 1999; McDougall et al., 2006). The parameters and behaviours from the dermal wound healing model that were found to be relevant in a cardiac setting were retained. However, new behaviours and additional model parameters were introduced to capture the specificity of the healing process in cardiac tissues. Parameter values were mostly determined by conducting *in-vitro* experiments using primary mouse cardiac fibroblast cells and, in some cases, by consulting the scientific literature. Details of the parameters and the methods used for determining their value (e.g. from previous models, experimental investigations, or literature) can be found later in this chapter in Table 4.

The basic setup of the model was a section of cardiac muscle representative from within the free left ventricle wall with a myocardial infarction in its central region. The square section of cardiac tissue had a length of 850 μm equivalent to an area of ≈ 0.72 mm^2, which is comparable to the typical area of a section of the left ventricle of murine heart (see Figure 3-16). The dimensions of the rectangular wounded region were 430 μm by 850 μm. At initiation of the simulation, two healthy tissue regions (containing both collagen and cells) surrounded a cell and collagen-free injured region (Figure 4-1). The wounded region was horizontally centred between two healthy regions of tissue and spanned the complete vertical axis.

Collagen fibre bundles were represented by vectors with an orientation and a length, with the latter denoting the local collagen density. The density of collagen was assumed to vary between the arbitrary values of 0 and 1.5. Initially, the collagen density in the healthy and injured regions was set to one and zero, respectively. The collagen matrix was given a random orientation at the start of a simulation. Over the course of a simulation, scarring was characterised by collagen densities greater than one and the alignment of collagen fibres.

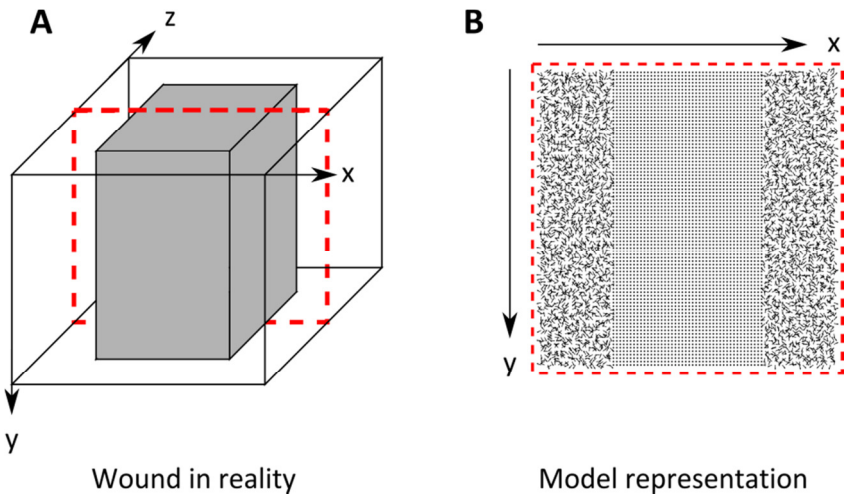

Figure 4-1 Two-dimensional model approximation of the cardiac wound. (A) The wound in reality is inherently three-dimensional. The wounded region (solid grey cuboid) is surrounded by healthy tissue (transparent cuboid). A two-dimensional section of the tissue is outlined (red dashed line) to represent the region considered in the model. (B) The initial two-dimensional model configuration of the collagen vector field (black arrows). The central injured region where no collagen was present (vectors with a magnitude of zero). The injured tissue was surrounded by healthy tissue with an initial collagen vector magnitude of one.

A single chemotactic gradient representing injury-induced signals was established in the wounded region and assumed to diffuse outwards into the surrounding tissue. The chemotactic gradient promoted the migration of the cells from the surrounding healthy tissue into the wound. The gradient was quickly established at the beginning of the simulation and decayed during its course. The timing of the chemotactic gradient activation coincided with that of the inflammatory phase of cardiac wound healing, during which factors promoting cell migration towards the wound are thought to be released (Nahrendorf et al., 2010).

The fibroblast cells (or agents) making up the healthy tissue had the ability to migrate, proliferate, produce (and lay down) collagen, reorient collagen, undergo apoptosis and differentiate into myofibroblast cells. Their migration was influenced by a diffusing chemotactic gradient generated in the wound, neighbouring cells, local collagen alignment and density, and the cells' previous direction. The starting time of the simulation was chosen to be equivalent to 48 hours post-MI in the mouse as this time corresponded to the start of the infiltration of the wound by fibroblast and myofibroblast cells. Indeed, myofibroblast cells were observed at the site of injury at 3 days post-MI in murine and rat models (Frangogiannis et al., 2000; Sun et al., 2000). At the start of a simulation there were 300 resident fibroblast cells located within the healthy tissue and no myofibroblast cells. The size of the initial population of fibroblast cells was approximated from *in-vivo* intact murine heart sections (Figure 4-2, see section 3.5.5.1 for details). Fibroblasts were identified based on their expression of vimentin (a marker expressed by fibroblasts) and their morphology (Camelliti et al., 2005a; Krenning et al., 2010). Fibroblast cells are initially positioned at random within the boundaries of the healthy tissue.

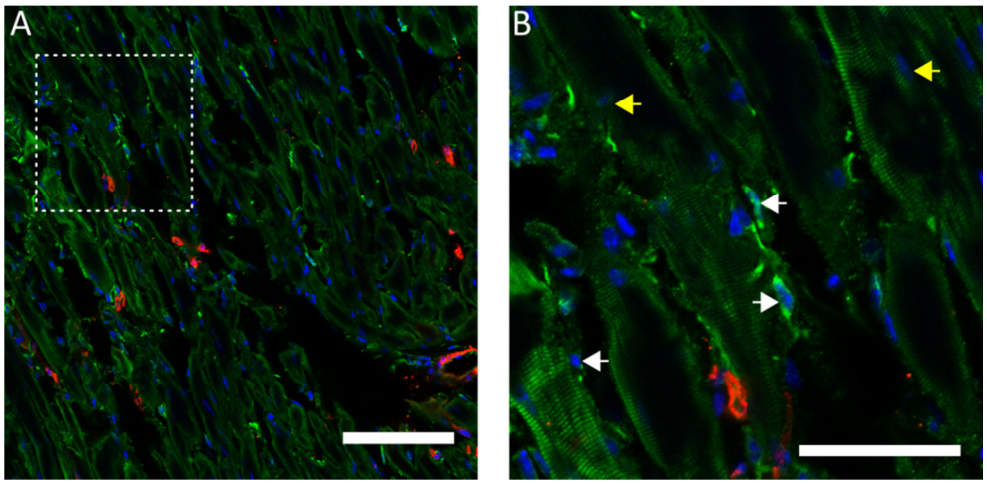

Figure 4-2 Images of intact heart tissue stained for cardiac fibroblast cells. (A) *In-vivo* uninjured murine heart section stained with anti-vimentin (a fibroblast cell marker, in green), α-SMA (a myofibroblast and smooth muscle cell marker, in red), and DAPI (4'-6-Diamidino-2-phenylindole, a nuclei stain, in blue) to label nuclei. The scale bar represents 100 µm. (B) Arrows used to indicate cells within the tissue: fibroblasts (white arrows) and other cell types based on morphology such as cardiomyocytes (yellow arrows). The scale bar represents 50 µm.

Elements of both the model setup and framework have been introduced. Subsequent sections will discuss the interaction between the cells and the collagen matrix, individual cell behaviours and the influence of the chemoattractant. The main components of the models are summarised in Figure 4-3.

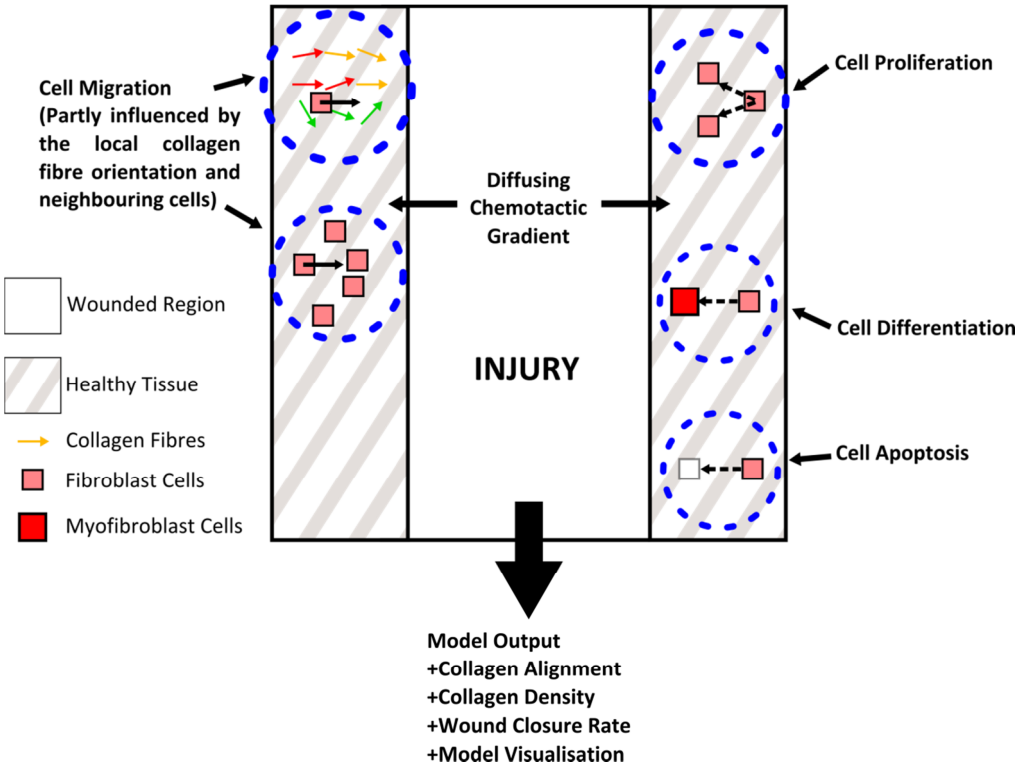

Figure 4-3 Overview of the mathematical model of cardiac wound healing. The central wounded region was surrounded on both sides by healthy tissue. A diffusing chemotactic gradient was initiated in the wound, attracting local fibroblast and myofibroblast cells. Fibroblast cells have the ability to migrate, proliferate, undergo apoptosis, and differentiate into myofibroblast cells. The migration of cells is partly influenced by local collagen fibres and neighbouring cells. Model outputs such as wound closure rate and a collagen density rate are used to evaluate and compare the simulation outcomes.

A simulation was made up of discrete time steps. The time interval (τ) between each of these steps was equivalent to 0.15 hours (McDougall et al., 2006). This value offered a good compromise between accuracy of a model simulation (e.g. for cell migration) and computational complexity. In the proposed setup, the maximum distance a cell could travel in one time step (maximum speed×time step interval) was less than the grid spacing. This provided a good approximation of cell migration and subsequent modifications of the collagen matrix.

4.4 Key model components and properties

4.4.1 Chemotactic gradient

The model simulated a post injury inflammatory response using a single generic chemoattractant. The chemoattractant represented the effects of pro-inflammatory stimuli cytokines such as tumor necrosis factor (TNF-α) and Interleukin-1 beta (IL-1β), which are known to be secreted by monocytes and macrophages during inflammation (Chen and Frangogiannis, 2012). The chemical signals generated in the wound were assumed to diffuse outwards into the healthy surrounding tissue and encouraged cells to migrate into the wound. The chemotactic gradient formulation was adapted from the dermal wound healing model (McDougall et al., 2006). The concentration of the chemoattractant, $A(\mathbf{x},t)$, changed with time following a modified diffusion equation (equation 4.1). The diffusion constant (D_A) was set to 0.9 and the degradation of the chemokine concentration (k_1) to 0.055. The production rate of the chemokine concentration (k_2) was set to 0.055 for the first 60 hours (400 time steps) and to zero thereafter. This timing was used to represent the decline in the number of inflammatory monocytes (Nahrendorf et al., 2010). After 142 hours (≈947 time steps), the chemotactic concentration has almost completely decayed and was set to 0 across the tissue.

$$\partial A / \partial t = D_{\mathrm{A}} \nabla^2 A - k_1 A + \begin{cases} k_2 & \text{In the wound} \\ 0 & \text{In the surrounding tissue} \end{cases} \qquad 4.1$$

For implementation in the cardiac model, equation 4.1 was discretised using an approximate form of the Laplacian (∇^2) (see equation 4.2) that was substituted into equation 4.1.

$$\begin{aligned} \nabla^2 A(x,y) &\approx \frac{A(x-g,y)+A(x+g,y)+A(x,y-g)+A(x,y+g)-4A(x,y)}{g^2} \\ &= h(x,y) \end{aligned} \qquad 4.2$$

where (x, y) is the corresponding grid point and g is the grid point interval, which in this case is equal to one. The discrete form of equation 4.1 is shown in equation 4.3. At each time step, the concentration of the chemotactic gradient was calculated for each grid points.

$$A_{t+\tau} = A_t + \tau\left(D_A h - k_1 A_t\right) + \begin{cases} \tau k_2 & \text{In the wound} \\ 0 & \text{In the surrounding tissue} \end{cases} \quad 4.3$$

The chemotactic gradient (∇A) influenced the direction and speed of the migrating fibroblast and myofibroblast cells. The gradient at each grid point was calculated using central difference approximation for each component (i) of ∇A as shown in equation 4.4.

$$\left(\frac{\partial A}{\partial x}\right)_i = \frac{A_{i+1} - A_{i-1}}{2g} \quad 4.4$$

In equation 4.4, g represents the grid point interval. Reflective boundary conditions were assumed and used either forward (see equation 4.5) or backward (equation 4.6) difference approximations depending on the boundary considered

$$\left(\frac{\partial A}{\partial x}\right)_i = \frac{A_{i+1} - A_i}{g} \quad 4.5$$

$$\left(\frac{\partial A}{\partial x}\right)_i = \frac{A_i - A_{i-1}}{g} \quad 4.6$$

In summary, the chemoattractant increased approximately linearly with time for the first 2.5 days of a simulation. This timing was chosen so that fibroblasts would enter the infarct by 3 days post-MI (corresponding to 24 hours of a simulation), in agreement with previous reports (Frangogiannis et al., 2000; Sun and Weber, 2000). Thereafter the concentration decreased following an exponential decay after setting the generating term to zero (k_2), representing the decrease in the number of inflammatory cells secreting these chemoattractant signals (Nahrendorf et al., 2010). A similar profile was observed at different regions (injured, infarct border zone and healthy) of the tissue (Figure 4-4A). As expected, the peak concentration decreased as the distance from the centre of the wound increased. The chemotactic gradient can be visualised in the 2-dimensional (2D) representation of the model (Figure 4-4B).

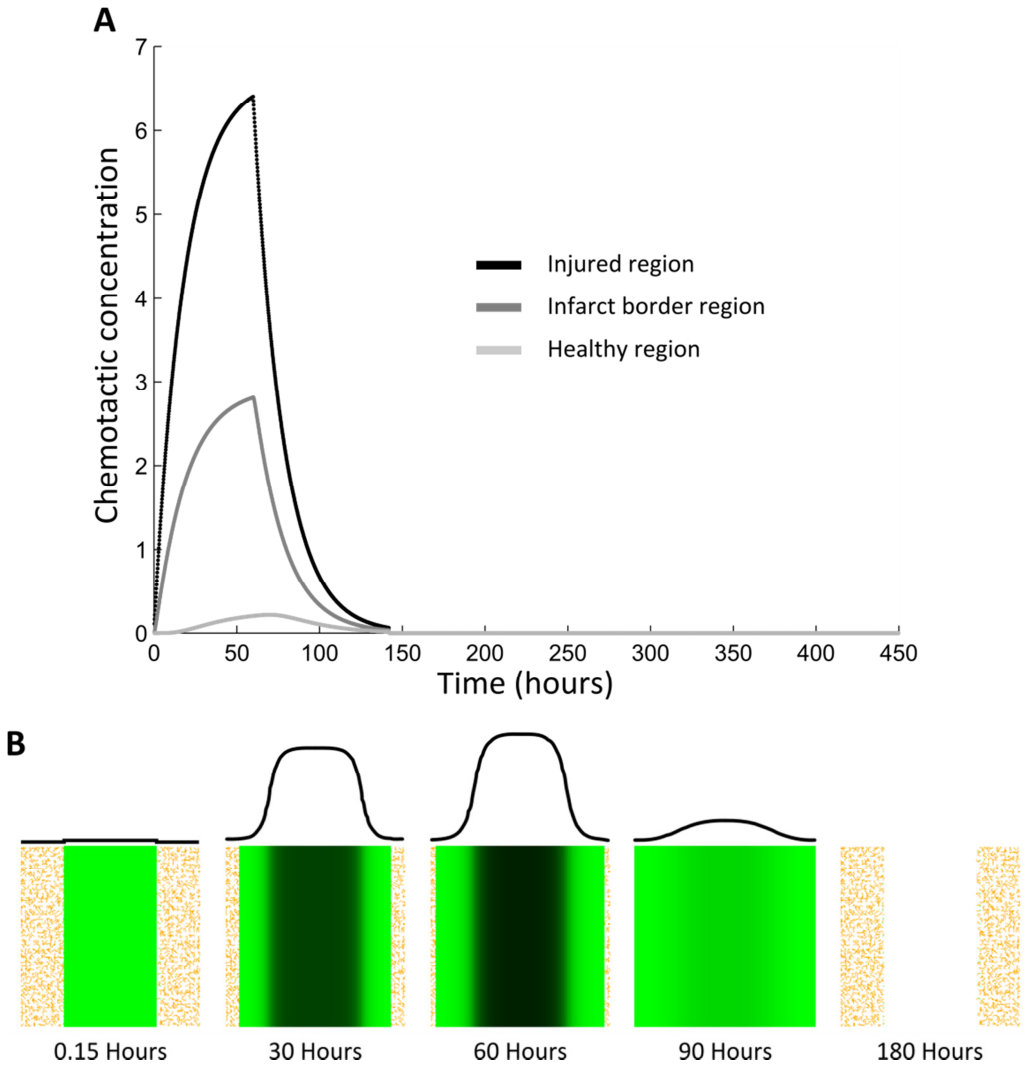

Figure 4-4 Implementation of the chemotactic gradient. (A) The change in the concentration of the chemoattractant with time at three different regions of the tissue (injured, infarct border and healthy). Initially, within the injured region the concentration increased and peaked at 60 hours (400 simulation steps). Afterwards the concentration levels decreased following an exponential decay. The concentration profiles in the infarct border and healthy tissue regions were similar to that of the injured region but the concentration peaked later and at a much lower concentration. (B) Model output images illustrating changes in the chemotactic concentration with time. The concentration is colour coded. The colours range from light to dark green, corresponding to low and high chemotactic concentration levels, respectively. Above each image, a line plot shows the intensity of the chemoattractant across the width of the simulated tissue.

4.4.2 Collagen fibrous matrix

The collagen matrix, denoted by $\boldsymbol{c}$, was modelled as a continuous vector field sampled at equally spaced grid points. The spacing between grid points was equivalent to 10 µm. The value for the collagen matrix at a location *(x,y)*, termed $\boldsymbol{c}(x,y)$, was computed by interpolation (estimation from values at neighbouring grid points). The magnitude and direction of the vectors corresponded to the collagen density and its orientation, respectively. The collagen vector lengths were constrained between 0 and 1.5, where a length of zero represented wounded tissue (i.e. very low density or no collagen at all), a value of one represented healthy tissue, and a length of 1.5 represented dense scar tissue (Dallon et al., 1999). Neighbouring fibroblast and

myofibroblast cells had the ability to produce, degrade and reorient the collagen matrix. Details relating to these cellular functions are discussed in the section devoted to fibroblasts (Section 4.4.3). An interpolation method was used to sample the collagen at a given position. The interpolated value $\boldsymbol{I}(\bar{\boldsymbol{c}}, \boldsymbol{x}, \boldsymbol{y})$ of the collagen at the coordinates *(x,y)* was calculated using an interpolation method formed from a combination of tensor product and quartic lagrangian interpolation methods (Dallon et al., 1999). Essentially, the value at position *(x,y)* was estimated based on the 25 nearest grid points, with the influence of each grid point varying with their distance from the position *(x,y)*. This was implemented as shown in equation 4.7, where (x_j, y_k) corresponded to the coordinates of the grid point nearest to *(x,y)*, $\bar{\boldsymbol{c}}_{\boldsymbol{j-m,k-n}}$ the collagen vectors at the grid points (x_{j-m}, y_{k-n}), and l_p the Lagrange basis function computed as shown in equation 4.8.

$$\boldsymbol{I}\left(\bar{\mathbf{c}}, \boldsymbol{x}, \boldsymbol{y}\right) = \sum_{\boldsymbol{n}=-2}^{2} \left(\sum_{\boldsymbol{m}=-2}^{2} \bar{\mathbf{c}}_{\boldsymbol{j-m,k-n}} \boldsymbol{l}_{\boldsymbol{j-m}}\left(\boldsymbol{x}\right) \right) \boldsymbol{l}_{\boldsymbol{k-n}}\left(\boldsymbol{y}\right), \tag{4.7}$$

$$\boldsymbol{l}_p\left(\boldsymbol{x}\right) = \frac{\left(\boldsymbol{x}-\boldsymbol{x}_{p-2}\right)\left(\boldsymbol{x}-\boldsymbol{x}_{p-1}\right)\left(\boldsymbol{x}-\boldsymbol{x}_{p+1}\right)\left(\boldsymbol{x}-\boldsymbol{x}_{p+2}\right)}{\left(\boldsymbol{x}_p-\boldsymbol{x}_{p-2}\right)\left(\boldsymbol{x}_p-\boldsymbol{x}_{p-1}\right)\left(\boldsymbol{x}_p-\boldsymbol{x}_{p+1}\right)\left(\boldsymbol{x}_p-\boldsymbol{x}_{p+2}\right)} \tag{4.8}$$

Bilinear interpolation was also implemented and compared to the results produced by the quartic lagrangian interpolation. The results obtained using the bilinear interpolation method showed a very smooth collagen matrix. During simulations, the bilinear method caused the cells to cluster together as they migrated across the grid. The quartic lagrangian interpolation used a wider reference frame for the interpolation. Example vector outputs of this method are shown in Figure 4-5.

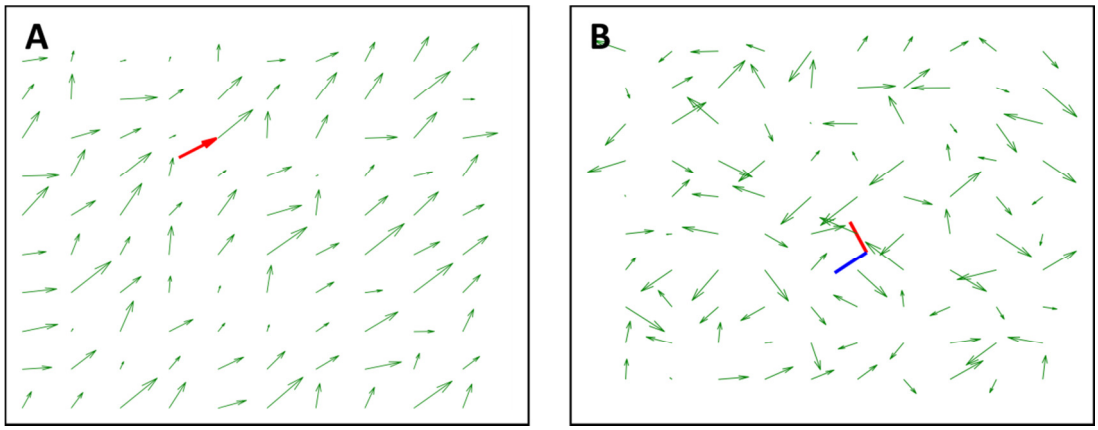

Figure 4-5 Comparison of interpolation methods. (A) Example of using the quartic lagrangian interpolation method to interpolate a vector (red) from a vector field (green). (B) Comparison of the two methods of interpolation: bilinear (blue) and quartic lagrangian (red) from a randomised vector field (green).

The effects on model simulations of different interpolation methods are discussed in more detail in section 4.9.3.

4.4.3 Cells

The fibroblast cells were modelled as discrete entities (agents) with a path $\boldsymbol{f}^i(t) = \left(f_1^i, f_2^i\right)$, where i corresponded to the ith cell at time t. Each cell had its own set of properties relating to its age, position and velocity (speed and direction). In general, reflective boundary conditions were used at the edge of the simulated tissue.

4.4.3.1 Cell Velocity

The velocity for a cell at position $\boldsymbol{x}$, at time t in the model was denoted by $\dot{\boldsymbol{f}}^i(\boldsymbol{x}, t)$ and was computed as shown in equation 4.9 where s was cell speed and $\boldsymbol{v(t)}$ its direction (Dallon et al., 1999). The latter will be dictated by the local collagen alignment, the chemotactic gradient, and neighbouring cells as further discussed below (section 4.4.3.2).

$$\frac{d\boldsymbol{f}^i(t)}{dt} \equiv \dot{\boldsymbol{f}}^i(t) = s\frac{\boldsymbol{v}(t)}{\left\|\boldsymbol{v}(t)\right\|} \tag{4.9}$$

The cell speed was influenced by multiple factors, including the local chemotactic gradient, the collagen density and the neighbouring cells. Cell speed was computed as shown in equation 4.10 where $S_{baseline}$ was the baseline cell speed of the cell, $\boldsymbol{c}$ the local collagen orientation, $\boldsymbol{f}$ the cell position, $\nabla\boldsymbol{A}$ the gradient of the chemotractant, and $\nabla\boldsymbol{A}_{MAX}$ the maximum value of said gradient (McDougall et al., 2006). The expression $\boldsymbol{I}(\bar{\boldsymbol{c}}, \boldsymbol{f}^i)$ denotes the interpolation of the collagen orientation at the position of the ith cell.

$$s = S_{baseline}\left(\frac{1}{8} + \left(\frac{7}{8 + 3\left\|\boldsymbol{I}\left(\bar{\mathbf{c}}, \boldsymbol{f}^i\right)\right\|^6}\right)\right)\left(1 + \frac{\left\|\nabla\mathbf{A}\right\|}{\left\|\nabla\mathbf{A}_{MAX}\right\|}\right) \tag{4.10}$$

The baseline speed corresponded to the speed of cell migration before other factors of influence (e.g. collagen density or chemotactic gradient) were taken into account. Baseline speed values were determined based on *in-vitro* experimental data (see section 2.4.2). For fibroblasts, a baseline cell speed (S_{fb}) of 28μm hr^{-1} was determined. In order to determine the value for myofibroblasts cells, the cultures were treated with TGFβ1 prior to the experiments, a promoter of differentiation towards myofibroblast lineages. In this case, the baseline cell speed (S_{myofb}) was estimated to be 25 μm hr^{-1}, a value slightly below that for undifferentiated fibroblast cells.

The cell speed was inversely proportional to the collagen density ($\boldsymbol{c}$) as it was previously shown that higher densities of collagen caused cells to migrate at a lower speed (Gaudet et al., 2003; Palecek et al., 1997). This relationship between cell speed and collagen density, described first in a dermal wound healing model (Dallon et al., 1999), can be illustrated by setting the chemotactic gradient influence (parameter $\nabla\boldsymbol{A}$) to zero in equation 4.10 (Figure 4-6).

Intermediate collagen densities had very mild effects on the cell speed while the speed decreased rapidly for densities beyond 0.75.

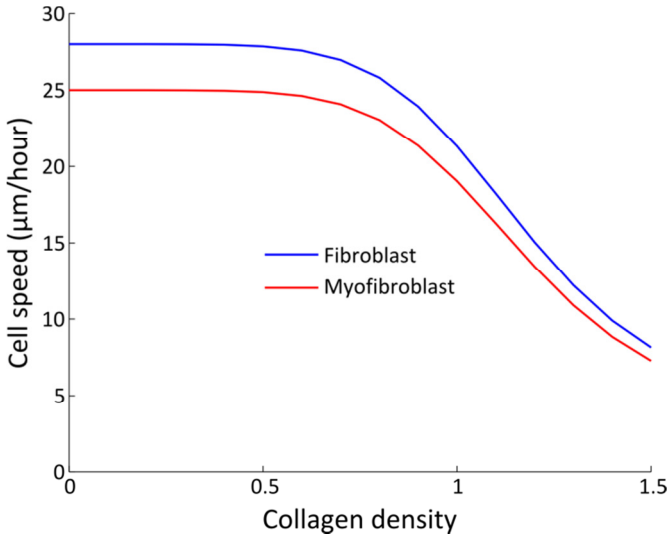

Figure 4-6 Relationship between the cell speed of fibroblast and myofibroblast cells and the collagen density. The blue and red lines correspond to fibroblast and myofibroblast cells, respectively. The plot was based on, equation 4.10 where the chemotactic gradient influence was set to zero.

The cell speed was also influenced by the steepness of the chemotactic gradient at the cell's position, as denoted by the parameter $\|\nabla \boldsymbol{A}\|$ in equation 4.10. The impact of the chemotactic gradient on cell speed for different collagen densities is shown in Figure 4-7. A steeper chemotactic gradient resulted in a faster cell speed (McDougall et al., 2006).

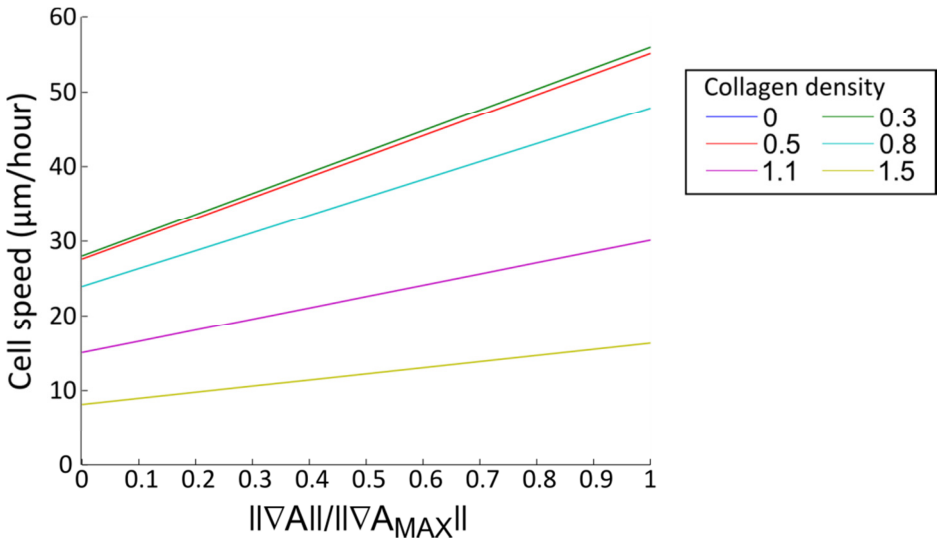

Figure 4-7 Relationship between cell speed of a fibroblast cell and the chemotactic gradient for different densities of collagen. The collagen density can vary between 0 and 1.5, the coloured lines reflect the different collagen densities considered.

The direction of the migration $\boldsymbol{v}(t)$ was influenced by the orientation of local collagen fibres, previous direction of the cell, the chemotactic gradient, and the presence of cells in the close neighbourhood. It was computed as shown in equation 4.11, where $\boldsymbol{c}$ was the collagen matrix, $\boldsymbol{f}^i(t)$ the position of the cell at current time step (t), ρ is the polarisation (dictates the influence

of previous motion and collagen matrix), ρ_2 was the influence of the chemotactic gradient, $\dot{\boldsymbol{h}}^i(t-\tau)$ was the normalised velocity at the previous time step $(t-\tau)$, and $\nabla \boldsymbol{A}$ the chemotactic gradient.

$$\mathbf{v}(t) = \left[(1-\rho)\boldsymbol{I}\left(\bar{\mathbf{c}}(\boldsymbol{t}), \boldsymbol{f}^i(\boldsymbol{t})\right) + \rho\dot{\mathbf{h}}^i(t-\tau)\right](1-\rho_2) + \rho_2\left(\frac{\nabla\mathbf{A}}{\|\nabla\mathbf{A}\|}\right) \qquad 4.11$$

The collagen matrix was interpolated from the 25 nearest grid points, corresponding to an approximate area of 40μm×40μm (see equation 4.7 and equation 4.8). The velocity at the previous time step was computed based on previous position in a normalised form: $\dot{\boldsymbol{h}}^i(t-\tau) = \dot{\boldsymbol{f}}^i(t-\tau)/\|\dot{\boldsymbol{f}}^i(t-\tau)\|$.

The polarisation parameter (ρ) dictated the relative contributions of the cell's previous direction and that of the local collagen matrix alignment (given by 1-ρ) on its direction of migration. ρ was estimated based on *in-vitro* experimental work that studied the effect that fibroblast cell migration had on the anisotropy of collagen fibres (Dickinson et al., 1994). A subsequent study used simulated cell migration to fit the experimental data in order to estimate the weighting values of two fibroblast guidance cues persistence (current direction of migration) and structural (collagen fibre alignment) (Rouillard and Holmes, 2012). It was found that a structural to persistence weighting ratio equal to 0.5 gave a good fit to the experimental data. In this work, ρ was set to 0.66 to fit with this ratio.

$$\rho_2 = \frac{\|\nabla\mathbf{A}\|^{\alpha}}{\left(\|\nabla\mathbf{A}\|^{\alpha} + \|\nabla\mathbf{A}_{critical}\|^{\alpha}\right)} \qquad 4.12$$

$$\nabla\mathbf{A}_{critical} = \frac{\nabla\mathbf{A}_{MAX}}{\beta} \qquad 4.13$$

The effect of the chemoattractant on cell velocity was implemented as previously described (McDougall et al., 2006) and was controlled by ρ_2 (equation 4.12). ρ_2 was defined in the form of a Hill function, which is frequently used in modelling to describe processes that increase following a sigmoidal profile. In this case, increasing the gradient magnitude ($\|\nabla\boldsymbol{A}\|$) first corresponded to modest increases in its influence on the cell's direction, whereas larger values for $\|\nabla\boldsymbol{A}\|$ led to a steep increase in the chemoattractant influence, until reaching a point of saturation beyond which increasing $\|\nabla\boldsymbol{A}\|$ did not have any effect. The steepness of the Hill function was controlled by the positive parameter α, and the point of saturation was affected by the positive parameter β. The different functions obtained by varying these two parameters are shown in Figure 4-8.

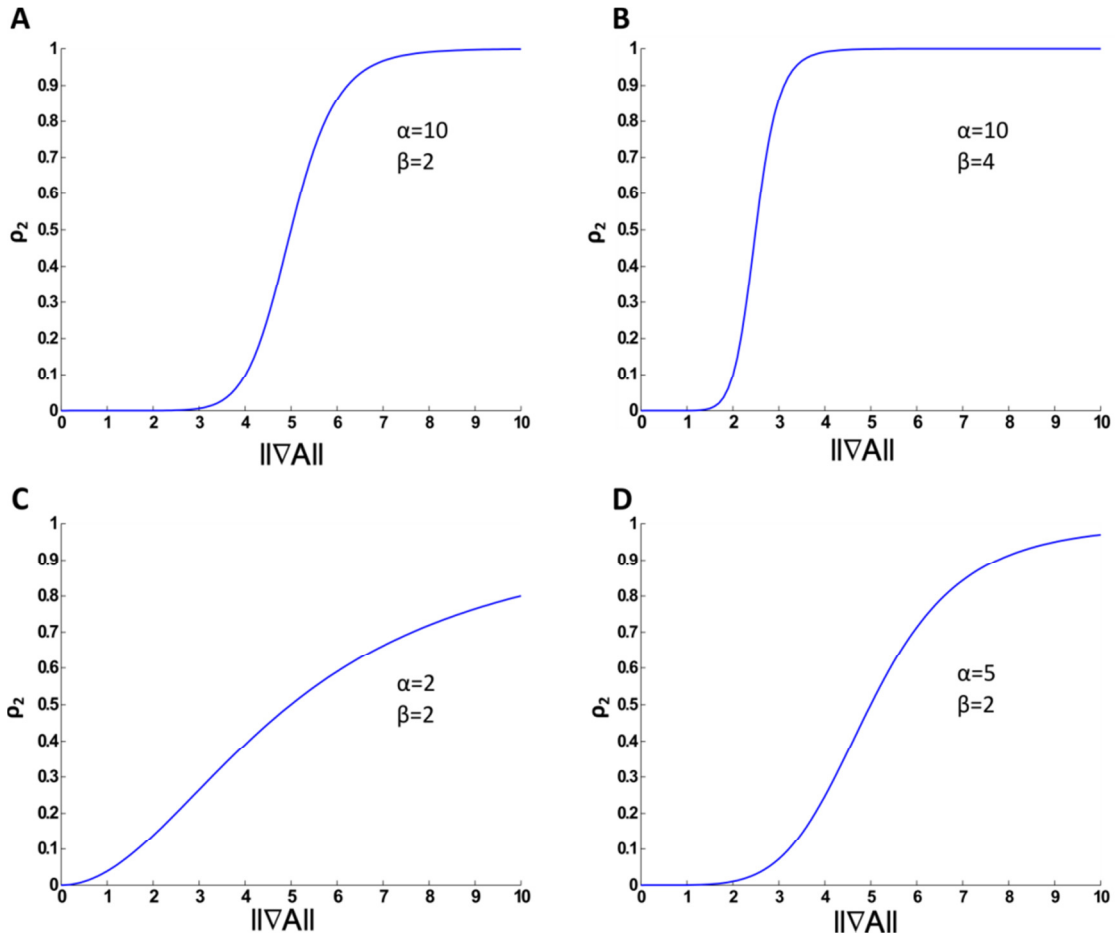

Figure 4-8 Influence of the chemoattractant on cell direction. Effect of increasing the magnitude of the chemoattractant gradient ($\|\nabla \mathbf{A}\|$) on its ability to influence cell direction (ρ_2) for different values of the parameters α and β. (A) α=10 and β=2, (B) α=10 and β=4, (C) α=2 and β=2 and (D) α=5 and β=2. The value of α affects the steepness of the curve and β effects of point of saturation.

For values of β greater than 2, the resulting Hill function quickly became saturated for small $\|\nabla \mathbf{A}\|$ values. Such a profile would not be realistic as it would cause the chemoattractant gradient to almost always dominate over the other factors that have an effect on the cell direction. Setting β to 2 was found to produce adequate profiles and was chosen as the default value for the parameter during simulations. Using these parameters, the effect of the gradient on cell migration was maximum at the infarct border zone and decreased with distance in either direction (i.e. towards both the centre of the infarct and remote tissue). The parameter α was varied between 2 and 10, which had an effect on the steepness of the resulting function (equation 4.12). Setting α to 2 caused the value of ρ_2 to never reach a value of 1 for the gradient magnitudes considered. However, it would make sense at very high gradient magnitudes, for the chemoattractant to be responsible for most, if not all, of the changes in migration direction. For this reason, the parameter α was chosen to be equal to 10, so that the influence could reach a maximum for large values of $\|\nabla \mathbf{A}\|$. The profile used by default in the model was thus the one shown in Figure 4-8A (α and β set to 10 and 2, respectively).

In addition to the determination of cell velocity (speed and direction), it was also necessary to determine whether other cells obstruct migration. Results from *in-vitro* experiments showed that if a neighbouring cell was in the path of a migrating cell, the latter would either attempt to avoid the obstructing cell by changing its direction or even stop if there was no other alternative. This phenomenon, termed cell avoidance is described in the next section (4.4.3.2).

4.4.3.2 Cell avoidance

Both fibroblast and myofibroblast cells produce pseudopodia, which are protrusions from the actin cytoskeleton that can be used by cells to sense and probe their immediate environment, including the presence of neighbouring cells (Abercrombie and Heaysman, 1953). Pseudopodia are readily observed in phase contrast microscopy images of migrating fibroblast cells (Figure 4-9).

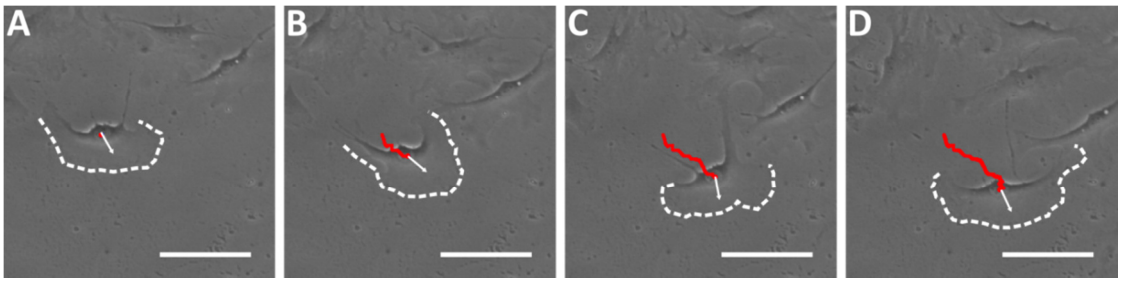

Figure 4-9 Pseudopodia observed during the migration of cardiac fibroblasts. (A-D) Phase contrast microscopy images of a migrating primary fibroblast cell. Images were acquired at intervals of 50 minutes. Scale bar represents 100 μm. The cell movement was tracked (red line) using ImageJ. The 'future' direction of the cell at each time point is indicated with a white arrow. The pseudopodia were outlined with a white dashed line.

Analysis of experimental data revealed the orientation of the pseudopodia correlated with the current and future directions of cell migration (Figure 4-9). Moreover, the pseudopodia appeared to span approximately 90º either side of this direction. Therefore, the region of pseudopodia was modelled as a semi-circular sensing region, positioned so that it faced towards the direction of migration (Figure 4-10). Neighbouring cells were considered an obstruction to migration if they were located within this region.

During a simulation, the velocity of a cell was computed as shown above (equation 4.11), then it was determined whether obstructing cells were present in the resulting direction. A neighbouring cell was considered a potential obstruction if it was at a distance of less than or equal to a set distance away from the migrating cell and if there was an angular difference (θ_d) within $[-\pi/2, \pi/2]$ between the migration direction and the position of the potentially obstructing cell. This method was termed the avoidance algorithm.

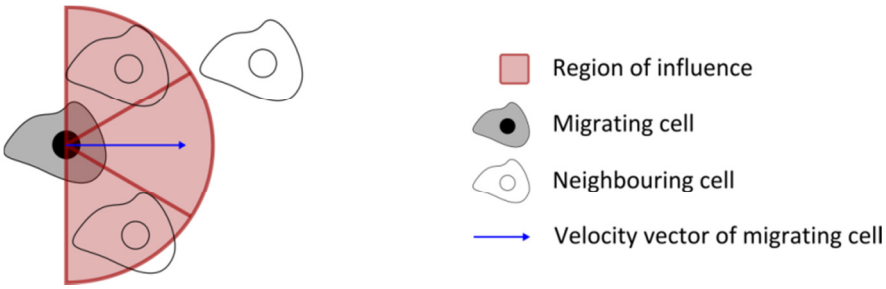

Figure 4-10 Illustration of the avoidance algorithm. A semi-circular region (shaded red) represented the region probed for potential obstructing cells. Neighbouring cells within this region have an influence on the migrating cell.

Before a cell was allowed to migrate, the effect from each influencing neighbour (I_j) was calculated as shown in equation 4.14, where $\boldsymbol{f_i}$ and $\boldsymbol{f_j}$ were the position of the cell and neighbouring cell respectively, and D was a threshold distance. Any cell further away than the threshold distance D was not considered.

$$I_j = 1 - \left(\frac{\left\| \boldsymbol{f}_i - \boldsymbol{f}_j \right\|}{D} \right), \quad i \neq j; I_j \geq 0 \tag{4.14}$$

The value for D was set to 40 µm according to the results obtained from *in-vitro* experiments that were designed to measure the minimum distance between two cells before one or both either changed direction or stopped (see section 2.4.2). The level of influence from a neighbouring cell varied linearly between 0 (no influence) and 1 (maximum influence). The total region of avoidance was divided into three discrete sub-regions, each corresponding to an angle $\theta_s = \pi/3$. The effect from a neighbouring cell (I_j) was assigned to one of the three regions (R_a) as shown in equation 4.15. Where, $\lfloor y \rfloor$ is the floor operator and rounds down the value of y to the nearest integer.

$$a = \left\lfloor \frac{(\theta_d + \pi/2)}{\theta_s} \right\rfloor, \quad where\ (\theta_d) \in \left[-\pi/2, \pi/2 \right] \tag{4.15}$$

The angular difference (θ_d) determined the region assigned to the neighbouring cell. The region number a could take the values 0, 1, or 2. The total effect from neighbouring cells in each region I_{Ra} was then calculated as the sum of the individual effects in that region (equation 4.16).

$$I_{R_a} = \sum_{j=1}^{N} I_j, \quad for\ a = 0,1,2 \tag{4.16}$$

Finally, each region was given a probability P_{Ra} of the cell migrating in its direction. *In-vitro* study of avoidance showed that a cell was more likely to move to an empty space if available (see Figure 2-16). Therefore, if any of the regions I_{Ra} was equal to zero, then a cell had a total probability (P_{EMPTY}) of migrating into one of these empty regions. Regions which contained neighbouring cells ($I_{Ra} > 0$) were assigned a total probability ($P_{OCCUPIED}$). The values 0.9 and 0.1

were assigned to P_{EMPTY} and $P_{OCCUPIED}$, respectively. With these values a cell was more likely to migrate into an empty region if any was available, as observed experimentally. With this additional probability weighting, the probabilities for each region were calculated as shown in equation 4.17, where P_T was the total probability of all the occupied bands ($P_T = \sum(1/I_{R_a})$) and N_{EMPTY} was the number of empty regions.

$$P_{R_a}(t) = \begin{cases} \dfrac{P_{OCCUPIED}}{I_{R_a} \cdot P_T}, & I_{R_a} > 0 \\ \dfrac{P_{EMPTY}}{N_{EMPTY}}, & I_{R_a} = 0 \end{cases} \qquad 4.17$$

If N_{EMPTY} was null, the values for $P_{OCCUPIED}$ and P_{EMPTY} were set to 1 and 0, respectively. Conversely, if P_T was null, $P_{OCCUPIED}$ was set to 0 and P_{EMPTY} to 1. The region towards which the cell will migrate was then chosen based on these probabilities.

An additional avoidance mechanism was implemented. If a neighbouring cell was located at distance of less than 15 μm, cell speed was then set to zero. This reduced the chance of cells clumping together in a manner that was not observed either *in-vitro* or *in-vivo*.

4.4.3.3 Differentiation towards a myofibroblast lineage

As a response to the injury, a fraction of the fibroblast population differentiates towards a myofibroblast fate. Myofibroblast cells are the activated form of fibroblasts with an increased ability to produce and degrade collagen. It has been shown that they generally are larger and migrate with a lower speed (see section 2.4.2 and 2.4.5). Initially, it is assumed that no myofibroblast cells were present. As the simulation progresses, a fibroblast will have a certain probability of differentiating into a myofibroblast if it is located within the border zone of the wound. Limiting differentiation to fibroblast cells located in the infarct was based on reports that myofibroblasts are initially mostly observed in the injured tissue (Yano et al., 2005). It was assumed that the differentiation signal was thus limited to the infarct zone. The probability of a fibroblast differentiating was estimated from *in-vitro* experimental results (see Figure 4-11, equation 4.18 and section 2.4.4).

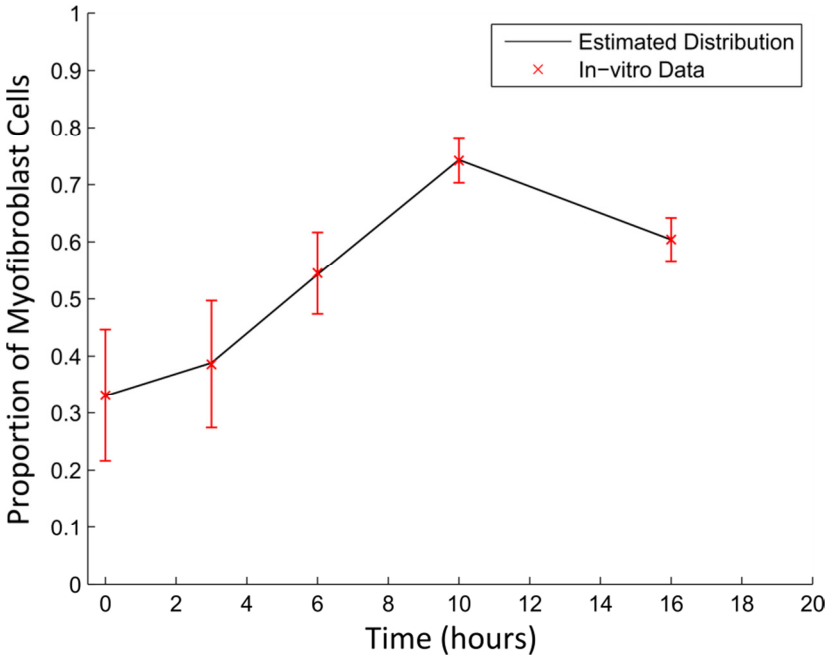

Figure 4-11 Estimation of differentiation probability. Plot illustrating the changes in the proportion of myofibroblast cells with time after wounding during an *in-vitro* scratch assay (red markers). The error bars represent standard deviation across 3 biological replicates. A polynomial was fitted to this data, with R^2=0.9998 (black line).

The *in-vitro* data was approximated with a polynomial function of order 3 (see equation 4.18). The probability was estimated as constant after 16 hours.

$$\begin{aligned}&\text{Prop. of myofibroblasts(t)} = \mathrm{M}_{EXP}(t)\\ &= \begin{cases} -6\times10^{-4}t^3 + 1.03\times10^{-2}t^2 - 6.8\times10^{-3}t + 0.3305, & t \le 16 \\ 0.6925 & t > 16 \end{cases}\end{aligned} \qquad 4.18$$

The proportion of myofibroblasts measured from *in-vitro* experiments was used to derive a probability function of fibroblast differentiation. It was implemented in the model by evaluating at each time step whether cells should be allowed to differentiate based on the difference between the proportion of myofibroblasts at time t observed experimentally (M_{EXP}) and the proportion of myofibroblast cells in the model at time t (M_{MODEL}) (see equation 4.19).

$$P_{DIFFERENTIATION}(t) = \begin{cases} \mathrm{M}_{EXP}(t) - \mathrm{M}_{MODEL}(t), & \mathrm{M}_{EXP}(t) \ge \mathrm{M}_{MODEL}(t) \\ 0, & \mathrm{M}_{EXP}(t) < \mathrm{M}_{MODEL}(t) \end{cases} \qquad 4.19$$

It was assumed that myofibroblasts cannot dedifferentiate back to fibroblast cells. Therefore, if there were a larger number of myofibroblast cells in the model than predicted experimentally the probability of differentiation was set to zero. The experimental results considered the proportion of myofibroblast cells for the first 16 hours post-injury. For later time points in the simulation, the proportions have been assumed to remain constant at the levels observed at 16 hours (equation 4.18). *In-vitro* experiments carried out in this project helped investigate the difference in phenotype between fibroblast and myofibroblast cells (see 2.4.2 and 2.4.4). These

experiments suggested that myofibroblast cells tended to migrate at a slower speed and had a larger average area. Moreover, it was previously reported that myofibroblast cells have a greater ability to produce collagen (Petrov et al., 2002). These phenotypic differences (e.g. cell speed, proliferation and influences on the density and orientation of the collagen matrix) were incorporated into the model. Both the fibroblast and myofibroblast phenotypes will be further discussed in the following sections.

4.4.3.4 Proliferation

Fibroblast and myofibroblast cells were both assumed to divide based on a probability function, which was approximated from experimental data. The fraction of BrdU positive myofibroblast cells was previously determined in murine infarcts at 2, 4, 7, 14 and 28 days post-MI (Virag and Murry, 2003). BrdU staining enabled the detection of cells actively proliferating (at the S phase of the cell cycle, which lasts approximately 6 hours). A probability function based on Gaussian functions was derived from the experimental data (see equations 4.20, 4.21, and 4.22). A combination of two Gaussian functions was used to produce an asymmetrical bell shaped curve. The two Gaussian functions $f_1(t)$ and $f_2(t)$ accounted for the left and right hand sides of the curve, respectively. The position of the centre of the peak was determined by c and the width of the bell on the left and right hand sides of the peak were set by σ_1 and σ_2, respectively.

$$f_1(t) = \begin{cases} e^{\left(\frac{-(t-c)^2}{2\sigma_1^2}\right)}, & t \le c \\ 1, & \text{otherwise} \end{cases} \quad 4.20$$

$$f_2(t) = \begin{cases} 1, & t \le c \\ e^{\left(\frac{-(t-c)^2}{2\sigma_2^2}\right)}, & \text{otherwise} \end{cases} \quad 4.21$$

$$f_{PROLIF}(t) = 0.095\tau f_1(t) f_2(t) \quad 4.22$$

The parameters had to be determined so that proliferation during the simulation would correspond to what was observed *in-vivo*. In order to do so, an unsynchronised cell population (i.e. with random 'age') was allowed to proliferate following the probability function with varying values for the parameters σ_1, σ_2 and c. At each time point, the number of cells that were to divide within the next 6 hours was recorded, to account for the duration of S-phase. Cells were only allowed to divide once in a period of 24 hours, a constraint based on *in-vitro* growth rate measurements (Agocha et al., 1997; Rouillard and Holmes, 2012). The best fit (Figure 4-12) was obtained using the following parameter values: $\{\sigma_1, \sigma_2, c\} = \{17, 39, 57\}$. The peak in the number of BrdU positive cells observed at 4 days post-MI (48 hours in terms of the model simulation time) was also present in the model representation of proliferation. Using the

proposed probability function thus allowed the model to closely replicate the proliferation dynamics observed *in-vivo*. Even though the *in-vivo* data was based on the study of myofibroblast cells, it was assumed that fibroblast cells would proliferate in a comparable manner.

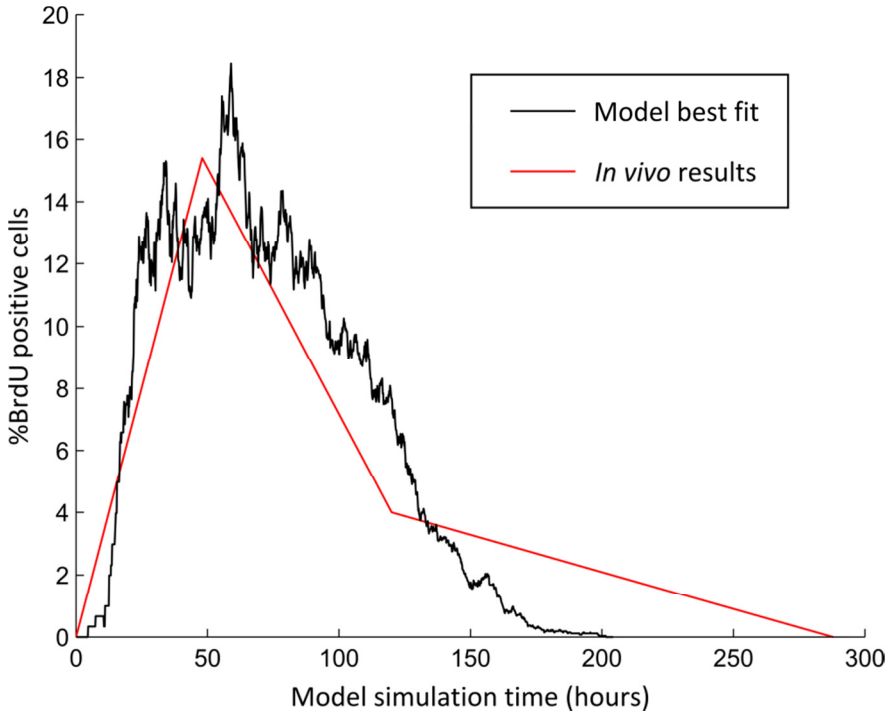

Figure 4-12 Implementation of cell proliferation. Results show the fraction of BrdU positive cells from *in-vivo* murine infarcts at various time points post-MI (red line). The data was adjusted to correspond to the start of the simulation (i.e. 2 days post-MI). The black line represents the best fit obtained by simulation.

The dividing cell resulted in two daughter cells. The first daughter inherited the properties (including position) of the mother cell and the second daughter cell was added as a new cell in the simulation. The second daughter cell was positioned at a predefined distance from the position that was occupied by the original cell. The initial distance between two daughter cells was approximated from *in-vitro* experimental measurements where the average distance was found to be 3µm (see section 2.4.3). Analysis of experimental data also showed that after proliferation, daughter cells tended to migrate in approximately opposite directions (see section 2.4.3). This behaviour was also simulated in the model: immediately after division, the velocity vectors of the two daughter cells were set so that there would be an angular difference of 180º between them. Finally, the age of both daughter cells was set to 0 hours.

Proliferation was constrained by the space available around cells. If a cell did not have a suitable amount of space in its direct neighbourhood, it was less likely to divide. This was based on *in-vitro* experimental evidence, which indicated that 3T3 fibroblast cells tended to stop dividing when cultures reached high confluency (Holley and Kiernan, 1968). This phenomenon is otherwise known as contact inhibition of proliferation. This was implemented in the model by

first determining the space available around a cell before division, which was defined here as the distance between the cell and its closest neighbours. If at least one of these distances is less than a predefined minimum distance (estimated to be equal to 15 μm), then it was determined that the cell did not have enough space to proliferate. The ability of the cell to divide was then evaluated in following simulation steps.

4.4.3.5 Apoptosis

Apoptosis is a key cell behaviour as, together with proliferation and migration, it contributes to tissue homeostasis. Experimental evidence revealed fibroblast and myofibroblast cells had different apoptotic profiles during the course of cardiac wound healing. The implementation of apoptosis in this model was informed by these experimental results and the incidence/rate of apoptosis was applied differently for both sets of cells (Takemura et al., 1998). TUNEL assays, a method for the detection of DNA fragmentation associated with apoptosis, showed very low numbers of apoptotic myofibroblasts in rabbit cardiac tissue at 2 days (~0%) and 4 weeks post-MI (0.23%), but a peak was measured at 2.5%, 2 weeks post-MI . Similarly the numbers of apoptotic fibroblast cells were low at 2 days (~0%) and 4 days post-MI (0.5%), and showed a peak at 1.2%, 2 weeks post-MI.

As the simulation starts at day 2 post-MI, the percentage of apoptotic myofibroblast cells was initially set to zero. The probability function for myofibroblasts being apoptotic was modelled as a Gaussian, which was fitted to the experimental data. The probability function with respect to the model simulation time is shown in equation 4.23, where optimal values for the parameters σ and c were found to be 100 and 288, respectively.

$$f_{APOP\_MYOFIB}(t) = \begin{cases} 4.0464\times10^{-4} e^{\left(\frac{-(t-c)^2}{2\sigma^2}\right)}, & t \le c \\ 4.0464\times10^{-4}, & \text{otherwise} \end{cases} \qquad 4.23$$

The changes in the number of apoptotic cells with time in the model are presented together with the *in-vivo* experimental results (Takemura et al., 1998) in Figure 4-13. This was done for three initial numbers of cells: 300, 3000, and 30,000. While TUNEL-positive cells are considered apoptotic, this process is not instantaneous. It can take place in a time period as short as 2 to 3 hours, but a conservative estimate of 6 hours was assumed for the analysis of simulation results (Sundquist et al., 2006). In the results shown, the proportion of myofibroblasts that were to be apoptotic within the next 6 hours were computed at each time point. Consequently, the duration of apoptosis was taken into account when calculating the percentage of apoptotic cells in the model.

This approach for the implementation of apoptosis provided a good fit between the profiles of apoptotic cells in the model and the experimental data. In particular, the model representation

included the peak observed approximately 288 hours (~2 weeks) post-MI. It was particularly challenging to devise a representation that would still be viable for different numbers of cells. However, as shown on Figure 4-13 B, D and F, the rate at which cells became apoptotic was similar for the three population sizes considered.

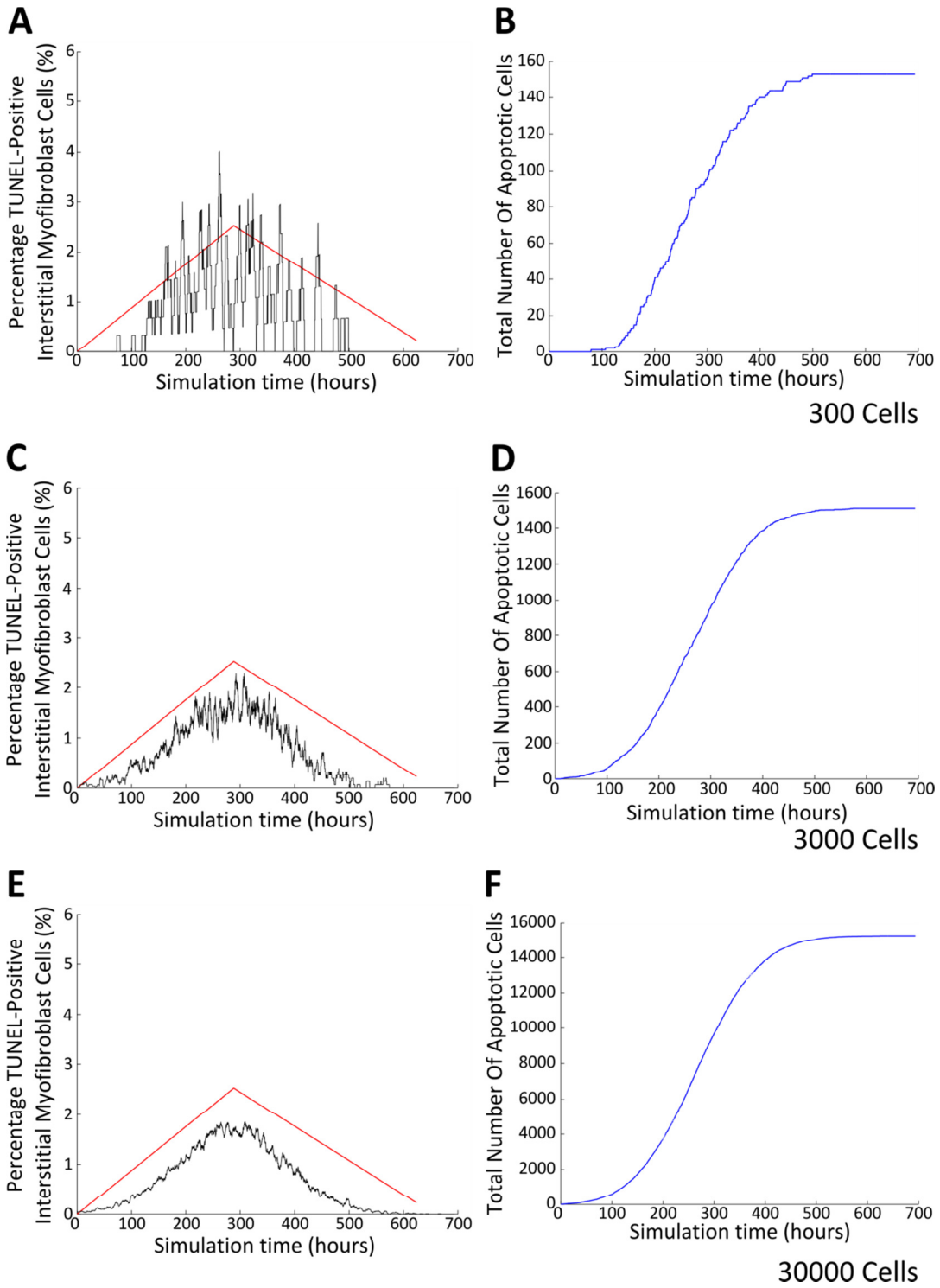

Figure 4-13 Implementation of myofibroblast apoptosis. (A,C,E) Represent the percentage of myofibroblast cells which are TUNEL-positive based on *in-vivo* data (red line) (Takemura et al., 1998) and model simulation (black line), where 300, 3000 and 30,000 cells are used for each simulation respectively. (B,D,F) Show the total number of apoptotic cells during a simulation with 300, 3000 and 30,000 cells respectively.

As mentioned above, the kinetics of apoptosis were shown to be significantly different between regular fibroblasts and myofibroblasts. These differences were also reflected in the way apoptosis for fibroblast cells was implemented in the model. Again, the initial proportion of fibroblast cells undergoing apoptosis was set to zero, consistent with the myofibroblast case. A combination of Gaussian functions was used to fit the asymmetrical experimental data. The probability function is described in equations 4.24, 4.25, and 4.26. The following set of parameters were chosen to best fit experimental data: $\{\sigma_1, c_1, \sigma_2, c_2\} = \{100, 288, 200, 288\}$.

$$f_1(t) = \begin{cases} e^{\left(\frac{-(t-c_1)^2}{2\sigma_1^2}\right)}, & t \le c_1 \\ 1, & \text{otherwise} \end{cases} \quad 4.24$$

$$f_2(t) = \begin{cases} 1, & t \le c_2 \\ e^{\left(\frac{-(t-c_2)^2}{2\sigma_2^2}\right)}, & \text{otherwise} \end{cases} \quad 4.25$$

$$f_{APOP\_FIB}(t) = 1.618 \times 10^{-4} f_1(t) f_2(t) \quad 4.26$$

The apoptotic profiles obtained in the model were compared with the experimental data in Figure 4-14. A good agreement between the two was achieved. The same peak as in the myofibroblast case was observed, but it corresponded to a lower percentage (1.2% vs 2.5%).

For each time step of a simulation, the probability of each cell object being apoptotic was evaluated. If assigned as undergoing apoptosis, the corresponding object was removed from the simulation.

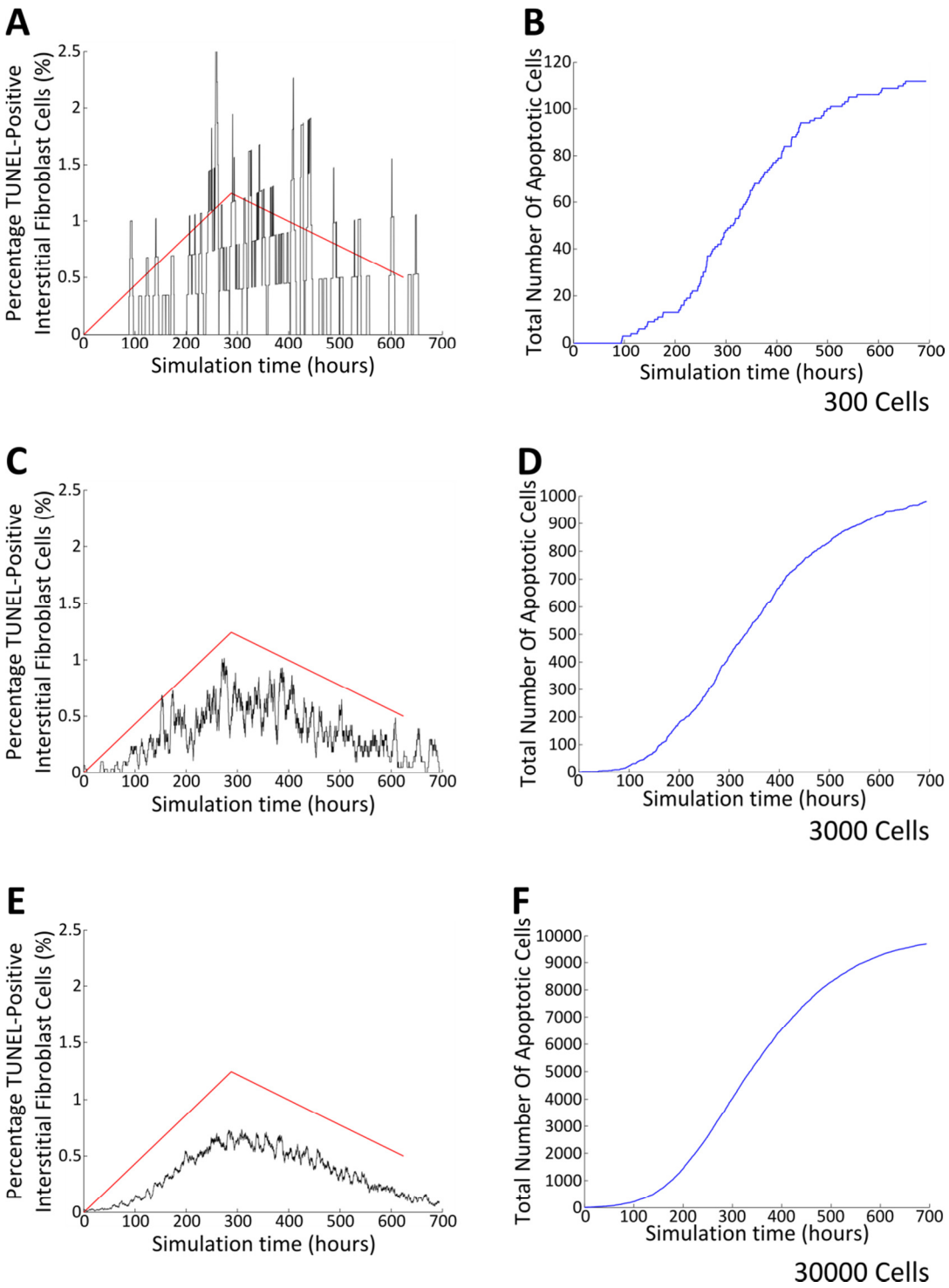

Figure 4-14 Implementation of fibroblast apoptosis. (A,C,E) Represent the percentage of fibroblast cells which are TUNEL-positive based on *in-vivo* data (red line) (Takemura et al., 1998) and model simulation (black line), where 300, 3000 and 30000 cells are used for each simulation respectively. (B,D,F) Show the total number of apoptotic cells during a simulation with 300, 3000 and 30000 cells respectively.

4.4.3.6 Cell area and influence

The fibroblast and myofibroblast cells areas were important model parameters as they dictated how the cells remodelled neighbouring collagen fibres while migrating. Each cell type had a defined area of influence which was estimated from *in-vitro* experiments. The area of cell

influence was modelled as a wedge shape, with the influence maximum along the dominant axis of migration. The dominant axis was determined based on the orientation of the velocity vector of the migrating cell. This assumption was based on evidence which showed that the force applied by a migrating cell was likely to be larger at its leading edge (du Roure et al., 2005) alongside the continuous formation of focal adhesion sites which exerted a traction force on the underlying ECM (Petroll et al., 2003).

As previously described (Dallon et al., 1999), the wedge-shaped region of influence of a cell was represented in the model by a weight function as shown in equation 4.27, where $w_i(\boldsymbol{x},t)$ are the weights at position $\boldsymbol{x}$ and time step t, $\boldsymbol{f}$ the position of the cell, R the distance between the centre of the cells and its edges, D the distance between two opposite edges of the cell (i.e. $2\times R$). A and B are constants.

$$w_i\left(\boldsymbol{x},t\right)=0.6B\left(\frac{\left(A\left(x_d-f_d^i\left(t\right)\right)+R\right)}{D}\right),\quad \left|\boldsymbol{f}^i\left(t\right)-\boldsymbol{x}\right|\le R \qquad 4.27$$

The subscript d denoted the coordinate corresponding to the dominant axis of migration. The constant A took the value +1 or -1 if the coordinate of the velocity vector corresponding to the dominant axis of migration was positive or negative, respectively. The weights were scaled by a constant B equal to 0.67, in order to maintain consistency between the different cell shapes considered later (see section 4.9.2.5)

In-vitro experiments revealed that fibroblast cells had an average cell area of 6,520 μm^2 (see Section 2.4.4). However, cells in heart tissue as assessed by examining histological sections tended to be much smaller at around 400 μm^2, consistent with that reported in a dermal wound healing model (Dallon et al., 1999). This major difference between *in-vitro* and *in-vivo* cell size could be explained by the cells being more tightly packed in tissue when compared with cultures where no external forces dictate cell organisation and the cells are able to spread in an unrestricted manner. For these reasons, the minimum and maximum cell areas in the model were informed by the *in-vivo* and *in-vitro* experimental measurements, respectively. In addition, it was assumed that the area of a cell was also influenced by the amount of unoccupied space in its neighbourhood. Therefore, the area of influence of a cell was altered based on the number of close neighbours. A circular region with a radius of 80 μm was defined around the cell. This distance was based on the mean minimum distance observed between two nuclei of colliding cells (Figure 2-16). This circular region was divided into 6 triangular sub-regions, each corresponding to an angle of $\pi/3$ radians. A sub-region was considered occupied if at least one neighbouring cell was located within its boundaries. The distance from the centre of the cell to its edges (R in equation 4.27) was dynamically adjusted based on the number of sub-regions detected as occupied, in the case of fibroblasts ranging from 40 μm to 10 μm (no neighbouring

sub-region occupied to all six occupied, respectively). Likewise, the same principle was applied to myofibroblasts, where R was varied from 47 µm to 17 µm, as estimated from experimental results (see Section 2.4.4).

Surface and contour plots of the fibroblast and myofibroblast wedge-shaped weight functions are shown in Figure 4-15.

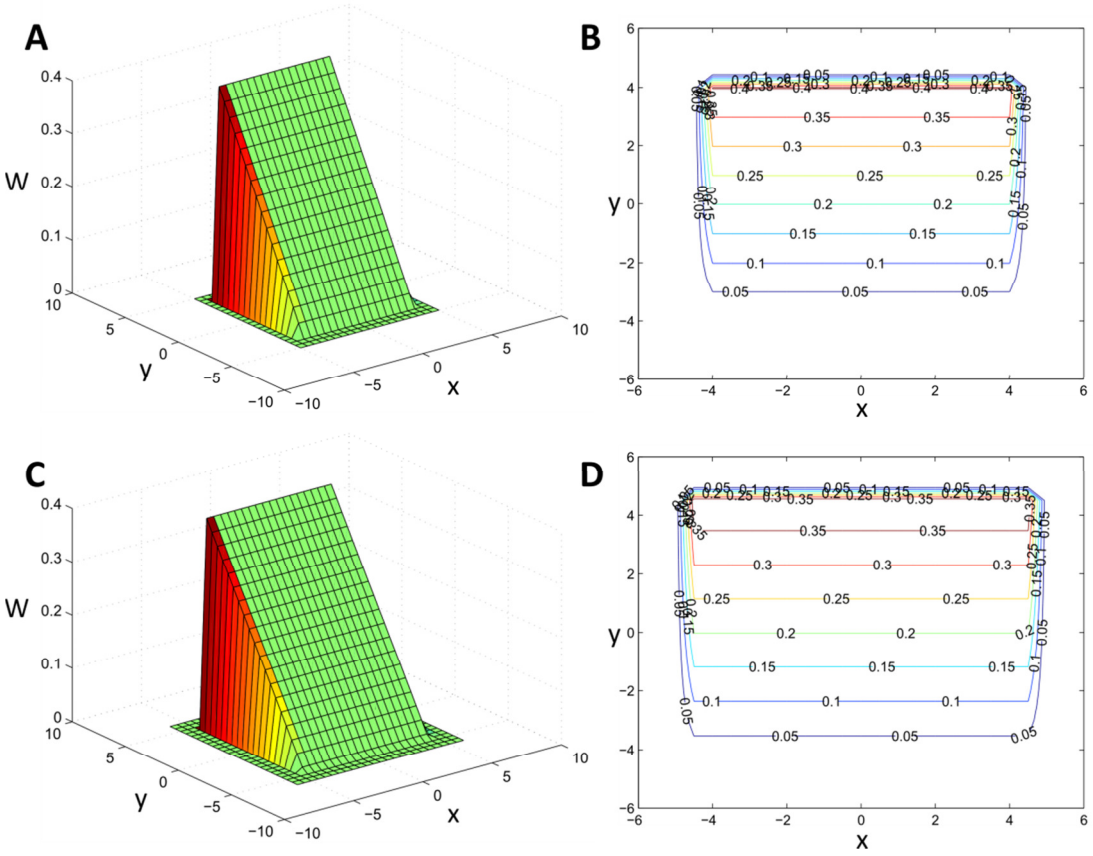

Figure 4-15 Wedge-shaped region of influence of a fibroblast (top row) and myofibroblast (bottom row) cell. The distance from the nucleus (centre of the cell) to edges for the fibroblast and myofibroblast cell was 40 µm and 47 µm, respectively. (A, C) 3D shaded surface plot of the region of influence of a fibroblast (A) and myofibroblast (C), with cell centre at (0,0). (B, D) Contour plots of the weights at different positions on the x,y-plane of a fibroblast (B) and myofibroblast (D).

The weights $w_i(\boldsymbol{x}, t)$ were calculated for each individual cell. At a given grid point, located at $\boldsymbol{x}$, the total cell influence $\boldsymbol{W}(\boldsymbol{x}, t)$ was then computed by summing the product of cells' influence weights by their normalised velocity vectors across all cells in the simulation (see equation 4.28).

$$\boldsymbol{W}(\boldsymbol{x},t) = \sum_{i=0}^{N} w_i(\boldsymbol{x},t) \frac{\dot{\boldsymbol{f}}^i(t-\tau)}{\left\|\dot{\boldsymbol{f}}^i(t-\tau)\right\|} \qquad 4.28$$

The influence of a cell played a key role in its interaction with the collagen matrix.

4.4.3.7 Production, degradation, and reorientation of the collagen matrix

Cells (i.e. both fibroblasts and myofibroblasts) can alter the collagen matrix density and orientation. The cells area of influence was represented by a weight function, as discussed in 4.4.3.6. The orientation of collagen fibres was altered based on the total cell influence at the corresponding grid point and on the stiffness of the collagen matrix. The latter was accounted for in the model by using a parameter κ, which represented the ability of the cells to alter the collagen matrix. This was previously introduced in the dermal wound healing model, where κ was set to a value of 5 (Dallon et al., 1999). This was formulated in the model as shown in equation 4.29, where $d\theta(\boldsymbol{x},t)/dt$ was the rate of angular change of the collagen fibres at the position $\boldsymbol{x}$, κ the ability of the cells to alter the collagen matrix, $\|\boldsymbol{W}\|$ was the normal of the total cell influence vector at the grid point, and ω its angle in relation to the x axis.

$$\frac{d\theta(\boldsymbol{x},t)}{dt} = \kappa\|\boldsymbol{W}\|\sin(\omega-\theta) \tag{4.29}$$

In this model, however, κ was not defined as a constant. Indeed, it was shown that the ability of cells to contract their neighbouring collagen matrix was inversely proportional to the density of the latter (Baxter et al., 2008; Loftis et al., 2003). Moreover, the force applied by each fibroblast was measured to be the same regardless of the collagen matrix stiffness (Freyman et al., 2002). In the model, it was, assumed therefore, that the ability of cells to alter the collagen matrix decreased as the density of latter increased (Figure 4-16). This was implemented as a Hill function whereby the value of the parameter κ, which denoted the ability of the cells to alter the matrix, was maximum and minimum for low and high densities of collagen, respectively. κ was computed as shown in equation 4.30, where κ_{max} the maximum stiffness of the collagen matrix, $\boldsymbol{c}$ the density of the collagen matrix, c_{max} the maximum density, and both α_1 and β_1 were constants controlling the shape of the function.

$$\kappa = \begin{cases} \dfrac{\kappa_{max}\|\boldsymbol{c}\|^{\alpha_1}}{\left(\|\boldsymbol{c}\|^{\alpha_1} + c_{max}/\beta_1)^{\alpha_1}\right)}, & \|\boldsymbol{c}\| > 0 \\ \kappa_{max}, & \|\boldsymbol{c}\| = 0 \end{cases} \tag{4.30}$$

During simulation, the α_1 and β_1 constant were set to -12 and -1.3 respectively, so that the ability of the cells to re-orient collagen matrix would be maximum for lower collagen matrix, before dropping sharply for values beyond a set threshold (~0.75), as shown on Figure 4-16.

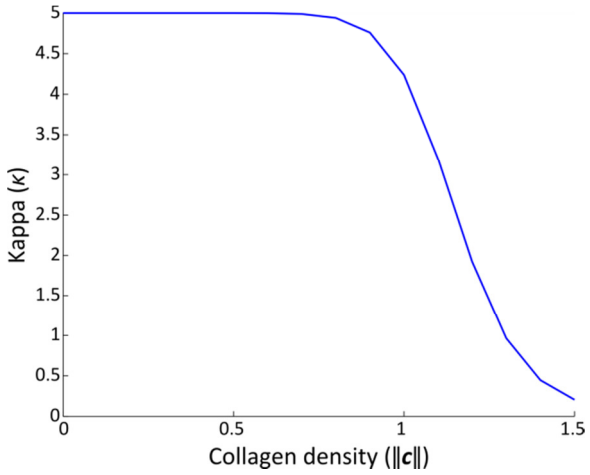

Figure 4-16 Ability of a cell to re-orient collagen (κ) based on the density of the collagen matrix.

The equation governing the rate of collagen fibres re-orientation (Equation 4.29) was discretised using a first-order approximation of the derivative. Intuitively, collagen fibres should have an orientation but not a direction. Given that vectors are inherently unidirectional, additional measures had to be taken to accurately represent the bidirectional nature of collagen fibres. The new collagen vector orientation resulting from the interaction with cells was chosen so that the least possible directional change was imposed on migrating cells. If the angle between the dominant direction of the migrating cells as defined by the total cell influence ($\boldsymbol{W}$) and the collagen direction was obtuse, then the collagen direction was taken to be the opposite, so that the angle became acute. When updating the collagen fibre orientation, Equation 4.31 thus had to be satisfied (Dallon et al., 1999). The constant δ was set to 0.1. In the case where the collagen and total cell influence vectors were perpendicular, the collagen vector direction was randomly assigned.

$$\langle \boldsymbol{c}, \mathbf{W} \rangle - \delta > 0 \qquad 4.31$$

This additional constraint effectively gave the collagen fibres two possible representations, enabling the approximation of their bidirectional nature.

The fibroblast cells are responsible for the collagen turnover and maintenance in the healthy heart. In order to do so, fibroblasts possess the ability to produce and degrade collagen I. This was implemented in the model as shown in equation 4.32, where $\boldsymbol{c(x,t)}$ was the collagen matrix at location $\boldsymbol{x}$, p_c the rate of collagen production, d_c the rate of collagen degradation, and $\|\boldsymbol{W}\|$ the norm of the total cell influence vector at that point. Equation 4.32 was solved in a discretised form using Euler's method (Dallon et al., 1999).

$$\frac{d\left\|\boldsymbol{c}(\boldsymbol{x},t)\right\|}{dt} = \left(p_c - d_c\left\|\boldsymbol{c}(\boldsymbol{x},t)\right\|\right)\left\|\boldsymbol{W}(\boldsymbol{x},t)\right\| \qquad 4.32$$

For fibroblast cells, which are capable of both degradation and production, the ratio of production to degradation rate was assumed to be equal to 1.3 with p_c and d_c set to 0.533 and

0.41, respectively. Myofibroblast cells, which are predominantly only present in the injured myocardium, are responsible for producing the majority of collagen in the form of a non-contractile scar to replace the lost tissue. Interestingly, studies have shown that matrix metalloproteinase-2 (MMP 2), a protein responsible of the degradation of collagen, was down-regulated in myofibroblast cells (Howard et al., 2012). Also myofibroblast cells produce increased levels of collagen compared to fibroblast cells (Souders et al., 2009). To reflect these observations, the ratio of production to degradation for myofibroblasts was higher at 1.5, with p_c and d_c set to 0.6 and 0.4, respectively. Given the parameters for fibroblast and myofibroblast cells were different, the change in collagen density was projected as the product of the individual effect of each cell type (see equation 4.33).

$$\frac{d\left\|\boldsymbol{c}(\boldsymbol{x},t)\right\|}{dt}=\left(\frac{d\left\|\boldsymbol{c}(\boldsymbol{x},t)\right\|}{dt}\right)_{Fib}+\left(\frac{d\left\|\boldsymbol{c}(\boldsymbol{x},t)\right\|}{dt}\right)_{Myofib} \qquad 4.33$$

4.4.3.8 Summary of differences between fibroblast and myofibroblast cells

There are a number of differences between the properties of fibroblast and myofibroblast cells. Some of the relevant differences have been incorporated into the cardiac model. These variations are defined in Table 3.

Table 3 Model parameters for the fibroblast and myofibroblast cell based on *in-vitro* experiments and data from the current literature.

Model parameter	Fibroblast	Myofibroblast	Reference
Baseline speed	28 μm/hr	25 μm/hr	*In-vitro (Section 2.4.2)*
Collagen production rate	0.533	0.6	(Dallon et al., 1999; Souders et al., 2009)
Collagen degradation rate	0.41	0.4	(Howard et al., 2012)
Cell apoptosis probability	Equation 4.23	Equation 4.24 Equation 4.25 Equation 4.26	(Takemura et al., 1998) *In-vitro* (*Section* 4.4.3.5)
Weighting area	6520μm^2	8829μm^2	*In-vitro (Section 2.3.3)*

4.5 Simulation outcome evaluation

The outcomes of simulations were evaluated qualitatively by inspection of model visualisations and quantitatively by using a variety of metrics.

4.5.1 Model visualisation

All the components of the model, including the collagen matrix (density and alignment), the chemoattractant, and the cells can be visualised at each time step of a simulation (Figure 4-17). This was a useful tool as it allowed behaviour such as cell-cell and cell-collagen interactions to be visually qualified and verified using various parameter settings.

The positions of the individual cells (both fibroblast and myofibroblast) were illustrated by either pink (fibroblast cells) or red (myofibroblast cells) squares. Myofibroblasts were slightly

larger consistent with the *in-vitro* observations, which showed that myofibroblast cells often had a larger cell area. The chemoattractant was sampled at the grid points, and could be overlaid on the other components in order to illustrate the spatial and temporal changes in local concentrations.

The collagen matrix could be represented by vectors that were colour coded to indicate local density. Alternatively, a method based on tracing cells described in a previous study (Dallon et al., 1999) also provided a good visual approximation of the continuous collagen matrix. In brief, 'visual' cells were placed at each grid point and their position was iteratively updated based solely on the local collagen orientation. Effectively, these cells were used to trace along the collagen matrix. For a single snapshot of the model simulation, the position of the cells was usually updated eight times. Larger numbers of iterations were more computationally expensive, thus unsuitable for live visualisation, and small numbers were not able to capture the continuous nature of the collagen matrix.

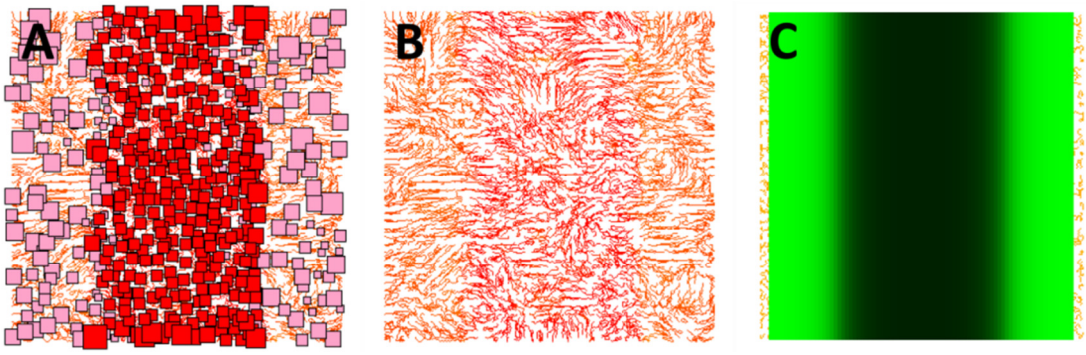

Figure 4-17 Different visual outputs from a model simulation (A) cells and collagen, (B) collagen only, and (C) chemotactic gradient.

At each iteration step, the density of the local collagen was measured. The path of visual cells was colour-coded based on the local collagen density, where green paths indicated low densities while red segments represented highly dense regions.

4.5.2 Quantitative analysis

A number of different metrics were developed and implemented to quantitatively analyse wound, cellular and collagen dynamics throughout model simulations. These metrics were especially useful for comparing model simulations with different parameters.

4.5.2.1 Analysing wound closure dynamics

Wound closure was a metric that reflected the fraction of the wounded region that was affected by the cells. Wound closure was assessed by determining the fraction of the wounded region covered by either fibroblast or myofibroblast cells. During this computation, the area of coverage by a cell was assumed to be equal to its area of influence (as discussed in 4.4.3.6).

4.5.2.2 Analysing the collagen matrix

The collagen matrix was analysed in terms of the orientation and density across the whole tissue section and within just the wound. The orientation was assessed on a local and global scale. The local alignment of the collagen matrix was quantified using a clustering method whereby neighbouring collagen vectors that had similar orientations were grouped together. The size and number of clusters provided an insight into the degree of local collagen alignment. This method is described and discussed in more detail in section 3.4.3.2. Global collagen orientation was quantified by the construction of collagen orientation histograms.

The second property of the collagen matrix analysed was the density. The average collagen density provided information about the level of collagen production and degradation. The average collagen density was calculated from the mean norm of the collagen vectors across either the whole tissue or wounded region.

4.5.2.3 Analysing the cell population

The magnitudes of both the fibroblast and myofibroblast cells were analysed across the whole tissue. The total number of cells for each population was recorded at each time step. Changes in the population sizes were mainly related to the cell proliferation, apoptosis, and differentiation mechanisms.

4.5.3 Database for simulation results exports

Model simulations were evaluated using a variety of metrics, including the wound closure rate, size of the cell populations as well as alignment and density of the collagen matrix (see Section 4.5.2). At the end of a simulation, data necessary for the computation of these metrics was recorded in a Microsoft Access database. The database consisted of three tables: RUNS, RESULTS and RESULTS_RATES. The first table RUNS (see Table 5 in Annex 1), stored information relating the parameters used in the model simulation (e.g. tissue dimensions, initial fibroblast population or cell speed). The RESULTS table (see Table 6 in Annex 1) stored information about the state of the collagen matrix, as well as that of the cell populations at the end of a simulation. This data included the number of collagen clusters (related to local alignment, see section 3.4.3.2), percentage wound closure, average collagen density as well as the number of fibroblasts and myofibroblast cells. This table also contained an ID field, which was used to link the data stored in the RESULTS table with that of the RUN table. This approach was adopted so that multiple series of results could be stored for a single entry in the RUN table, to enable simulations to be run multiple times to account for stochastic effects.

The last table RESULTS_RATES was used to store information at each time point of a simulation (see Table 7 in Annex 1).

4.6 Model implementation

The model was implemented in C++ using the Microsoft Foundation Class Library (MFC). The model implementation relied on object-oriented programming for the representation of agents (cells). The underlying model representation was an 85 x 85 lattice with unit grid spacing equivalent to 10 μm.

Cells were modelled as individual objects (agents) and were free to move within the boundaries of the grid. A cell class was created to encapsulate all of the properties of cellular objects (e.g., position, velocity). Inheritance was then used to define cell objects with specific properties and rules (e.g. fibroblasts or myofibroblasts). They inherited all of the properties from the cell class with the addition of other functions and/or properties unique to the particular class (Figure 4-18). While both fibroblast and myofibroblast objects were representations of biological entities, visual cells objects were only used to create the visualisation of the collagen matrix (section 4.5.1).

The cells had the ability to produce, degrade and reorient the collagen matrix. The collagen matrix was modelled as a discrete vector field and was defined at equally spaced grid points (i.e. each intersection between the vertical and horizontal lines on the lattice grid). At each grid point, the vector length and angle corresponded to the collagen density and orientation respectively. In this implementation the collagen vector field is defined as a two dimensional array.

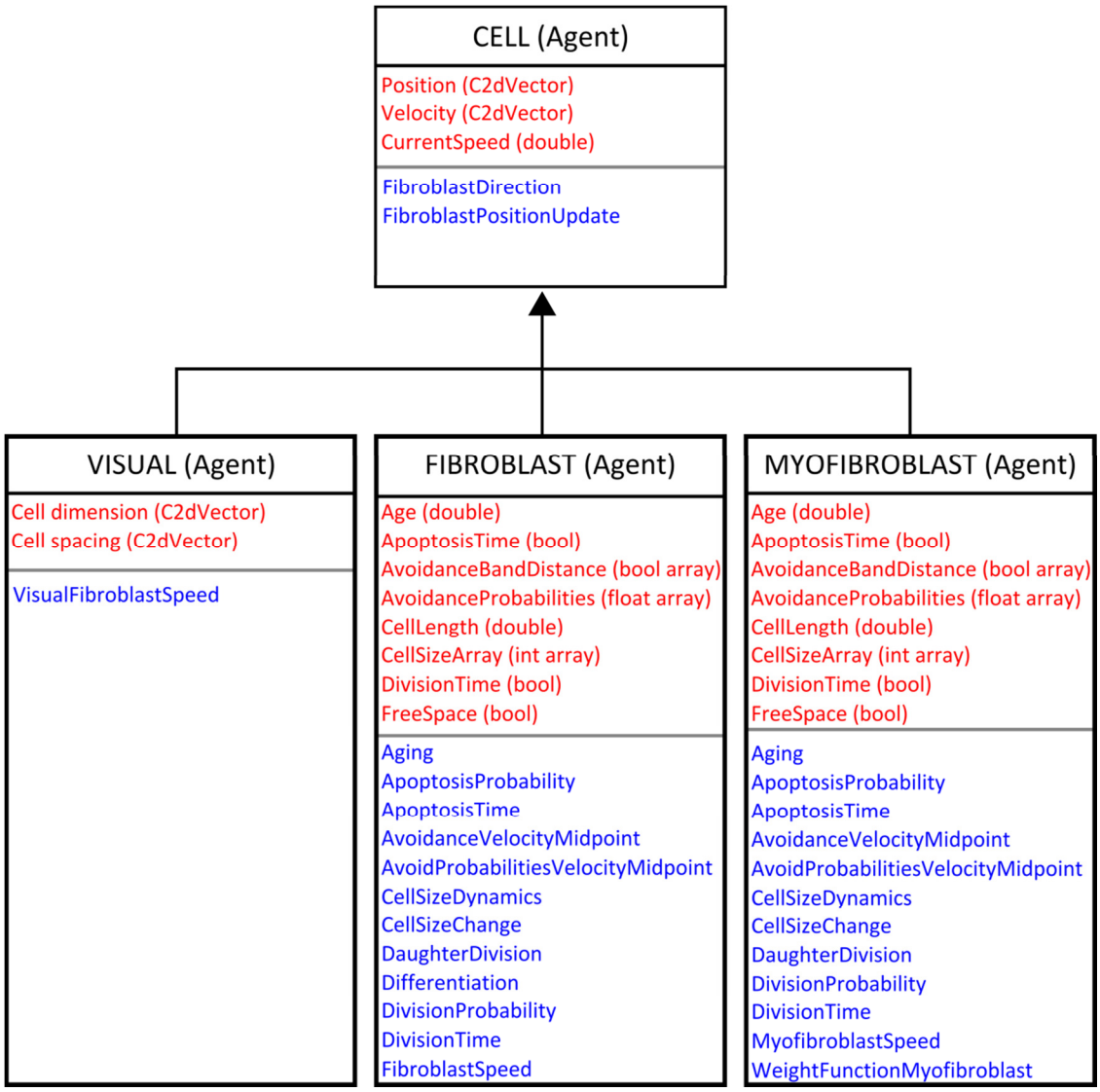

Figure 4-18 Illustration of the cell class with the derived visual, fibroblast, and myofibroblast classes. The members of each class are shown in red and the methods in blue.

A Graphical User Interface (GUI) was designed and implemented to allow most model parameters to be easily modified, including parameters related to the wound, the cells, and general properties of the simulation (e.g. presence of a chemotactic gradient). The GUI was also used to produce a dynamic visualisation of the model, where the time could be essentially rewound or fast-forwarded (see Figure 4-19). After selection of the parameters, the user can start a simulation.

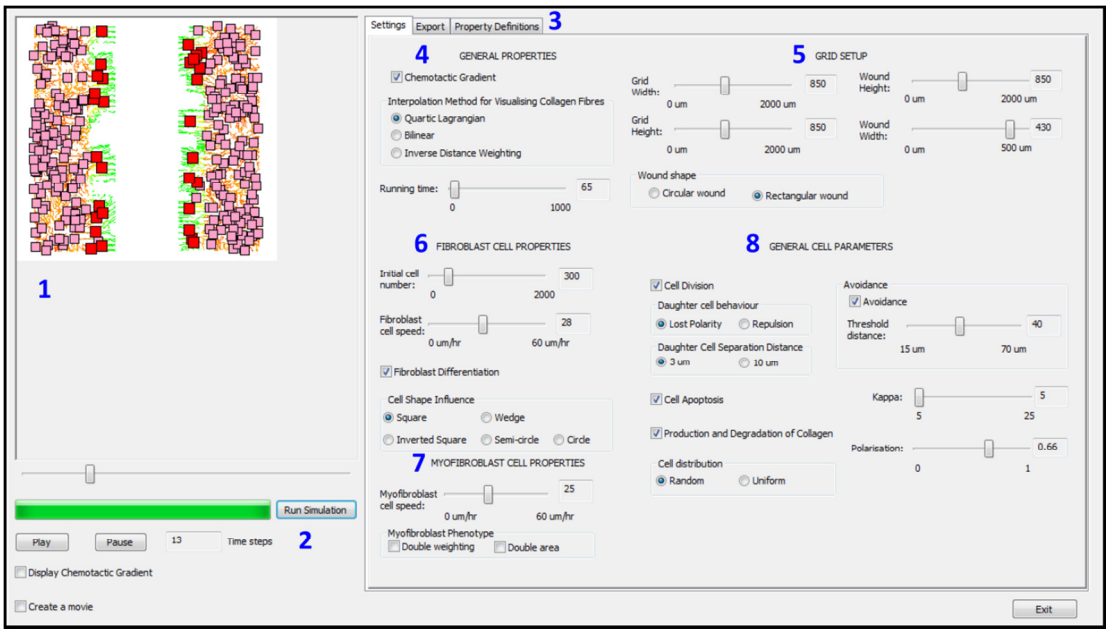

Figure 4-19 The model graphical user interface (GUI) allows the user to easily modify parameter values, to start a simulation run (2), and to visualise the outcome of the simulation (1). The model parameters may be altered with a slider bar, check box or radio button. The model parameters corresponded to general properties of the model (4), the wound (5), properties specific to fibroblast cells (6) properties specific to myofibroblast cells (7), and general properties of the cells (8). Individual images at each time step are saved during the simulation.

The steps taken to perform a typical model simulation are shown in Figure 4-20. The simulation is run for a predefined number of time steps (as defined by the user). The output measurements from the model simulation are stored in a Microsoft Access Database (wound closure rate, collagen alignment and density).

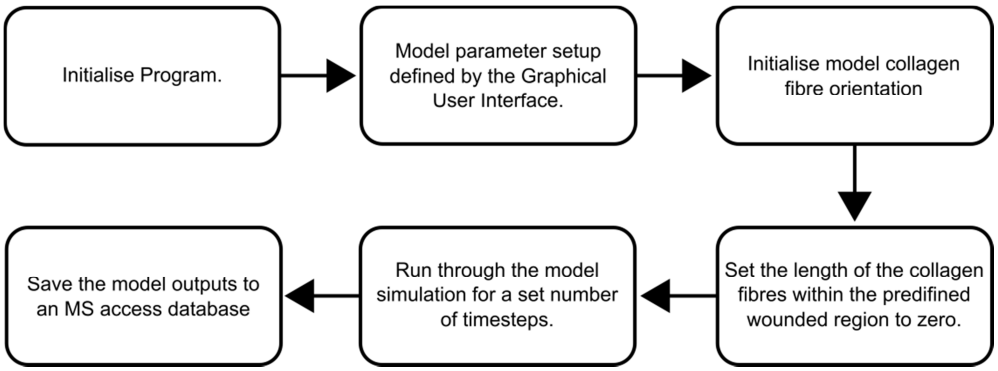

Figure 4-20 Typical use of the model. The program is executed and the user defines the model parameters using the graphical user interface (GUI). The simulation is initialised with the model parameters selected and a random collagen vector orientation. Collagen vectors within the defined wounded region are set to (0,0). The model simulation is started and the model iterates for a set number of time steps. The model output measurements are exported to a MS Access database.

4.7 Summary of the model simulation and parameter values

The cardiac wound healing model is a discrete agent based model. A whole simulation is made up of repeated model iterations. At each iteration the fibroblast/myofibroblast cell positions, chemotactic gradient, collagen orientation, and density are updated (Figure 4-21).

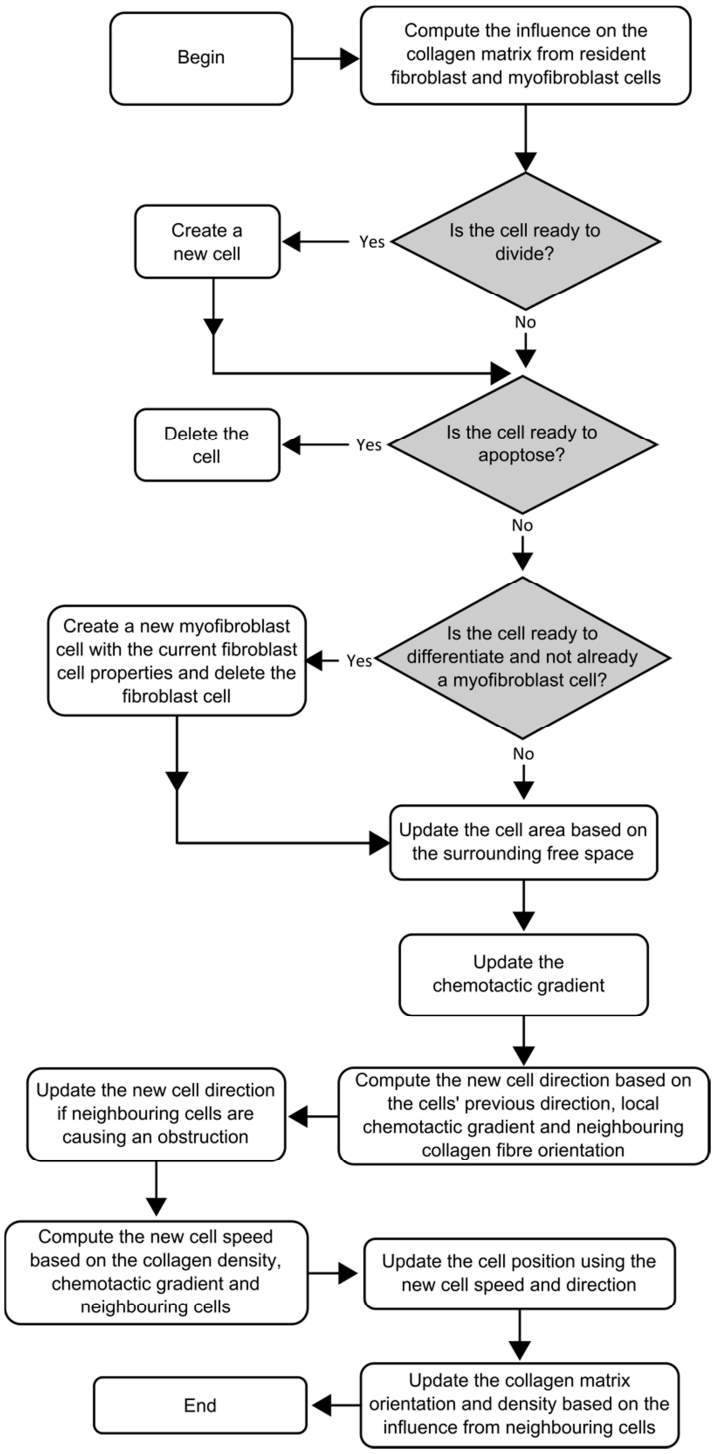

Figure 4-21 Typical model iteration.

The model parameters used in the simulations were either derived from previously published relevant studies or from purpose-designed experiments carried out in the context of this project using primary cardiac fibroblast cells (Table 4).

Table 4 Summary of the model parameter values relating to the tissue structure, chemoattractant, properties of the cell (e.g. migration, proliferation) and the simulation itself (e.g. time step duration).

	Model Parameter	Notation	Value	Reference
Tissue structure	Grid height (μm)	-	850 μm	*Section 3.5.5.3*
	Grid width (μm)	-	850 μm	*Section 3.5.5.3*
	Wound height (μm)	-	850 μm	*Section 3.5.5.3*
	Wound width (μm)	-	430 μm	*Section 3.5.5.3*
	Fibroblast cell population	-	300	*Section 3.5.5.1/3.5.5.3*
	Fibroblast cell spacing	-	3.5	-
Cell migration	Fibroblast baseline speed	S_{fb}	28 μm/hr	*Section 2.4.2*
	Myofibroblast baseline speed	S_{Myofb}	25 μm/hr	*Section 2.4.2*
	Polarisation	ρ	0.66	(Rouillard and Holmes, 2012)
Cell differentiation	Probability of differentiation	$P_{DIFFERENTIATION}$	Equation 4.18 Equation 4.19	*Section 2.4.4*
Avoidance	Threshold distance (μm)	D	40 μm	*Section 2.4.2*
	Minimum distance (μm)	-	15 μm	*In-vivo*
	Empty set proportion	$P_{OCCUPIED}$	0.9	*Section 2.4.2*
	Occupied set proportion	P_{EMPTY}	0.1	*Section 2.4.2*
Collagen Matrix	Production rate (fibroblast)	p_{cf}	0.533	(Souders et al., 2009)
	Degradation rate (fibroblast)	d_{cf}	0.41	(Howard et al., 2012)
	Production rate (myofibroblast)	p_{cm}	0.6	(Dallon et al., 1999; Souders et al., 2009)
	Degradation rate (myofibroblast)	d_{cm}	0.4	(Dallon et al., 1999; Howard et al., 2012)
	Maximum ability to alter matrix	κ_{max}	5	(Dallon et al., 1999)
Chemoattractant	Diffusion constant	D_A	0.9	(Dallon et al., 1999)
	Degradation rate	k_1	$5.5x10^{-2}$	(Dallon et al., 1999)
	Production rate in wound	k_2	$5.5x10^{-2}$	(Dallon et al., 1999)
Time step simulation	Time step interval (hours)	τ	0.15 hours	(Dallon et al., 1999)
Simulation duration	Run time (No. of time steps)	-	3040	*In-vivo*
Proliferation	Minimum proliferation interval	-	24 hours	(Agocha et al., 1997; Rouillard and Holmes, 2012)
	Daughter cell distance		3 μm	*Section 2.4.3*
	Daughter cell angle		180º	*Section 2.4.3*

	Proliferation probability	f_{PROLIF}	Equation 4.20 Equation 4.21 Equation 4.22	*Section 4.4.3.4*
Apoptosis	Apoptosis probability (fibroblast)	f_{APOP_FIB}	Equation 4.24 Equation 4.25 Equation 4.26	*Section 4.4.3.5*
	Apoptosis probability (myofibroblast)	f_{APOP_MYOFIB}	Equation 4.23	
Cell area of influence	Maximum cell area (fibroblast)		6400 μm^2	*Section 2.4.4*
	Minimum cell area (fibroblast)		400 μm^2	*In-vivo*
	Maximum cell area (myofibroblast)		8836 μm^2	*Section 2.4.4*
	Minimum cell area (myofibroblast)		1156 μm	*In-vivo*
Interpolation	Tensor product interpolant using the quartic Lagrangian interpolation	*I*	Equation 4.7 Equation 4.8	*Section 4.4.2*

4.8 Illustration of cell behaviours in the model

As described in the previous section, a wide range of cell behaviours were implemented in the model. In this section, small simulation experiments are used to illustrate the various cell behaviours in the model, and to provide an intuitive understanding of the various processes simulated. From this simple simulation of individual cell behaviour, complex interactions (cell-cell; cell-matrix) and behaviours can emerge, which are further discussed in later sections.

4.8.1 Interactions between cells and the collagen matrix

As cells migrated across the tissue, they altered the collagen matrix density as well as its orientation (section 4.4.3.7). Conversely, the collagen fibres affected the migration direction of the cells (section 4.4.3.1). In this section, the interactions between cells and the collagen matrix are illustrated in a variety of scenarios (e.g. initial collagen alignment, different collagen densities).

4.8.1.1 Effect of initial collagen alignment

The effect of a cell on the collagen matrix orientation was shown in artificial scenarios where collagen fibres were uniformly aligned horizontally or vertically. In addition, the case of a random alignment was also considered. As only the initial alignment of the matrix was of interest, the density of all collagen vectors was set to 1. Moreover, the chemotactic gradient, cell proliferation, cell differentiation, and avoidance were disabled for these experiments. In each

case, three cells were positioned at various locations in the tissue and given a different initial velocity vector.

First, the collagen matrix was set to be uniformly horizontally aligned (Figure 4-22). As cells migrated, alterations of the collagen matrix could be observed. Fibres that were perfectly aligned at first were re-oriented after cells had moved over them. This was most visible when the direction of migration was sufficiently different than the matrix orientation. Similarly, the collagen fibres altered the migration of the cells. After only 4.5 hours into the simulation, all cells were migrating along the collagen fibres, including a cell whose velocity vector was initially close to a 90° angle with the collagen orientation. As the cells aligned with the fibres, their effect on the orientation of the later was greatly diminished. This simple example also demonstrated how collagen density increased after deposition by the migrating cells.

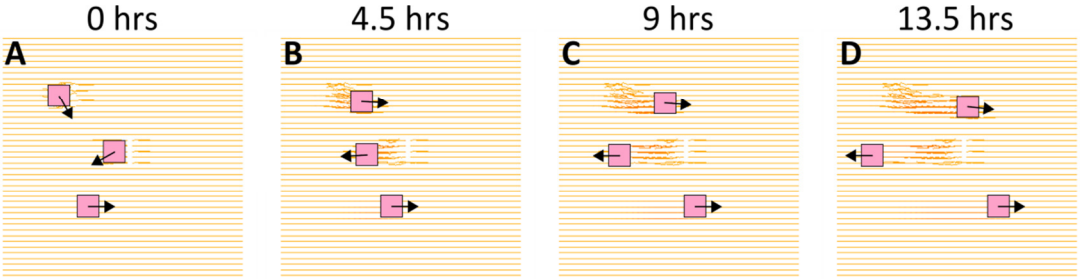

Figure 4-22 Interactions between migrating cells and the collagen matrix in the case where all fibres were uniformly aligned horizontally. Four time points were considered: (A) 0 hours (one simulation step), (B) 4.5 hours, (C) 9 hours, and (D) 13.5 hours. The pink squares denote the cell area of influence, and the black arrows indicate its current migration direction (i.e. velocity vector). The collagen density can vary between 0 (green) and 1.5 (red) and initially begins at a density of 1 (orange).

Similarly, the case where all collagen fibres were initially uniformly aligned vertically was considered (Figure 4-23). The cell migrating vertically (i.e. in a direction parallel to the matrix orientation) maintained its direction, and did not noticeably alter the collagen matrix, except for a slight increase in local density due to deposition by the cell. In contrast, the cell travelling almost perpendicularly to the collagen orientation was very quickly re-oriented so that it travelled along the collagen fibres. During the course of this re-orientation of its migration, the cell altered the orientation of the matrix.

In the case of an initially vertically aligned collagen matrix the effect was identical to the horizontally aligned case. However the cells are travelling in a vertical direction in line with the dominant fibre orientation (Figure 4-23).

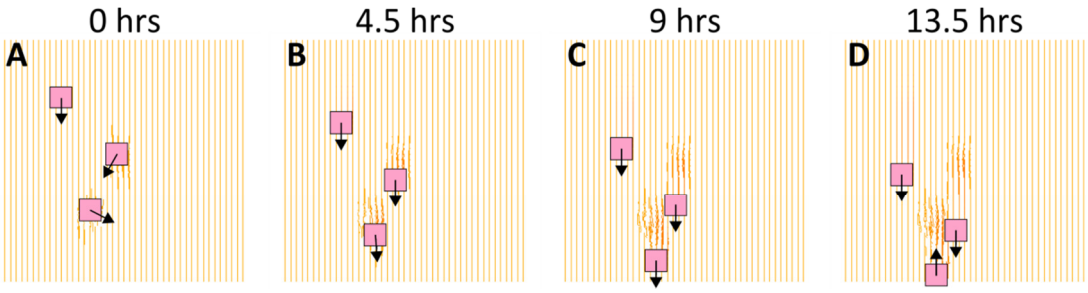

Figure 4-23 Interactions between migrating cells and the collagen matrix in the case where all fibres were uniformly aligned vertically. Four time points were considered: (A) 0 hours (one simulation step), (B) 4.5 hours, (C) 9 hours, and (D) 13.5 hours. The pink squares denote the cell area of influence, and the black arrows indicate its current migration direction (i.e. velocity vector). The collagen density can vary between 0 (green) and 1.5 (red) and initially begins at a density of 1 (orange).

The case where fibres were assigned a random orientation was also considered (Figure 4-24). As expected, the movement of the cells was much more erratic. Similarly, pockets of aligned collagen appeared as an effect of the migrating cells.

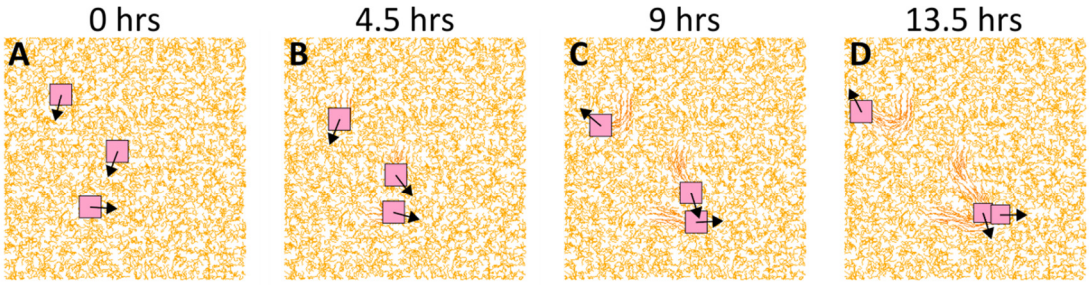

Figure 4-24 Interactions between migrating cells and the collagen matrix in the case where the orientation of the fibres was randomised. Four time points were considered: (A) 0 hours (one simulation step), (B) 4.5 hours, (C) 9 hours, and (D) 13.5 hours. The pink squares denote the cell area of influence, and the black arrows indicate its current migration direction (i.e. velocity vector). The collagen density can vary between 0 (green) and 1.5 (red) and initially begins at a density of 1 (orange).

4.8.1.2 Effect of initial collagen density

Another key aspect of the relationship between cells and the collagen matrix was the density of the latter. Based on experimental evidence, it was assumed that the ability of the cell to alter the collagen matrix orientation was inversely proportional to its density (section 4.4.3.7). In addition, the density of the collagen matrix partly dictated the speed of migration of the cells (section 4.4.3.1). The impact of collagen density was illustrated by simulating the same scenario using collagen densities set to 0.5, 1.0, 1.3, and 1.5, which was the maximum value the collagen density was allowed to take (Figure 4-25).

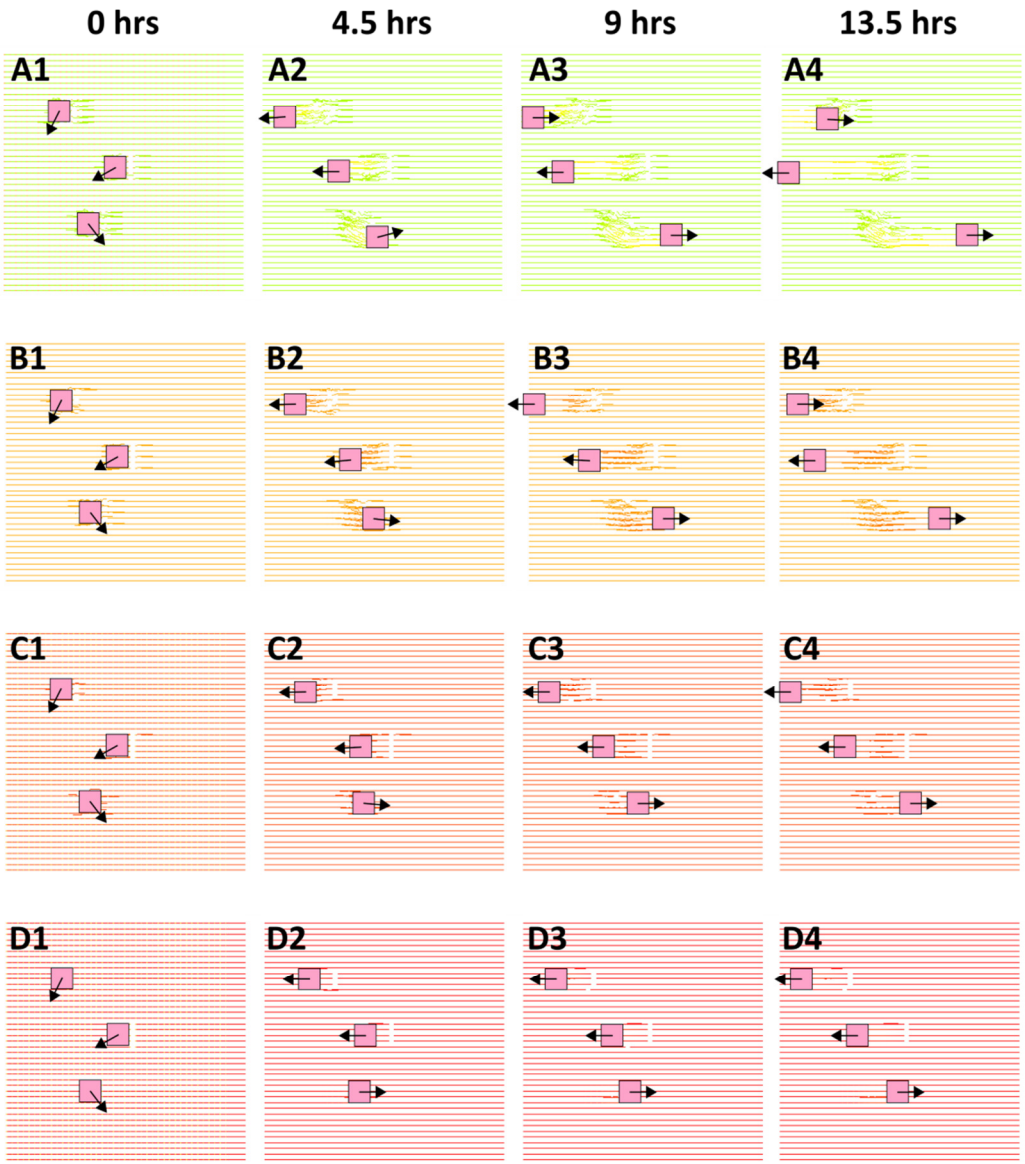

Figure 4-25 Effect of collagen matrix densities on cell migration. Each row (A, B, C, and D) corresponded to a different matrix density: (A) 0.5, (B) 1.0, (C) 1.3 and (D) 1.5. Each column corresponded to a different time point: 0 hour (single simulation step), 4.5 hours, 9 hours, and 13.5 hours. The pink squares denote the cell area of influence, and the black arrows indicate its current migration direction (i.e. velocity vector). The collagen density can vary between 0 (green) and 1.5 (red) and initially begins at a density of 1 (orange).

This example illustrated how the cell motion was impeded by high density collagen. Indeed, while at low collagen density the cells travelled a long distance within the 13.5 hours considered, cells hardly moved in the case with a matrix density set to 1.5. Moreover, the change in cell direction caused by the collagen matrix at lower density was gradual, as shown by the curvature observed as a consequence of the migrating cells. In contrast at higher densities, the collagen was almost perfectly horizontal, indicating that the cell changed direction very abruptly.

4.8.2 Contact inhibition of locomotion

Contact inhibition was implemented in the model, whereby cells were predicted to alter their migration direction in order to avoid collisions with neighbouring cells (section 4.4.3.2). This was illustrated in a simple scenario where two cells were positioned at a distance of 200 µm away from one another, with their velocity vectors facing towards one another (Figure 4-26). The collagen density was set to zero to avoid interference from the collagen matrix.

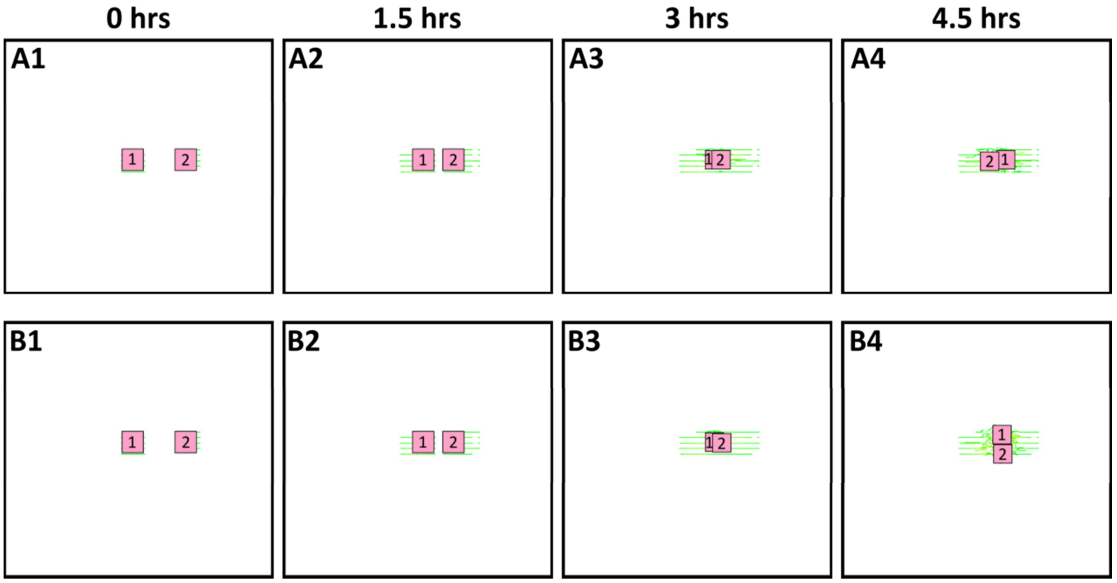

Figure 4-26 Illustration of the avoidance algorithm. Time course simulations results without (top row, A) and with (bottom row, B) the avoidance algorithm. In both cases the cells were positioned at a distance of 200 µm apart and the initial collagen density was set to zero. For clarity, cells were labelled 1 and 2.

Without avoidance, the cells migrated without taking into account neighbouring cells, which resulted in cells moving through one another. This behaviour was unrealistic as cells usually tend to avoid each other, with overlapping or direct contact being a relatively rare occurrence. When the avoidance algorithm was used, the cells migrated until they were in close proximity, at which point their migration direction was altered so that they avoided each other.

4.8.3 Contact inhibition of proliferation

Proliferation was implemented in the model based on a probability function, which takes into account the age of the cell, as well as a mechanism that determined whether there was enough free space for division (section 4.4.3.4). If space was limiting and cells were confluent this resulted in contact inhibition of proliferation. In practice, a cell was prohibited from dividing if there was a neighbouring cell located within a distance of 15 µm. This was illustrated using a simple simulation experiment where division probability was set to 100% and the age of the cell to 25 hours, in order to ensure it would divide right away (Figure 4-27). When another cell was positioned within 15 µm, proliferation was inhibited and the cell did not divide (Figure 4-27 A). In contrast, when no other cell was present, the cells were allowed to divide, with the two resulting cells being positioned according to mutual repulsion (Figure 4-27 B).

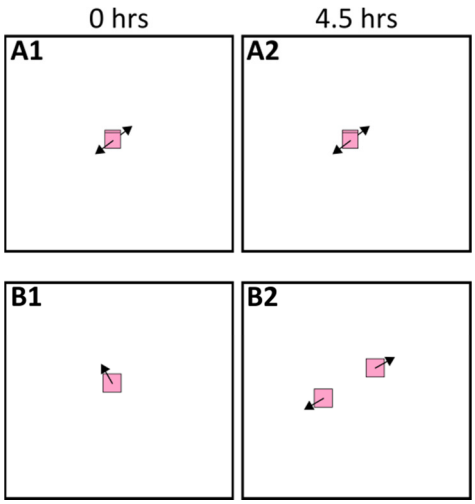

Figure 4-27 Illustration of contact inhibition of proliferation. (A, first row) Simulation results for the case with a cell placed within 15 μm of the cell about to divide, thus preventing division. (B, second row) Simulation results for the case where no other cell is present in the immediate neighbourhood of the dividing cell. The pink squares denote the cell area of influence, and the black arrows indicate its current migration direction (i.e. velocity vector).

Analysis of time-lapse microscopy movies from *in-vitro* experiments revealed that after division, the two daughter cells tended to migrate in opposite directions (see section 2.4.3). However, another variation of this mechanism was implemented in the model, whereby cells would lose polarity upon division and were consequently assigned a random velocity vector. Both cases were illustrated by simple simulation experiments (Figure 4-28).

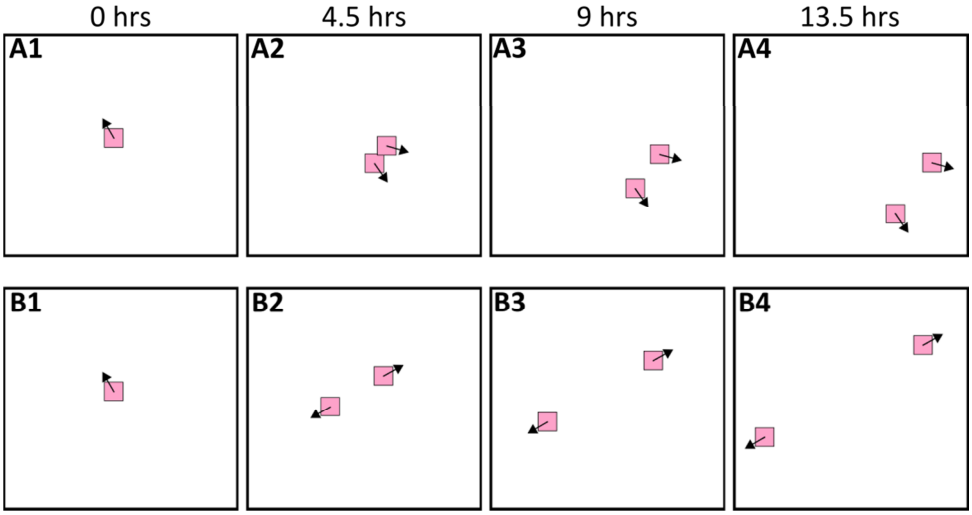

Figure 4-28 Illustration of cell polarity changes following division. (A, first row) Loss of polarity after division, the velocity vector was randomly set for each daughter cell. (B, second row) Daughter cells migrate in opposing directions after division. The pink squares denote the cell area of influence, and the black arrows indicate its current migration direction (i.e. velocity vector).

4.8.4 Dynamic cell area changes in response to crowding

In order to account for changes in cell area observed both *in-vitro* and *in-vivo*, the model dynamically altered the area of a cell based on the presence of other cells in its immediate vicinity (see section 4.4.3.6). This was illustrated using a simple simulation where an increasing number of neighbours were placed proximal to a centrally positioned cell, thus resulting in

dynamic variation in area across a range established by maximum and minimum size parameters (Figure 4-29).

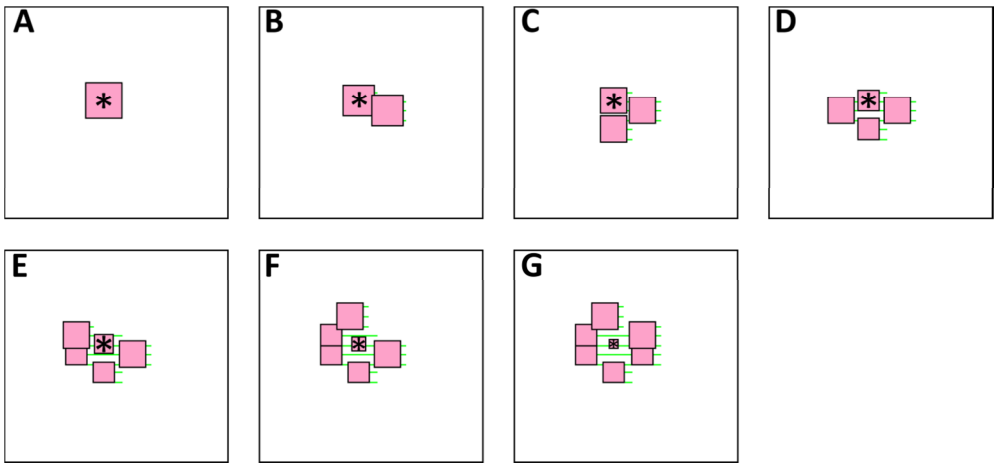

Figure 4-29 Illustration of the dynamic change in cell area in response to crowding. (A-G) Model simulations for a cell (*) with increasing numbers of neighbouring cells (with a maximum of 6).

4.8.5 Typical output of the wound healing model

After examining individual behaviours in isolation, simulations were established using all the functions and behaviours of the model with the parameters as presented in Table 4. The simulation ran the course of 21 days, or an equivalent of 3040 time steps. The model was setup so its initial state corresponded to a wound two days post-MI, when infiltration by fibroblast cells at the wound site is sufficiently well established (Frangogiannis et al., 2000; Sun et al., 2000). The ability to visualise the simulations was essential to understand the dynamics of the model (Figure 4-30).

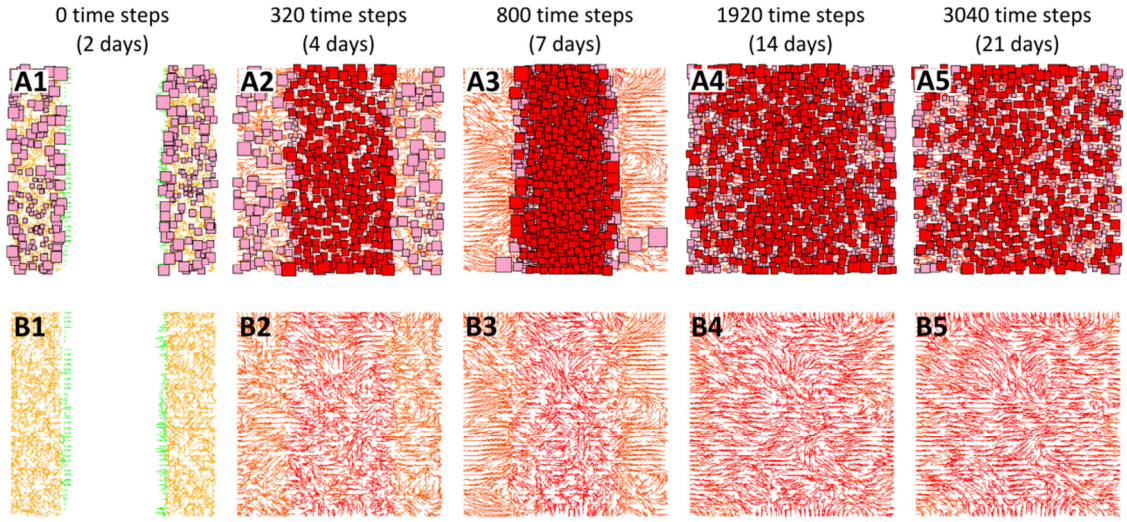

Figure 4-30 Typical simulation including all functions and behaviours of the model. The simulation is visualised at different time steps: 0 (A1, B1), 320 (A2, B2), 800 (A3, B3), 1920 (A4, B4) and 3040 (A5, B5). The simulation is visualised in terms of both the collagen and cells (top row) and just the collagen (bottom row). The fibroblast cells (pink squares) have the ability to differentiate into myofibroblast cells (red squares). The collagen fibres range between a density of 0 (green) and 1.5 (red). (A1, B1) Initially a wounded region is positioned in the centre of the tissue (collagen density null), surrounded by healthy tissue (collagen density of 1, orange) with resident fibroblast cells.

To represent a typical full simulation, the total area of tissue considered for this simulation had dimensions of 850 μm by 850 μm, with a central wounded region of dimensions 850 μm by 430 μm. The collagen density of the wounded region was set to zero, which represented the disruption of the matrix during MI, while that of the surrounding healthy was set to an intermediate value of 1 (1.5 being the maximum density considered in the model).

Shortly after the beginning of the simulation, fibroblast cells migrated into the wounded tissue, partly governed by the chemoattractant diffusing outwards from the wounded region. A fraction of the fibroblasts entering the wound differentiated into myofibroblasts (Figure 4-30A2). The massive influx of cells towards the wound significantly altered the collagen matrix, producing well-aligned and relatively dense patches (Figure 4-30A3). After 1000 time steps (e.g. ~14 days post-MI), the chemotactic gradient was effectively negligible. Cells were, therefore, able to migrate outwards towards the uninjured tissue, in a randomised stochastic manner, resulting in a more even distribution of cells throughout the simulated tissue (Figure 4-30A4). This was associated with an increase in the density of collagen in the surrounding tissue (Figure 4-30B4). At later time steps, the probability of cell apoptosis increased, thus leading to a relatively stable total resident cell number (Figure 4-30A5).

Simulation dynamics were also investigated using a more quantitative approach. The following metrics were employed: collagen density, number of local collagen clusters (i.e. inversely proportional to collagen alignment), percentage of the wound covered by cells, and the total number of cells (Figure 4-31). Most of these measurements were carried out taking into account either the whole simulated tissue or only the wounded region.

At the start of a simulation, the average collagen density for the entire tissue was 0.5 as the healthy tissue and wounded regions had a density of 1 and 0, respectively (Figure 4-31A). As the simulation progressed, the density increased sharply to first stabilise at values of about 1.4 for the entire tissue and 1.5 for the wounded region. This difference between the two was due to the presence of myofibroblasts in the wound, which were assumed to have a higher rate of collagen deposition and a lower rate of collagen degradation. After about 1000 time steps (150 hours), the density in the two regions were nearly identical as the myofibroblast that were until then kept in the wound by the chemotactic gradient were allowed to migrate out as the latter completely decayed.

The collagen alignment was analysed by a clustering algorithm (see Section 3.4.3.2). In brief, clusters were defined as local patches of collagen with similar orientation. As such, the number of clusters tended to decrease as the collagen transitioned from a random orientation to a locally aligned state. The initial number of clusters in the wounded region was 0 as areas without collagen were not taken into account by the cluster algorithm. The number of clusters soared and peaked shortly after the start of the simulation as collagen was deposited in the wounded

region by migrating cells (Figure 4-31B). The number of clusters in the entire tissue decreased following an exponential decay trend, indicating that the collagen matrix was getting re-oriented and aligned by the cells. At time point 1000, a small drop in the collagen alignment measured across the whole tissue was observed as the cells migrated into the healthy tissue coincident with when the chemotactic gradient became inactive, and further aligned the collagen while doing so.

A typical model simulation began with 300 fibroblast cells and no myofibroblast cells (Figure 4-31C). A decrease in the number of fibroblast cells was observed during the first part of the simulation alongside an increase in the myofibroblast population as a result of the differentiation of the cells migrating into the wound. Both populations of cells then continued to increase due to the combined effects of both differentiation and proliferation. After a peak in the cell population at around 1000 time steps (150 hours), both populations started declining due to reduced levels of proliferation and increased chances of apoptosis.

The coverage of the wounded region by the cells was also investigated (Figure 4-31D). Coverage had a value of 0 at the start of the simulation as no cells were present in the wound. As the cells were directed towards the wound by the chemotactic gradient, there was a sharp increase in cell coverage, rapidly reaching a value of 80% of the available tissue surface area. The rate of increase then slowed down as the cells co-occupied smaller areas due to the high population density at this point. Coverage reached a peak of nearly 100% at around 500 time steps. Thereafter, the coverage decreased overtime due to a decline in the number of cells and the decay of the chemotactic gradient.

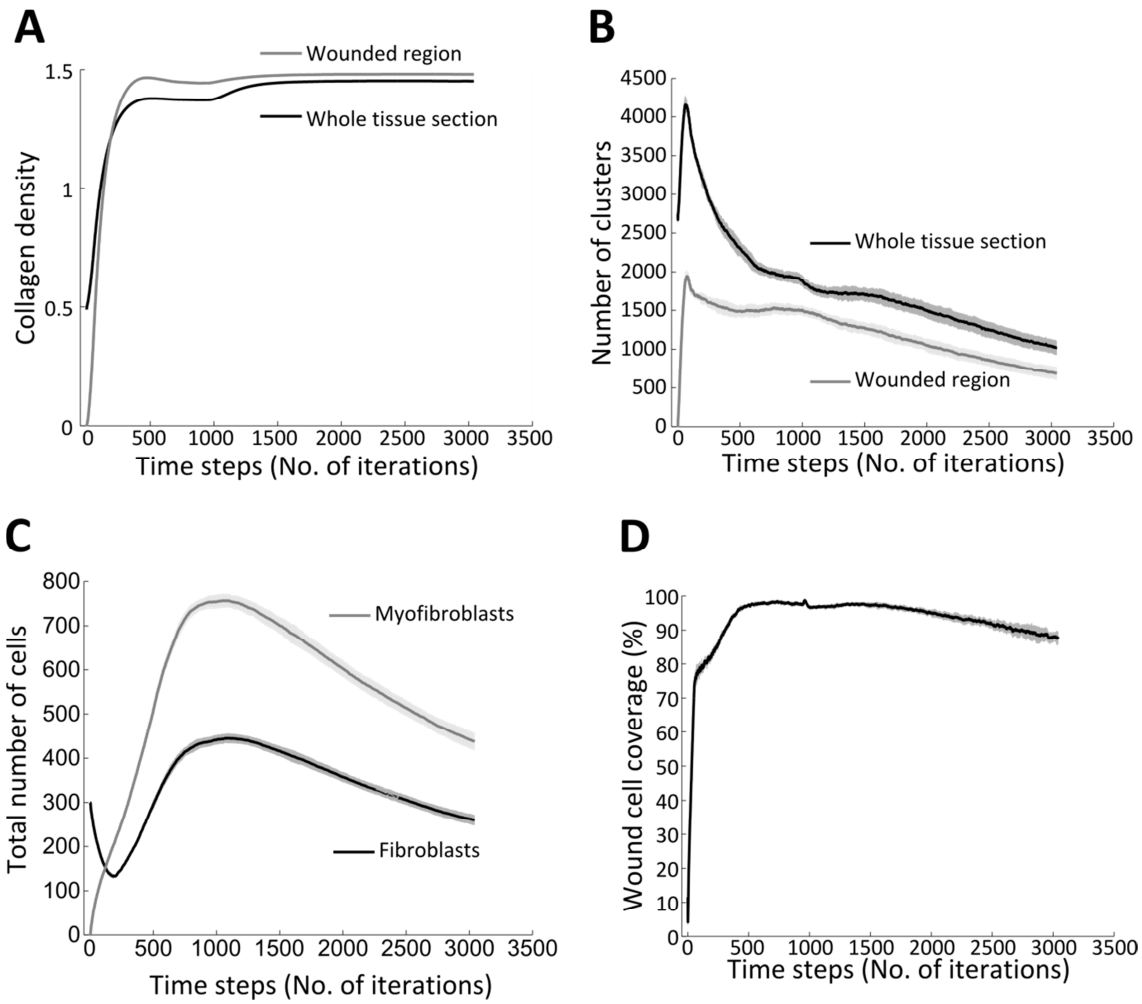

Figure 4-31 Typical simulation dynamics including all functions and behaviours of the model. Quantitative measurements of the (A) collagen density, (B) collagen alignment in terms of the number of clusters, (C) cell population size and (D) percentage wounded region covered by cells. The shaded regions represent the standard deviation of 11 simulations runs.

4.9 Evaluation of the impact of parameters on simulation outcomes

The main aim of this work was to devise a model whose parameters could be derived from carefully designed *in-vitro* and *in-vivo* experiments where possible, and from the literature otherwise. However, the main advantage of a computational model of a biological system is the ability to change individual behaviours and rules, however unrealistically, to investigate various scenarios that could give an insight into potential experimental approaches that might be worth pursuing.

This section thus focuses on the impact of varying parameter values on the simulation outcomes. Unless specified otherwise, the parameter values shown in Table 4 were used as baseline. All the components and functions of the model were enabled for the simulations discussed herein.

4.9.1 Cell population size and distribution

Model parameters that related to the size of the population of cells were considered as well as their distribution throughout the tissue.

4.9.1.1 The size of the fibroblast population

The impact of different values for the initial number of cardiac fibroblasts at the start of a simulation was evaluated. The population size estimated from *in-vivo* heart sections was 300 cells (section 3.5.5.1). In a first instance, alternative initial population sizes (75, 150, 300, and 450) were chosen arbitrarily to study sensitivity to higher and lower numbers of cells. Outcome was assessed using both the average collagen density as well as the number of clusters (Figure 4-32).

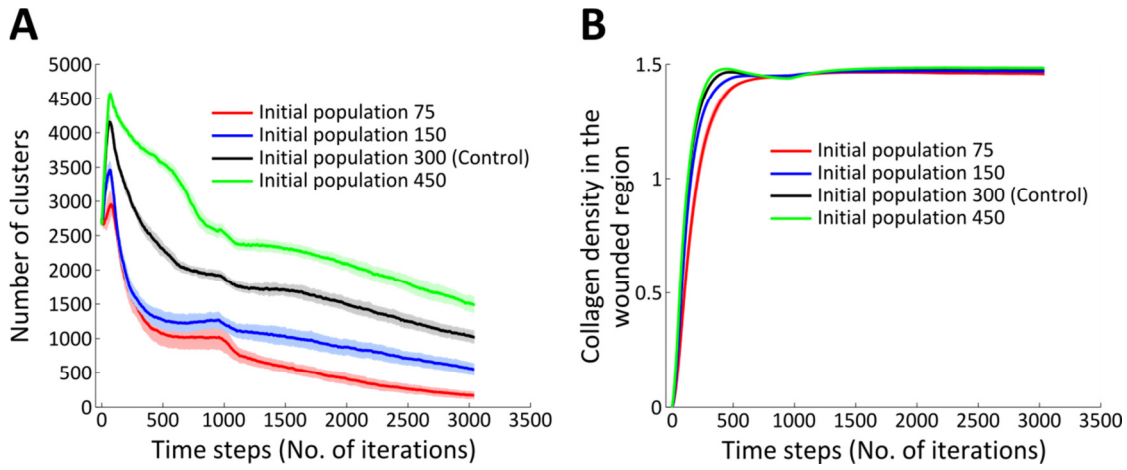

Figure 4-32 Impact of starting fibroblast population size on collagen matrix remodelling. Initial fibroblast populations of 75 (red), 150 (blue), and 450 (green) cells were compared with the value estimated from *in-vivo* tissue sections (300 cells, black). Impact on (A) the number of clusters across the whole tissue, and (B) the average collagen density in the wounded region. The shaded regions represent the standard deviation of 11 simulations runs.

The results showed that the initial population size had only a modest effect on the profile of increased collagen density during the course of the simulation (Figure 4-32B). In all cases, a plateau in density was attained after ~750 time steps. The main difference between the conditions considered was the initial rate of increase in collagen density, which was proportional to the size of the initial cell population. In contrast, the number of local collagen clusters measured at various time steps was clearly impacted by the initial number of cells (Figure 4-32A). For all conditions tested, the number of collagen clusters rose sharply within the first 100 time steps, peaking at values that increased with the number of cells considered. This initial increase was due to the creation of a large number of clusters by the cells initially migrating into the wound. Thereafter, the number of clusters plummeted, at a rate that was inversely proportional to the number of initial cells. In other words, a small number of cells resulted in highly aligned collagen fibres, whereas larger number of cells led to more disorganised patterns, most likely due to a constant re-orientation at all locations of the tissue.

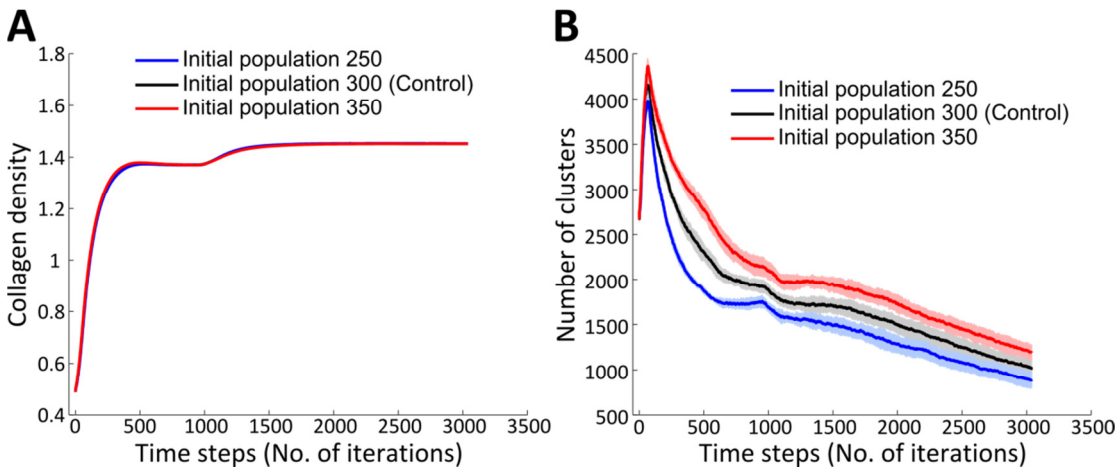

Figure 4-33 Impact of starting fibroblast population size on collagen matrix remodelling in the whole tissue. Initial fibroblast populations of 250 (blue) and 350 (red) cells were compared with the control (i.e. estimated from experiments) case of 300 cells (black). The standard deviation is shown for each case by a shaded region surrounding the points (N=11). Profiles of (A) average collagen density and (B) number of clusters as computed across the entire tissue.

The sensitivity of the model to minute variations in the number of initial cells was assessed by comparing simulations results when using the initial number of cells estimated experimentally (300, see section 3.5.5.1), with two others cases varying by 50 cells (i.e. initial population of 250 and 350 cells). When considering the average collagen density across the whole tissue, identical profiles were obtained regardless of the initial number of cells (Figure 4-33A), thus indicating that a ~17% change in the initial population of cells did not have a measurable effect. However, this small difference in the size of the initial cell populations resulted in profiles for the number of clusters measured throughout the simulation that differed significantly (Figure 4-33B). The trend was consistent with what was observed previously, i.e. the number of clusters at the end of the simulation was inversely proportional to the initial number of cells.

4.9.1.2 Cell distribution

The initial population of cells were placed randomly throughout the uninjured tissue by default. However, the initial distribution of cells in reality might be more ordered and homogeneous. This could be represented by placing the cells so that they are evenly spaced throughout the healthy tissue. Both situations were considered. In the case of the uniform distribution of cells, a random small displacement was introduced in the cell's x and y coordinates so that cells didn't line up in perfect rows and columns but instead adopted a configuration that was more biologically relevant as a perfect distribution would be unlikely in real tissue. The differences between the two methods for initial cell distribution are illustrated in Figure 4-34.

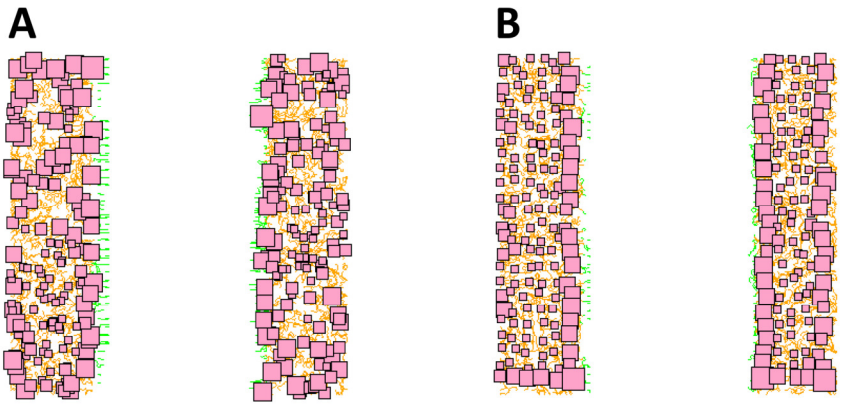

Figure 4-34 Initial cell distribution, using (A) randomly assigned locations (model default) and (B) uniformly distributed locations.

First, the difference between the two configurations was evaluated based on the total number of myofibroblasts (Figure 4-35A). This was a metric of interest as the initial distribution of fibroblasts would dictate the kinetics of infiltration of the wound, and thus that of differentiation towards myofibroblast lineages. Indeed, there was a marked difference in the peak number of myofibroblasts, as well as in the rate at which it was attained, with randomly positioned cells resulting in higher values for both. The uniform cell distribution appeared to produce a lower peak in the number of myofibroblast cells compared with the control at approximately 1000 time steps into the model simulations (see Figure 4-35). When comparing the effects of both configurations on the number of collagen clusters (Figure 4-35B), only a mild difference was observable with the uniform cell distribution resulting in a slightly lower number of clusters (i.e. higher degree of alignment).

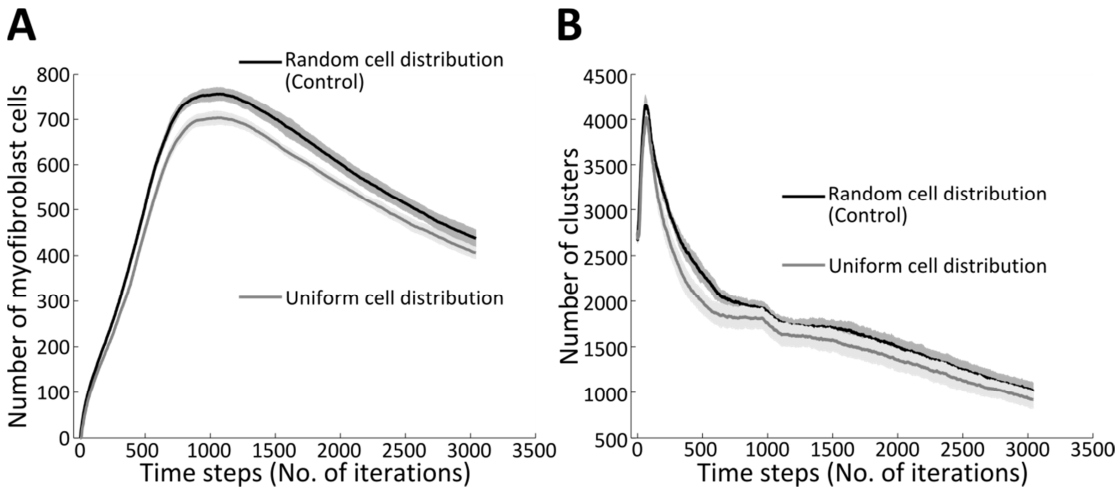

Figure 4-35 Effects of two different methods for initial cell distribution: randomly distributed tissue (model default) and evenly spaced within the healthy tissue. The metrics considered were (A) the number of myofibroblasts and (B) the average number of clusters across the whole tissue.The shaded areas denote the standard deviation for 11 simulation runs.

4.9.1.3 An initial population of myofibroblast cells

One of the model assumptions is that there were no myofibroblast cells present at the beginning of a simulation and instead the initial cell population was made up of 300 non-activated

fibroblast cells by default. It was of interest to determine the impact on simulation outcomes if the initial population of resident cells was made up of 10%, 25% or 50% myofibroblast cells, with the total number being kept constant at 300 cells (Figure 4-36). The changes in the initial number of myofibroblasts only had a slight impact on the changes in collagen alignment (as measured using the number of clusters) throughout the tissue. In general, higher number of myofibroblast cells present at the beginning of simulations resulted in a lower degree of alignment (i.e. larger number of clusters). The differences were more marked in the first half of the simulations, with the profiles becoming more similar after the 1000 time steps mark that corresponds to the chemotactic gradient being switched off.

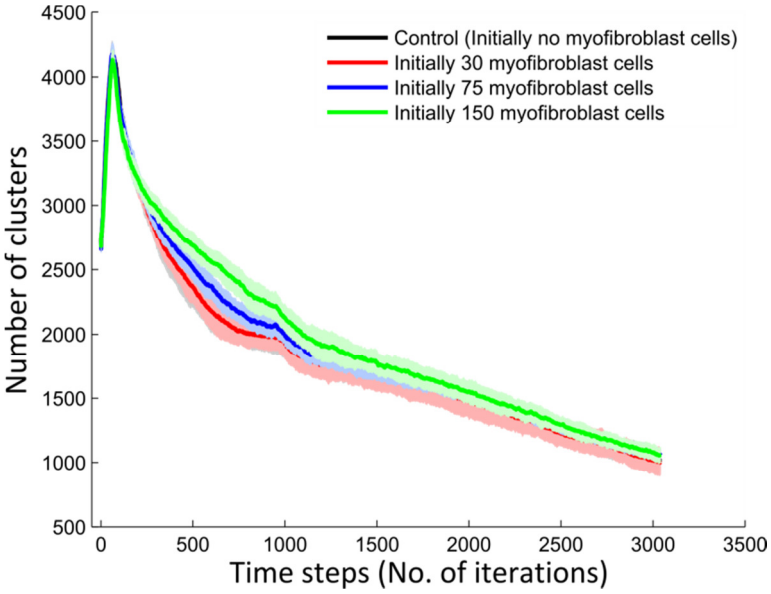

Figure 4-36 Effects of having myofibroblasts present at the start of a simulation on collagen matrix alignment. The number of clusters across the whole tissue was measured for initial population of resident cells made up of 0% (control, black), 10% (red), 25% (blue), and 50% (green) myofibroblasts. The 0% case (control, black) is obscured by the 10% case (red). The total number of cells was kept constant at 300. The shaded areas represent the standard deviation across 11 simulations.

4.9.2 Cellular properties and functions

This section focuses on parameters that dictate the properties and functions of individual cells in the model such as proliferation, migration or shape.

4.9.2.1 Cell proliferation

Cell proliferation was mostly dictated by rates derived from *in-vivo* experiments (Virag and Murry, 2003). It was of interest to investigate how alterations in the proliferation rate of cells would impact on the simulation outcome, hence the ability of cells to proliferate was removed and the values of the different parameters relating to cell proliferation were varied.

4.9.2.1.1 Disabling cell proliferation

The impact of cell proliferation on the wound simulation was first assessed by removing the ability of the cells to divide. As shown by simulation visualisations for the cases with and

without proliferation (Figure 4-37), the proliferation had a significant impact on most components of the model. The number of cells was much higher for the case with proliferation, with cells mostly having the minimum area possible due to crowding. In contrast, larger cells were visible when proliferation was disabled. Moreover, the orientation of the collagen fibres was also markedly impacted during the final stages of the simulation.

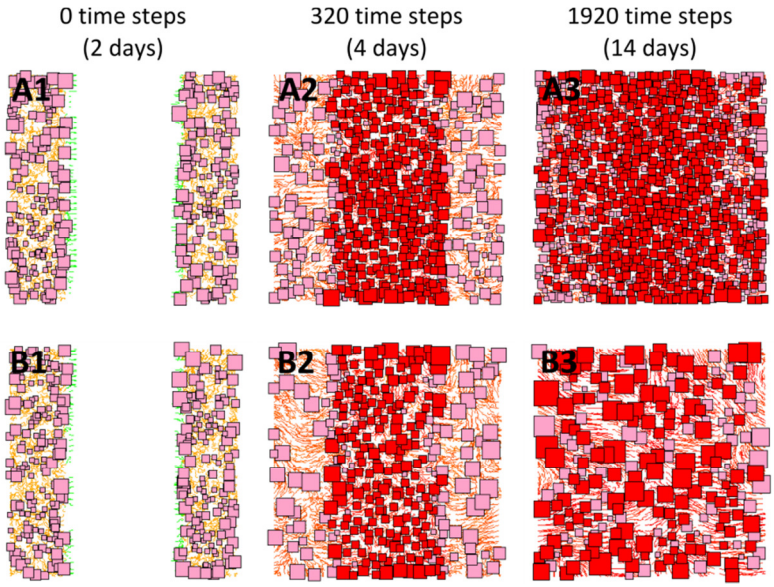

Figure 4-37 Impact of cell proliferation on simulation visualisation. Comparison of simulation visualisations for the cases with (A, first row) and without (B, second row) cell proliferation.

The impact of proliferation on key simulation components was further investigated. With proliferation activated, the total number of cells initially increased to reach a maximum ~1200 cells, before slowly decreasing due to cells undergoing apoptosis. The case with no proliferation followed a different profile such that the initial number of cells did not increase but decreased, at a relatively slower rate, due to cells undergoing apoptosis.

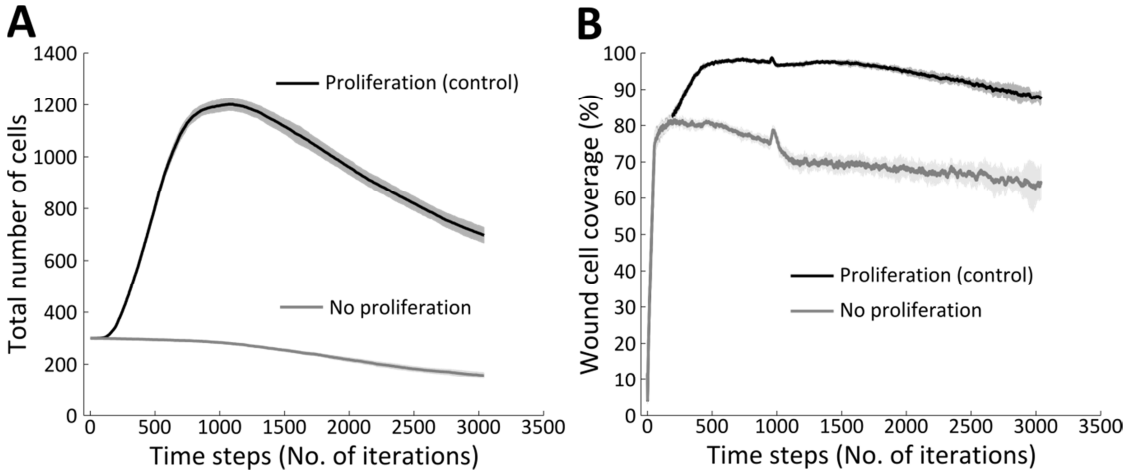

Figure 4-38 Impact of cell proliferation on the cell population size and wound closure rate. (A) Number of cells at a given time point, and (B) the fraction of wound effectively covered by cells. In both cases, the shaded areas represent the standard deviation for 11 simulations.

Proliferation also had a clear effect on the percentage of wound closure, i.e. the fraction of the wound occupied by cells, as calculated from their area of influence (Figure 4-38B). Whereas with proliferation the fraction of wound covered eventually reached 100%, when cell division was disabled a similar initial increase in coverage due to the rapid influx of cells was observed. However, after peaking at ~80%, the fraction of the wound covered by cells decreased as the simulation progressed. The population of resident cells was not maintained at a level that allowed complete closure of the wound when proliferation was omitted.

4.9.2.1.2 Minimum cell age requirement for division

The minimum age required for a cell to divide was estimated to be 24 hours based on the doubling time of cardiac fibroblasts *in-vitro* (Agocha et al., 1997). Changes in cell number and wound closure dynamics were investigated for minimum cell age requirements of 6, 12, 24 (model default) and 36 hours (Figure 4-39).

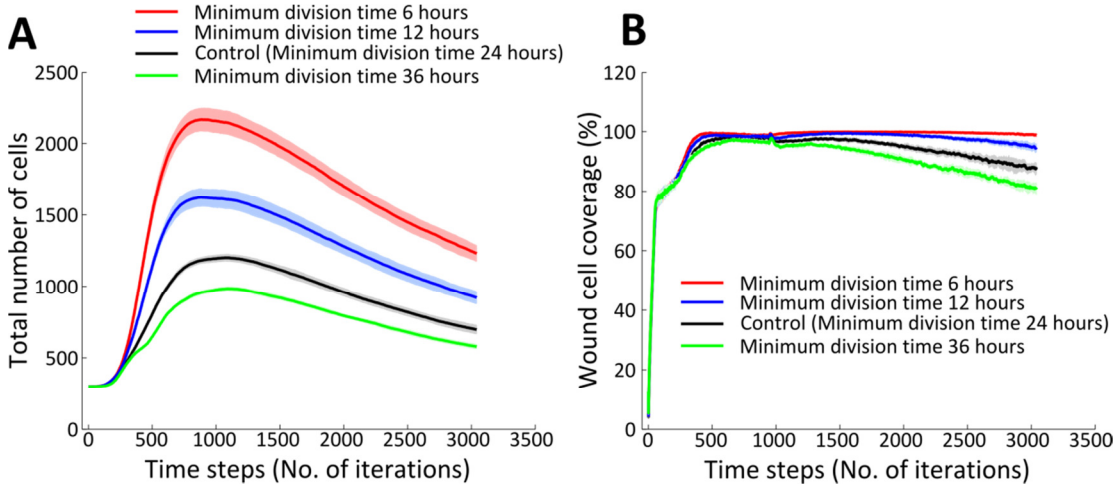

Figure 4-39 Impact of the minimum cell age requirement for division on simulation outcomes. (A) The number of cells and (B) the wound closure percentage. In both cases, the default value of 24 hours (black) was compared to 6 (red), 12 (blue) and 36 (green) hours. The standard deviation is represented by the shaded regions across 11 simulations.

The changes in cell number during the course of a simulation followed similar profiles for all minimum cell age values considered (Figure 4-39A). As previously discussed, the number of cells first increased, before decreasing later on when proliferation was overtaken by apoptosis. The peak number of cells, however, differed significantly for the various minimum cell age values, and was inversely proportional to the latter. In contrast, the percentage of wound closure was mostly similar until the later stage of the simulations where the different profiles obtained started diverging (Figure 4-39B). Indeed, end-point closure percentages were lower for higher minimum age values. Again, this was directly related to the number of cells necessary to ensure a full coverage of the wound, which was not maintained when proliferation was impeded by large minimum age threshold values. It is also important to note that the wound closure metric

was also a function of the distribution of the cells, which was likely impacted upon by changes in proliferation mechanisms.

4.9.2.1.3 Daughter cell behaviour after proliferation

The default method for the model with regards to placement and polarisation of daughter cells after division was to set the cells migrating in opposite directions (e.g. repulsion), starting at a distance of 3 µm. Alternatively, the daughter cells could be positioned at a distance of 10 µm after division instead, or lose polarity upon division, i.e. migration in random and uncorrelated directions (Dallon et al., 1999). The impact of those different assumptions on the model outcomes was evaluated based on the changes in local collagen alignment during simulations, as quantified by the number of collagen clusters (Figure 4-40). The results revealed little to no difference between the different approaches investigated.

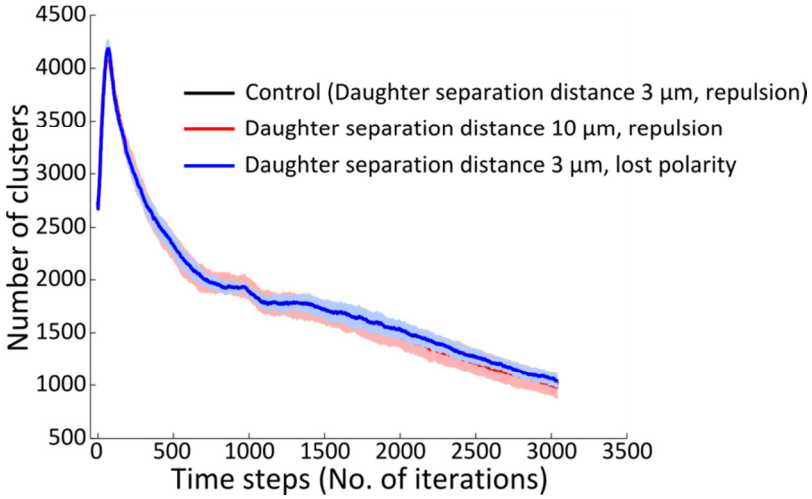

Figure 4-40 Impact of daughter cell behaviour implementation on local collagen alignment as quantified by the number of collagen clusters. Model default (repulsion at 3 µm distance, in black) was compared with repulsion at a distance of 10 µm (red), and loss of polarity (blue). The model default (black) is obscured by the case where the distance was set to 10 µm (red). The shaded areas represent the standard deviation across 11 simulations.

4.9.2.2 Cell migration speed

The fibroblast cell migration speed was based on multiple factors, including the chemotactic gradient, collagen density, and the neighbouring cells (section 4.4.3.2). The speed of a cell, in absence of the previously mentioned factors, was computed based on the baseline speed. The default value of 28 µm hr^{-1} was estimated from *in-vitro* experimental data (see Section 2.4.2). It was of interest to determine the sensitivity of model outcome to varying baseline speed value. The wound coverage by cells as well as the local collagen alignment were calculated during the course of simulations using fibroblast baseline cell speeds of 25 µm hr^{-1}, 28 µm hr^{-1} (default), 35 µm hr^{-1}, and 40 µm hr^{-1} (Figure 4-41). Changes in cell baseline had virtually no effect on wound coverage by cells (Figure 4-41A). End-point coverage figures were slightly higher for slower cells. The impact on collagen alignment was also mild but slightly more pronounced (Figure

4-41B). Slower cells appeared to result in slightly more aligned local collagen regions (i.e. lower number of clusters), when compared to higher baseline cell speeds.

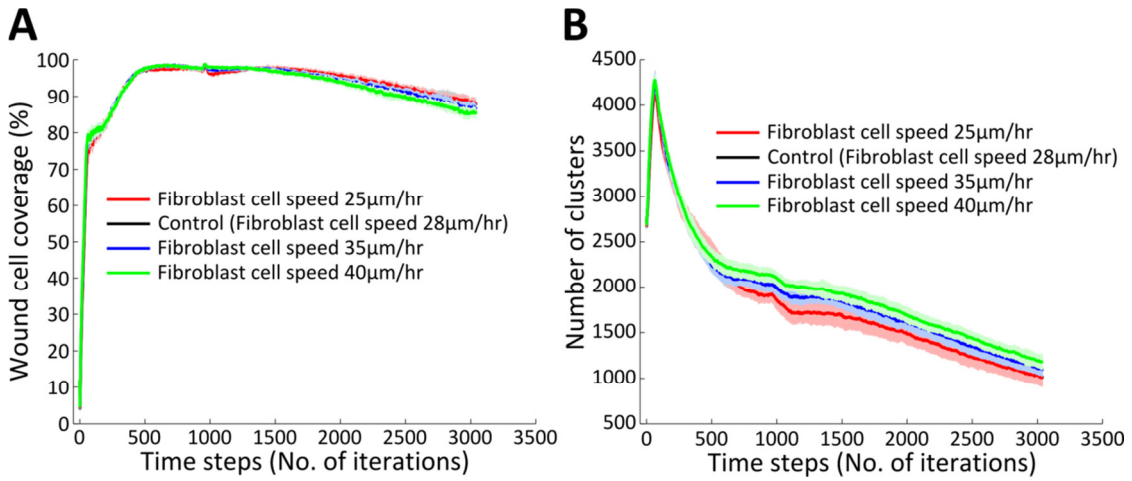

Figure 4-41 Impact on fibroblast cell migration baseline speed on simulation outcome. (A) Wound coverage by cells and (B) number of clusters. The different baseline speeds were 25 µm hr^{-1} (red), 28 µm hr^{-1} (the model default, black), 35 µm hr^{-1} (blue) and 40 µm hr^{-1} (green). The model default (black) is obscured by the fibroblast cell speed 25 µm hr^{-1} case (red). The shaded areas represented the standard deviation for 11 simulations.

These results highlighted the effects of altering the fibroblast baseline cell speed. It was also of interest to assess how varying the baseline speed of myofibroblasts would impact the simulation outcome, especially in the wounded area. In addition to the model's default value of 25 µm hr^{-1}, baseline myofibroblast cell speed of 20 µm hr^{-1} and 30 µm hr^{-1} were considered (Figure 4-42). In all cases, varying the baseline speed of myofibroblast cells did not greatly impact the outputs considered. It is important to note that these simulation experiments only varied the baseline cell speed of the cells. The actual migration speed was, as mentioned above, altered by a number of other factors (i.e. avoidance, effect of chemotactic gradient, and influence of collagen density) that were kept constant in these examples.

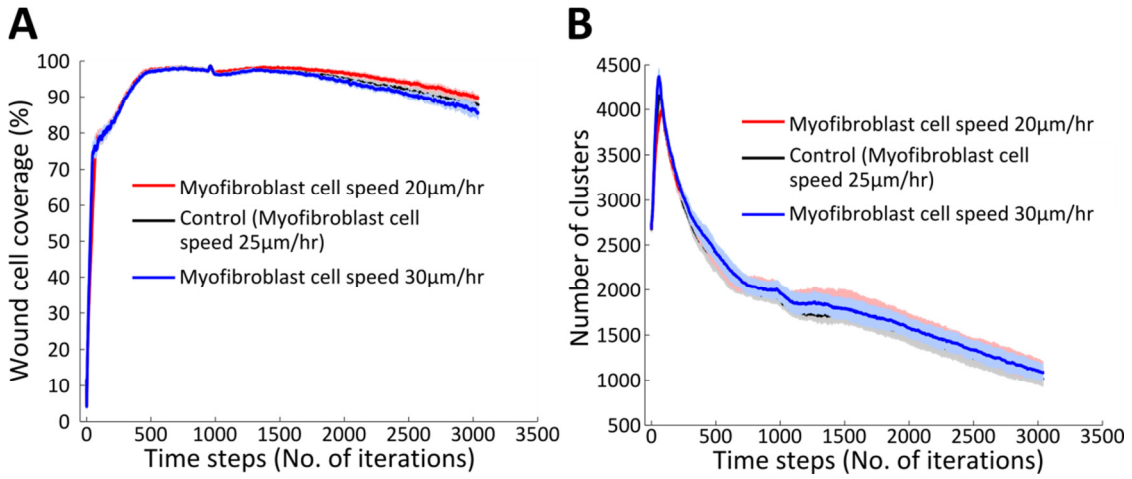

Figure 4-42 Impact of myofibroblast baseline cell speed on simulation outcome. (A) Wound coverage by cells and (B) number of clusters. The baseline speeds considered were 20 µm hr^{-1} (red), 25 µm hr^{-1} (model default, in black), and 30 µm hr^{-1} (red). The shaded areas represent the standard deviation of 11 simulations.

4.9.2.3 Cell polarity during migration

The polarisation parameter was used to define to what degree the migration direction of a cell was influenced by its previous direction and by the collagen matrix (section 4.4.3.1). For instance, a value of 0 for the polarisation meant that previous motion did not influence the direction of migration but instead the direction was only determined by the collagen matrix orientation (in addition to other factors such as the chemotactic gradient and the presence of neighbouring cells). At the other extreme, a polarisation parameter value of 1 signified that the cells ignored the collagen matrix when deciding which direction to migrate towards. The default value for the polarisation parameter in the model was set to 0.66 based on experimental data (Dickinson et al., 1994; Rouillard and Holmes, 2012). It was of interest to determine whether other values for the parameter would significantly impact simulation outputs. Therefore, simulations were run using 0, 0.3, 0.66 (model default), and 1 as values for the polarisation parameter (Figure 4-43).

When considering the density of collagen in the wounded region, all values resulted in similar profiles, at the exception of 0, which caused a decrease in the accumulation rate of collagen in the wounded region (Figure 4-43A). A more striking result was observed when comparing the average number of clusters in the whole tissue for the different values tested (Figure 4-43B). In most cases, the number of clusters peaked rapidly (due to initial production of collagen in the wounded region), before decreasing continuously thereafter. However, for a polarisation parameter value of 1, the number of clusters remained relatively constant following the initial peak, thus the collagen remained mostly unaligned. In this edge case scenario, cell migration was not influenced by the collagen matrix. The results showed that matrix-induced polarisation was necessary to achieve high collagen alignment. End-point number of clusters was the lowest for polarisation values of 0 and 0.3, while a value of 0.66 (the model default value) resulted in a slightly higher number of clusters.

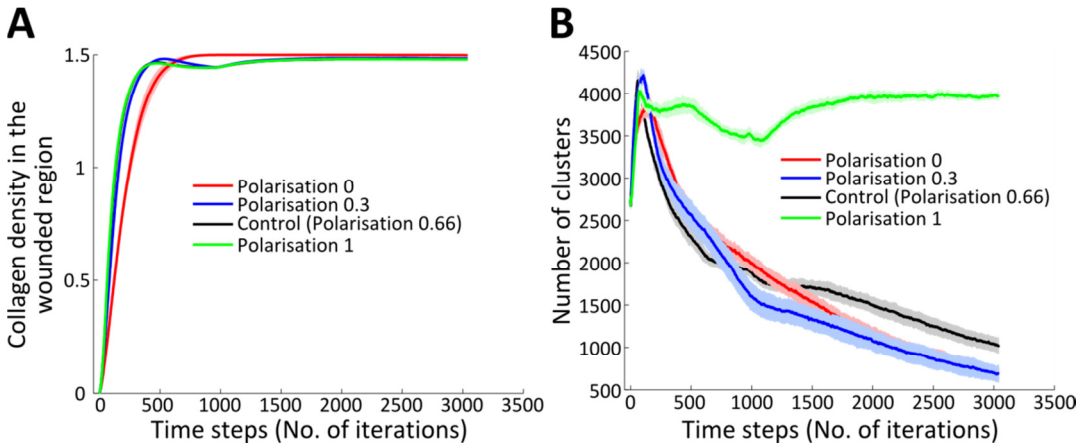

Figure 4-43 Impact of polarisation parameter values on simulation outputs. (A) Collagen density in the wound region, and (B) number of collagen clusters. The values considered for the polarisation parameter were 0 (red), 0.3 (blue), 0.66 (model default, black) and 1 (green). The shaded areas represent the standard deviation for 11 simulations.

4.9.2.4 Cell avoidance

Cell avoidance was implemented in the model to reproduce contact inhibition of locomotion (section 4.4.3.2). The avoidance mechanism was determined by a minimum distance threshold parameter, which defined the distance within which a neighbouring cell would be considered an obstacle to migration. In other words, it represented how far the cell was able to sense its environment.

First, the impact on collagen matrix density and alignment was evaluated for simulations with and without the avoidance mechanism enabled (Figure 4-44). The profiles obtained for the collagen density in the wounded region were nearly identical, showing the avoidance did not impact upon this component of the model (Figure 4-44A). In the case of the number of clusters, there was a clear difference between the cases with and without avoidance (Figure 4-44B). After an initial increase in the number of clusters (due to the deposition of collagen in the wounded region by the migrating cells), a slow decrease was observed in the normal case with avoidance, indicating that the collagen was steadily being aligned. In contrast for the case without avoidance, the number of clusters reduced rapidly, to a value close to zero, indicating that most of the collagen was, at least at a local level, perfectly aligned. Without avoidance, the cells were free to move over each other, and thus could continue migrating in their initial direction, according to the chemotactic gradient.

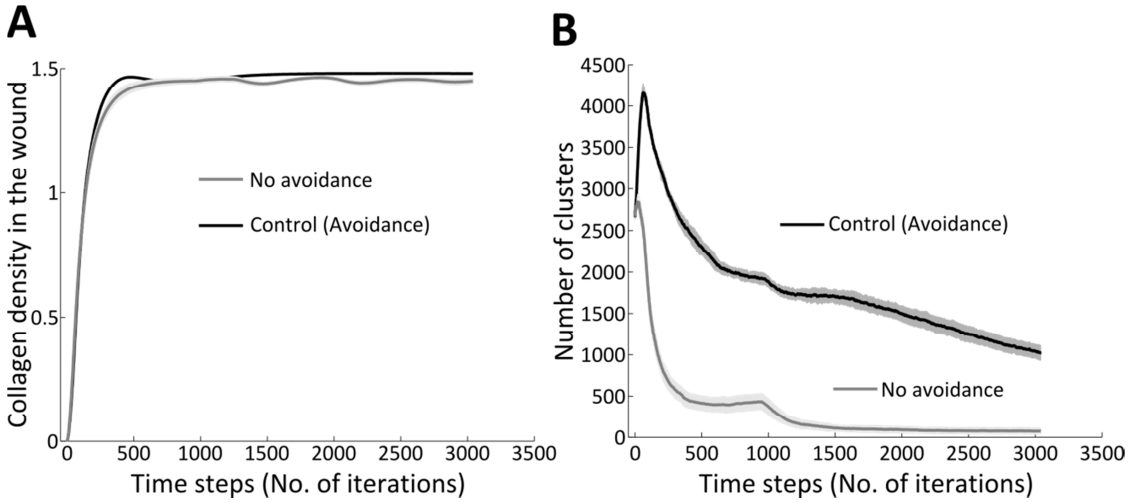

Figure 4-44 Impact of cell avoidance on simulation outcome. (A) Collagen density in the wounded region, and (B) number of clusters. Shaded areas represent the standard deviation for 11 simulations.

The difference in local collagen matrix alignment was further investigated by generating model visualisations for the cases with and without avoidance enabled at 0, 320, and 3040 time steps (Figure 4-45). The difference in alignment could be clearly observed, as early as 320 steps into the simulation. By 3040 steps, the collagen matrix was almost perfectly aligned at a local level.

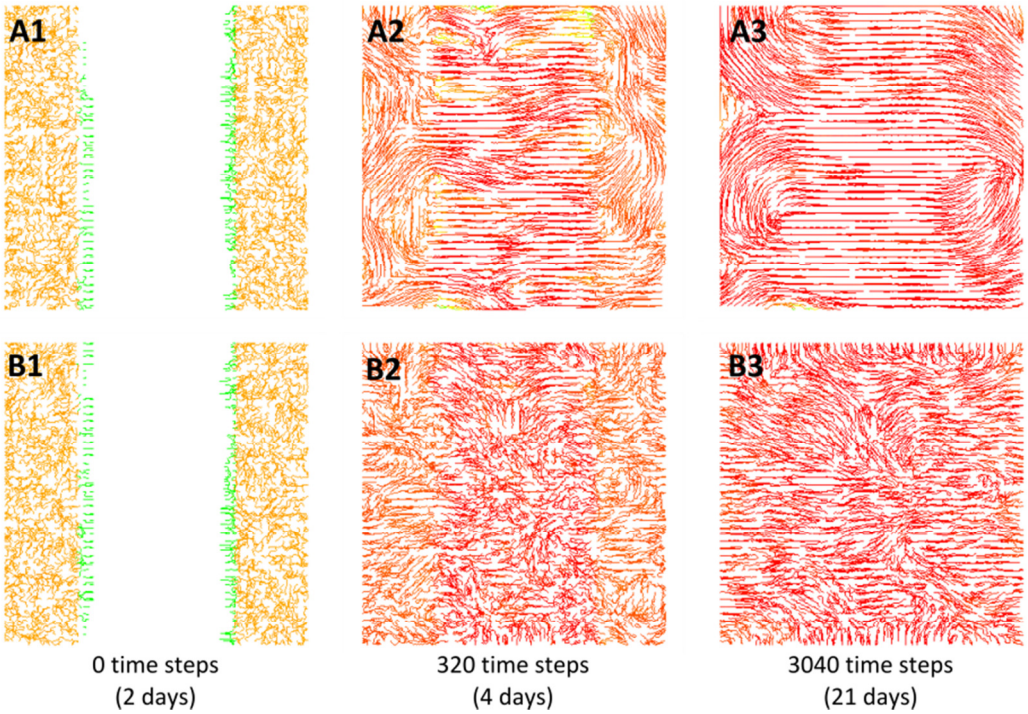

Figure 4-45 Simulation visualisations of the collagen matrix with and without cell avoidance. The first row (A1-A3) shows a simulation with the avoidance algorithm disabled, while it was enabled for the simulation shown in the second row (B1-B3). The collagen matrix ranges from a low density (green) to a high density (red).

The threshold distance, which defined the extent of the region considered by the avoidance algorithm, had a default value of 40 µm in the model, as based on *in-vitro* results (section 2.4.2). The sensitivity of the model with regards to this parameter was evaluated by running simulations with the threshold distance set to 20 µm and 60 µm, in addition to the default value of 40 µm (Figure 4-46). The smaller threshold parameter (20 µm), resulted in a cluster number profile resembling that obtained without avoidance. The collagen alignment was reduced as the parameter value was increased. This was explained by the fact that the cells tended to change direction erratically, as they sensed other cells over a longer distance. Adjusting the threshold distance appeared to have a large impact on the local alignment of the collagen matrix. This result indicated the importance of obtaining an accurate value for the avoidance threshold distance.

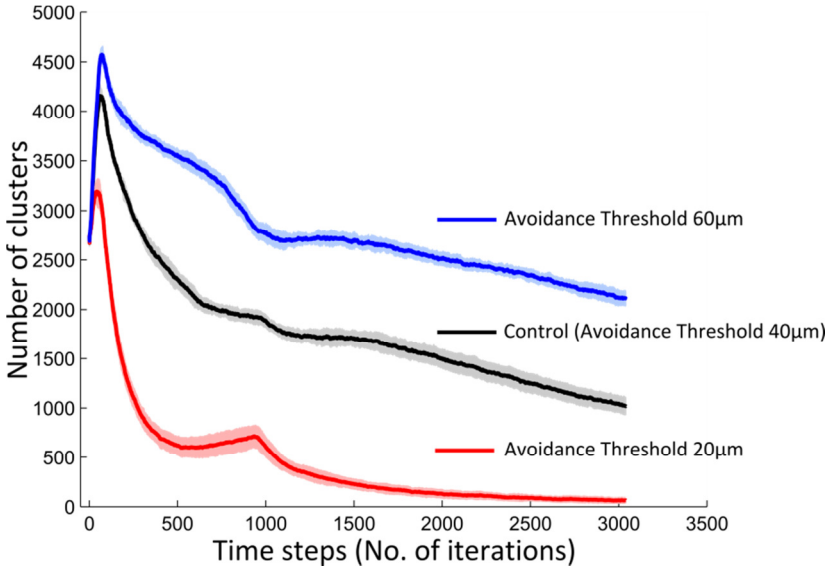

Figure 4-46 Sensitivity of the collagen alignment (as quantified by the number of collagen clusters) to the value of the distance threshold parameter. The different values considered were 20 µm (red), 40 µm (model default value, black) and 60 µm (blue). The shaded area indicated the standard deviation for 11 simulations.

4.9.2.5 Cell shape of influence

The cell shape defined the area of influence of a cell, which in turn dictated how the cells interacted with the local collagen matrix. The dimensions of the region of influence were derived from experimental results (sections 4.4.3.6). By default, the current model used a square representation, orientated along the dominant axis of migration. The level of influence was maximal along the leading edge of the square, and decreased linearly with distance from the leading edge. This representation was termed a wedge shape.

Alternative representations of cells are also possible, and should be investigated. Indeed, *in-vitro* experiments showed that the shape of migrating cells was highly variable, as in the cell would continuously morph between a set of shapes. The previously described dermal wound healing model used a square-based pyramid, with the centre of the base as the point of maximum influence and the edges as the minima (Dallon et al., 1999). Other possible representations include shapes with circular or semi-circular base areas. For comparison purposes, the radius of the cell was set to ensure the surface area was constant in all cases considered.

The different representations are described below before their assessment in simulations.

4.9.2.5.1 Alternative shape representations

Simulations with the influence area of cells modelled as a square based pyramid was compared with the default wedge-shaped region of influence. The areas and volumes of both shapes have been kept constant by scaling the maximum level of influence. For the square based pyramid shape, the influence within the region was weighted depending on the distance from the centre

of the cell. Influence was maximum at the centre of the cell (value of 0.6), and decreased linearly to reach zero at the edges of the square base, as shown in equation 4.34, where ***w(x,t)*** was the weights at position ***x*** and time step *t*, *R* was the distance from the centre of cell to the edges, and a_1 and a_2 were computed as shown in equation 4.35. In this last equation, *j* was the direction considered (i.e. 1 for x, 2 for y), ***f*** the position of the cell, and ***x*** the position on the grid.

$$w_i(\boldsymbol{x},t) = \frac{0.6a_1a_2}{R^2} \qquad 4.34$$

$$a_j = max\left\{R - \left|f_j^i(t) - x_j\right|, 0\right\} \qquad 4.35$$

An illustration of a square-based pyramid region of influence, with *R* equal to 40 µm and centred at the origin, is shown in Figure 4-47.

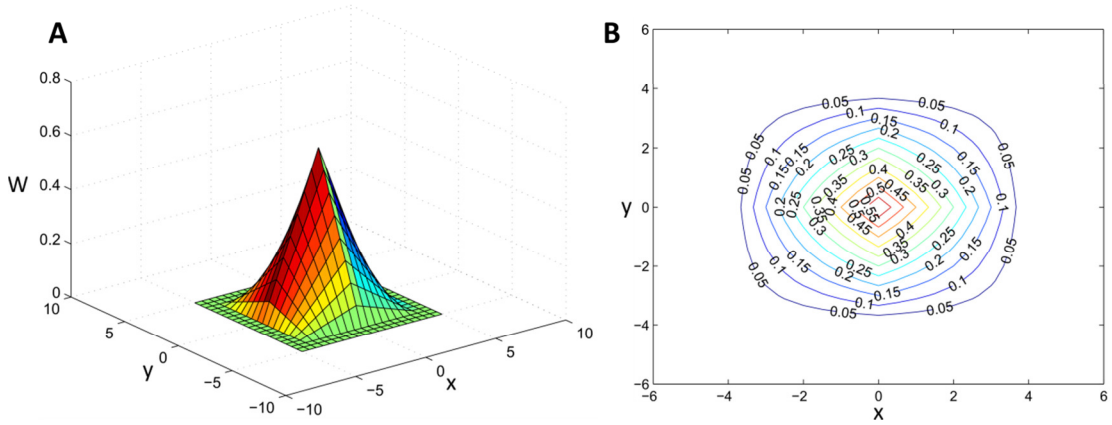

Figure 4-47 Illustration of a square-based pyramid cell representation. The shape is positioned at the origin and the distance from its centre to the edges (R) was 40 µm (equivalent to 4 grid points). (A) 3D shaded surface plot, with the z-axis representing the weights. (B) Contour plot of the weights at different position on the x-y plane. The numbers show the weighting value of the corresponding contour.

A conical cell representation was also investigated. The area of influence was defined by a circular base. The weighting was maximal at the centre of the base, and decreased linearly until it reached zero at the perimeter of the base. The weights were defined as shown in equation 4.36 , where *w(**x**,t)* was the weights at position ***x*** and time step *t*, *R* was the radius of the circular base, and *a* was computed as shown in equation 4.37. In the latter equation, *f* was the position of the cell.

$$w_i(\boldsymbol{x},t) = \frac{0.6a^2}{R^2} \qquad 4.36$$

$$a = max\left\{R - \left\|f^i(t) - \boldsymbol{x}\right\|, 0\right\} \qquad 4.37$$

The shape of the area of influence for the cone-shaped representation is shown in Figure 4-48.

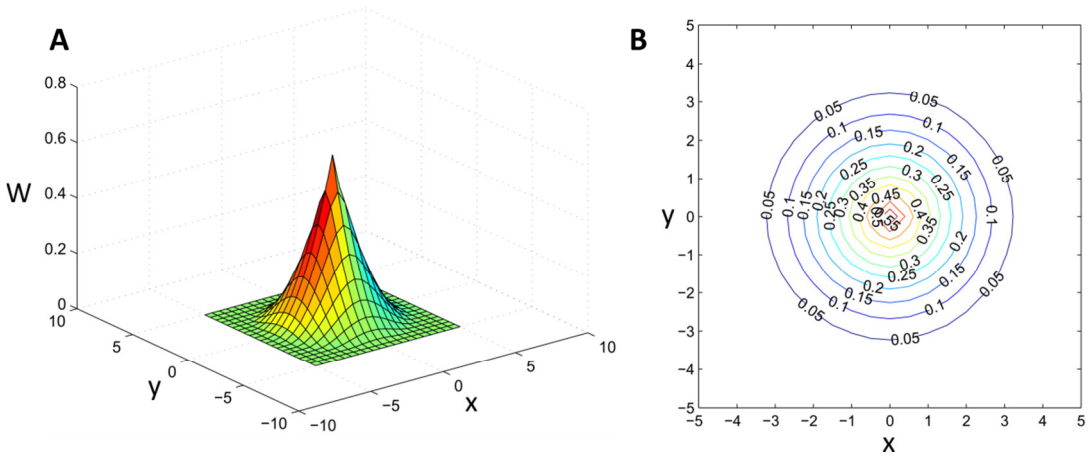

Figure 4-48 Illustration of a conical cell representation. The cell had a radius of 45 µm (equivalent to 4.5 grid points) and was centred at the origin. (A) 3D shaded surface plot, with the z-axis representing the weights. (B) Contour plot of the weights at different position on the x-y plane. The numbers show the weighting value of the corresponding contour.

The conical representation could be altered into one with a semi-circular base. The radius and semi-circle were adjusted accordingly to maintain a constant area, and was computed as shown in equation 4.38, where ***w(x,t)*** was the weights at position ***x*** and time step *t*, *R* was the radius of the circular base, and *a* was calculated as shown in equation 4.39. In the latter equation, ***f*** was the position of the cells, θ was the angular difference between the velocity vector of the cell and a vector positioned at the centre of the cell, and pointing towards the position ***x***. For a given position ***x***, the cell thus had an influence if θ was less than or equal to $\pi/2$ radians and ***x*** was within the area of the semi-circle.

$$w_i(\boldsymbol{x},t) = \frac{0.6a^2}{R^2} \tag{4.38}$$

$$a = f(x) = \begin{cases} max\left\{R - \left\|f^i(t) - \boldsymbol{x}\right\|, 0\right\}, & \theta \le \pi/2 \\ 0, & otherwise \end{cases} \tag{4.39}$$

A graphical representation of this shape is shown in Figure 4-49.

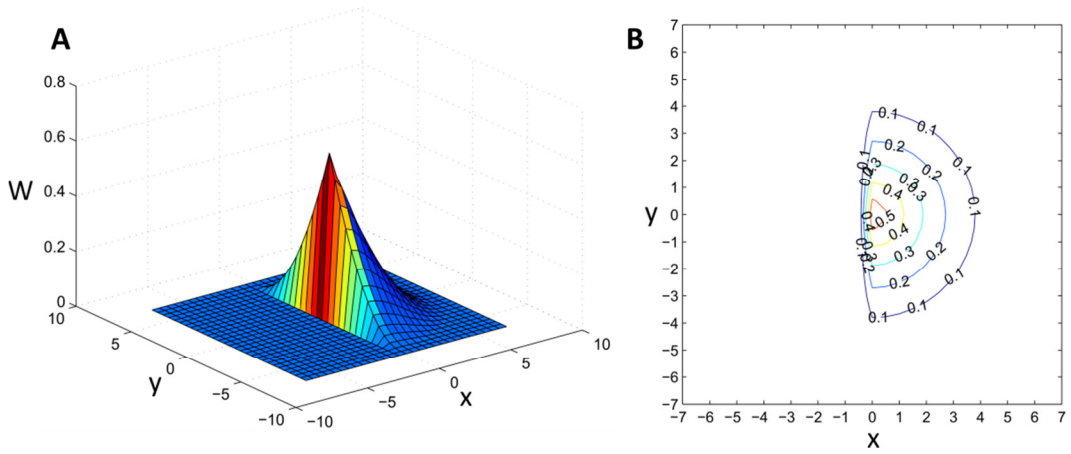

Figure 4-49 Illustration of a semi-circular base cone cell representation. The cell had a radius of 64 µm (equivalent to 6.4 grid points) and was centred at the origin. (A) 3D shaded surface plot, with the z-axis representing the weights. (B) Contour plot of the weights at different position on the x-y plane. The numbers show the weighting value of the corresponding contour.

All these representations, with the exception of the model default wedge shape, assumed that the influence maximum would be at the centre of the cell. Another cell representation was generated by taking the square base pyramid and effectively inverting it. In other words, the maximum influence was found at the edges of the shape, and decreased linearly to reach zero at the centre of the cell. Biologically, this could be related to cell borders and eventual protrusions (e.g. pseudopodia) exerting most of the force on the collagen matrix. The weights were computed as shown in equation 4.40, where $\boldsymbol{w(x,t)}$ was the weights at position $\boldsymbol{x}$ and time step t, R was distance between the centre of the cell and its edges, B was a scaling factor in order to maintain consistency between the different cell shapes considered (set to 0.5) and a was calculated as shown in equation 4.41. In the latter equation, j denoted the direction considered (e.g. 1 for x, 2 for y), and f was the position of the cell.

$$w_i(\boldsymbol{x},t)=\begin{cases}0.6\mathrm{B}\left(1-\left(a_1a_2/R^2\right)\right), & \left|f_j^i(t)-x_j\right|\le R\\ 0, & \left|f_j^i(t)-x_j\right|>R\end{cases} \qquad 4.40$$

$$a_i=max\left\{R-\left|f_j^i(t)-x_j\right|,0\right\} \qquad 4.41$$

An example of such a representation is shown in Figure 4-50.

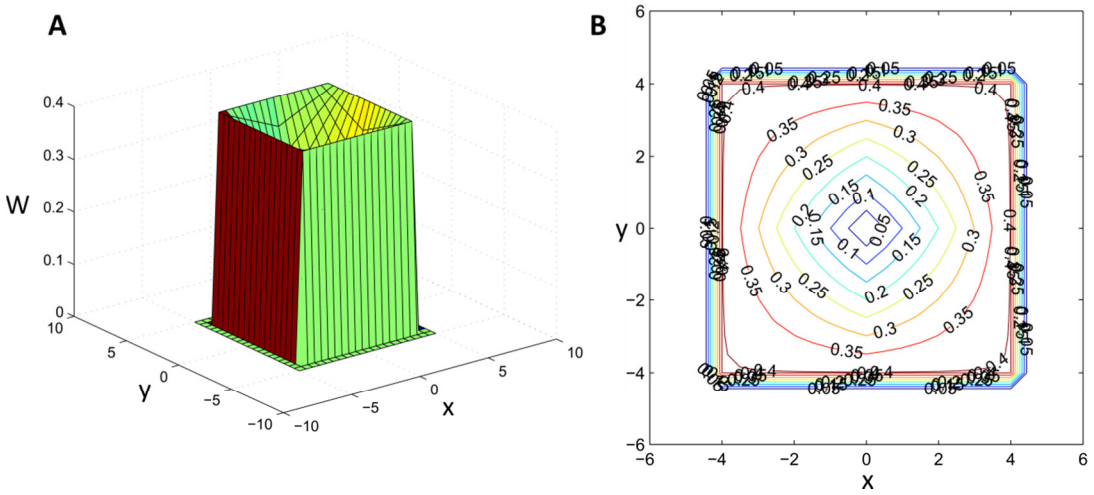

Figure 4-50 Illustration of an inverted square pyramid cell representation. The cell was centred at the origin. (A) 3D shaded surface plot, with the z-axis representing the weights. (B) Contour plot of the weights at different position on the x-y plane. The numbers show the weighting value of the corresponding contour.

4.9.2.5.2 Impact of the cell representation on simulation outcomes

Four alternative cell representations were discussed (regular and inverted square base pyramid, cone, and semi-circular base cone). Each was implemented in the model so their impact on a simulation could be assessed based on overall collagen density and alignment, as quantified using the number of clusters (Figure 4-51). Representations could be grouped into two broad categories according to their impact on the collagen density throughout a simulation (Figure 4-51A). The wedge (model default), inverted square base pyramid, and conical representations had nearly identical profiles and performed as previously observed. The other category included square base pyramids as well as semi-circle base cones, which had lower initial rates of increasing collagen density when compared to the other representations, though the semi-circle based cone reached comparatively higher collagen densities.

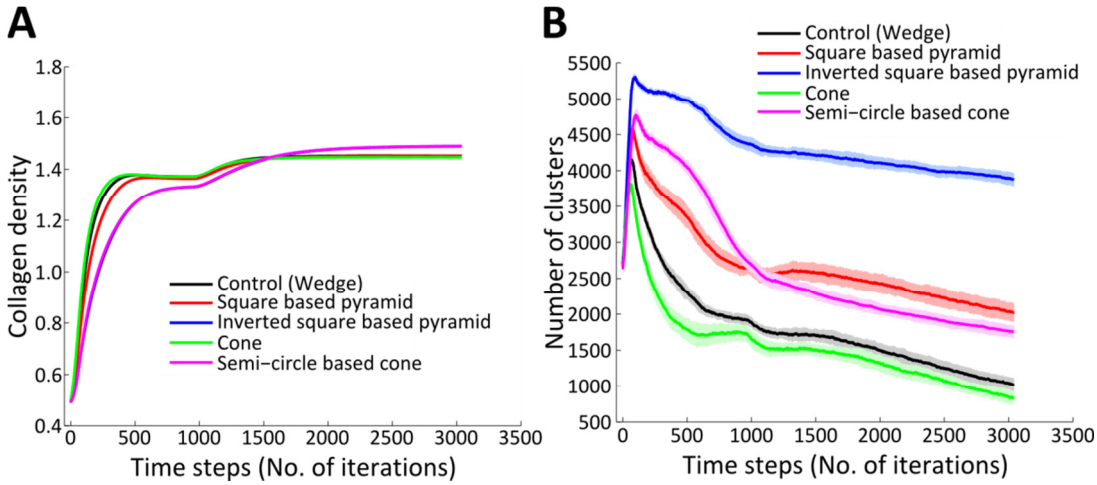

Figure 4-51 Impact of cell area of influence representations on collagen matrix properties. (A) Collagen density and (B) number of clusters across the entire tissue. The shapes considered were wedges (model default, black), square based pyramids (red), inverted square based pyramids (blue), cones (green), and semi-circle based cones (pink). The shaded areas represent the standard deviation for 11 simulations.

Variation in the representation of cell shape had a significant effect on the collagen alignment (Figure 4-51B). The conical and wedge representations both resulted in high collagen alignment (i.e. low number of clusters). Slightly higher numbers of clusters were obtained for both semi-circular based cones and square based pyramids. The clear outlier was the inverted square based pyramid, which resulted in a very low degree of alignment of collagen fibres.

4.9.2.6 The ability of the cells to reorient the collagen matrix

The ability of the cell to reorient the collagen matrix was controlled by the parameter κ. Its value was determined using a Hill function, which had a maximum value of κ_{max} for low collagen densities and a value tending to zero as the density approach 1.5 (see section 4.4.3.7). By default, the value of κ_{max} was set to 5. However, it was of interest to assess the sensitivity of the model to varying values for κ_{max}. The impact of κ_{max} values of 1, 3, 5 (the model default), and 10 on the collagen alignment were evaluated (Figure 4-52). Intermediate values of 3 and 5 had similar profiles, resulting in a high degree of alignment at the end of the simulations (i.e. low number of clusters). For a κ_{max} value of 10, the end-point number of clusters was slightly greater than that obtained for the two intermediate values. In contrast, a value of 1 resulted in a drastically different profile, with a very high number of clusters remaining at the end of the simulation, which hinted at a low degree of local collagen alignment. The model was thus very sensitive for low values of κ_{max}.

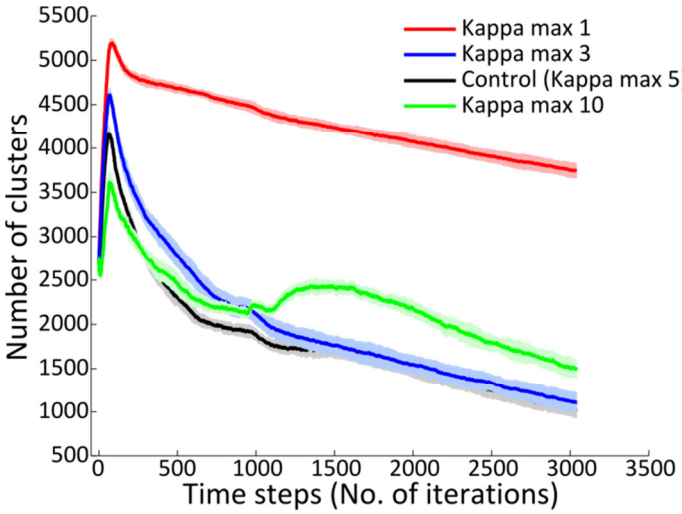

Figure 4-52 Impact of changes in parameter κ_{max} (ability of the cells to re-orient collagen fibres) on the collagen matrix alignment. Number of clusters obtained for κ_{max} values of 1 (red), 3 (blue), 5 (model default, 5), and 10 (green). The shaded area represents the standard deviation for 11 simulations.

In addition to evaluating the sensitivity of the model to changes in parameter values related to collagen matrix re-orientation by migrating cells, an alternative method previously described in a study of 3-dimensional (3D) migration of mesenchymal cells (Groh and Wagner, 2011) was introduced. In this later study, re-orientation of the collagen matrix was based on the two cells with the highest weights at the location considered. This is shown in equation 4.42, where $\bar{V}$

was the weighted cumulative velocity vector equivalent to the total cell influence $W(\boldsymbol{x},t)$, ω(0) the mean orientation of the collagen matrix, $V^{(1)}$ and $V^{(2)}$ were the velocity vectors of the two most influencing cells at the grid point, and S_v was computed as shown in equation 4.43. In the latter equation, w_1 and w_2 corresponded to the weights of the two most influencing cells at the grid point.

$$\bar{V}\left(t,x,\omega(0),S_v\left(\tilde{V}_{t-\tau}^{(i_1)},\tilde{V}_{t-\tau}^{(i_2)}\right)\right)=sgn\left(\left\langle\omega(0),S_v\left(\tilde{V}_{t-\tau}^{(i_1)},\tilde{V}_{t-\tau}^{(i_2)}\right)\right\rangle\right)\times S_v\left(\tilde{V}_{t-\tau}^{(i_1)},\tilde{V}_{t-\tau}^{(i_2)}\right) \quad 4.42$$

$$\boldsymbol{S}_v\left(\boldsymbol{V}^{(1)},\boldsymbol{V}^{(2)}\right)=w_1\boldsymbol{V}^{(1)}+sgn\left(\left\langle\boldsymbol{V}^{(1)},\boldsymbol{V}^{(2)}\right\rangle\right)w_2\boldsymbol{V}^{(2)} \quad 4.43$$

When compared with the method used in this model, this alternative approach resulted in better aligned collagen (i.e. lower number of clusters) throughout the simulation (Figure 4-53).

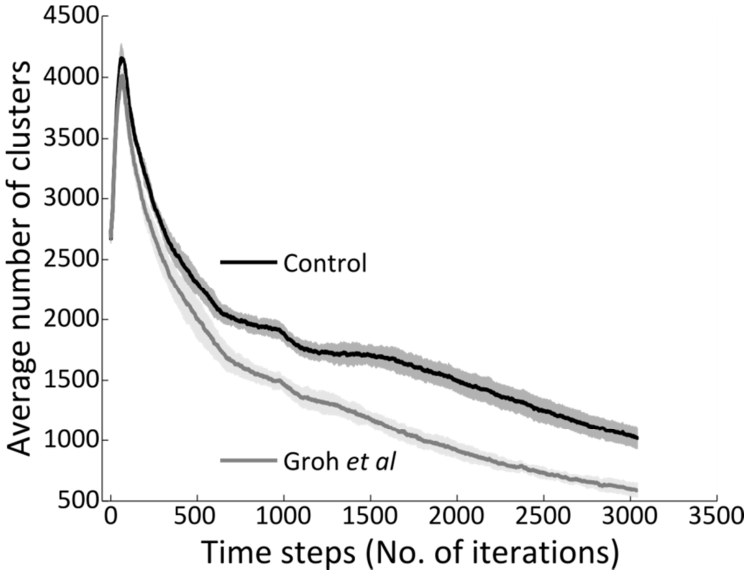

Figure 4-53 Alternative approach to the modelling of matrix re-orientation by migrating cells. The default case was compared to the method described in (Groh and Wagner, 2011). The shaded areas represent the standard deviation for 11 simulations.

4.9.2.7 Cell differentiation

The differentiation of fibroblast cells into myofibroblasts is a key event underpinning cardiac wound healing. In this model, the differentiation rate was based on a probability function, which was derived from *in-vitro* experimental data (see section 2.4.4). The impact of myofibroblast cells on the model simulation was evaluated by running simulations without differentiation, with the collagen density in the wounded region as the main metric of interest (Figure 4-54). In both cases, the collagen density first quickly increased as cells migrating into the wound started deposing collagen, before reaching a plateau. The maximum density values reached were ~1.3 and ~1.5 for the simulations without and with differentiation, respectively. These numbers corresponded to the collagen production to degradation ratio for each cell type (1.3 and 1.5 for

fibroblast and myofibroblast, respectively). A density of 1.5 would thus never be reached without the ability of the cells to differentiate into myofibroblasts.

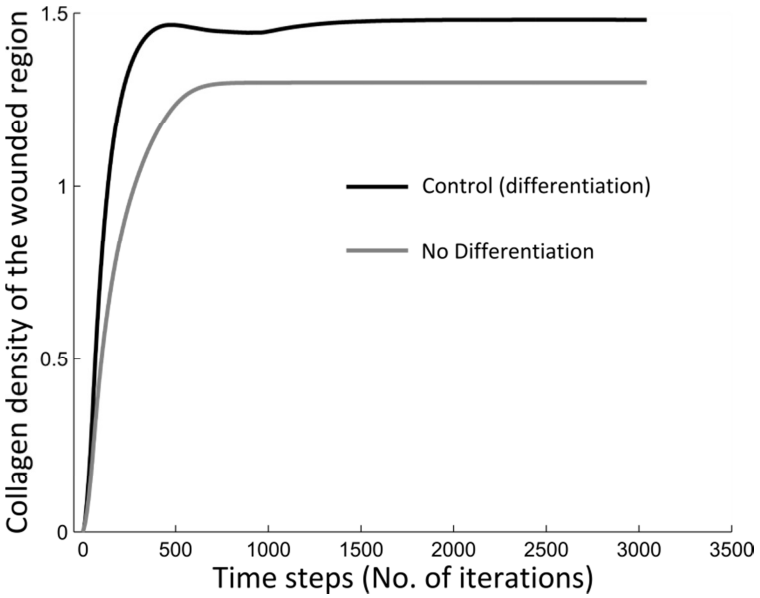

Figure 4-54 Impact of the differentiation of fibroblasts into myofibroblasts on the collagen density in the wounded region. Shaded areas represented the standard deviation for 11 simulations.

4.9.3 Interpolation functions

The collagen matrix was modelled as a continuous vector field and sampled at uniformly spaced grid points, therefore, it was necessary to employ an interpolation method to determine the local collagen properties at any given location. This had a direct impact on cell migration which was in part influenced by the properties of the local collagen matrix (section 4.4.3.1). The interpolation method not only affected how the cells migrated, it also impacted upon the model visualisation, based on the tracing of cells (section 4.5.1).

The default interpolation function adopted was a quartic lagrangian approach (equations 4.7 and 4.8). However, it was of interest to determine the impact on the simulation outcome when using alternative interpolation methods, described below prior to being compared across simulation outputs.

4.9.3.1 Alternative interpolation methods

The bilinear interpolation method used the four grid points that surrounded the location to be interpolated. The value of the collagen matrix at location *(x,y)* was computed as shown in equation 4.44, where $\boldsymbol{c}(x_1, y_1)$ was the collagen matrix at the bottom left grid point, $\boldsymbol{c}(x_1, y_2)$ at the top left grid point, $\boldsymbol{c}(x_2, y_2)$ at the top right grid point, and $\boldsymbol{c}(x_2, y_1)$ at the bottom right grid point.

$$\begin{aligned}\boldsymbol{I}(\overline{\boldsymbol{c}}, x, y) = {} & \overline{\boldsymbol{c}}(x_1, y_1)(x_2 - x)(y_2 - y) + \overline{\boldsymbol{c}}(x_2, y_1)(x - x_1)(y_2 - y) \\ & + \overline{\boldsymbol{c}}(x_1, y_2)(x_2 - x)(y - y_1) + \overline{\boldsymbol{c}}(x_2, y_2)(x - x_1)(y - y_1)\end{aligned} \quad 4.44$$

Alternatively, the inverse distance weighting interpolation method used 4×4 grid points around the location to be interpolated. The influence of a grid point was inversely proportional to its distance from the location to be interpolated. Thus, the collagen matrix at location *(x,y)* could be computed as shown in equation 4.45, where $\lfloor (x_i, y_j) \rfloor$ were the coordinates of the closest grid point (rounded down to the nearest integer), and $w(x_{i+n},y_{j+m})$ the weight of the grid point located at (x_{i+n},y_{j+m}) as calculated in equation 4.46.

$$\boldsymbol{I}\left(\bar{\boldsymbol{c}}, x, y\right) = \frac{\sum_{n=-1}^{2}\sum_{m=-1}^{2}\left(\boldsymbol{w}\left(x_{i+n}, y_{j+m}\right)\bar{\boldsymbol{c}}\left(x_{i+n}, y_{j+m}\right)\right)}{\sum_{i=-1}^{2}\sum_{j=-1}^{2}\boldsymbol{w}\left(x_{i+n}, y_{j+m}\right)} \tag{4.45}$$

$$\boldsymbol{w}\left(x_{i+n}, y_{j+m}\right) = \frac{1}{\left\|\left(x_{i+n}, y_{j+m}\right) - \left(x, y\right)\right\|} \tag{4.46}$$

4.9.3.2 Effect of the interpolation method used on simulation outcome

The three interpolation methods (Quartic Lagrangian, the model default, as well as bilinear and inverse distance weighting) were compared based on the local alignment of collagen, as measured using the number of clusters. The latter was chosen to illustrate the differences between the interpolation methods because it was likely to be affected by the resulting changes in cell migration behaviours. It is important to note the number of clusters was a metric that was independent of the interpolation method chosen.

Bilinear and inverse distance weighting produced very similar profiles, and both resulted in slightly more alignment (i.e. lower number of clusters) when compared to the quartic Lagrangian (see Figure 4-55). To further illustrate the difference between the different values, model visualisations only containing the collagen matrix were generated for all three cases (Figure 4-56).

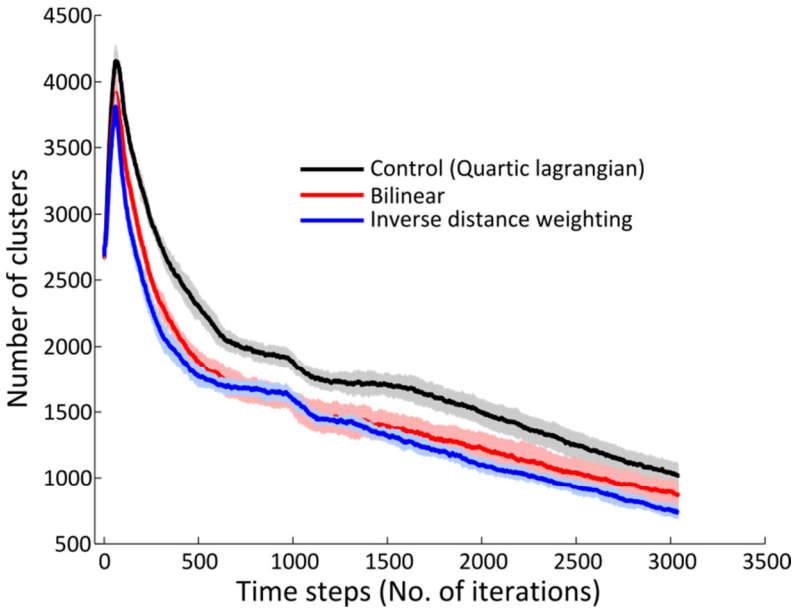

Figure 4-55 Effect of the interpolation method on collagen alignment. Three methods were compared: quartic lagrangian (model default, black), bilinear (red), and inverse distance weighting (blue). The shaded area represents the standard deviation for 11 simulations.

Visualisations for both bilinear and inverse distance weighting interpolation methods were again very similar, especially at intermediate and late simulation stages (320 and 3040 simulation time steps, respectively). When using the default function (quartic Lagrangian), the visualisation was not as smooth, due to the consideration of a much larger area during interpolation.

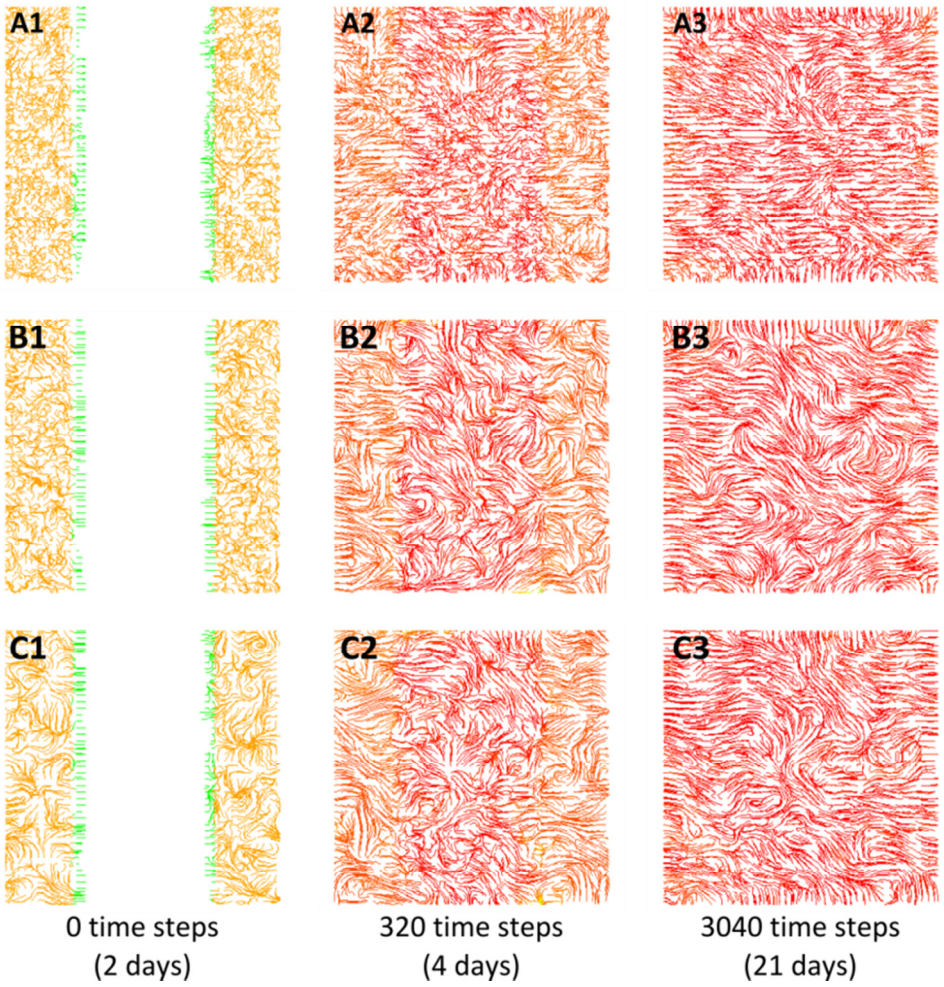

Figure 4-56 Impact of the interpolation method on collagen matrix visualisation. Each row corresponds to an interpolation method: (A) quartic Lagrangian, (B) bilinear, and (C) inverse distance weighting. The columns correspond to three different simulation steps: 0 (A1-C1), 320 (A2-C2), and 3040 (A3-C3).

4.9.4 The model visualisation

Visual fibroblast cells were used in the model to create a visualisation of the collagen matrix at each time step. These cells did not have access to any of the fibroblast or myofibroblast functions (e.g. production and degradation of collagen). They only had one capability which is to migrate based on the orientation of neighbouring collagen fibres. The collagen matrix was visualised by tracking cell migration. For each image created at a specified time point within the simulation, the visual fibroblast cells had their position updated 15 times (Figure 4-57A). Reducing the number of position updates reduced the clarity of the collagen matrix alignment and density (Figure 4-57B). Whereas if the number of position updates was increased the collagen matrix was too detailed making it difficult to infer information about the matrix (Figure 4-57C). The model default value was set to 15 time steps to provide an appropriate time course for visualising the collagen matrix.

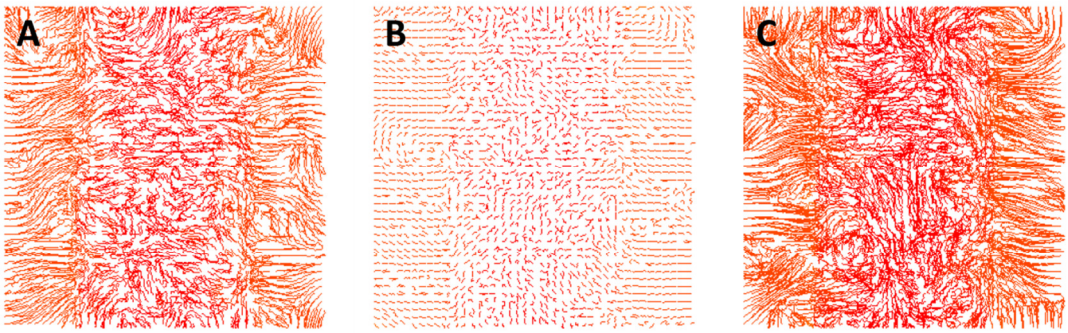

Figure 4-57 Model simulation output images of the collagen matrix at 800 time steps for (A) 15 (model default), (B) 5 and (C) 25 visual iterations.

4.9.5 Chemotactic gradient

The chemotactic gradient was implemented in the model to represent the inflammatory response typically observed post-MI, whereby fibroblast cells are attracted into the wound by diffusing inflammatory signals. The chemoattractant was active for the first 150 hours (equivalent to 1000 time steps) of the model simulations. The impact of the chemoattractant on the dynamics of the simulation was illustrated by generating visualisations of the model with, and without the gradient enabled (Figure 4-58). As one could expect, without a chemotactic gradient the cells were not directed towards the wound, resulting in a much slower infiltration of the cells. Indeed, the cells were then allowed to freely migrate in any direction, only constrained by the avoidance algorithm, collagen matrix orientation and their previous direction.

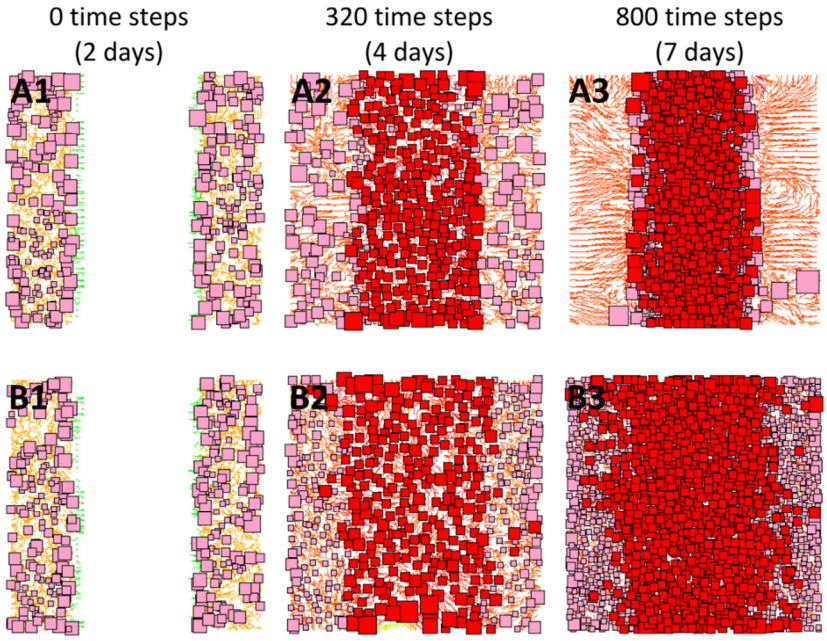

Figure 4-58 Simulation visualisations of the collagen matrix, fibroblast (pink squares) and myofibroblast (red squares) cells with and without the chemotactic gradient. The first row (A1-A3) shows a simulation with a chemoattractant enabled, while it was disabled for the simulation shown in the second row (B1-B3). For each case a visual from the model simulation is shown at 2 (A), 4 (B) and 7 (C) days post-MI.

The impact of the chemotactic gradient was further assessed based on the number of cells in the simulation, as well as the local alignment of collagen as quantified using the number of clusters

(Figure 4-59). One would not expect at first the chemoattractant to have a sizable effect on the number of cells as it is not directly related to the proliferation rate of the cells. However, without chemotactic gradient, the number of cells during the course of a simulation was significantly higher than the control case with the gradient enabled (Figure 4-59A). This was explained by the high level of cell crowding with the chemotactic gradient enabled, leading to contact inhibition of proliferation (section 4.4.3.4). The presence of the gradient also led to a higher degree of collagen alignment, as shown by the number of clusters significantly lower when compared to the case with the gradient disabled (Figure 4-59B). As the gradient attracted the cells towards the wound, it created migration patterns that were favourable for collagen alignment.

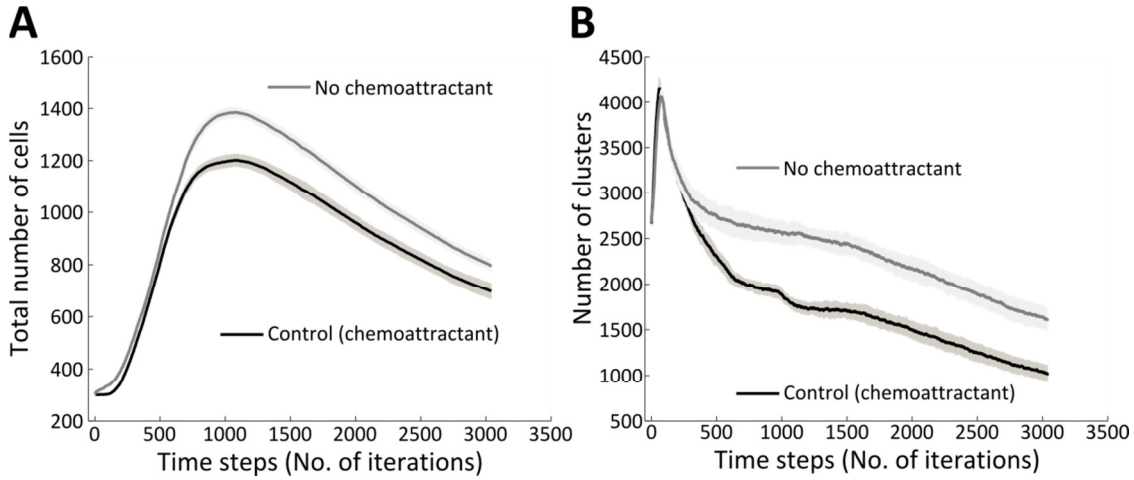

Figure 4-59 Further investigating the impact of the chemotactic gradient on simulation components. (A) Total number of cells in the simulation, and (B) number of clusters. The shaded areas denote the standard deviation for 11 simulations.

The chemotactic gradient was also altered in three different ways. These were keeping the production of the chemoattractant in the centre of the wound constant, delaying the chemotactic production to stop after 120 hours (instead of 60 hours in the control case) and adjusting the amount produced by half compared to the control. The chemotactic concentration within the wounded region differs significantly for these four scenarios during a simulation (Figure 4-60).

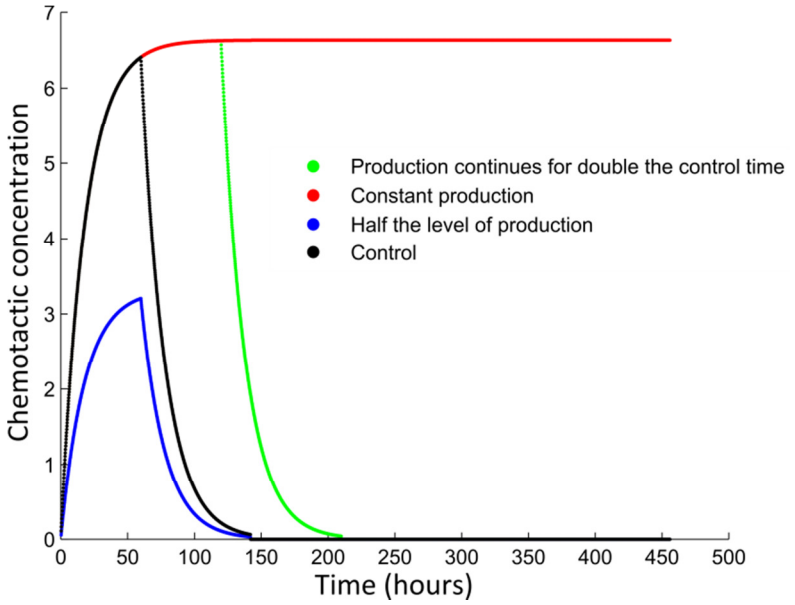

Figure 4-60 Chemotactic gradient manipulations. Chemoattractant concentration measured at the centre of the wound for three different scenarios compared to the control (black). These scenarios were: maintaining a constant production rate (red), doubling the duration of the production of chemoattractant (green), and halving the level of chemoattractant produced (blue).

The influence of different features of the chemotactic gradient on the local collagen alignment and number of myofibroblast cells has been analysed during model simulations (Figure 4-61). Longer productions of the chemoattractant in the wound resulted in an increased number of myofibroblast cells from approximately 700 time steps into the simulation. The proportion of myofibroblast cells is constrained in the model. An increased number of myofibroblast cells would require an increased total cell population size. The longer production of chemoattractant seems to increase the proliferation rate in the model simulation. This also seems to be a factor which effects the local collagen alignment. For all scenarios the alignments decreased throughout the simulation. The rates of decreasing alignment were similar up until 500 time steps, where both the double and constant production time cases levelled out. The remaining two cases continued to decrease in alignment, which is most likely connected to the decrease of the chemotactic concentrations measured in the wounded regions of these two configurations.

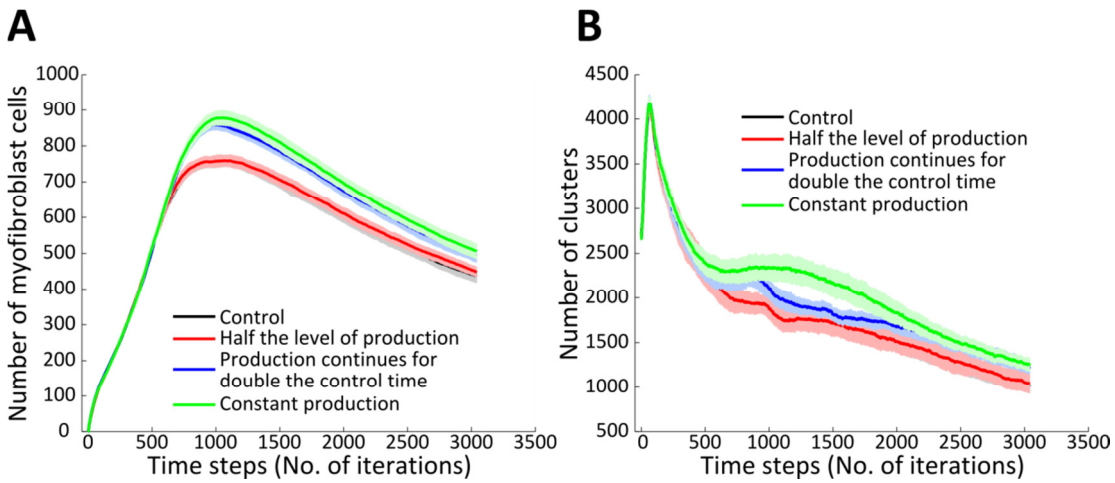

Figure 4-61 Model simulation results from varying both the duration and production rate of the chemotactic gradient. The number of myofibroblast (A) and clusters (B) have been compared over the entire simulation. (A-B) The control case (black) is obscured by the case with half the level of production (red).

4.9.6 Wound shape

The wound in the model was represented by a rectangular area surrounded by healthy tissue from which cells migrated. This representation was generic, and could be related to both *in-vitro* and *in-vivo* experimental data (section 4.3.2). However, alternative representations might also be suitable depending on the type of process considered. A previously described cardiac wound healing model was based on cryoinfarction experimental data (Rouillard and Holmes, 2012). To better represent the type of information gained through such protocols, the cryo-infarct model represented the wound as a circle surrounded by healthy tissue. For comparison purposes, this wound shape was implemented in the model, and compared with the default rectangular wound shape (Figure 4-62). The radius of the circular wound was set to 350 µm so that its area would be consistent with that of the rectangular representation.

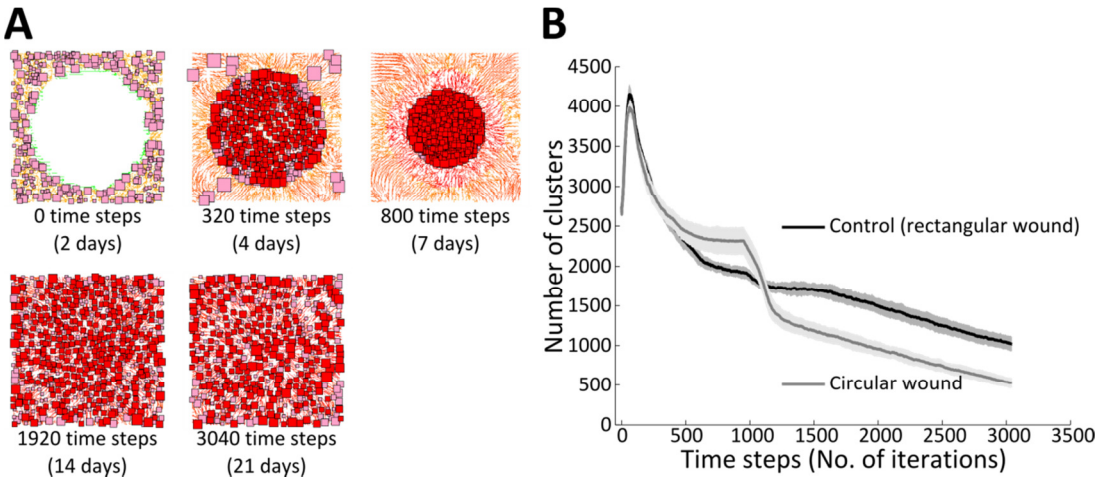

Figure 4-62 Implementation of a circular wounded region. (A) Visualisation of the model, with fibroblasts (pink squares) and myofibroblasts (red squares). Time points corresponding to 2 days, 4 days, 7 days, 14 days, and 21 days post-MI were considered. (B) Average number of clusters for the rectangular wound (black) and the circular implementation (grey). The shaded areas represent the standard deviation for 11 simulations.

Simulation visualisations indicated that the model was compatible with circular wounds, with the cells migrating radially into the wounded region as expected (Figure 2-12A). Consequently, the collagen was also essentially aligned radially. The shape of the wound thus influenced what type of local collagen patterns would be formed. Indeed, the changes in the number of clusters during the course of a simulation followed significantly different profiles (Figure 2-12B). In the case of a rectangular wound, the collagen was re-aligned overtime following an exponential decay profile. A similar profile was observed for the circular wound until about a 1000 steps into the simulation, where a sudden drop in the number of clusters was observed. This corresponded with the loss of the chemotactic gradient, at which point cells were free to migrate randomly re-aligning the collagen in the process.

4.9.7 Collagen content in the wounded region

An assumption of the model was that the wounded region would be devoid of collagen at the start of a simulation. This was motivated by reports of inflammatory cells eliminating apoptotic cells through phagocytosis and degrading the collagen matrix in the wounded region by secretion of matrix metalloproteinases (MMPs) (Nahrendorf et al., 2010). This also reflected the experimental conditions of the *in-vitro* experiments where most of the collagen was most likely mechanically removed during scratching. Alternative initial conditions were investigated by altering the initial collagen density within the wounded region. The initial density was to be uniformly set to 0 (control case), 0.5, and 1, or randomly assigned between 0 and 1. The impact of these various initial conditions was assessed based on collagen visualisation (Figure 4-63A), analysis of histograms of altered collagen orientation (Figure 4-63B), and changes in number of clusters during the course of a simulation (Figure 4-64).

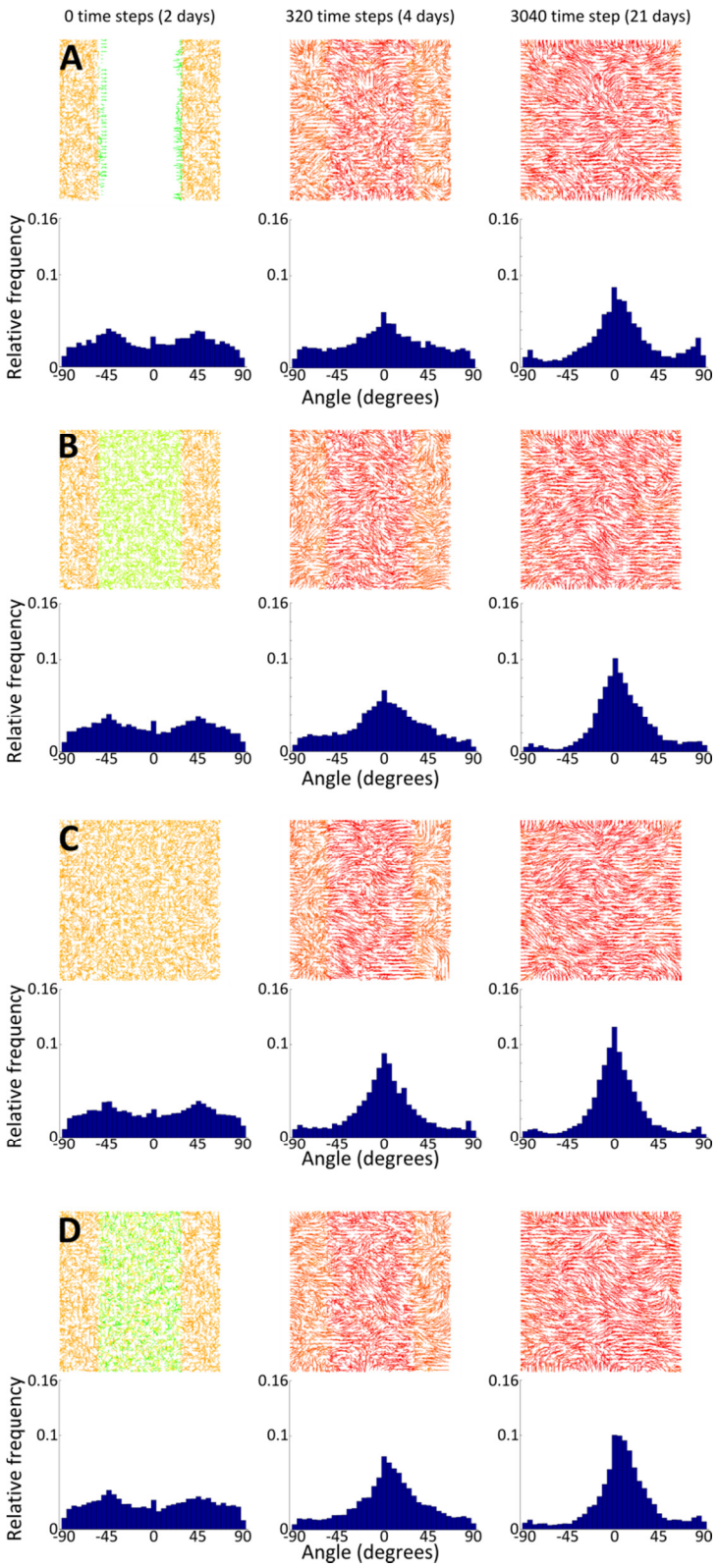

Figure 4-63 Effects of initial collagen density on matrix remodelling outcomes. Initial collagen uniformly set to 0 (A), 0.5 (B), 1 (C), and randomly between 0 and 1 (D). For each case, the collagen fibres visualisation is shown at simulation time step 0 (2 days post-MI), 320 (4 days post-MI) and 3040 (21 days post-MI), respectively. The fibre colour indicates density, ranging from 0 (green) to 1.5 (red). Similarly, for each case the collagen direction histograms are shown below each collagen fibre visualisation at simulation time step 0 (2 days post-MI), 320 (4 days post-MI) and 3040 (21 days post-MI), respectively. The fibres are considered bi-directional and thus their orientation range from -90° to 90°.

As expected, the changes in initial collagen density in the wounded region did not alter the direction of the collagen at the start of the simulation, which showed the same flat histogram in all four cases, indicating random orientations. After 320 simulation steps (i.e. 4 days post-MI), all conditions appeared to have reached the maximum density of collagen allowed by the model, regardless of the initial density. The initial density, however, had a measurable effect on the global alignment of collagen fibres as shown by the histogram representation. Indeed, at 320 time steps the distribution of angles was increasingly narrower as the initial collagen density increased. This difference was also visible, albeit not as clearly, for the histograms of directions computed at the end of the simulation. The profiles of changes in number of collagen clusters as the simulations progressed further confirmed these observations (Figure 4-64). While all four conditions had similar profiles, the number of clusters decreased proportionally with the initial density of the collagen in the wounded region. In other words, the collagen tended to be more aligned for higher densities. This phenomenon was caused by the interplay between collagen density and the ability of the cells to re-align neighbouring fibres. Early on during simulations, cells migrated towards the wounded region as steered by the chemotactic gradient. As their migration pattern was mostly horizontal (beyond fluctuations induced by the avoidance algorithms and unaligned collagen fibres), the collagen tended to be re-orientated horizontally, as shown by the unimodal angle histograms. When the density was low, small fluctuations in migration patterns resulted in re-alignment of local fibres, eventually disrupting the alignment obtained after the initial infiltration of the wound by the cells. Conversely for high collagen densities, the ability of the cells to re-align the fibres was much lower, thus small fluctuations in migration patterns had little effect and the highly aligned structure obtained after the initial migration was, therefore, maintained.

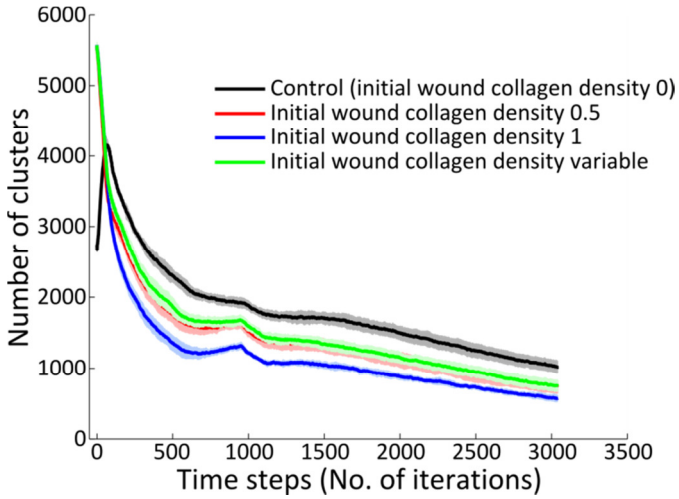

Figure 4-64 Effect of changes in initial collagen density in the wounded region on the number of collagen clusters thorough a simulation. Four initial collagen density conditions were investigated: no collagen (density of 0, control case in black), uniform density of 0.5 (red), uniform density of 1 (blue), and random density between 0 and 1 (green). The shaded region surrounding each set of points represents the standard deviation (N=11).

4.9.8 Initial orientation of the collagen matrix

By default, the initial collagen orientation in the healthy tissue surrounding the wounded region was assumed to be random. However, quantification of the collagen alignment on *in-vivo* tissue sections from healthy hearts suggested that the collagen arrangements differed significantly from a random distribution, and instead had a defined structure (see section 3.5.5.2). It was, therefore, of interest to determine whether this initial configuration would have an effect on the dynamics of the simulation. In order to do so, the collagen fibres in the healthy tissue were either randomly orientated, or had their directions set according to the vector field obtained from processing and analysis of an immunofluorescence microscopy image of a tissue section from an uninjured heart. The effect was assessed by computing the number of collagen clusters during the course of simulations for both conditions (Figure 4-65).

The results suggested that using different initial collagen arrangements in the health tissue surrounded the wounded region only had an effect during the early stage of the simulations. The initial peak in the number of clusters was much lower for the case where the collagen orientation was set to what was observed *in-vivo* due to a higher degree of local alignment when compared to the random arrangement in the control simulations. Thereafter, the control case a much higher rate of re-alignment, thus rapidly closing the gap and showing similar profiles from about 1000 steps into the simulation (equivalent to ~8.25 days post-MI). These results suggested that while there was a noticeable early effect on (i.e. increased alignment for *in-vivo* configuration), different initial orientation of collagen in the healthy tissue did not impact upon the end-result of simulations given the eventual re-alignment by the migrating cells.

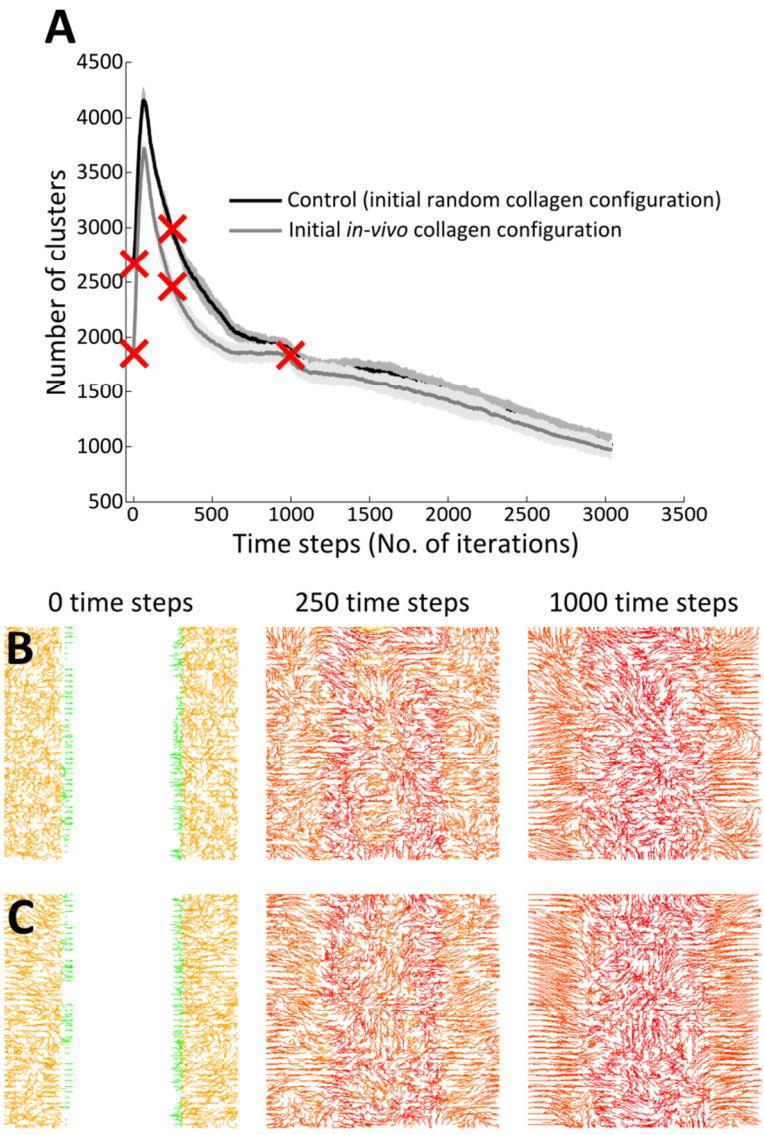

Figure 4-65 (A) Impact of the initial collagen arrangement in the healthy tissue on the number of collagen clusters during the course of simulations. The collagen fibres were either randomly orientated (control in black) or had their directions set according to that determined from the analysis of an *in-vivo* tissue section from an uninjured heart (grey). The shaded region surrounding each set of points represents the standard deviation (N=11). Model simulation outputs at 0, 250 and 1000 time steps indicated by red markers in (A), for an initially randomly orientated collagen matrix (B) and the initial collagen matrix determined from an *in-vivo* uninjured tissue section (C).

4.9.9 Initial wound dimensions

The simulated tissue in the computational model had dimensions of 850×850 μm, within which the wound was represented by an 850×430 μm rectangle. These dimensions were based on the field of view of a typical immunofluorescence confocal microscopy image of a cardiac tissue section, the main source of *in-vivo* data used in this work (see section 3.5.5.3). However, the size of a wound is likely to vary significantly between different MI events, potentially impacting upon the outcome of the simulation. Smaller (850×220 μm) and larger (850×650 μm) wounded regions were, therefore, evaluated based on the changes in collagen density as well as alignment (computed using the number of collagen clusters) during the course of the simulations (Figure 4-66). For each case, the numbers of cells were scaled proportionally to the fraction of healthy

tissue considered. In total, 300, 150, and 450 cells for the control, large and small wounds respectively.

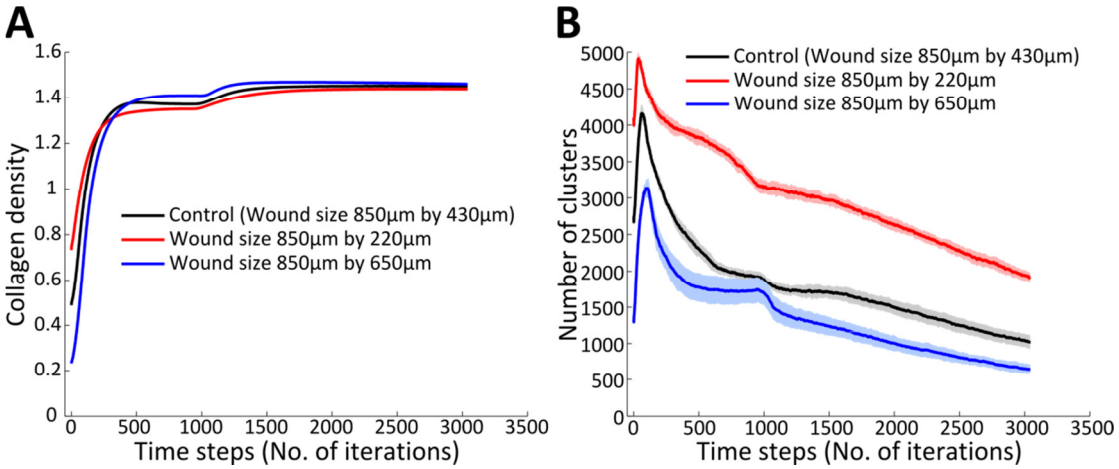

Figure 4-66 Impact of the wound size on the simulation outcome. (A) Collagen density and (B) number of clusters (inversely proportional to alignment) as a function of the number of simulation time steps. Small wound (850×220 µm, red), medium would (control 850×430 µm, black), and large wound (850×650 µm, in blue). The shaded areas shows the standard deviation (N=11).

The size of the wound and that of the resident fibroblast population had a small effect on the collagen density. The size of the wound dictated that of the healthy tissue, which in-turn influenced the collagen density measured across the entire tissue at time zero. As soon as the simulation started, the density increased rapidly for all conditions, the larger the wound the faster the rate of increasing collagen density. Towards the end of the simulation there were negligible differences in collagen density between the three profiles (Figure 4-66A). In contrast, the size of the wound and the number of cells had a marked effect on the local collagen alignment as measured by changes in the number of clusters (Figure 4-66B). The degree of alignment at the end of the simulations was proportional to the size of the wound, with the large wound resulting in a highly aligned collagen arrangement. Similar trends were obtained when only the number of cells was varied (see section 4.9.1.1), thus indicating that the size of the resident fibroblast population was responsible for a large fraction of the effect observed. Indeed, a smaller number of cells led to comparatively less crowding, and in-turn less obstruction of migratory trajectories by neighbouring cells, resulting in an overall higher degree of collagen alignment.

4.10 Discussion

In summary, the cardiac wound healing model described in this study was implemented informed by experiments where possible, or by published evidence otherwise. The complex cardiac healing process was broken down into components that could be both abstracted in the model and studied using simple biological experiments. This chapter gave an overview of the model where individual components were considered in isolation before being combined and allowed to interact with one another.

The agent-based nature of the model was based on principles previously described for the dermal wound healing process (Dallon et al., 1999; McDougall et al., 2006). This consisted of a collection of individual entities (i.e. agents), each associated with a set of properties, and given a collection of behaviours constrained by simple rules. During a simulation, the individual entities often interact with one another allowing complex behaviours, which were not explicitly encoded within the model formulation, to emerge.

This agent-based modelling framework, together with the capability of object-oriented programming, were found to be suitable for the implementation of a cardiac wound healing model, given that individual entities, the cells, are the key players during this process. The cells (i.e. agents) had a position in a Cartesian space, a velocity that encoded both their speed and migration direction, a size, and an age. The main cell behaviours playing a role in cardiac wound healing were also abstracted in the model: migration, proliferation, cell death, and differentiation (Chen and Frangogiannis, 2012; Souders et al., 2009). Importantly, these behaviours not only depended on the state of the cell itself, but also on the state of neighbouring cells as well as their local environment. The local environment was very dynamic, and consisted in both signalling molecules promoting the migration of the cells towards the wound and a collagen extracellular matrix, a major constituent of the scar post-MI. The matrix was critical, as the structure and nature of the scar are key determinants in the outcome of MI.

While the model setup chosen could accommodate 3D simulations with some adjustments, it was decided to restrict the scope to 2D due to the lack of 3D experimental data. Both *in-vitro* cell culture experiments and analysis of murine heart sections carried out for this work used well established techniques and protocols, which do not necessarily exist for 3D experiments. Computational complexity would also be much higher for a 3D model, limiting the number of parameter values that could be realistically evaluated. Moreover, visualisation of 3D simulations would be technically challenging. Instead, the cardiac tissue was abstracted as a 2D plane.

The dimensions of the simulated tissue were chosen based on the field of view of a typical immunofluorescence microscopy image from murine heart sections, so that model and *in-vivo* data shared a common scale, thus facilitating their direct comparison. While the cell position could adopt any value within this area (continuous variable), the collagen matrix was sampled along equally spaced grid points. At each grid point, a vector encoded for the matrix density (vector length) and orientation (direction). An interpolation function had thus to be used to estimate the value of the collagen matrix at any location between the grid points. The choice of the interpolation function significantly altered cell migration patterns, as well as simulation visualisations. In the absence of an unbiased and objective criterion for the selection of the most appropriate interpolation function, the choice was made based on previous models (Dallon et al., 1999). A combination of the tensor product and quartic Lagrangian interpolation was used.

Upon qualitative inspection of the results, the estimates produced by this method based on the 25 nearest grid points appeared reasonable. Bilinear interpolation was also considered, whereby only the immediate neighbours were considered for interpolation, produced smoother collagen fibres with higher alignment but resulted in cell flocking, which was deemed not biologically realistic.

Model outcome evaluation was completed on a qualitative basis using simulation visualisations, as well as quantitatively based on various metrics of interest. The visualisation showed the cells together with the collagen matrix. As mentioned above, the matrix was only defined at grid points, therefore, in order to visualise it as continuous bundles of collagen fibres, a tracing method was employed whereby cells whose motion was only dictated by the local collagen matrix were used to trace the location of the fibres. The main advantage of this approach when compared to a more simple representation of the matrix as a collagen vector field was that it related directly to how the local collagen matrix was perceived by the cells. The quantitative metrics used for simulation outcome evaluation included the fraction of the wound covered by cells, the number of cells present in the simulation, as well as the number of local collagen clusters.

In the model, the state of the cells and that of the collagen matrix were fundamentally linked, such that, cells were responsible for the deposition and degradation of the collagen matrix, as well as its re-orientation. Conversely, the matrix partly dictated the speed and direction of cell migration. A cell travelling in a direction other than that of the local collagen matrix caused the latter to re-orient itself, while the cell was also encouraged to alter its direction so it travelled alongside the local matrix. Another element added to the dynamic nature of this relationship: the ability of the cells to re-orient the collagen was inversely proportional to the density of the matrix. Intuitively it might be expected that cells would not be able to efficiently re-orient collagen past a certain density as the force that would need to be applied would be too high. A cell can only affect the local collagen matrix located within the area it covers. As the model did not account for cell boundaries, this was approximated using areas of influence, whose dimensions corresponded to experimental measurements of cell area. The level of influence was not homogeneous, but instead had a peak influence at the leading edge of the cell. In other words, the collagen matrix in contact with the leading edge of the cell was altered to a higher degree than that in contact with the rear of the cell. This was consistent with measurements of the force exerted by cells on the surrounding extracellular matrix (du Roure et al., 2005).

The changes in collagen density through deposition by migrating cells were not the main focus of this model, but instead a by-product of the simulation as no readily usable experimental data was available. During simulations, the collagen quickly attained the maximum density allowed by the model. This high rate of increase was related to the large area and migration speed of the

cells. The implementation based on an equilibrium between production and degradation would need to be revisited as appropriate data becomes available. As it is, the changes in collagen density were used as a mechanism to represent collagen fibre stiffness and its effect on both re-orientation potential by cells and on the migration speed of the latter.

The orientation of the collagen matrix was either set randomly at the start of a simulation, or based on determination of *in-vivo* collagen fibre bundles orientation in cardiac tissue sections from murine models of MI. While the *in-vivo* collagen configuration had a higher initial degree of alignment than the random case, 1000 time steps into the simulations (equivalent to ~8 days post-MI) both had converged and remained at similar levels thereafter. This suggested that the difference in alignment between the random case and the slightly more ordered *in-vivo* configuration did not significantly impact the long-term collagen matrix re-organisation. In contrast, the degree of collagen alignment throughout a simulation increased together with the initial collagen density in the wounded region. Indeed, higher collagen densities meant that the rapid re-alignment resulting from the initial infiltration of the wound by resident fibroblast cells was less likely to be disrupted later on as the collagen fibres, through further deposition from said cells, quickly reached a critical density beyond which cells had much less effect on their orientation. A key assumption was that the initial density of the collagen matrix was essentially null, given that it is known to be significantly degraded by metalloproteinases (MMPs) early on during the inflammatory response (Nahrendorf et al., 2010). Intuitively, the collagen matrix is unlikely to be completely removed but instead exists in a state of flux where fibres damaged during ischemia are progressively replaced by freshly deposited collagen. However, the assumption that no collagen remained post-injury was employed since it permitted a focus on the dynamics of collagen matrix production and alignment by the infiltrating cells, and was also consistent with the *in-vitro* cell culture model where most of the collagen coating the dish was mechanically removed during the scratch assay.

The signalling molecules promoting infiltration of the wound by resident fibroblast cells was another key aspect of their environment that was abstracted in the model. In the model, pro-inflammatory stimuli cytokines such as TNF-α and IL-1β secreted during inflammation by monocytes and macrophages were combined into a single signal (chemoattractant) that diffused outwards from the central wounded region (Chen and Frangogiannis, 2012; McDougall et al., 2006). The chemoattractant was constantly produced in the wounded region and degraded over time. The intensity of the chemoattractant decreased as the distance from the wound increased, thus creating a spatial gradient. The signal peaked at around 400 time steps (108 hours post-MI) and decayed thereafter, reaching zero after 1000 time steps (198 hours post-MI) as suggested by experimental evidence showing that the inflammatory cells (responsible for the secretion of the molecules represented by the chemotactic gradient) had depleted by approximately 5 days post-MI (Nahrendorf et al., 2010). The chemoattractant influenced both the speed and direction of

cell migration. The steepness of the concentration gradient at the cells location dictated to what degree the chemoattractant would influence the cells. By influencing cell migration, the chemoattractant had multiple effects on the dynamics of the model, including collagen alignment as cells were more likely to migrate in straight lines, and the number of cells as the local cell density had an effect on proliferation.

The effects of altering the rate of chemoattractant production, as well as the length of the period of time during which it is produced, were investigated. Decreasing the rate of production only had a small effect on the local collagen alignment. This could be related to the influence of the chemotactic gradient on a cell being scaled relative to the maximum gradient across the simulated tissue. Larger effects were observed when the chemoattractant was produced within the wounded region for a longer period of time. The increased duration of production slowed down the rate at which the local alignment increased. This simple approach to chemotaxis demonstrated how an influence on cell migration could lead to the formation of highly aligned collagen patterns. Instead of using a single generic diffusing signal, it would be more appropriate to have multiple temporally-overlapping signals with distinct effects on the cells. This way, different effects (e.g. chemotactic, proliferative) could be decoupled. The framework described in this study could be extended to allow for such signalling cascades to be implemented in future iterations of the model. A better approach would be the modelling of individual immune cells infiltrating the infarct during the inflammatory phase of wound healing. The cells would produce localised diffusing signals that would then influence the behaviours of neighbouring fibroblast and myofibroblast cells.

In addition to migration, individual cells could also divide, undergo apoptosis, and differentiate. All of these behaviours were controlled by probability functions that were derived from experimental data. Essentially, at each time step and for each cell, it was determined whether one of those behaviours should be activated based on the state of the overall cell population in the simulation. While this approach proved to be efficient and allowed faithful replication of dynamics of a cell culture and/or tissue, it also added a set of constraints to the model that might decrease its generalisation to other cell-based processes. Instead, those dynamics could be re-created based on simpler rules not constrained by pre-defined probability functions. The model would gain in flexibility but also in complexity. Indeed, the additional rules would not necessarily be relatable to known and understood biological concepts, and the additional parameter values might not be derivable based on experimental evidence.

In the model, fibroblasts and myofibroblasts differ in key aspects, such as their migration speed, their size, and their ability to alter the collagen matrix. Collagen production and degradation rates of myofibroblasts were assumed to be higher and lower than those of fibroblasts, respectively. While this myofibroblast phenotype was based on previously published

experimental observations (Howard et al., 2012; Souders et al., 2009), the actual parameter values were arbitrarily chosen.

While in the heart a complex signalling cascade would lead to the activation of the differentiation pathways, the model used a simplified approach whereby cells were allowed to differentiate (as controlled by a probability function) as soon as they entered the wound, as it was assumed they would then be exposed to differentiation-promoting signals. This simple approach to model how external cues and stimuli promote differentiation could be further improved. For instance, differentiation rate could be directly related to the local concentration of TGFβ, which could be represented by an abstract chemical gradient similar to the implementation of the chemotactic gradient. Alternatively, TGFβ could be modelled as being secreted in the local neighbourhood of specific cell types, which could be added to the model as discussed below.

Other cell types, such as cardiomyocytes, vascular cells and tissue resident monocytes/macrophages are also present in the heart before and after injury (Chen and Frangogiannis, 2012; Nahrendorf et al., 2010). Additional cell types can be added in the model and assigned specific properties, functions, and constraints. If experimental data became available for these other cell types, they could therefore be implemented in future iterations of the model. For instance, cardiomyocytes that survived post-MI could be positioned in the infarct (Cleutjens et al., 1999). Their presence would induce changes in migration patterns of infiltrating fibroblasts (through contact inhibition of locomotion) and thus in the structure of the collagen matrix. The main advantage of the agent-based modelling approach, namely the fact that parameters can be informed directly from both qualitative and quantitative experimental investigations, can also be a limitation. Indeed, some parameters that appear obvious can be difficult to estimate with a high degree of confidence. This was the case for the size of the initial population of cells. This number was of critical importance as small variations impacted the main simulation outcome, namely the degree of alignment of collagen. The model did not account for the infiltration of additional fibroblasts from surrounding tissue during the course of a simulation. The size of the cell population was only dependent on the initial number of cells, their proliferation, and removal from the simulation due to apoptosis. It was assumed through the use of reflective boundary conditions that cells leaving the simulated tissue would be effectively replaced by another cell with the same properties migrating in the 'reflected' direction.

In addition to its size, the distribution of the cell population at the beginning of a simulation was also of importance. In the model, it was assumed that cells were randomly distributed in the healthy tissue surrounding the wounded region. A more ordered alternative configuration did not produce significantly different results. In the heart, a certain degree of order is likely due to

the presence of cardiomyocytes, acting to spatially constrain the fibroblasts (Camelliti et al., 2005a). The size of the wound was also found to be of importance. Simulations with smaller wounds resulted in less collagen alignment. For these cases, more cells were initially present as their number was scaled to the area of healthy tissue simulated. These results were consistent with those obtained for simulations for the baseline wound size but with increased cell numbers.

The cells were made aware of each other through mechanisms such as contact inhibition of location and proliferation. In principle, the agents in the model (i.e. the cells) could be modelled as physical entities with the ability to deform so that such collision could be detected in advance and the cell behaviour altered accordingly (Osborne et al., 2010). This approach would result in high computational complexity, therefore an alternative method based on an approximation of this behaviour was adopted. A semi-circular region was positioned in front of the cell and aligned with its direction of migration. This region was a representation of the ability of the cell to sense and probe its immediate environment. If neighbouring cells were detected, the direction of migration was altered. Cell avoidance greatly impacted the outcome of simulations. Without avoidance, cells could congregate and migrate along similar paths in a way that would not be physically possible, resulting in an excessively high degree of collagen alignment. The approximation of cell avoidance had limitations; for example, cells could still collide and migrate over each other in some edge cases where the distribution of neighbouring cells made them choose colliding trajectories. Moreover, it was challenging to implement, as the cell objects were not entirely independent but instead had to be updated synchronously in order to take into account changes in direction from other cells. In addition to migration, crowding also impacted proliferation, which was inhibited when no free space was available around the potentially dividing cell. Finally, the cell area was dynamically altered depending on the number of neighbouring cells so that the model could be consistent with both *in-vitro* experimental results (very large cells) and *in-vivo* observations (small cells tightly packed).

Cell migration was influenced by numerous factors: the collagen matrix, the chemotactic gradient, and other cells. A cell's baseline speed, before taking into account these external influences, was set by a model parameter. Interestingly, varying this parameter did not produce significantly different simulation outcomes. The main reason for this was that the contributions of the aforementioned factors outweighed that of the baseline speed. For example, the collagen matrix and other cells tended to slow down migration, while the chemotactic gradient increased migration speed. This highlighted the highly dynamic nature of the model. Its versatility was also demonstrated by the inclusion of a circular wound, as described in a previously published cardiac wound healing model (Rouillard and Holmes, 2012). Circular-shaped wounds are common for cryoinfarction models of myocardial infarction. Being able to simulate different wound geometries thus extends the range of experimental data that could potentially be used to inform or validate the model. Initialisation of the model with a circular wound produced radially

aligned collagen fibres upon infiltration of the wound by migrating cells. The reflux of cells following the decay of the chemotactic gradient further increased the alignment. The end-point alignment was markedly higher for a circular wound when compared to a rectangular geometry.

An important aspect of the wound healing process that was omitted from the model was the effect of mechanical forces caused by the difference in structural properties between the healthy tissue and the adjacent infarct tissue. In the model described in this study, the main focus was on the interaction between the cells and the collagen matrix, in particular how the former altered the latter during migration. The inclusion of an external stimulus such as a mechanical tension might have negated the effect of the cells. Nevertheless, mechanical tension could be added to the model in future iterations to assess its relative effect on collagen alignment. Such a mechanical stimulus could also promote differentiation, as previously shown (Chen and Frangogiannis, 2012; Hinz et al., 2001).

Potential major limitations of the model presented here were related to the source, quality, and relevance of the experimental data employed. Many parameters were estimated from *in-vitro* cell assays. Even though these experiments were carefully planned and conducted with the most relevant cells (primary cardiac fibroblasts), it is difficult to determine to what degree the data was relevant to the *in-vivo* process. Moreover, the parameters estimated from the literature were often derived from different experimental setups, including different organisms. Whereas this model was based on the time course of a typical response in the murine heart, the timing of the same events in humans or other animals might differ significantly (Frangogiannis et al., 2002). However, as quantitative approaches (e.g. quantitative polymerase chain reaction, flow cytometry, high resolution time-lapse microscopy) become more and more prevalent in biology, these gaps in data might be filled, thus allowing a faithful *in-silico* representation to be built. Until then, it was assumed that the data available represented a reasonable starting point.

The model described in this chapter enabled the simulation of the highly dynamic process of wound healing in the heart post-MI. The agent-based framework allowed an approach akin to bottom-up biology, whereby the various components were first broken down, before being assembled in order to form a system more complex than the sum of its individual parts. Unlike other modelling approaches where all the components of the model are intrinsically linked together, it was possible to selectively activate or deactivate certain components to investigate their effect on simulation outcomes. The agent-based approach remained compatible with more conventional modelling concepts, such as diffusion equations (i.e. chemotactic gradient). This ability to interchangeably use different levels of abstraction and modelling approaches (‘mix and match’) allowed the generation of very complex, yet easily understandable and interpretable simulations.

Chapter 5

Model validation and predictions of the effects of pharmacological interventions

5.1 Introduction

The cardiac wound healing process is highly complex and intricate, initiated by an inflammatory response and resulting, after several weeks, in a fibrotic scar (van Nieuwenhoven and Turner, 2013). The fibrotic scar has detrimental effects on the heart post-MI as it promotes myocardial stiffness, cardiac dysfunction, adverse ventricular remodelling and ultimately heart failure (van den Borne et al., 2010; Dean et al., 2005). The heart has a limited ability to regenerate post-MI and a scar is formed to replace the damaged tissue, moreover, the scar provides structural support to the myocardium and aims to prevent cardiac rupture (Sun et al., 2002). The formation and maturation of the scar post-MI, whose main component is collagen, is mainly mediated by fibroblast cells (Chen and Frangogiannis, 2012). These cells, most active during the proliferative phase of cardiac wound healing, synthesise, deposit collagen in an attempt to repair the wound (Chen and Frangogiannis, 2012; Souders et al., 2009). The traction forces exerted by fibroblast cells during their migration also remodel the local collagen matrix (Petroll et al., 2003). Moreover myofibroblasts, an activated form of fibroblasts, possess contractile stress fibres which are alpha-smooth muscle actin (α-SMA) positive that can pull on the surrounding collagen fibres, leading to the contraction of the wound and the re-alignment of the collagen matrix (Porter, 2007). Alteration of fibroblast behaviours and properties would have a direct impact on scarring post-MI. Pharmacological interventions aiming at optimising the outcome of cardiac wound healing could thus target fibroblast cell behaviours such as migration, proliferation, and differentiation into myofibroblasts, as well as their ability to produce and degrade collagen. Manipulation of the fibroblast cells would be achieved through conditioning of their local environment. The ideal sequence of events would be to first ensure the rapid formation of a scar to support normal cardiac function. Scarring could then be slowed down or inhibited to avoid the formation of a fibrotic scar associated with risks of heart failure (Dean et al., 2005).

In order to optimise scarring, the wound healing process and the main factors influencing scarring need to be well studied and characterised. *In-vivo* (experimental) studies have improved

the understanding of the variables involved by inhibiting molecular pathways that are thought to play a role in the modulation of scarring levels post-MI. Some examples of relevant pathways that have been targeted include transforming growth factor-beta (TGFβ) (Tan et al., 2010), fibroblast growth factor (FGF) (Detillieux et al., 2003) and vascular endothelial growth factor (VEGF) (Zhao et al., 2014). Evidence suggests that TGFβ influences fibrosis by promoting differentiation, proliferation and collagen deposition in fibroblast cells (Frantz et al., 2009; Nahrendorf et al., 2010; Souders et al., 2009). Myofibroblast cells express α-SMA and secrete increased levels of collagen, the main constituent of the scar, compared to fibroblasts (Ignotz and Massagué, 1986; Souders et al., 2009). Gene therapy has been used to inhibit TGFβ1 in the murine heart within 10 days post-MI (Okada et al., 2005). Results showed improved heart function and decreased levels of fibrosis and apoptosis of myofibroblasts cells. TGFβ signalling can be inhibited with activin receptor-like kinase 5 (ALK5) inhibitor (Inman et al., 2002). ALK5 activity is an important component of the TGFβ-mediated control of the extracellular matrix (ECM) (Inman et al., 2002; Laping et al., 2002; Tan et al., 2010), ALK5 phosphorylates and activates Smad2/3 (Figure 5-1).

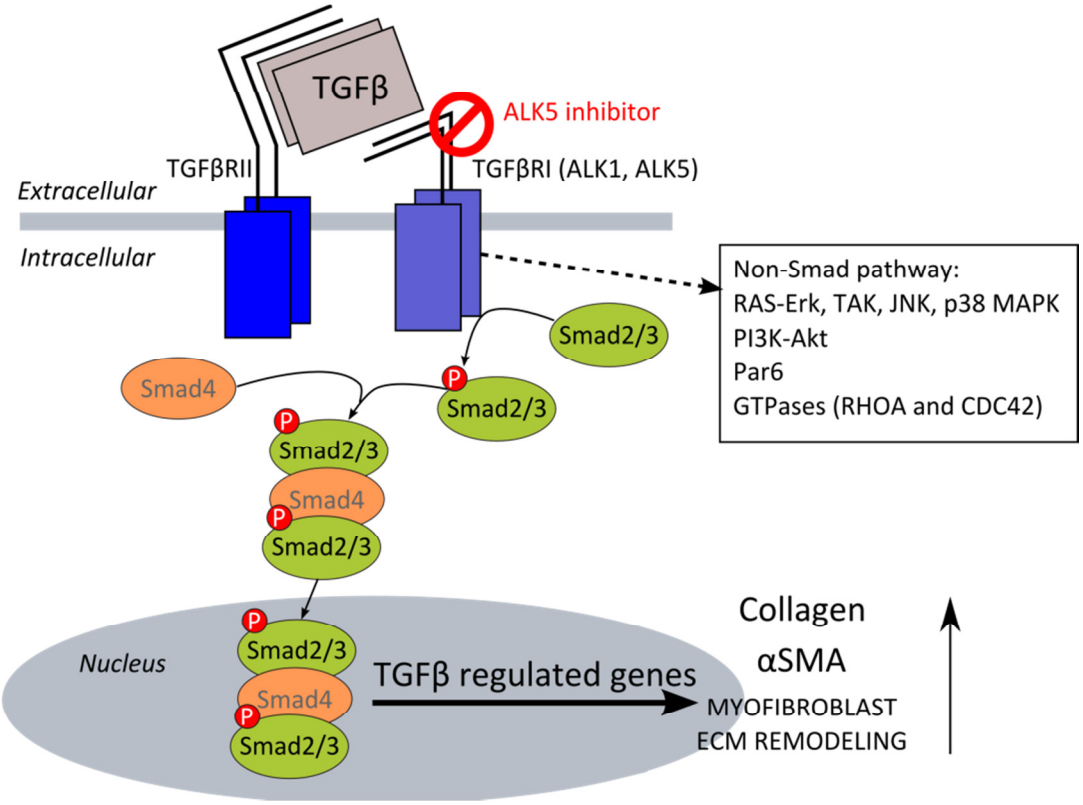

Figure 5-1 The TGFβ signalling pathway. TGFβ can bind with receptors TGFβRII and TGFβRI (ALK5) located on the cell membrane. TGFβRI activates and phosphorylates (P) Smad2/3 which binds and forms a complex with Smad4. In the nucleus this complex regulates TGFβ related gene expression. A non-Smad pathway which includes RAS-Erk, JNK and p38 MAPK can also be activated by TGFβ. An inhibitor activin receptor-like kinase 5 (ALK5) can be used to block TGFβ binding with TGFβRI. This figure has been adapted from (Buijs et al., 2012; Leask, 2010).

Post-MI rats treated with ALK5 inhibitor showed attenuated systolic dysfunction, accompanied by reduced expression of α-SMA and collagen I in the non-infarct zones (Tan et al., 2010). In

addition, scar formation that generally occurs following glaucoma surgery was inhibited after treatment with ALK5 inhibitor (Xiao et al., 2009).

FGFs could also be a potential target for scarring modulation (Figure 5-2). FGF-1 and FGF-2 have been shown to have cardioprotective effects during ischemia and reperfusion (Detillieux et al., 2003; Palmen et al., 2004). FGF-2 promotes proliferation in both fibroblasts and myofibroblasts, which may result in increased levels of collagen deposition post-MI (Detillieux et al., 2003; Galzie et al., 1997). Reduced levels of collagen deposition and fibroblast proliferation were shown post-MI in mice with a deletion of FGF-2 (Virag et al., 2007). Moreover, FGF-2 has also been shown to inhibit fibroblast differentiation induced by TGFβ1 (Fedak et al., 2012; Khouw et al., 1999). Fibroblast growth factor receptor 1 (FGFR-1) plays a key role in cardiac morphogenesis (Zhu et al., 1996). SU5402, a pharmacological compound, has an inhibitory effect on vascular endothelial growth factor (VEGFR) and fibroblast growth factor receptors (FGFR), both of which are involved in the regulation of fibroblast differentiation and migration (Kaftan et al., 2012; Mohammadi et al., 1997; Murakami et al., 2008; Zhao et al., 2014).

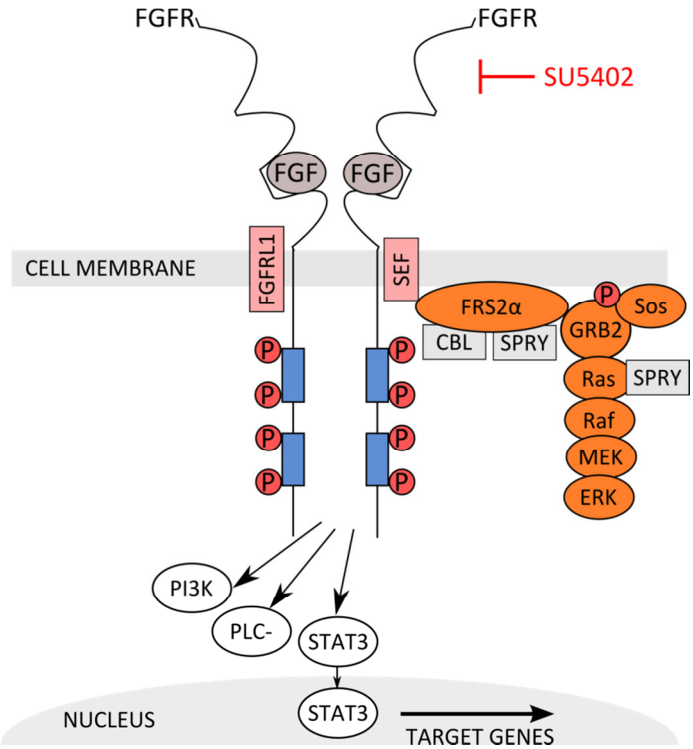

Figure 5-2 The FGF signalling pathway. Initially both ligand binding and receptor dimerization occurs. Transphosphorylation occurs between each of the kinase domains. The molecule FRS2α binds to the FGF receptor complex. Subsequent binding with GRB2 can lead to activation of the pathway Ras-Raf-ERK. FGF signalling may also activate the following pathways PI3K, PLCγ and STAT. SU5402 is a FGFR-specific tyrosine kinase inhibitor. Figure adapted from (Kwabi-Addo et al., 2004; Turner and Grose, 2010).

The addition of SU5402 to rats which had undergone bilateral myringotomies (small incision in the eardrum) resulted in a dose dependent reduction of the wound closure rate (Kaftan et al., 2012). Moreover, cardiac functional recovery induced by the addition of FGF-1, was completely

abolished with the addition of SU5402 (Palmen et al., 2004). The pan FGF inhibitor SU5402 has caused significant impairment to the caudal fin regeneration capability in zebra fish, by blocking the proliferation of fibroblast-like cells (Poss et al., 2000). Reducing the levels of proliferation may indeed reduce scarring levels post-MI. The VEGF pathway is also associated with wound healing. Indeed, treatment of rats with BIBF 1000, a small molecule inhibitor which targets the receptor kinases of VEGF, FGF-2 and platelet derived growth factor (PDGF), was shown to cause a reduction in pulmonary fibrosis. The impact on fibrosis was analysed by the measurement of collagen deposition rates and expression levels of pro-fibrotic growth factor genes (Chaudhary et al., 2007).

Gaining a complete understanding of the complex *in-vivo* cardiac wound healing process is challenging. *In-vitro* analysis is often used as a controlled environment to study specific cell properties and behaviours. However, the experimental settings employed are generally unable to recapitulate the complexity of *in-vivo* systems, thus producing results which are not necessarily directly applicable for devising new therapeutic strategies. Mathematical models are a useful intermediate tool for predicting and enhancing the understanding of a complex system. The computational model of cardiac wound healing described in this work was devised as a tool to complement experimental investigations at two different levels of complexity. First, the model can be used to combine easily attainable *in-vitro* experimental data of individual cell behaviours into a complex system which is representative of the *in-vivo* process. The model can simulate multiple interactions and dynamic events that would be difficult to mimic experimentally. Secondly, the model may be used as an exploratory tool to reverse engineer the process leading to the formation of a scar. This could facilitate the identification of system components which can be targeted for the manipulation of scarring post-MI. Once identified, these manipulations could be implemented in the form of pharmacological interventions, for example by altering cell behaviours such as differentiation and migration in the damaged tissue. The overall aim would be to optimise scarring and improve the outcome of patients post-MI. Assessing the ability of the mathematical model to recapitulate the events of the wound healing process is key. In addition, the model should accurately predict the effects of system perturbations such as the manipulation of specific pathways by either pharmacological or genetic approaches (e.g. gene knockout or editing). Both of these can be determined by comparing model outputs with experimental data.

Aims

The aims of this chapter are:

1. Compare the results of model simulations with *in-vivo* experimental data in a setting mimicking wound healing without pharmacological intervention. Firstly, by utilising the clustering method detailed in chapter 3, which quantifies the level of local

alignment. Secondly, by producing histogram plots which are used to qualitatively compare the level of global alignment (i.e. over the entire region considered).

2. Use differences in model predictions and *in-vivo* experimental results to identify further refinements to the model.
3. Use the model to predict the effects of various experimental pharmacological interventions (TGFβ1, ALK5 inhibitor and SU5402) on scarring outcome. For each intervention, the migratory speeds and differentiation rates of cardiac fibroblast cells as measured *in-vitro* (chapter 2) have been incorporated into the model parameters.

5.2 Comparison of simulation results with *in-vivo* experimental data

The simulation results were compared to experimental data from animal models based on local and global collagen alignment as previously described (see section 3.4.3). For a one-to-one comparison with immunofluorescence images of tissue sections from murine hearts, the model output considered for analysis was a 430×430 μm square positioned in the wounded region (Figure 5-3). The model results were generated using parameter values for cell speed (Section 2.4.2), proliferation (Section 2.4.3), cell area (Section 2.4.5) and differentiation (Section 2.4.4) which were derived from *in-vitro* experimental investigations as described in chapter 2. Initially, the simulation begins with a wounded region (with no collagen and no cells), flanked by healthy tissue (Figure 5-3A and F). The healthy tissue collagen matrix initially consisted of randomly orientated collagen fibres (Figure 5-3A). As the simulation progressed, fibroblast cells migrate towards the wound. These cells proliferate, differentiate and modify the collagen matrix through production, degradation and re-orientation. An increasing density of collagen was observed, first in the wounded region and then in the healthy tissue (Figure 5-3A-E). Up to 7 days post-MI (800 simulations steps), collagen in the wounded region was mostly unaligned, whereas a high degree of alignment was observed in the healthy tissue (Figure 5-3C). The high alignment was caused by fibroblast cells migrating into the wounded region mainly dictated by a chemoattractant (Figure 5-3H). At later time points (1920 and 3040 time steps) both the wounded region and surrounding tissue contained pockets of aligned collagen fibres (Figure 5-3D-E). Apoptosis is responsible for a reduction in the number of cells observed between these two time points (Figure 5-3I-J).

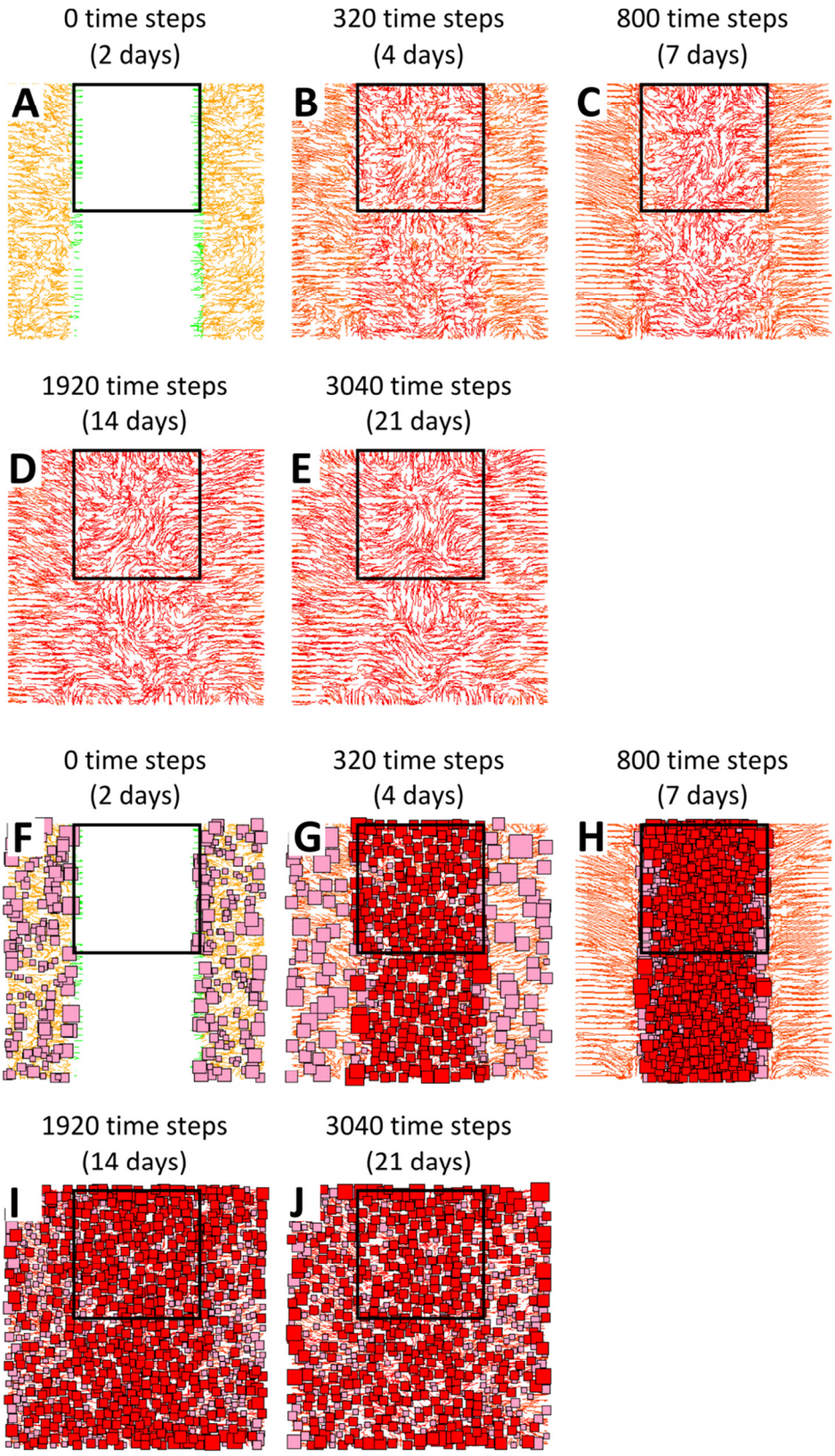

Figure 5-3 Representative images of the cells and collagen matrix from a simulation using all *in-vitro* and *in-vivo* estimated parameters. (A-E) Visualisations of the collagen matrix from the model simulation at 2 (A), 4 (B), 7 (C), 14 (D) and 21 (E) days post-MI. (F-J) Visualisations of the collagen matrix and cells at 2 (F), 4 (G), 7 (H), 14 (I) and 21 (J) days post-MI. The output of the model considered for quantitative analysis is a 430×430 μm square positioned in the wounded region (black overlay).

Dynamics of collagen re-organisation in the murine heart post-MI were compared with simulation outputs based on the number of local collagen clusters (Figure 5-4). The number of local collagen clusters can be quantified with the measure developed in this study (section 3.4.3.2). The number of clusters represents the number of regions containing highly aligned collagen fibres. The lower the number of clusters the higher the level of alignment. In comparison to healthy tissue, scar tissue is highly anisotropic (i.e. directionally dependent) and this structure may contribute to the increased stiffness of the scar tissue (Holmes et al., 1997; Przyklenk et al., 1987; Whittaker et al., 1989). Scar tissue has shown greater resistance to mechanical deformation, likely to be related to the increased collagen fibre alignment (Holmes et al., 1997; Przyklenk et al., 1987). The initial profiles of both the *in-vivo* and *in-silico* outputs up to 7 days post-MI (equivalent to 800 simulation time steps) were similar both in terms of their absolute numbers of clusters and in the apparent decrease in number of clusters with time (i.e. increased alignment). However, model predictions and experimental results diverged beyond this point. According to model predictions, after approximately 7 days post-MI the number of clusters decreased linearly, indicating a continuous increase in local alignment (Figure 5-4A-B). In contrast, the number of clusters determined from the *in-vivo* data (Figure 3-11A) first levelled off, before increasing again by day 21 post-MI, reaching levels similar to that of an intact heart (Figure 5-4 A and C).

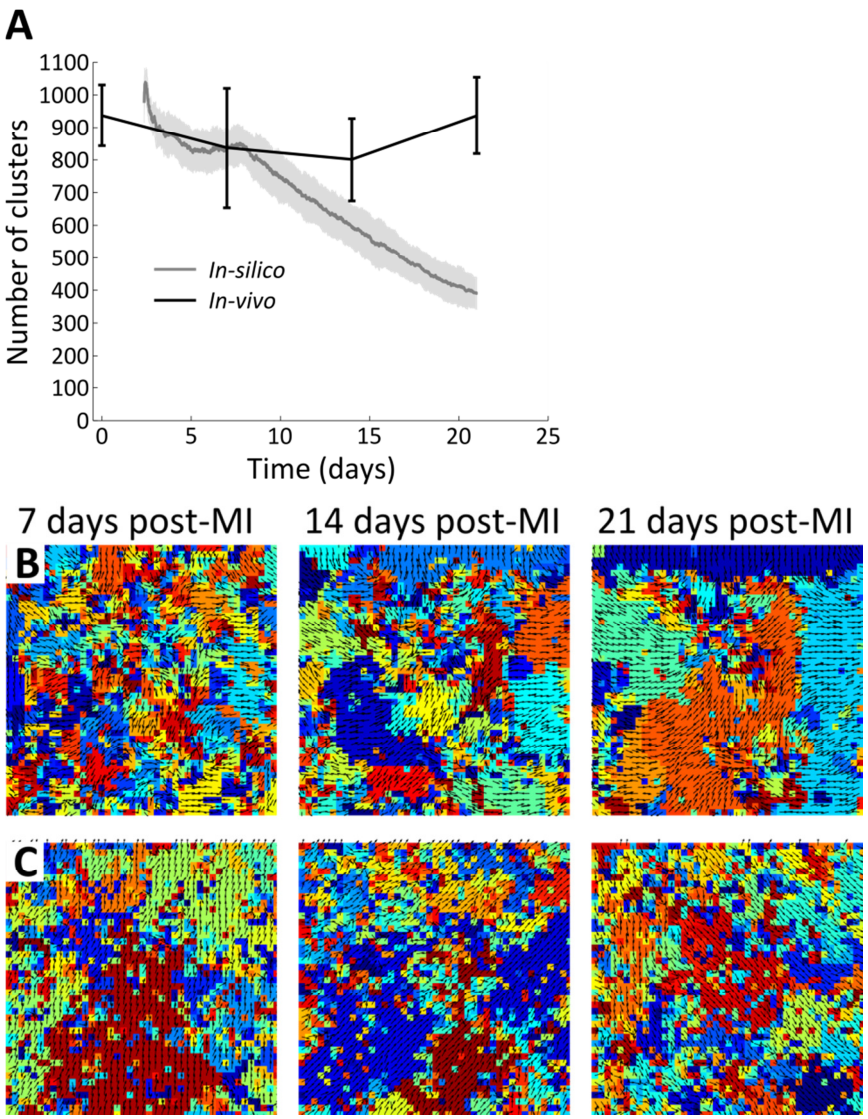

Figure 5-4 Changes in local collagen alignment in model simulations and on heart tissue section images. (A) Number of clusters as a function of time post-injury in model simulations (grey) and on heart tissue section immunofluorescence microscopy images (black). For the simulation results, a 430×430 μm in the wounded region was analysed. The initial 9 hours of the simulation have been omitted as the wound was not completely contained with collagen. Shaded region represents standard deviation across 11 simulations. For *in-vivo* results, an image processing tool was used for the analysis of tissue section from intact hearts and hearts 7, 14 and 21 days post injury as previously detailed (section 3.4.2). In total, 54 images were analysed from 13 different hearts were analysed and error bars represent standard deviation. Visual representation of the local collagen clusters (B) from model simulations and (C) from immunofluorescence images of tissue sections. The columns represent the time points 7, 14, and 21 days post-MI. Each cluster was assigned a random colour.

Histograms of collagen orientations were generated in order to compare the global alignment of collagen structures between the simulation predictions and the *in-vivo* data (Figure 3-12B-D and Figure 5-5). From the model results, it was clear that collagen became more aligned as the simulations progressed, starting as a mostly flat histogram at day 7 and a peak emerging at 14 days post-MI that spanned 45 degrees (Figure 5-5A). This peak remained present at 21 days post-MI, although was slightly less pronounced relative to the earlier time point at 14 days post-MI (Figure 5-5A). As was the case for local alignment, the global alignment results differed markedly for the *in-vivo* analysis when compared to simulation predictions. The *in-vivo* results

showed that by day 7, the collagen was much more aligned, with a major peak (Figure 5-5B). Similarly to model results, at day 14 the orientation histogram was mostly unimodal (i.e. having a single peak) with the single peak spanning about 90 degrees. At day 21, the shape of the orientations histogram changed drastically with two smaller peaks, representing an overall decrease in global alignment (Figure 5-5B).

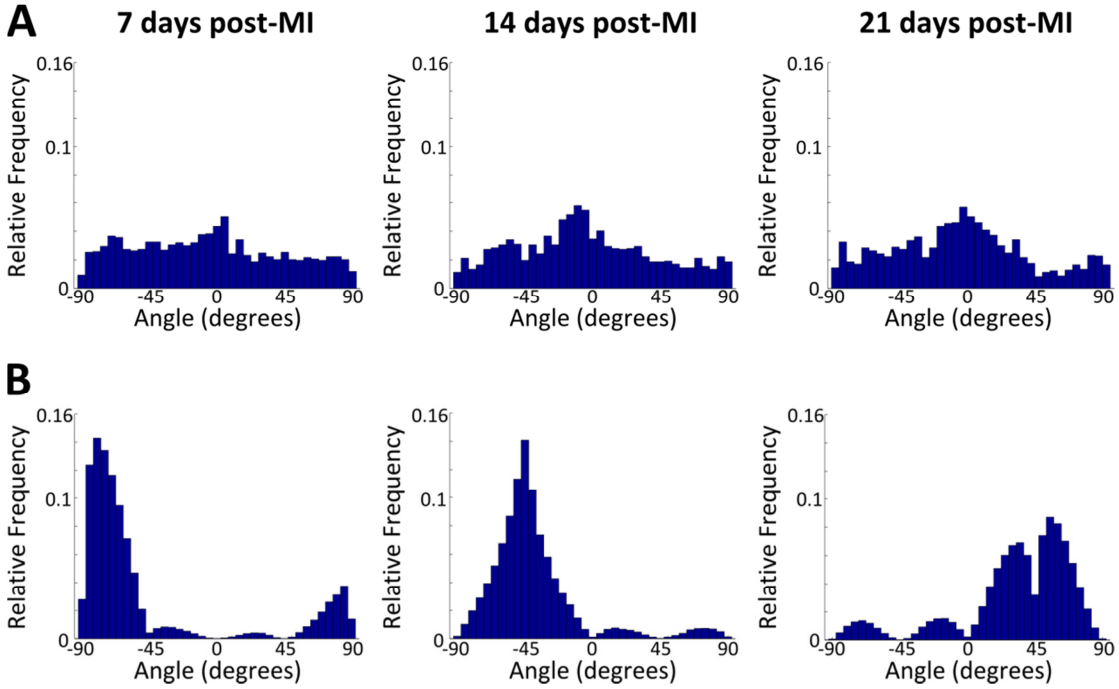

Figure 5-5 Comparison of global collagen alignment between model predictions and *in-vivo* data. (A) Histograms of collagen orientations computed from the output of model simulations, and (B) analysis of representative images of hearts tissue section at 7, 14, and 21 days post-MI. Collagen fibres are assumed bilinear with angles defined between -90° and 90°.

The global alignment patterns differed considerably between the *in-vivo* data and model predictions at 7 and 14 days post-MI. At 21 days post-MI, the global alignments decreased in both cases when compared with their respective results at day 14 post-MI.

5.3 Potential model refinement

In an effort to better understand the sources of discrepancies in measured local collagen alignment between *in-vivo* and *in-silico* results, adjustments to the model and their effects on simulation outcomes were investigated. In order to avoid continuous re-orientation of the collagen fibres, the parameter dictating how easily collagen can be re-orientated by neighbouring cells (κ) had its value change depending on the local collagen density (see section 4.4.3.7). Based on experimental evidence, it was assumed that the ability to re-orient collagen would be maximal for low collagen densities. As the cell deposited more collagen, the latter became increasingly difficult to re-orient. This effectively conferred the fibres a resistance to re-orientation, thus preventing instantaneous and potentially unrealistic collagen re-orientation by cells. Consequently, the early stages of the wound healing process during which alignment

rapidly increased as the chemotactic gradient promoted migration of the cell towards the wound had a long-lasting effect. Past that point, the alignment was continuously refined through small alterations of fibre orientations. In contrast, *in-vivo* data suggested that alignment increased in the first two weeks but decreased thereafter. The limitation in the ability of the cells to re-orient the collagen may have been too stringent. The effects of relaxing this rule were investigated by setting κ to a constant value corresponding to the value normally associated with very low collagen densities (κ=5).

Concerning the number of collagen clusters across the whole tissue (Figure 5-6A), the simulations with a constant κ value diverged from the control situation (i.e. κ varying according to collagen density) from about 300 simulation steps onwards. Instead of the decreasing number of clusters observed in the control case, the number of clusters for simulations with a constant κ showed large fluctuations until 1000 time steps. At this point, a steep increase in number of clusters was measured from 2553 ± 88 to 4510 ± 54 (n=11) clusters for the simulation with constant κ. The alignment subsequently remained relatively constant for the rest of the simulation. When considering only the local alignment of wounded region of the tissue, simulation results were also different for κ constant and κ variable (Figure 5-6 B). For both cases there was initially a sharp increase in the number of clusters to approximately 2015 ± 53 (n=11) as cells begin to produce collagen. The number of clusters for simulations with a constant κ decreased for 68 time steps before increasing sharply to a high number of clusters (i.e. less alignment) that remained approximately constant for the rest of the simulations (Figure 5-6 B). This differed from the control for which, at approximately 138 time steps, the number of clusters continuously decreased. Overall, setting κ constant led to a much lower degree of alignment in the model. The profiles obtained were more akin to those obtained from *in-vivo* data (Figure 5-4).

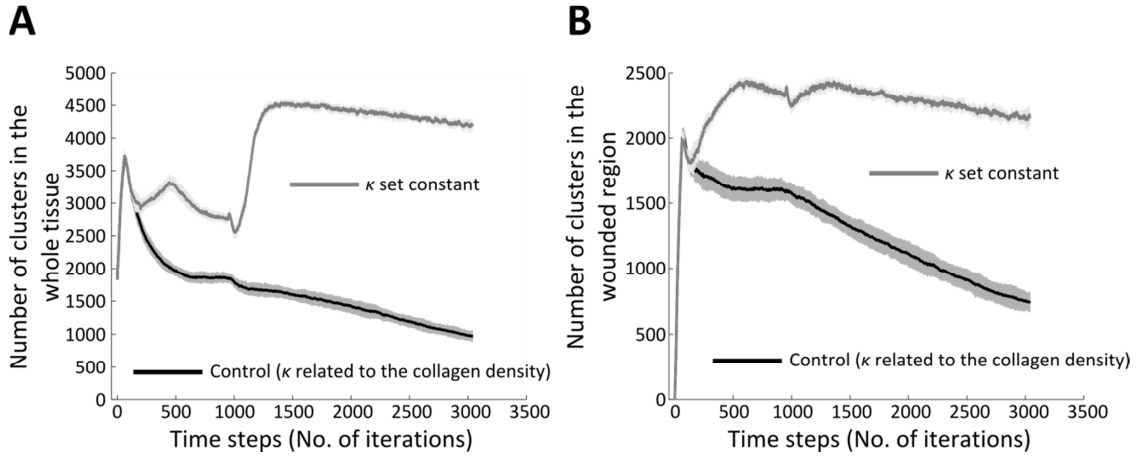

Figure 5-6 Altering the dynamics of collagen remodelling in the model. Number of clusters as a function of the simulation time steps when the parameter controlling the ability of the cell to re-orient collagen (κ) was set to a constant value, enabling collagen to be easily re-oriented by migrating cells or have its value dynamically adjusted depending on the collagen density (control). Either (A) the whole tissue or (B) only the wounded region were considered. The shaded areas represent the standard deviation across 11 simulations.

5.4 Model prediction of pharmacological intervention outcomes based on *in-vitro* experimental data

The model was used to predict the effects of potential pharmacological interventions on the dynamics of cardiac wound healing based on data collected from *in-vitro* experiments. The *in-vitro* experiments were carried out using a scratch assay experimental model with primary cardiac fibroblast cells (sections 2.4.2 and 2.4.4). The interventions investigated were the addition of recombinant human TGFβ1, synthetic ALK5 inhibitor and synthetic SU5402. For each of these interventions, the *in-vitro* results were used to create a new phenotype (i.e. set of specific model parameter values) of the fibroblast cell that was then implemented in the model. Model evaluation was based on both cell population changes (e.g. number of myofibroblasts) and local collagen alignment as measured using the cluster number metric (section 3.4.3.2).

5.4.1 Transforming growth factor-beta 1 (TGFβ1)

TGFβ1, one of the isoforms of the TGFβ superfamily, is known to promote fibroblast differentiation towards a myofibroblast fate, fibroblast proliferation and collagen production (Frantz et al., 2009; Nahrendorf et al., 2010; Souders et al., 2009). Based on these effects the addition of TGFβ1 post-MI is likely to promote increased collagen deposition and fibrosis. *In-vitro* experiments showed that the addition of TGFβ1 to the culture medium both positively impacted the differentiation rate of fibroblast cells (as measured based on the expression of a known myofibroblast marker, section 2.4.4) and reduced their migratory speed (section 2.4.2). These changes were implemented in the model to determine whether the effects of TGFβ1 on migration and differentiation would, in turn, have an effect on the model predictions for scarring. The probability functions controlling the rate of differentiation of fibroblasts towards a myofibroblast lineage in the model were altered to fit the experimental data obtained after addition of either TGFβ1 and or that of the vehicle control (BSA) (Figure 5-7 and Figure 2-22).

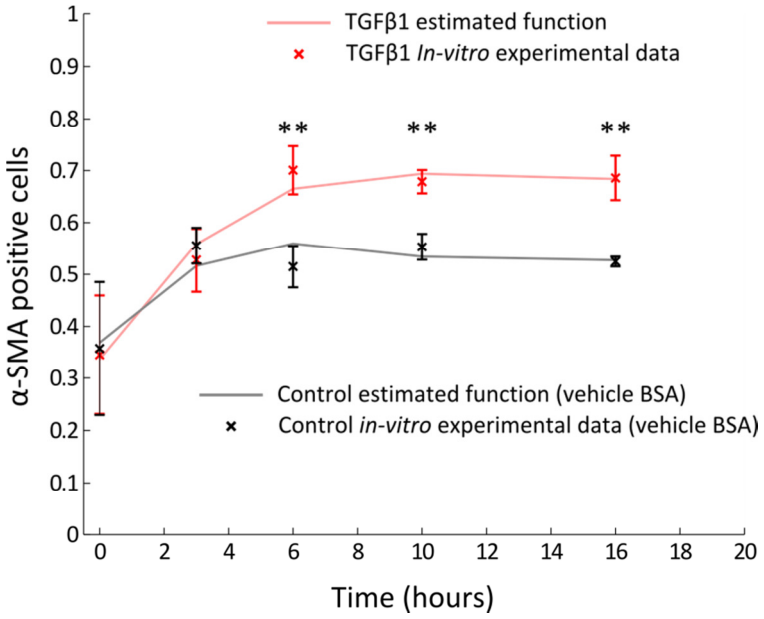

Figure 5-7 Differentiation probability functions fitted to *in-vitro* differentiation data. The proportion of cells expressing α-SMA (a myofibroblast marker) as a function of time during the course of a scratch assay experiment was determined for the case where TGFβ1 (red markers) or vehicle control (BSA, black markers) was added. The error bars represent the standard deviation across three independent experiments. The lines represent cubic polynomial fits (estimated function) with R^2 of 0.8490 and 0.9723 for the control and TGFβ1 cases, respectively. Independent t-test used to compute significance in comparison to control proportion at the same time point after scratch as ** (p-value < 0.01).

The probability functions for the TGFβ1 and BSA myofibroblast differentiation rates ($M_{EXP}(t)$) were approximated from *in-vitro* data with a polynomial function of order 3 (Figure 5-7) and were formally implemented in the model as shown in equations 5.1 and 5.2, respectively. The probability was assumed to be constant for time points greater than 16 hours.

$$M_{EXP}(t) = \begin{cases} 2.4111\times10^{-4}t^3 - 8.6\times10^{-3}t^2 + 9.77\times10^{-2}t + 0.3365 & t \le 16 \\ 0.6857 & t > 16 \end{cases} \quad 5.1$$

$$M_{EXP}(t) = \begin{cases} 2.7336\times10^{-4}t^3 - 8.2\times10^{-3}t^2 + 7.13\times10^{-2}t + 0.3686 & t \le 16 \\ 0.5299 & t > 16 \end{cases} \quad 5.2$$

In addition to the changes to the probability function controlling cell differentiation, the fibroblast migratory speed was set to 25 μm hr^{-1} for the TGFβ1 simulations, as opposed to 28 μm hr^{-1} for the BSA control case, as approximated from *in-vitro* scratch assay experiments (Figure 2-9).

The TGFβ1 differentiation probability function resulted, as expected, in higher numbers of myofibroblasts present throughout the simulation when compared to the control case (Figure 5-8A). For both simulations the number of myofibroblasts peaked at around 1009 time steps with 830±11 (n=11 simulations) and 644±16 myofibroblasts for TGFβ1 and control simulations, respectively. In terms of collagen alignment, the TGFβ1 simulations had fewer clusters (i.e. greater alignment) than the control simulations (p=0.006). Moreover, the average collagen

density within the wounded region was shown to be higher for TGFβ1 simulations compared to control (Figure 5-8C). Early into the simulations (~480 time steps) the average collagen density within the wounded region was higher for the TGFβ1 simulations ($p<0.001$) with a density of 1.48±0.0018 compared to 1.45±0.0034 for control simulations. During the time course of the simulations reductions in the differences in the number of myofibroblasts and collagen density in the wounded region between the TGFβ1 and control simulations were observed. According to the model, therefore, the phenotype associated with interventions with TGFβ1 would impact the remodelling outcome in terms of increased collagen alignment and density.

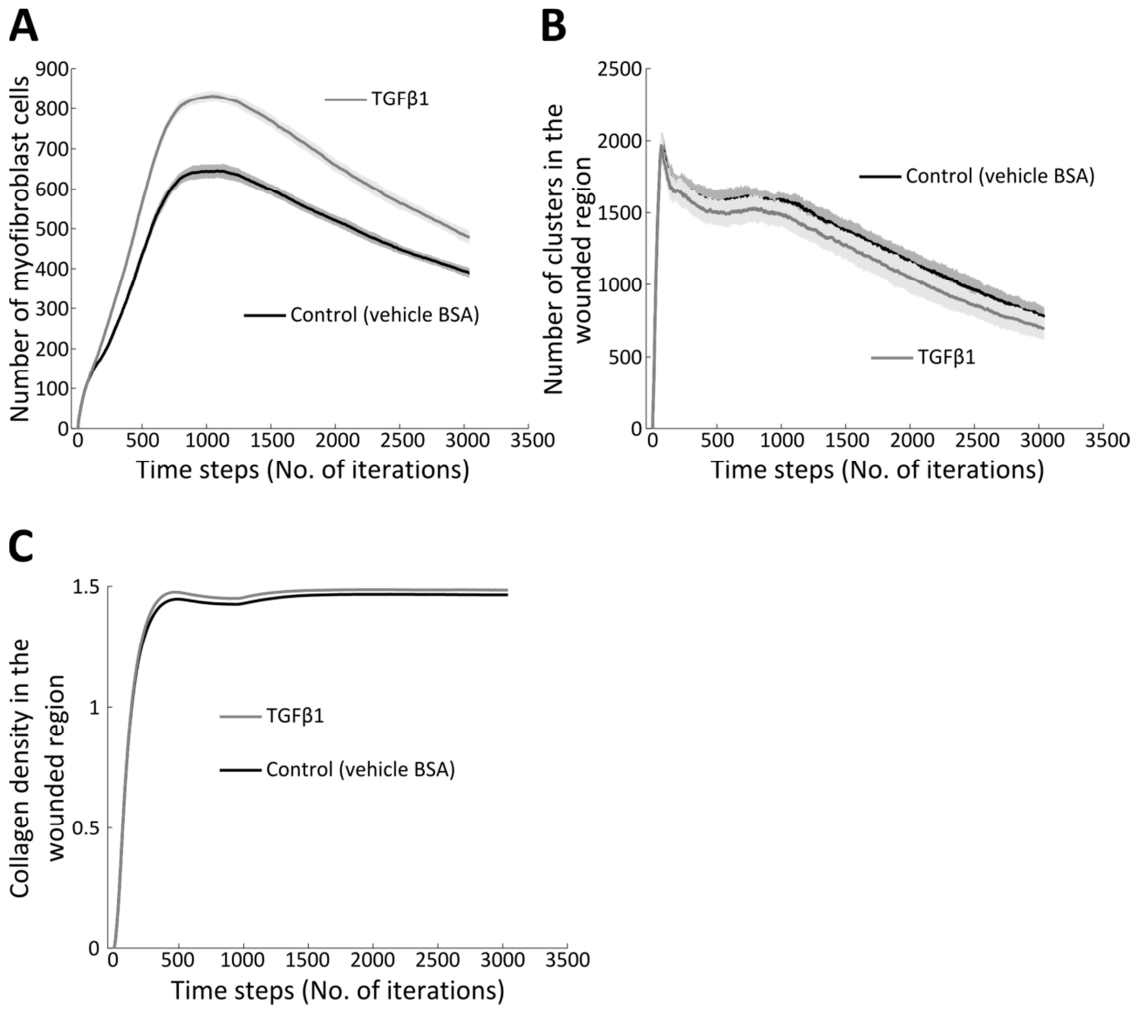

Figure 5-8 Model predictions of the effects of a TGFβ1 pharmacological intervention. Comparison of the changes in number of (A) myofibroblasts, (B) collagen clusters in the wounded region of the tissue and (C) collagen density in the wounded region throughout simulations for the parameters associated with TGFβ1 and the vehicle control (BSA). The shaded areas represent the standard deviation across 11 simulations.

5.4.2 Inhibition of activin receptor-like kinase 5

The activin receptor-like kinase 5 (ALK5) is a receptor of TGFβ1 (Inman et al., 2002). *In-vitro* TGFβ1 activity was inhibited with an ALK5 inhibitor resulting in a small detrimental effect on the differentiation kinetics during the course of a scratch assay when compared to the vehicle (DMSO) control (Figure 2-24). Inhibition of TGFβ1 has been shown to reduce fibrosis post-MI

(Okada et al., 2005). The probability functions controlling the rate of differentiation of fibroblasts towards myofibroblasts lineages in the model were altered to fit the experimental data (Figure 2-24) obtained after addition of either ALK5 inhibitor or the vehicle control (DMSO) (Figure 5-9).

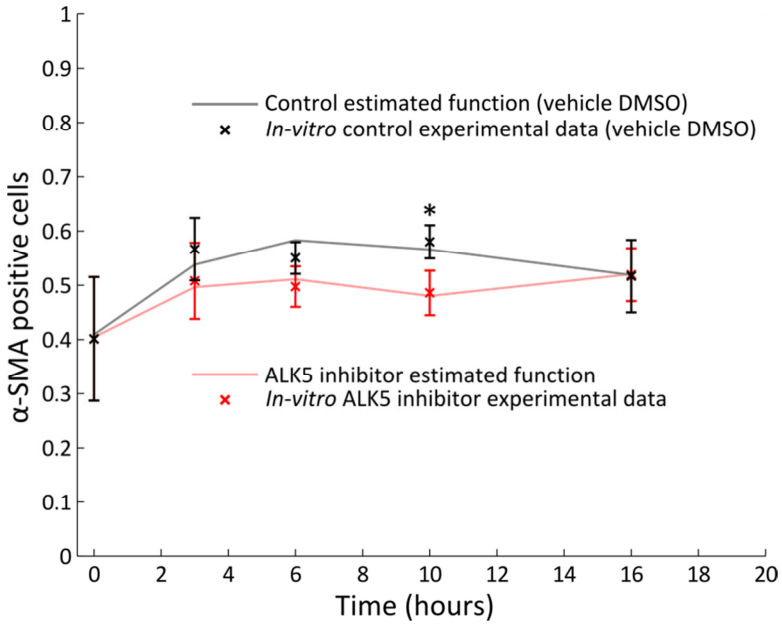

Figure 5-9 Differentiation probability functions fitted to *in-vitro* differentiation data. The proportion of cells expressing alpha-smooth muscle actin (α-SMA, a myofibroblast marker) as a function of time during the course of a scratch assay experiment was determined for the case where ALK5 inhibitor (red markers) or vehicle control (DMSO, black markers) was added. The error bars represent the standard deviation across three independent experiments. The lines represent cubic polynomial fits (estimated function) with R^2 of 0.8953 and 0.9583 for the control and ALK5 inhibitor cases, respectively. Independent t-test used to compute significance in comparison to control proportion at the same time point after scratch as * (p-value < 0.05).

The probability functions for the ALK5 inhibitor and DMSO data were based on a cubic polynomial fit and were formally implemented in the model as shown in equations 5.3 and 5.4, respectively.

$$M_{EXP}(t) = \begin{cases} 2.4908\times10^{-4}t^3 - 6.5\times10^{-3}t^2 + 4.79\times10^{-2}t + 0.4044 & t \le 16 \\ 0.5270 & t > 16 \end{cases} \quad 5.3$$

$$M_{EXP}(t) = \begin{cases} 1.8505\times10^{-4}t^3 - 6.3\times10^{-3}t^2 + 6\times10^{-2}t + 0.4093 & t \le 16 \\ 0.5145 & t > 16 \end{cases} \quad 5.4$$

Moreover, the cell speeds were also found to be affected by both the ALK5 inhibitor and DMSO control treatments. In addition to the changes to the probability function controlling cell differentiation, the instantaneous migratory speed was set to 25 μm hr^{-1} for the ALK5 inhibitor simulations, as opposed to 20 μm hr^{-1} for the control case (Figure 2-11). A reduction in the cell migratory speed with DMSO may be related to the compounds reported cytotoxic effects (Cao et al., 2007). In comparison with the control the ALK5 inhibitor resulted in an increased cell

speed, possibly related to the reduced number of myofibroblast cells observed *in-vitro*. Myofibroblast cells have been shown to migrate at slower speeds compared to fibroblast cells (Thampatty and Wang, 2007). A reduction in cell speed was observed with the addition of TGFβ1, along with an increase in the number of myofibroblast cells (Figure 2-9 and Figure 2-22).

Simulations with the ALK5 inhibitor associated phenotype showed a small decrease ($p<0.001$) in the number of myofibroblasts (649±12 myofibroblasts, n=11) when compared to the vehicle control (669±11 myofibroblasts, n=11), as expected due to the changes in the probability function controlling differentiation in the model (Figure 5-10A). In terms of collagen matrix remodelling, the number of clusters measured between approximately 150 and 900 time steps were different for the two conditions assessed, with ALK5 inhibitor simulations resulting in less aligned collagen fibres (Figure 5-10B). As the number of myofibroblasts was almost identical for that time frame, this difference was most likely due to the alterations of cell speed. At later time points, both conditions showed nearly identical collagen fibre alignments in the wounded region. The effect of ALK5 inhibitor measured was only transient. In comparison when considering the whole tissue section ALK5 inhibitor simulations predicted an increased level of alignment compared to control ($p=0.04$). Conversely, inhibition of ALK5 has been shown to reduce the levels of collagen I and α-SMA in the non-infarcted regions (Tan et al., 2010).

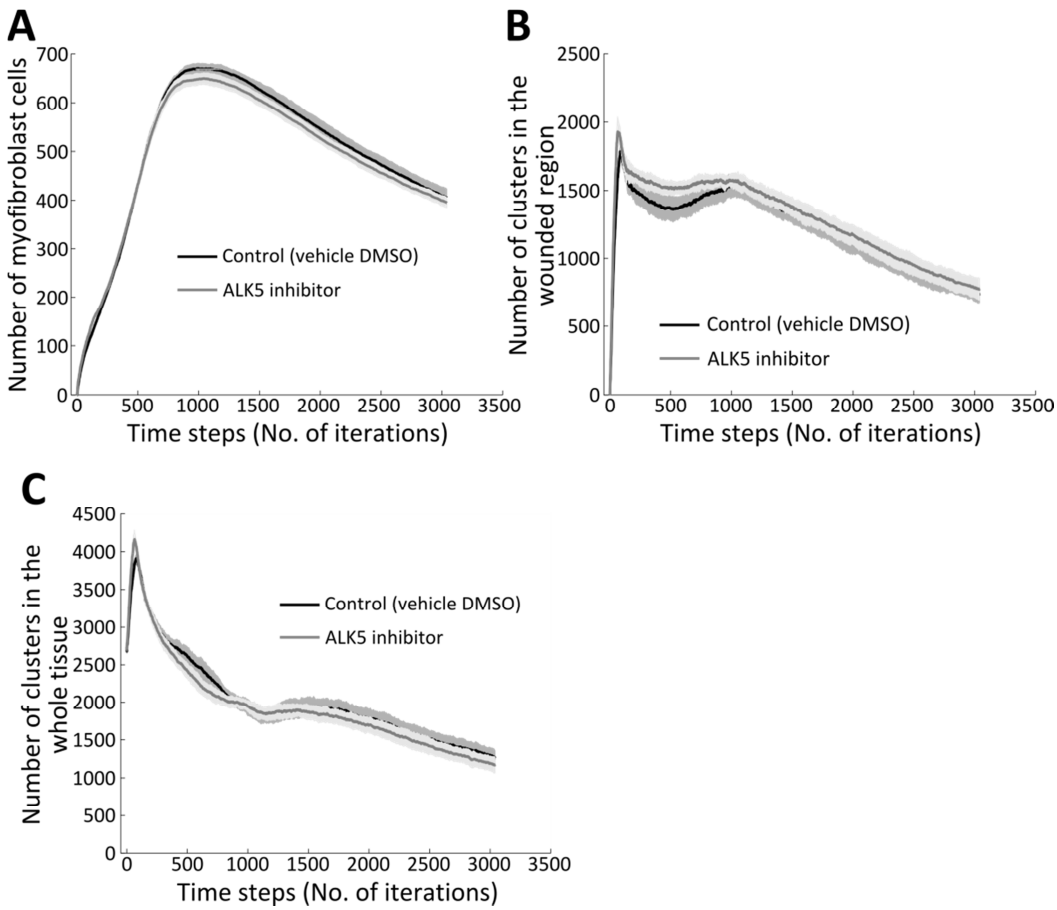

Figure 5-10 Model predictions of the effects of ALK5 inhibitor pharmacological intervention. Comparison of the changes in number of (A) myofibroblasts, (B) collagen clusters in the wounded region of the tissue and (C) collagen clusters in the whole tissue throughout simulations for the parameters associated with ALK5 inhibitor and the vehicle control (DMSO). The shaded areas represent the standard deviation across 11 simulations.

5.4.3 Inhibition of FGF receptor 1

Inhibiting the tyrosine kinase activity of FGFR1 using the compound SU5402 only resulted in very mild, non-significant effects on both *in-vitro* fibroblast differentiation kinetics (Figure 2-24) and migratory speed (Figure 2-11) when compared to the vehicle control (DMSO). The probability functions controlling the rate of differentiation of fibroblasts to myofibroblasts in the model were altered to fit the experimental data (Figure 2-24) obtained after addition of either SU5402 or the vehicle control (Figure 5-11).

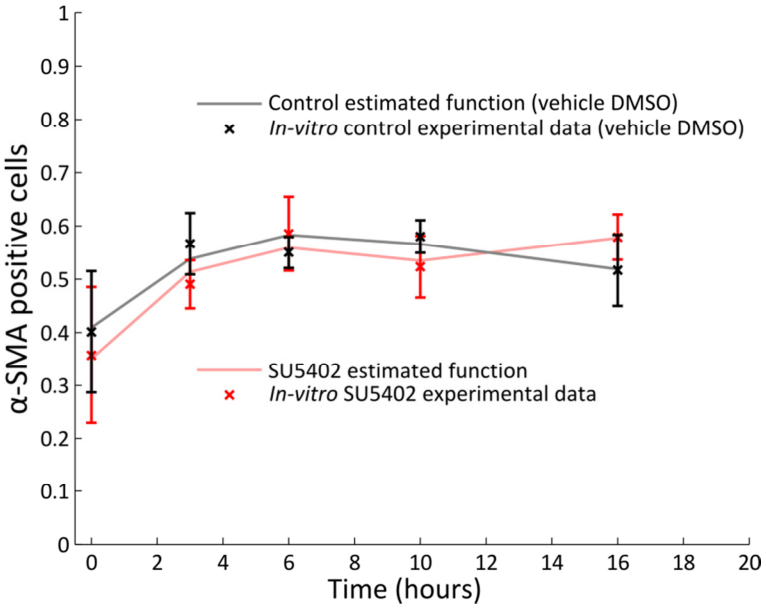

Figure 5-11 Differentiation probability functions fitted to *in-vitro* differentiation data. The proportion of cells expressing alpha-smooth muscle actin (α-SMA, a myofibroblast marker) as a function of time during the course of a scratch assay experiment was determined for the case where SU5402 (red markers) or vehicle control (DMSO, black markers) was added. The error bars represent the standard deviation across three independent experiments. The lines represent cubic polynomial fits (estimated function) with R^2 of 0.8953 and 0.9599 for the control and SU5402 cases, respectively.

The probability functions for the SU5402 and DMSO data were based on a cubic polynomial fit and were formally implemented in the model as shown in equations 5.5 and 5.4, respectively.

$$M_{EXP}(t) = \begin{cases} 3.3965\times10^{-4}t^3 - 9.5\times10^{-3}t^2 + 7.97\times10^{-2}t + 0.3509 & t \le 16 \\ 0.5777 & t > 16 \end{cases} \quad 5.5$$

In addition to the changes to the probability function controlling cell differentiation, the instantaneous migratory speed was set to 19 μm hr^{-1} for the SU5402 simulations, as opposed to 20 μm hr^{-1} for the vehicle control case (Figure 2-11).

The effects of altering the differentiation rate and migratory speed on the model predictions were investigated. The cell phenotypes for SU5402 and control resulted in marked differences in terms of collagen alignment in the model (Figure 5-12B). Throughout the simulations, the number of collagen clusters was consistently lower (i.e. higher alignment) for SU5402 when compared to the vehicle control. The model parameters relating to SU5402 resulted in a larger number of myofibroblast cells throughout the entire simulation when compared to the control (Figure 5-12 A). A maximum difference in the number of myofibroblast cells ($p<0.001$) was reached between the SU5402 simulation (778 ± 11 myofibroblasts, n=11 simulations) and the control simulation (669 ± 9 myofibroblasts, n=11 simulations) at 1073 time steps (~9 days post-MI).

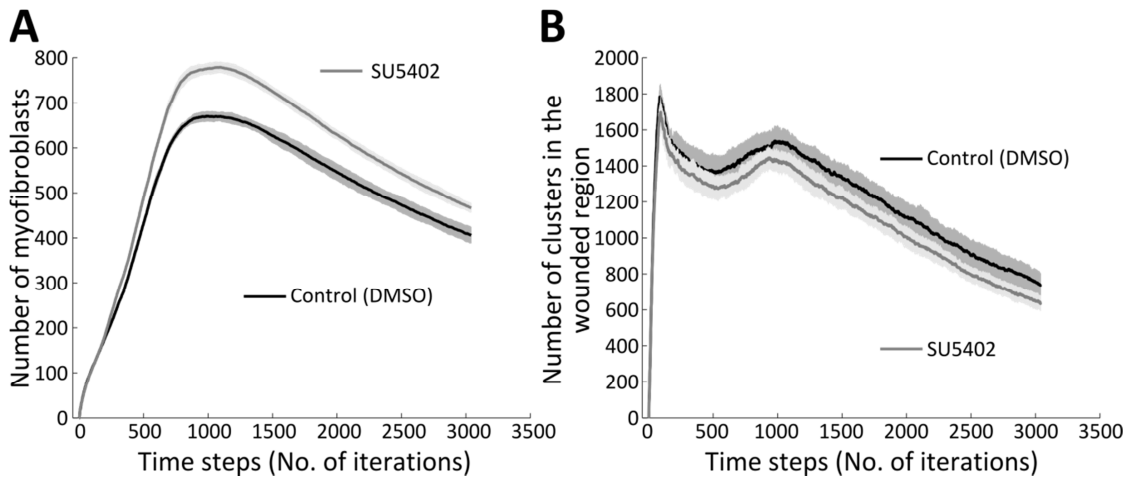

Figure 5-12 Model predictions of the effects of SU5402 pharmacological intervention. Comparison of the changes in number of (A) myofibroblasts and (B) collagen clusters in the wounded region of the tissue throughout simulations for the parameters associated with SU5402 and the vehicle control (DMSO). The shaded areas represent the standard deviation across 11 simulations.

In summary, the model has been used to generate predictions for the following pharmacological interventions recombinant human TGFβ1, ALK5 inhibitor and SU5402, effecting either TGFβ1 or FGF signalling. The addition of TGFβ1 to cardiac fibroblast cells *in-vitro* resulted in an increase in the relative number of myofibroblast cells and a decrease in the cell speed. Model predictions were generated with these parameters and predicted an increase in the number of myofibroblast cells, collagen density and alignment. *In-vitro* inhibition of TGFβ1 signalling was carried out with an ALK5 inhibitor. This intervention had the opposite effects to TGFβ1 on *in-vitro* fibroblasts with decreased relative numbers of myofibroblasts and increased cell speeds. The model predicted a reduction in the number of myofibroblast cells and a higher collagen alignment during the early stages of the simulation. Analysing the whole tissue showed an increase in the level of collagen alignment. *In-vitro* a pan FGF inhibitor SU5402 resulted in a small increase in the relative number of myofibroblast cells during the later stages of the scratch assay experiment (t=16 hours) and a small reduction in cell speed. The model predicted that these effects on fibroblast cells would result in an increased number of myofibroblasts and increased collagen alignment.

5.5 Discussion

A greater understanding of cardiac wound healing in general and of the development of fibrotic scar tissue in particular is required to devise adequate therapeutic strategies. A predictive model combined with *in-vitro* and *in-vivo* experimental investigations could facilitate the design of specific treatments for the manipulation of scarring. Optimal healing depends on a balance between the prevention of tissue rupture by the formation of a scar of sufficient strength and the minimisation of pathological remodelling resulting from over-scarring (fibrosis). The mathematical model could provide information about how the local injury environment could be conditioned to attain this optimal balance through modulation of cell behaviours and properties.

In this chapter the model's ability to predict the collagen organisation of the scar produced post-MI was investigated. The comparisons made between *in-silico* and *in-vivo* results focused on the alignment of collagen I, given that the increasing level of collagen over time after injury is a key mechanism in wound healing (Whittaker et al., 1989). The local collagen alignment was quantified with a clustering measure developed and discussed previously (section 3.4.3.2) and the global alignment was investigated with histograms of the collagen orientations. These measurements are complementary; global alignment reflects the overall direction bias of collagen fibres regardless of their location. Extensive remodelling is necessary to alter global alignment. In contrast, local alignment is the measure of the tendency of collagen fibres to form small pockets or clusters that are highly aligned in a close neighbourhood but not necessarily at the gross tissue scale. Local alignment is more likely to be influenced by small changes of the collagen matrix introduced by local fibroblast cells. Local alignment measured for the *in-vivo* data initially increased in agreement with the model predictions. However, at day 21 post-MI the local alignment decreased to a level close to that of an intact heart (chapter 3, Figure 3-11), a behaviour that contradicted the continuously increasing alignment predicted by the model. There were also discrepancies between the global alignment results from simulations and *in-vivo* data. The *in-vivo* data showed a decrease in global alignment between day 7 and later time points. In contrast, a slight increase was measured for the model data over the same period of time. A study where post-MI hearts were imaged *ex-vivo* using a method akin to magnetic resonance imaging (MRI) reported results consistent with the model data presented here (Strijkers et al., 2009). Fractional anisotropy, a measure of collagen alignment, was shown to continuously increase after injury for the period of time considered in the mathematical model (up to 21 days post-MI). Increasing fractional anisotropy represents increasing levels of collagen alignment.

The discrepancies observed may have been due to the model itself, the *in-vivo* data or the way the *in-vivo* hearts were analysed. In the model, the initial wounded region is represented by an empty space with no collagen fibres. As cells migrate inwards from the flanking healthy tissue, they produce collagen fibres in a direction partially influenced by that of the local collagen matrix. The local alignment measurements of neighbouring collagen fibres are thus likely to be higher and more variable, than the global alignment measurements because of this model property. A known limitation of the cardiac wound healing model described in this study is the omission of mechanical forces. Mechanical forces can develop at the infarct boundary zone as a result of the differences in structural properties between healthy and scar tissue. A model of cardiac wound healing developed by Holmes and co-authors showed that the presence of a mechanical guidance cue (cell migration influenced by mechanical stimuli) resulted in increased collagen alignment (Rouillard and Holmes, 2012). In their model, the mechanical guidance was implemented as a tension field represented by a cumulative Gaussian function with a maximum

tension at the infarct border and a mostly flat profile in both the infarct and healthy remote tissues. Depending on the location of the infarct considered, the strain was uniaxial (in the circumferential direction) or equibiaxial (in both circumferential and longitudinal directions). The tension field influenced the direction of cell migration and consequently the remodelling of the collagen matrix. The study showed that mechanical guidance in the presence of a uniaxial strain was necessary to support long-term alignment of the collagen matrix. The introduction of a mechanical cue in the mathematical model described here is likely to result in increased global collagen alignment in agreement with the observed *in-vivo* data as it affects the collagen matrix at a tissue level. This is in contrast with other cues such as contact guidance, which acts at a local level.

When qualitatively comparing the collagen I alignment between intact hearts and hearts 21 days post-MI, the overall collagen alignment appeared to be similar, especially, when contrasted with the highly aligned collagen structures observed at days 7 and 14 post-MI (see Figure 3-4). These results seemed to indicate that the changes in collagen alignment during healing post-MI were transient. However, there were visible differences between the sections from intact hearts and those from hearts at 21 days post-MI that are not related to the alignment of the collagen, but to packing density instead. At 21 days post-MI the collagen fibres appeared much closer together. One possible explanation for this is the decrease in the number of cardiomyocytes which may cause the honeycomb-like architecture observed in intact tissue to disappear and facilitate the the continuous deposition of collagen by infiltrating cells (Frangogiannis et al., 2002; Sun et al., 2002). This may explain why the collagen fibres appeared more compact at 21 days post-MI compared to intact hearts, while having a similar apparent degree of alignment (Cleutjens et al., 1995b). This change in compactness post-MI is likely to be a result of a process termed infarct expansion, which is described as the disproportionate thinning and dilatation of the infarct region (Weisman and Healy, 1987). Neither the model, nor the image processing tool were equipped to capture changes in packing density of the fibres, as both use evenly spaced sampling strategies. Similarly, because the model only considers the dominant collagen orientation at each grid point, it was not possible to re-create the situation where collagen fibres would be overlaid on top of one another, which would result in an apparent decrease in local collagen alignment. Both the model and the image processing tool would have to be appropriately adjusted in order to recapitulate and quantify the changes in collagen structures that were qualitatively observed during visual inspection of histological heart sections image. The clustering measure could be adjusted to take into account local collagen density in addition to its alignment. This new metric would be able to differentiate between dense regions of aligned fibres (high packing density) and region of similar alignment but with a lower density.

The differences in the collagen alignment measurements between the model predictions and *in-vivo* tissue sections could also be related to other model assumptions, such as the ability of the

cells to remodel the collagen matrix or to produce collagen. The sensitivity of the model to changes in the assumptions was investigated. The model property that defines the extent to which cells can alter the collagen matrix (model parameter κ) has also been investigated. By default the value of κ was inversely related to the collagen density, so that at high collagen densities the cells would have a very limited ability to reorient the surrounding matrix. This dynamic behaviour was replaced with a constant value for κ, which was used previously in two dermal wound healing models (Dallon et al., 1999; McDougall et al., 2006). Interestingly, this change did not affect early remodelling dynamics as these were most likely to be solely dictated by the chemotactic gradient (Figure 5-6). The cells situated in the surrounding tissue were attracted into the wound and reoriented the collagen along their migratory trajectories. After the depletion of the chemotactic gradient, the cells' direction was dependent upon the local collagen orientation, their previous motion and neighbouring cells. Using the default model configuration, local alignment increased with time. In contrast, setting κ to a constant value resulted in a steep decrease in alignment. The local alignment of the matrix during the final part of the simulation was similar to that of a random matrix. The local alignment was 2.4 fold lower compared to the *in-silico* control (κ not constant). It might be biologically and mechanically unrealistic for collagen fibres to be so easily re-oriented by migrating cells. The ability of cells to contract the collagen matrix has been shown to be inversely proportional to the density of the collagen matrix (Baxter et al., 2008; Loftis et al., 2003). This could indicate that the model assumption is correct, but requires some adjustment. In particular, the restrictions imposed on cell remodelling capabilities for high collagen densities could be relaxed. A rigorous experimental investigation of collagen matrix remodelling by cells would be necessary to determine which case is most likely to be relatable to the *in-vivo* dynamics of cardiac wound healing. Such an experiment could be carried out by seeding primary cardiac fibroblast in collagen gels of various concentrations and determining how the cells remodel the matrix overtime. One possible remodelling measurement is the change in surface area of the gel as it gets contracted by the cells (Loftis et al., 2003).

The model was used to predict the effect on collagen organisation of pharmacological interventions with growth factors known to alter one or multiple processes involved in wound healing in the heart: TGFβ1 and FGF. For each intervention, parameter values such as cell speed and differentiation rate were derived from *in-vitro* experimental investigations (see section 5.4). The parameter values were then used to carry out simulations and predict changes in the collagen arrangement (relatable to the degree of fibrosis). The changes in TGFβ1-induced differentiation dynamics were incorporated into the model and resulted in a larger myofibroblast population in simulations, which in turn led to an increased local alignment when compared to the control case. This is consistent with reports of TGFβ1 promoting fibrosis post-MI (Kuwahara, 2002). For TGFβ1 the differentiation probability was higher than the control.

Therefore, an increased number and proportion of myofibroblast cells in the model for TGFβ1 was anticipated. In another study, interleukin-13 knockout mice with induced myocarditis (cardiac muscle inflammation) showed increased levels of TGFβ1 and impaired cardiac function (Cihakova et al., 2008; Leask, 2010). Another pharmacological intervention that was investigated was based on the inhibition of the TGFβ pathway. Experimentally this was done by the addition of ALK5 inhibitor (Inman et al., 2002). The effects on migratory speed and differentiation rates were quantified *in-vitro*. The opposite effects to that of TGFβ were observed, with a decrease in the fibroblast differentiation rate, which agreed with a previous study (Tan et al., 2010). For simulations performed with the corresponding parameter values, lower alignment was predicted early on (< 8 days post-MI), due to the lower number of myofibroblasts when compared to the control. This is consistent with studies where inhibition of ALK5 reduced scar formation after glaucoma surgery and attenuated systolic dysfunction post-MI in rats (Tan et al., 2010; Xiao et al., 2009). More specifically, treatment with an inhibitor of ALK5 led to a significant reduction in collagen I deposition in the intact tissue post-MI.

Finally, the model was used to predict the effects of the inhibition of the FGF pathway on the properties of cell-mediated scarring post-MI. Experimentally this was done using the compound SU5402, which was found to eliminate the cardiac functional recovery induced with FGF-1 (Palmen et al., 2004). Both FGF-1 and FGF-2 were described as cardioprotective (Detillieux et al., 2003). In rats with induced injury in ear tissue, SU5402 was shown to decrease the wound closure rate (Kaftan et al., 2012). In another study, the deletion of FGF-2, which could potentially be emulated by the administration of SU5402, led to reduced fibroblast proliferation and collagen deposition in mice post-MI (Virag et al., 2007). FGF pathways could thus be used to control the balance between the need for the formation of a scar and risk of fibrosis. However, *in-vitro* experiments using primary cardiac fibroblasts did not show any significant changes in either migratory speed or differentiation rate in the scratch model after addition of SU5402 when compared to the control case. This difference was enough, however, to predict an effect on scarring properties when using these experimental values in the model. Indeed, a higher degree of alignment was attained for conditions mimicking the SU5402 intervention, mostly due to the increase in the myofibroblast population size. It is interesting to note that the effects of SU5402 on wound healing have been reported as dose dependent (Kaftan et al., 2012). A 5-fold increase in the administrated dose of SU5402 led to a 2-fold increase in the time taken for tympanic membrane wounds to heal in rats. Here, experiments were carried out at a single concentration (2 nM), which could explain the lack of a measurably significant effect.

Based on the assumption that a high degree of collagen alignment is detrimental to longer term cardiac function post-MI, the model predicted that both inhibiting FGF with SU5402 and a gain of function of TGFβ1 signalling interventions would have a negative impact on the wound process. Moreover, the model predicted that the ALK5 inhibitor intervention could have a

beneficial effect in the wounded region during the early stages of wound healing. These interventions were investigated experimentally in a 2-dimensional (2D) scratch assay. The 2D scratch assay is limited and does not incorporate all of the components involved during *in-vivo* cardiac wound healing. A thorough experimental investigation of the effects of these interventions would involve assessing the effects of administrating these interventions in animal models post-MI. The analysis of these hearts post-MI could then be used to validate the *in-silico* model predictions.

These three interventions (ALK5 inhibitor, TGFβ1 and SU5402) demonstrated how the computational model and the experimental framework complemented each other because parameters were in most cases, corresponding to a measureable quantity. New parameters could be investigated as soon as the corresponding data was generated. The correlation between simulation outcomes and experimental data could be further improved. Parameter space optimisation methods would most likely result in parameter values giving a better fit, although this may also undermine the biological relevance of the experimentally approximated model parameters. Refinements of the experimental model, together with improvements of the core model behaviours, should be favoured instead. Suggestions along those lines will be discussed in the next chapter.

Chapter 6

Future work

This study has used individual cardiac fibroblast cell behaviours and properties obtained from *in-vitro* experiments to inform and refine a mathematical model of cardiac wound healing with a focus of cell-mediated scar formation. The mathematical model was validated and compared with *in-vivo* measurements of the properties of the scar post-MI. The experimentally attained baseline model parameters were altered to simulate the effects of pharmacological interventions on cell behaviours and properties, and consequently on the predicted properties of the post-MI wound. These predictions were then compared to relevant studies in the literature.

Further refinements and improvements in both the experimental and computational components of this project fall into three broad categories:

- Improvement of the *in-vitro* experimental model and quantification of additional cell behaviours and properties.
- Refinement of the methodology used for *in-vivo* data generation.
- Extension of the computational model, including new cell behaviour and more realistic representations of the physical environment of the wound post-MI.

6.1 Further *in-vitro* investigation of cell behaviours and properties

While every effort were made to only use model parameters whose value could be measured experimentally, it was necessary to make approximations or assumptions in some cases. Such parameters include the ability of cells to alter the matrix, the effect of the collagen and chemoattractant on the fibroblast speed and direction, dose-dependent effects of TGFβ1 on differentiation, and the rates of ECM secretion and degradation (Figure 6-1). Each of these model parameters, with the proposed corresponding experimental approaches, will be discussed in detail in the following sections.

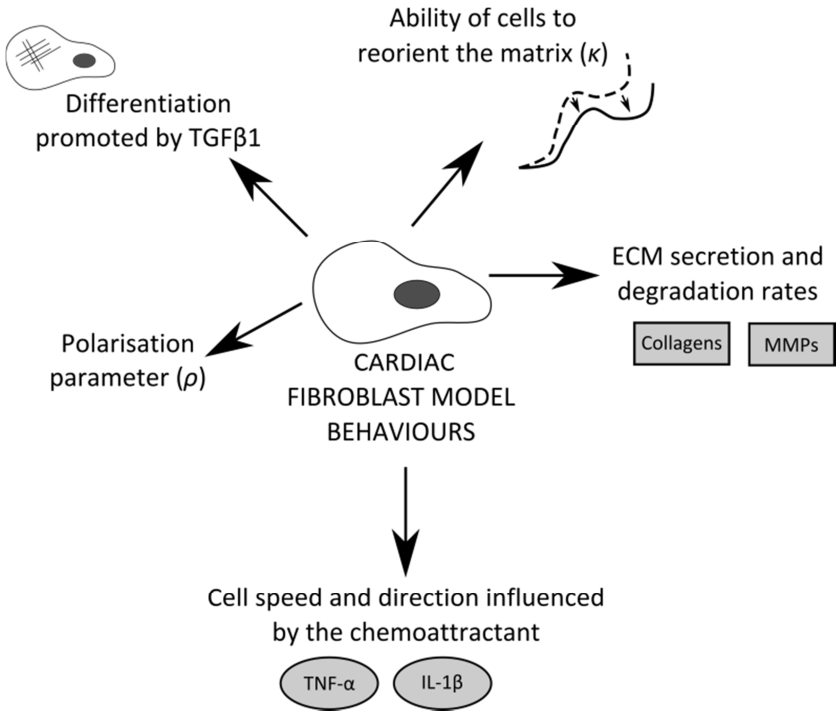

Figure 6-1 Potential refinements of cell behaviours in the computational model.

6.1.1 Ability of the cells to alter the matrix

In the model the parameter κ was used to define the extent to which cells could reorient the local collagen matrix. The value of κ was assumed to decrease with an increasing collagen density, in other words the cells had a reduced ability to reorient dense collagen fibres. This assumption was based on previous experiments that measured the force applied by fibroblasts onto collagen matrices of varying stiffness (Freyman et al., 2002). The relationship between κ and the collagen density was given by a Hill function (see section 4.4.3.6). The value of κ corresponding to low collagen densities was estimated from a previously described dermal wound healing model (Dallon et al., 1999; McDougall et al., 2006) while the value at high densities was set so that no re-orientation of the collagen matrix would occur. A more accurate estimate for κ and the relationship with the collagen density are required. However, the experimental setup used throughout this project was not suitable for such investigations. Some potential approaches are described here.

The relationship between κ and the collagen density could be evaluated by seeding primary cardiac fibroblasts onto 3-dimensional (3D) collagen gels of different concentrations and measuring the level of collagen remodelling using a gel contraction assay (Chiu et al., 2013). As the experiment progresses, cells will remodel the collagen matrix. The degree of remodelling is then estimated by analysing the level of collagen compaction. A high degree of collagen compaction can be associated with a high degree of collagen remodelling. Second harmonic generation (SHG) microscopy images of these collagen gels can be processed automatically to compute their spatial correlation, which in-turn informs on collagen compaction (Chiu et al.,

2013). The relationship between collagen compaction and collagen density could then be assessed to provide a more accurate representation of these two variables in the model.

6.1.2 The relationship between cell velocity and collagen fibres properties

In the model, the impact of the local collagen matrix on cell migration velocity was two-fold. First, migration direction was influenced by the mean orientation of the surrounding fibres. The degree of influence was controlled by a polarisation parameter ρ. For smaller values of ρ migration direction is mostly determined by the cell's previous motion (i.e. momentum), while for larger ρ values it is almost entirely dictated by the orientation of neighbouring fibres. The collagen matrix also influences the migration speed of the cells, with the latter being inversely proportional to the local collagen density.

In this study, ρ was estimated from *in-vitro* experiments which studied the effects of collagen fibre anisotropy on the velocity of migrating fibroblast cells (Dickinson et al., 1994). However, recently proposed experimental approaches could be applied to obtain a better estimate. The proposed experiments would study the influence of the collagen orientation on the cell migration direction. Primary cardiac fibroblast cells would be cultured on three different ECM patterns: no ECM, horizontally aligned ECM and vertically aligned ECM (Figure 6-2). The horizontally and vertically aligned ECM patterns could be created by either physically patterning collagen using a microbrush (Pijnappels et al., 2008) or by using silicon micro-/nano-gratings, whose thickness and spacing can be fully controlled (Crouch et al., 2009).

Given that a scratch assay may not be suitable for these experiments (the scratch may alter the collagen/grating structure), cells could be cultured on one half of the surface by seeding cells onto a tilted culture plate instead. This way, the other half would be cell-free, thus promoting cell migration as for a scratch. The cells would be imaged using time lapse phase contrast microscopy, manually tracked and this migratory data analysed using the effectiveness measurement (Arboleda-Estudillo et al., 2010; Deforet et al., 2012) previously described in this work (section 2.3.1). The effectiveness measurement calculates the level of movement directionality of a cell in the range [0,1], where a value of 1 indicates that a cell migrates along a straight trajectory. The relationship between the directional change of a cell and the dominant collagen orientation could then be estimated.

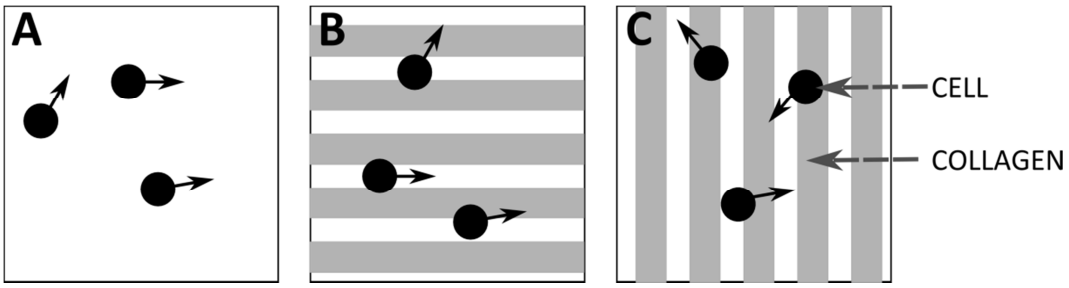

Figure 6-2 Measuring the effects of local collagen orientation on cell migration direction. Cardiac fibroblast cells (black circles) cultured on three different surfaces (A) no collagen, (B) horizontal and (C) vertical collagen patterns (grey).

The relationship between collagen density and fibroblast migratory speed could be estimated by culturing cells on different collagen densities using a similar approach. Culture vessels could be coated with a thin layer of collagen gel of controlled thickness and density (Matsuo et al., 2001).

6.1.3 Effects of chemotaxis on the cell migratory speed and direction

For this work, the effects of pro-inflammatory stimuli TNF-α and IL-1β, and anti-inflammatory stimulus TGFβ1 on cell migratory speed were investigated. However, these experiments did not measure does-dependent changes in cell speed but rather were limited to a single concentration per stimulus. Moreover, the chemotactic effects of these stimuli were not measured as the compounds were mixed homogeneously across the entire culture medium volume, thus not presenting the concentration gradient found *in-vivo*. The effects of the various stimuli could be better investigated using Boyden chamber assays (Mitchell et al., 2007). A Boyden chamber assay involves two vertically stacked wells. Cells are seeded onto the upper compartment which is lined with a porous membrane, and a chemoattractant is added to the bottom well. A gradient is established and remains for a few hours before the eventual equilibration of the two media. If the stimulus used has a chemotactic effect on the cells, a significant number of cells will migrate through the membrane to the bottom of the well, where they can be counted. Unstimulated cells will be less likely to cross the membrane as it requires their deformation due to the pore size (Muinonen-Martin et al., 2010). Results from these experiments could thus be used to estimate the relationship between the concentration of both pro- and anti-inflammatory stimuli and cell migratory speed.

One limitation of Boyden chamber experiments is that they do not usually allow for cell migration to be imaged. Therefore, these experiments cannot provide quantitative data related to the trajectory of the cells (e.g. degree of bias in migration induced by the chemoattractant) or to mechanisms such as contact inhibition of locomotion. Cell migration can be directly visualised using an Insall chamber, which is a variation to the bridge chamber method (Muinonen-Martin et al., 2010). A coverslip on which cells are attached is placed face down onto the chamber filled with culture medium (without chemoattractant). Another well surrounding the first one is filled with a chemoattractant. The chemoattractant well is recessed so that the gap left under the

coverslip prevents fluid flow while allowing the diffusion of the chemoattractant and the formation of a stable gradient. Viewing bridges on either side of the main well allow imaging of the cell as they migrate in the direction of the gradient using time-lapse light or fluorescence microscopy. Cell tracking methods can then inform on the dynamics of migration. The chemotactic effect and the mechanical stress resulting from injury could be studied simultaneously in an Insall chamber by scratching either side of the coverslip prior to the start of the experiment.

6.1.4 Dose dependent response of cardiac fibroblasts to TGFβ1

The experimental results for fibroblast differentiation into myofibroblasts presented in this work were obtained by quantifying the proportion of myofibroblast cells present along the edge of the wound at different time points following a scratch. In order to do so, immunofluorescence microscopy was used to evaluate the expression of α-SMA, a myofibroblast marker. These experiments were extended to study the effects of TGFβ1, a known promoter of myofibroblast differentiation (Chen and Frangogiannis, 2012; Souders et al., 2009; Walker et al., 2004). TGFβ1 was added to the culture medium at a concentration of 2 ng ml^{-1} based on previous work (Petrov et al., 2002) and its effect on the proportion of myofibroblasts was assessed. Moreover, the effects of a single concentration of ALK5 inhibitor (10 μM), an inhibitor of the TGFβ1 pathway, were studied in the same way. The addition of TGFβ1 did lead to a significant increase in the expression of α-SMA. The mathematical model was setup so that the differentiation would follow the same time profile as that observed experimentally. However, studies suggest that the response to TGFβ1 is dose-dependent (Petrov et al., 2002). It would thus be necessary to repeat these experiments with varying concentrations of TGFβ1 to better understand this effect on the cells. In addition, during wound healing, the cells most likely respond to a spatial gradient of TGFβ1 rather than to a single homogeneous concentration. It would also be interesting to determine how cells would respond to a TGFβ1 gradient generated, for example, using an Insall chamber as discussed above.

6.1.5 Collagen matrix production and degradation by fibroblast cells

In the mathematical model, cells are responsible for the formation and maintenance of the collagen-based scar, mainly through deposition and degradation. The parameters controlling both these behaviours were adapted from a dermal wound healing model (McDougall et al., 2006). As myofibroblasts were previously shown to secrete increased levels of collagen (Ignotz and Massagué, 1986; Souders et al., 2009), the associated parameter values were modified accordingly. However, the parameter values used are unlikely to be representative of the true rates of collagen deposition and degradation *in-vivo*. Improved estimates could be derived from *in-vitro* experiments where collagen I and III expression are quantified using techniques such as reverse transcription quantitative polymerase chain reaction (Fowlkes et al., 2013). Similar

analyses could be carried out for MMP-2 and MMP-9, two proteases that are known to degrade collagen matrices (Turner and Porter, 2012). While gene expression analysis does not inform directly on how much collagen is actually deposited or degraded, they can be used to estimate the relative effects of different experimental conditions (e.g. relative changes in expression between fibroblasts and myofibroblasts).

Degradation rate could be better characterised using zymography, an electrophoretic technique where proteolytic enzymes are detected, and their activity estimated, based on substrate degradation (Loftis et al., 2003). Not only could such a method be used to assess the activity of MMPs in culture medium (in-gel zymography) in the context of *in-vitro* experiments, its application to tissue sections (*in-situ* zymography) and even intact organisms (*in-vivo* zymography) was recently demonstrated (Vandooren et al., 2013). In an ideal scenario, the activity of these proteolytic enzymes would be quantitatively mapped around the cardiac tissue, providing enough information for the model to accurately simulate spatial and temporal patterns of collagen matrix degradation during cardiac wound healing.

Imaging methods such as immunofluorescence microscopy and second-harmonic imaging can be used to estimate collagen content (Bayan et al., 2009). However, these measurements are usually relative (e.g. percent of tissue covered by collagen) and thus cannot be used directly in the model. Absolute rates of deposition and degradation could potentially be estimated from total collagen content determination through biochemical methods (Lareu et al., 2010; Pataridis et al., 2009; See et al., 2008). Collagen is first enzymatically dissociated and subsequently solubilized before being analysed using methods such as colorimetric assays, spectrophotometry, chromatography or mass spectrometry. Knowing the number of cells in culture, may enable the derivation of a net deposition collagen rate per cell. These methods are destructive and as thus do not allow for the dynamics of deposition to be studied directly.

6.1.6 Effects of FGF-pathway manipulation

In this study the effects of a pan FGF inhibitor (SU5402) on the migratory speed and differentiation rate of cardiac fibroblast cells were investigated *in-vitro*. The model predicted that inhibiting FGFs would result in an increased level of scarring. Conversely, the addition of FGF-1 and FGF-2 may cause the opposite effect and reduce the level of scarring. There is evidence suggesting that FGF-1 and FGF-2 are cardioprotective and could possibly be used to manipulate the scarring process post-MI (Detillieux et al., 2003; Jiang et al., 2002; Palmen et al., 2004). In order to simulate the addition of these growth factors using the mathematical model, it would be necessary to investigate the migratory speed and differentiation rate *in-vitro* after addition of FGF-1 and FGF-2. FGF-2 has been shown to promote fibroblast proliferation (Detillieux et al., 2003; Galzie et al., 1997). Moreover, *in-vitro* cardiac fibroblast proliferation

rate in a scratch assay setting should thus be investigated for FGF-1, FGF-2 and SU5402 (pan FGF inhibitor).

6.2 Cardiac wound healing model refinement

In this section, potential refinement and extensions to the cardiac wound healing model are discussed. Those include mechanical stimuli, the addition of other cell types, and the extension of the model to 3D (Figure 6-3).

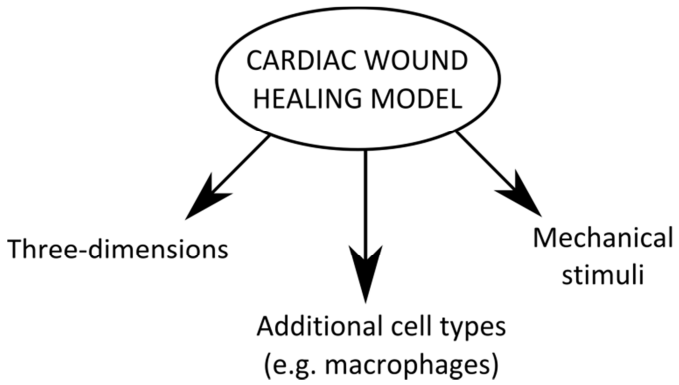

Figure 6-3 Potential refinements and extensions to the mathematical model.

6.2.1 Mechanical stimuli

The mathematical model presented in this work focused on the simulation of the interactions between cells and their surrounding ECM in an effort to understand the fibroblasts role in the development of a fibrotic scar. The cells exert forces, which lead to the re-orientation of local ECM fibres. However, the model does not explicitly simulate tension forces that contribute to the contraction of the wound. Having appropriate wound tension is critical as it leads to a reduction of the wound area and thus to a decrease in the time required for complete healing of the wound. However, both the lack of tension and excessive tension are detrimental, resulting in chronic wound or fibrotic scars, respectively (Czubryt, 2012). It is still unclear how wound tension is generated. It has been suggested that the tension forces are generated by the contraction of α-SMA rich myofibroblasts (Gabbiani et al., 1971; Porter, 2007). These forces might contribute to the alignment of the ECM fibres during wound healing, either directly by pulling on the fibres or indirectly by directing cell trajectories.

A recent model of cardiac wound healing implemented mechanical stimuli (e.g. contraction and strain due to deformation of the infarct) with a tension field (Rouillard and Holmes, 2012). The field was modelled as a modified cumulative Gaussian (Normal) distribution that peaked at the infarct border and was mostly flat in the infarct and healthy tissue regions. Cell migration was then partly influenced by the tension field. It was found that mechanical guidance was mostly responsible for long-term remodelling of the matrix. Unlike chemical and contact guidance cues that are mostly local, the mechanical guidance acted at the tissue level. The assumption was

made that the field remained constant during the course of the experiment. However, it might be interesting to model the individual contribution of each cell so that the field could be adjusted over time to take into account the increase in myofibroblast numbers as well as the changes in the wound size. The main challenge for this implementation would be the determination of the relevant parameters in experiments.

It would also be of interest to investigate the effects of intraventricular pressure on cardiac wound healing. Indeed, if the scar does not have sufficient mechanical strength to resist the intraventricular pressure, it will expand. The resulting infarct dilatation is usually associated with poor prognosis for the patient (Nijland et al., 2002). Gaining an understanding of how processes at the cellular level (e.g. ECM deposition, degradation, and re-orientation) and tissue level (contraction strength) interact to provide the wound strength, or lack thereof, necessary to counteract the intraventricular pressure is important.

6.2.2 Additional cell types

A benefit of using agent based modelling, combined with object-oriented programming, is that a new cell type can easily be added to simulations.

The cardiac wound healing model focused on the interactions between cardiac fibroblast cells, and their activated myofibroblast form, with the ECM. This choice was based on the knowledge that both cell types are responsible for ECM deposition, degradation, and remodelling post-MI (Chen and Frangogiannis, 2012; Dobaczewski et al., 2010). This is a simplified representation of the cardiac wound healing process, which in reality involves the interactions of a large number of cell types, including cardiomyocytes that survived the infarction and macrophages. The latter, amongst other functions, release TGFβ and thus promote the infiltration of the wound by surrounding fibroblasts and their subsequent differentiation into myofibroblasts (Frangogiannis, 2008; Frantz et al., 2009). This mechanism is already simulated in the model through the generic chemotactic gradient and the stochastic differentiation process as fibroblasts enter the wounded region. However, a more accurate representation could be achieved by having these signals localised to agents representing the macrophages. The healing outcome would likely be highly sensitive to the initial distribution of these macrophage agents. A good approximation could be obtained by analysing tissue sections of hearts shortly after injury, before the proliferative phase and infiltration by fibroblasts. As such, the model would simulate part of the inflammatory phase in addition to the proliferative phase.

The addition of macrophages would also have an effect on cell migration due to the contact inhibition of locomotion mechanism of the model. While macrophages tend to lose contact inhibition in monocultures, it was shown that the behaviour was present when co-cultured together with fibroblast (Holt et al., 2010). The initial distribution of macrophages in the model

would thus dictate the pattern of migration of fibroblasts after infiltration, and thus that of ECM remodelling.

6.2.3 Extending the experimental and mathematical models to three-dimensions

One of the biggest simplifications made during the development of the mathematical model was the representation of cardiac wound healing as a 2-dimensional (2D) process. This representation could be directly related to *in-vitro* experiments that are often carried out in 2D monolayers of cells. This approach greatly simplified the interpretation of simulation outcomes and kept the computational complexity at a manageable level. However, many potentially key aspects of cardiac wound healing are likely to be lost in this reduction of dimensionality as the process is inherently 3D. One of these aspects is the morphology of the heart, whose curvature and wall thickness are altered after injury and during the repair process (Weisman et al., 1985). Cell behaviours and properties differ significantly between 2D monolayer cultures and 3D settings (Baker and Chen, 2012). The most obvious one being that cellular adhesion to the surrounding ECM is distributed in all directions rather than being limited to a single plane, thus leading to a hindrance of spreading and migration. Cells are also exposed to discrete and structured ECM fibrous meshes in 3D systems instead of a continuous layer in *in-vitro* 2D cultures. Furthermore, gradients of concentration occur naturally in volumes made up of heterogeneous materials with varying diffusion properties.

An extension of the model to 3D would enable a more realistic simulation of cell behaviours during the cardiac wound healing process. Yet, it would also require an estimate of the model parameter values in a 3D setting. In the following section, potential approaches for the extension of the model to 3D are proposed. Strategies for parameter estimation and preliminary results are then presented.

6.2.3.1 A three-dimensional cardiac wound healing model

Three main areas have to be considered for a 3D implementation of the model: validity of the assumptions in a 3D setting, computational complexity, and method for visual representation of simulation outcomes.

Most of the fundamental aspects of the 2D model can be extended to 3D relatively easily. The simulated tissue would be represented as a volume rather than a plane. Agents (cell) properties (e.g. position, velocity) would be modified accordingly to have a third coordinate corresponding to depth. The heat equation used to simulate the chemotactic gradient in 2D can be readily formulated for a 3D problem. An approximation of the solution would require the use of the 3D discrete Laplace operator. Preliminary tests showed that the desired gradients could be generated, taking into account diffusion, degradation, and production (Figure 6-4). Initially, the overall concentration increases as the production term outweighs degradation before reaching a

steady state. The production term can be set to zero in order to have the gradient gradually decay to simulate the end of the inflammatory phase.

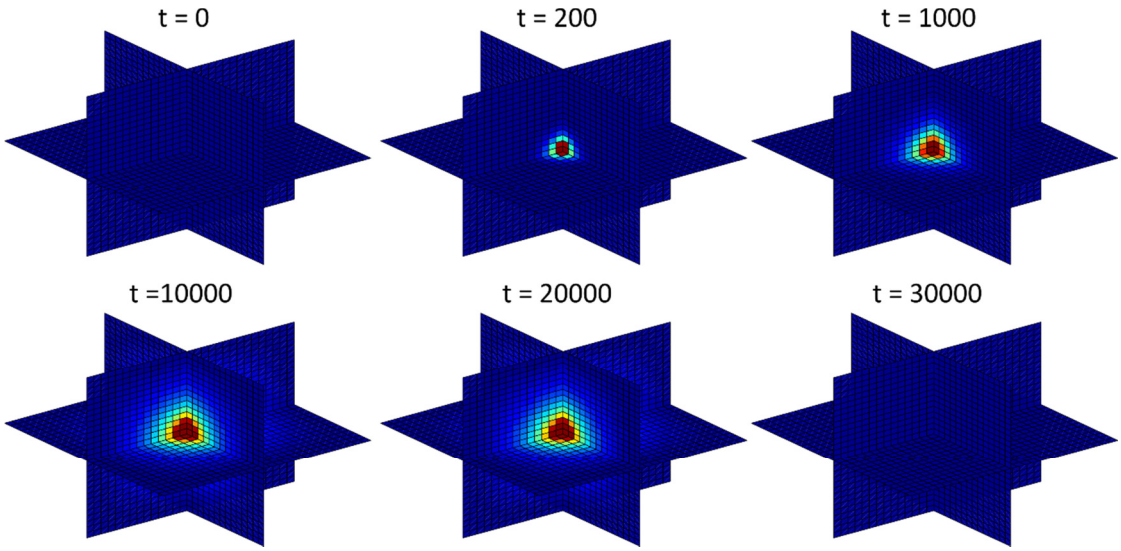

Figure 6-4 Chemotactic gradient formulation extended to 3D. Computation based on a 3D solution of the Heat equation containing a diffusion term, degradation term, and production term. The initial concentration across the simulated volume is 0. At around t = 10000, a steady-state is established and the gradient is stable. To simulate the end of the inflammatory response, the production term is disabled after t = 20000, resulting in a zero concentration across the volume at t = 30000. Red and blue indicate high and low chemoattractant concentrations, respectively.

The 3D implementation of the generic chemotactic gradient is significantly more computationally expensive in comparison to the 2D case. Alternatively, a method was proposed to approximate the source of the gradient as a sphere, enabling the determination of chemokine concentration at any point of a volume based on the distance from the edges of the source modelled as a sphere (Groh and Wagner, 2011). A downside of this approach is that it is not possible to directly simulate the effect of gradual increases and decreases in concentration following initiation and termination of the inflammatory phase. It would thus be of interest to compare the results obtained when using this approximation and the 3D approximate solution of the heat equation. The latter could potentially be used to simulate multiple sources of gradient, which would allow every cell to produce local gradients as suggested above.

In 3D, the ECM would be represented by a 3D discrete vector field. In 2D, the ECM orientation at any point was based on the interpolation of the 25 nearest vectors using a combination of tensor product and quartic Lagrangian interpolation methods. In 3 dimensions, it would most likely be more efficient to employ methods such as trilinear or tricubic interpolation (Lekien and Marsden, 2005). Regardless of the method chosen, there will be a computational cost as a larger number of points will have to be evaluated for each interpolation.

The methods used for visualisation and quantitative evaluation of model outputs would also have to be modified accordingly. The visualisation for the 2D model shows the cells (position, size, orientation) and the ECM (orientation, density). Visualisation is a key aspect of the model,

made possible by its agent-based nature, as it facilitates the interpretation of simulation outcomes and direct comparison with experimental data. There is a risk of losing this intuitive representation of the model during the transition to 3D. A potential solution would be to use a hybrid visualisation combining a 3D view of the simulated volume, including cells and ECM, with the ability to produce 'virtual slices' that would look similar to the current 2D visualisations (Figure 6-5). This would give a sense of the 3D dynamics of the model, while preserving a representation that is easily comparable to microscopy images and more straightforward to interpret. The 3D visualisation would require the use of libraries such as VTK (the Visualization Toolkit) or Qt3D. The cells can be represented by spheres with a radius proportional to their area. The ECM fibres can be drawn using the same method as in the 2D case, which is using tracer cells to delineate the fibres.

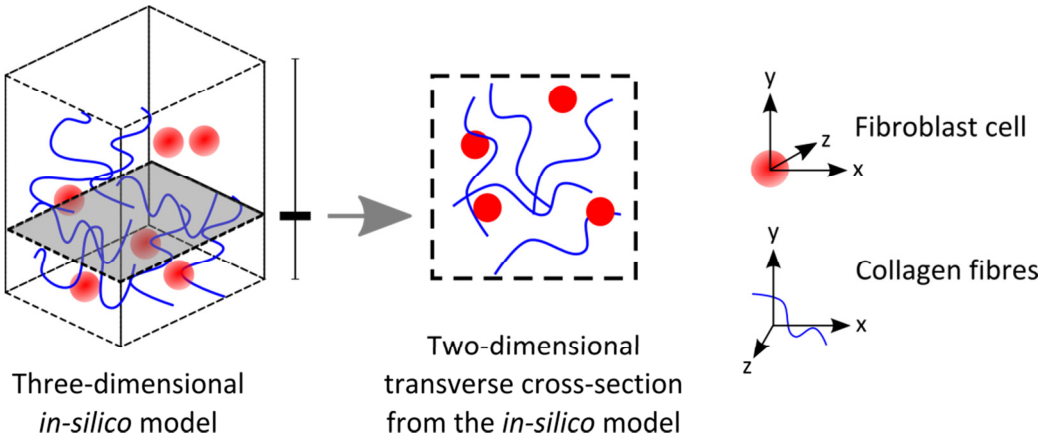

Figure 6-5 Potential visualisation scheme for a 3D model of cardiac wound healing.

The methods employed for the quantification of collagen alignment would also have to be revised. The clustering approach proposed in this work could eventually be extended to 3D, but it remains to be seen whether its result would still be meaningful in this context. Alternatively, a method based on graph theory was successfully used for collagen alignment quantification in 3D (Bilgin et al., 2010). One advantage of this approach is that 3D reconstructions of tissues can be obtained directly from immunofluorescence confocal and second harmonic microscopy images. As such, it would in theory allow direct comparison of the model results with experimental data.

6.2.3.2 Three-dimensional in-vitro experimental model

The transition of the mathematical model to a 3D framework has to be accompanied by the development of a suitable *in-vitro* experimental model for the determination of associated parameter values. The experiments described in chapter 2 were carried out using conventional methodologies where cells were cultured as a 2D monolayer. This was an approximation of the actual wound healing process in the heart, which occurs in a 3D volume with structures that cannot readily be replicated in simple culture dishes. Methods for 3D *in-vitro* culture could be, at least in principle, a better and more representative experimental model. Assessment of

experimental outcome can be complicated in a 3D setting. Indeed, whereas it was possible to use traditional light and fluorescence microscopy to image and subsequently analyse monolayer cultures, 3D culture systems are usually incompatible with such approaches due to the optical properties of the materials used. Instead, it is often necessary to employ confocal microscopy, which enables optical sectioning of the 3D culture and thus its visualisation. This can only be undertaken if the cells are fluorescently labelled.

Preliminary experiments in a 3D collagen gel were carried out to assess the feasibility of such an approach. Primary cardiac fibroblasts isolated from β-actin cre; R26R-EYFP mice expressed the yellow fluorescence proteins (YFP). Cells were first grown in a conventional 2D culture before being seeded in a 3D collagen gel using a two layer method whereby the cells suspension was embedded in a thin collagen gel matrix placed on-top of a thicker one towards which they should in principle migrate due to gravitational forces (Tasaki et al., 2004). Shortly after seeding, the cells had a spherical morphology (Figure 6-6 A-D). As expected, the cells then only occupied the top layer in which they were seeded uniformly.

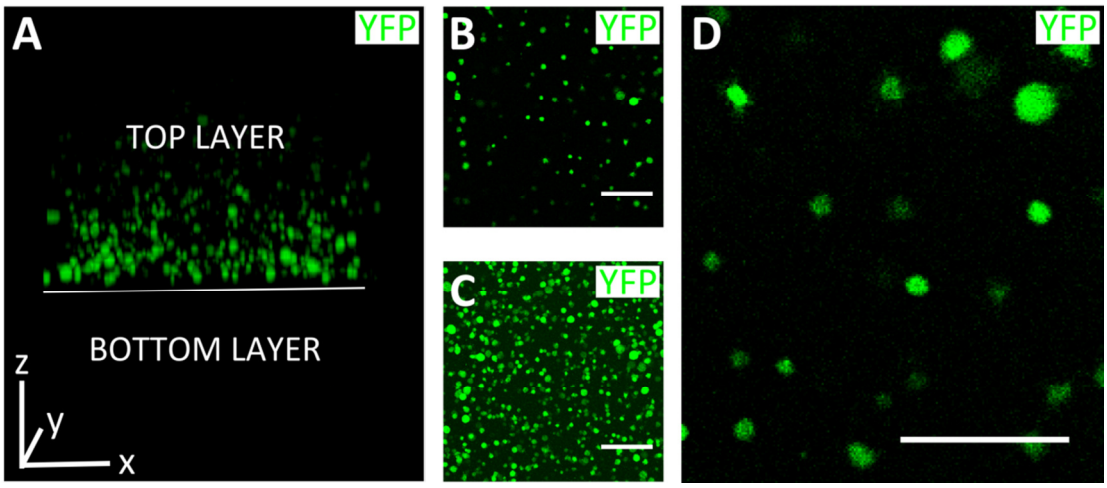

Figure 6-6 3D primary cardiac fibroblast culture shortly after seeding. YFP positive cells isolated from β-actin cre; R26R-EYFP mice cultured in a 3D collagen gel were imaged using confocal microscopy. (A) 3D view of the collagen gel. (B) Bird-eye view of a single z-slice of the culture. Scale bar represents 150 µm. (C) Maximum intensity projections across all z-slices. Scale bar represents 200 µm. (D) Magnified image of a single z-slice of the culture (scale bar represents 150 µm). Method for 3D culture described in Annex A.2.

The cells were expected to migrate down through the gel. However, after 20 hours of culture most of them remained in the top layer where they were initially seeded (Figure 6-7 A-D). Only a single cell appeared to have successfully migrated across the seeding layer, into the second layer and reached the bottom of the latter. The morphology of the cells differed drastically from that observed shortly after seeding with cells adopting a spindle-like shape with the apparent production of pseudopodia-like protrusions.

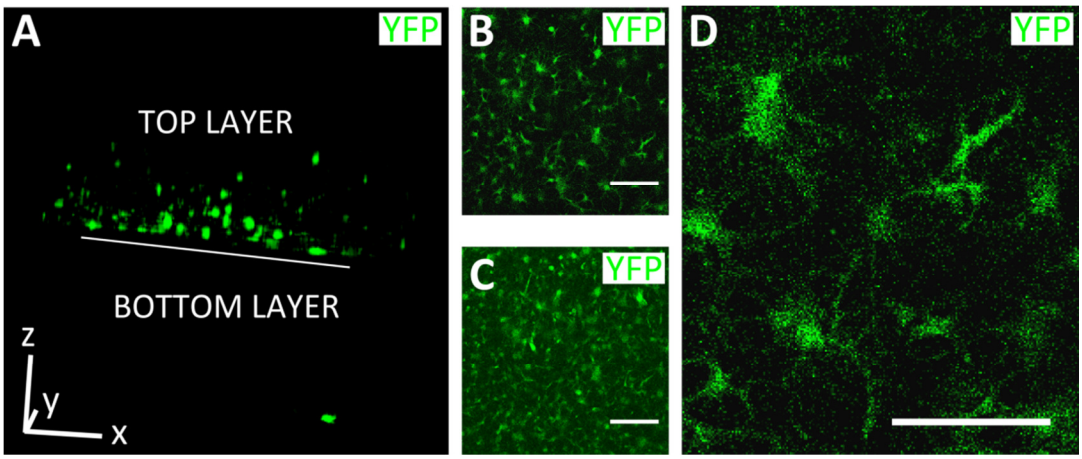

Figure 6-7 3D primary cardiac fibroblast culture 20 hours after seeding. YFP positive cells isolated from β-actin cre; R26R-EYFP mice cultured in a 3D collagen gel were imaged using confocal microscopy. (A) 3D view of the collagen gel. (B) Bird-eye view of a single z-slice of the culture. Scale bars represent 200 µm. (C) Maximum intensity projections across all z-slices. Scale bars represents 200 µm. (D) Magnified image of a single z-slice of the culture (scale bar represents 200 µm). Method for 3D culture described in Annex A.2.

These results demonstrated the feasibility of a 3D culture system. However, the issue with the apparent lack of cell migration would have to be solved before it can be used to measure relevant cell behaviours and properties such as migratory speed. The collagen concentration of the 3D gel has been shown to influence the level of cell migration. In general, higher collagen concentrations resulted in decreased cell migration (Sun et al., 2004). Further experiments would thus entail exploring how the collagen gel concentration effects fibroblast migration in order to devise an optimal experimental setup.

It was difficult to consistently prepare identical collagen gels. Moreover, it was not possible to control the properties of the gels beyond their concentration. A structurally consistent collagen setup would be preferred when comparing the effects of different pharmacological interventions on the cell migration. The structural arrangement of fibres within a 3D matrix can be controlled in terms of the fibre density, stiffness and alignment with electrospun poly-ε-caprolactone nanofibre scaffolds (Johnson et al., 2009; Venugopal et al., 2008). This setup was previously used to study differences in cell migration patterns between isotropic and anisotropic nanofibre scaffolds (Agudelo-Garcia et al., 2011; Johnson et al., 2009).

6.3 Further *in-vivo* analysis for mathematical model validation

Validation of the model was mainly carried out by comparison with data generated from tissue sections from both intact and injured murine hearts. The main basis for comparison was the degree of collagen type I alignment, which was quantified by automated processing of immunofluorescence confocal microscopy images. Further model validation can be carried out in two main areas: additional scar properties (e.g. ECM density), and the generation of *in-vivo* data for pharmacological interventions.

6.3.1 Quantifying other scar properties

The experimental data regarding the collagen matrix was mostly limited to its organisation. However, the rate of collagen accumulation would also be an interesting point of comparison with the mathematical model. Collagen density can be estimated using light microscopy of section stained with Masson's trichrome (Strijkers et al., 2009; Virag and Murry, 2003). Profile of collagen accumulation over the whole tissue as well as local deposition patterns could be quantified this way. A similar approach was employed to quantify the changes in infarct size post-MI (Lian et al., 2010).

The collagen bundle orientation and spacing has been compared between controls and patients with scleroderma an autoimmune condition which results in fibrosis (de Vries et al., 2000). The collagen architecture provides some indication of the severity of dermal sclerosis. Microscopy images of the collagen fibre bundles were obtained and analysed with fast Fourier transform. Fourier analysis enables the switching between a signal in time (or space) and the signal in terms of its frequency.

6.3.2 Generation of *in-vivo* data for pharmacological interventions

The mathematical model was used to predict the effects of various pharmacological interventions on the remodelling of the ECM matrix during the cardiac wound healing process. In order to do so, *in-vitro* experiments were carried out to determine the parameter values corresponding to these different conditions. The interventions considered included the addition of recombinant TGFβ1, the inhibition of TGFβ1 using an ALK5 inhibitor, and the inhibition of FGFs using SU5402. The experiments focused on a handful of cell behaviours (e.g. cell speed, differentiation). The investigation of additional parameters such as proliferation rate would likely improve the accuracy of model predictions as, for example, both SU5402 and TGFβ1 were shown to influence the proliferative rate of cardiac fibroblasts (Frantz et al., 2009). Furthermore, only qualitative assessment of the simulation outcomes could be carried out as there was no *in-vivo* data available to thoroughly evaluate the predictive power of the mathematical model. It would thus be of great value to analyse the collagen structure in tissue section of hearts from mice that were administrated the pharmacological compounds considered.

Bibliography

Abercrombie M, Heaysman JE. 1953. Observations on the social behaviour of cells in tissue culture. I. Speed of movement of chick heart fibroblasts in relation to their mutual contacts. *Exp. Cell Res.* **5**:111–31.

Agocha A, Sigel A V, Eghbali-Webb M. 1997. Characterization of adult human heart fibroblasts in culture: a comparative study of growth, proliferation and collagen production in human and rabbit cardiac fibroblasts and their response to transforming growth factor-beta1. *Cell Tissue Res.* **288**:87–93.

Agudelo-Garcia PA, De Jesus JK, Williams SP, Nowicki MO, Chiocca EA, Liyanarachchi S, Li P, Lannutti JJ, Johnson JK, Lawler SE, Viapiano MS. 2011. Glioma cell migration on three-dimensional nanofiber scaffolds is regulated by substrate topography and abolished by inhibition of STAT3 signaling. *Neoplasia* **13**:831–40.

Amigoni F, Schiaffonati V. 2007. Multiagent-Based Simulation in Biology : A Critical Analysis. In: . *Model. Reason. Sci. Technol. Med.*, pp. 179–191.

Anderson RH, Ho SY, Redmann K, Sanchez-Quintana D, Lunkenheimer PP. 2005. The anatomical arrangement of the myocardial cells making up the ventricular mass. *Eur. J. Cardiothorac. Surg.* **28**:517–25.

Annes JP, Munger JS, Rifkin DB. 2003. Making sense of latent TGFbeta activation. *J. Cell Sci.* **116**:217–224.

Arboleda-Estudillo Y, Krieg M, Stühmer J, Licata N a, Muller DJ, Heisenberg C-P. 2010. Movement directionality in collective migration of germ layer progenitors. *Curr. Biol.* **20**:161–9.

Arora PD, McCulloch C a. 1994. Dependence of collagen remodelling on alpha-smooth muscle actin expression by fibroblasts. *J. Cell. Physiol.* **159**:161–75.

Azuma K, Ichimura K, Mita T, Nakayama S, Jin WL, Hirose T, Fujitani Y, Sumiyoshi K, Shimada K, Daida H, Sakai T, Mitsumata M, Kawamori R, Watada H. 2009. Presence of alpha-smooth muscle actin-positive endothelial cells in the luminal surface of adult aorta. *Biochem. Biophys. Res. Commun.* **380**:620–6.

Baker BM, Chen CS. 2012. Deconstructing the third dimension: how 3D culture microenvironments alter cellular cues. *J. Cell Sci.* **125**:3015–24.

Banerjee I, Fuseler JW, Price RL, Borg TK, Baudino T a. 2007. Determination of cell types and numbers during cardiac development in the neonatal and adult rat and mouse. *Am. J. Physiol. Heart Circ. Physiol.* **293**:H1883–91.

Bashey RI, Martinez-Hernandez A, Jimenez S a. 1992. Isolation, characterization, and localization of cardiac collagen type VI. Associations with other extracellular matrix components. *Circ. Res.* **70**:1006–17.

Baum J, Duffy HS. 2011. Fibroblasts and myofibroblasts: what are we talking about? *J. Cardiovasc. Pharmacol.* **57**:376–9.

Baxter SC, Morales MO, Goldsmith EC. 2008. Adaptive changes in cardiac fibroblast morphology and collagen organization as a result of mechanical environment. *Cell Biochem. Biophys.* **51**:33–44.

Bayan C, Levitt JM, Miller E, Kaplan D, Georgakoudi I. 2009. Fully automated, quantitative, noninvasive assessment of collagen fiber content and organization in thick collagen gels. *J. Appl. Phys.* **105**:102042.

Benedicto HG, Bombonato PP, Macchiarelli G, Stifano G, Prado IMM. 2011. Structural arrangement of the cardiac collagen fibers of healthy and diabetic dogs. *Microsc. Res. Tech.* **74**:1018–23.

Bilgin CC, Lund AW, Can A, Plopper GE, Yener B. 2010. Quantification of three-dimensional cell-mediated collagen remodeling using graph theory. *PLoS One* **5**.

Van den Borne SWM, Diez J, Blankesteijn WM, Verjans J, Hofstra L, Narula J. 2010. Myocardial remodeling after infarction: the role of myofibroblasts. *Nat. Rev. Cardiol.* **7**:30–7.

Brown RD, Jones GM, Laird RE, Hudson P, Long CS. 2007. Cytokines regulate matrix metalloproteinases and migration in cardiac fibroblasts. *Biochem. Biophys. Res. Commun.* **362**:200–5.

Buijs JT, Stayrook KR, Guise T a. 2012. The role of TGF-β in bone metastasis: novel therapeutic perspectives. *Bonekey Rep.* **1**:96.

Bujak M, Frangogiannis NG. 2007. The role of TGF-beta signaling in myocardial infarction and cardiac remodeling. *Cardiovasc. Res.* **74**:184–95.

Bujak M, Ren G, Kweon HJ, Dobaczewski M, Reddy A, Taffet G, Wang X-F, Frangogiannis NG. 2007. Essential role of Smad3 in infarct healing and in the pathogenesis of cardiac remodeling. *Circulation* **116**:2127–38.

Camelliti P, Borg TK, Kohl P. 2005a. Structural and functional characterisation of cardiac fibroblasts. *Cardiovasc. Res.* **65**:40–51.

Camelliti P, Devlin GP, Matthews KG, Kohl P, Green CR. 2004. Spatially and temporally distinct expression of fibroblast connexins after sheep ventricular infarction. *Cardiovasc. Res.* **62**:415–25.

Camelliti P, McCulloch AD, Kohl P. 2005b. Microstructured cocultures of cardiac myocytes and fibroblasts: a two-dimensional in vitro model of cardiac tissue. *Microsc. Microanal.* **11**:249–59.

Campagnola PJ, Clark H a, Mohler W a, Lewis a, Loew LM. 2001. Second-harmonic imaging microscopy of living cells. *J. Biomed. Opt.* **6**:277–86.

Cao X-G, Li X-X, Bao Y-Z, Xing N-Z, Chen Y. 2007. Responses of human lens epithelial cells to quercetin and DMSO. *Invest. Ophthalmol. Vis. Sci.* **48**:3714–8.

Carmona-Fontaine C, Matthews HK, Kuriyama S, Moreno M, Dunn G a, Parsons M, Stern CD, Mayor R. 2008. Contact inhibition of locomotion in vivo controls neural crest directional migration. *Nature* **456**:957–61.

Casal A, Sumen C, Reddy TE, Alber MS, Lee PP. 2005. Agent-based modeling of the context dependency in T cell recognition. *J. Theor. Biol.* **236**:376–91.

Chambard J-C, Lefloch R, Pouysségur J, Lenormand P. 2007. ERK implication in cell cycle regulation. *Biochim. Biophys. Acta* **1773**:1299–310.

Chang HY, Chi J-T, Dudoit S, Bondre C, van de Rijn M, Botstein D, Brown PO. 2002. Diversity, topographic differentiation, and positional memory in human fibroblasts. *Proc. Natl. Acad. Sci. U. S. A.* **99**:12877–82.

Changoor a, Tran-Khanh N, Méthot S, Garon M, Hurtig MB, Shive MS, Buschmann MD. 2011. A polarized light microscopy method for accurate and reliable grading of collagen organization in cartilage repair. *Osteoarthritis Cartilage* **19**:126–35.

Chaudhary NI, Roth GJ, Hilberg F, Müller-Quernheim J, Prasse a, Zissel G, Schnapp a, Park JE. 2007. Inhibition of PDGF, VEGF and FGF signalling attenuates fibrosis. *Eur. Respir. J.* **29**:976–85.

Chavali AK, Gianchandani EP, Tung KS, Lawrence MB, Peirce SM, Papin J a. 2008. Characterizing emergent properties of immunological systems with multi-cellular rule-based computational modeling. *Trends Immunol.* **29**:589–99.

Chen H, Wang J, Xiang M-X, Wang J-A, Lin Y, He A, Jin C-N, Guan J, Sukhova GK, Libby P, Shi G-P. 2013. Cathepsin S-Mediated Fibroblast Trans-Differentiation Contributes to Left Ventricular Remodeling After Myocardial Infarction. *Cardiovasc. Res.*

Chen J, Tung C-H, Allport JR, Chen S, Weissleder R, Huang PL. 2005. Near-infrared fluorescent imaging of matrix metalloproteinase activity after myocardial infarction. *Circulation* **111**:1800–5.

Chen J, Song S-K, Liu W, McLean M, Allen JS, Tan J, Wickline S a, Yu X. 2003. Remodeling of cardiac fiber structure after infarction in rats quantified with diffusion tensor MRI. *Am. J. Physiol. Heart Circ. Physiol.* **285**:H946–54.

Chen W, Frangogiannis NG. 2012. Fibroblasts in post-infarction inflammation and cardiac repair. *Biochim. Biophys. Acta* **1833**:945–53.

Cheng T-H, Cheng P-Y, Shih N-L, Chen I-B, Wang DL, Chen J-J. 2003. Involvement of reactive oxygen species in angiotensin II-induced endothelin-1 gene expression in rat cardiac fibroblasts. *J. Am. Coll. Cardiol.* **42**:1845–1854.

Chiu C-L, Digman M a, Gratton E. 2013. Cell matrix remodeling ability shown by image spatial correlation. *J. Biophys.* **2013**:532030.

Cihakova D, Barin JG, Afanasyeva M, Kimura M, Fairweather D, Berg M, Talor M V, Baldeviano GC, Frisancho S, Gabrielson K, Bedja D, Rose NR. 2008. Interleukin-13 protects against experimental autoimmune myocarditis by regulating macrophage differentiation. *Am. J. Pathol.* **172**:1195–208.

Cleutjens JP, Blankesteijn WM, Daemen MJ, Smits JF. 1999. The infarcted myocardium: simply dead tissue, or a lively target for therapeutic interventions. *Cardiovasc. Res.* **44**:232–41.

Cleutjens JP, Kandala JC, Guarda E, Guntaka R V, Weber KT. 1995a. Regulation of collagen degradation in the rat myocardium after infarction. *J. Mol. Cell. Cardiol.* **27**:1281–92.

Cleutjens JP, Verluyten MJ, Smiths JF, Daemen MJ. 1995b. Collagen remodeling after myocardial infarction in the rat heart. *Am. J. Pathol.* **147**:325–38.

Cox G, Kable E. 2006. Second-harmonic imaging of collagen. *Methods Mol. Biol.* **319**:15–35.

Cox G, Kable E, Jones A, Fraser I, Manconi F, Gorrell MD. 2003. 3-Dimensional Imaging of Collagen Using Second Harmonic Generation. *J. Struct. Biol.* **141**:53–62.

Creemers EEJM, Cleutjens JPM, Smits JFM, Daemen MJ a. P. 2001. Matrix Metalloproteinase Inhibition After Myocardial Infarction: A New Approach to Prevent Heart Failure? *Circ. Res.* **89**:201–210.

Crosier M, Griffin LD. 2010. Using Basic Image Features for Texture Classification. *Int. J. Comput. Vis.* **88**:447–460.

Crouch AS, Miller D, Luebke KJ, Hu W. 2009. Correlation of anisotropic cell behaviors with topographic aspect ratio. *Biomaterials* **30**:1560–7.

Cumming BD, McElwain DLS, Upton Z. 2010. A mathematical model of wound healing and subsequent scarring. *J. R. Soc. Interface* **7**:19–34.

Czubryt MP. 2012. Common threads in cardiac fibrosis, infarct scar formation, and wound healing. *Fibrogenesis Tissue Repair* **5**:19.

Dallon JC, Sherratt J a, Maini PK. 1999. Mathematical modelling of extracellular matrix dynamics using discrete cells: fiber orientation and tissue regeneration. *J. Theor. Biol.* **199**:449–71.

Dallon JC, Sherratt J a, Maini PK. 2001. Modeling the effects of transforming growth factor-beta on extracellular matrix alignment in dermal wound repair. *Wound Repair Regen.* **9**:278–86.

Dallon J, Sherratt J, Maini P, Ferguson M. 2000. Biological implications of a discrete mathematical model for collagen deposition and alignment in dermal wound repair. *IMA J. Math. Appl. Med. Biol.* **17**:379–93.

Daskalopoulos EP, Janssen BJA, Blankesteijn WM. 2012. Myofibroblasts in the infarct area: concepts and challenges. *Microsc. Microanal.*35–49.

Dean RG, Balding LC, Candido R, Burns WC, Cao Z, Twigg SM, Burrell LM. 2005. Connective tissue growth factor and cardiac fibrosis after myocardial infarction. *J. Histochem. Cytochem.* **53**:1245–56.

Deforet M, Parrini MC, Petitjean L, Biondini M, Buguin A, Camonis J, Silberzan P. 2012. Automated velocity mapping of migrating cell populations (AVeMap). *Nat. Methods* **9**.

Desmoulière a, Geinoz a, Gabbiani F, Gabbiani G. 1993. Transforming growth factor-beta 1 induces alpha-smooth muscle actin expression in granulation tissue myofibroblasts and in quiescent and growing cultured fibroblasts. *J. Cell Biol.* **122**:103–11.

Desmoulière a, Redard M, Darby I, Gabbiani G. 1995. Apoptosis mediates the decrease in cellularity during the transition between granulation tissue and scar. *Am. J. Pathol.* **146**:56–66.

Detillieux K a, Sheikh F, Kardami E, Cattini P a. 2003. Biological activities of fibroblast growth factor-2 in the adult myocardium. *Cardiovasc. Res.* **57**:8–19.

Dickinson RB, Guido S, Tranquillo RT. 1994. Biased cell migration of fibroblasts exhibiting contact guidance in oriented collagen gels. *Ann. Biomed. Eng.* **22**:342–56.

DiMilla P a, Barbee K, Lauffenburger D a. 1991. Mathematical model for the effects of adhesion and mechanics on cell migration speed. *Biophys. J.* **60**:15–37.

Dobaczewski M, Akrivakis S, Nasser K, Michael LH, Entman ML, Frangogiannis NG. 2004. Vascular mural cells in healing canine myocardial infarcts. *J. Histochem. Cytochem.* **52**:1019–29.

Dobaczewski M, Frangogiannis NG. 2011. The cellular specificity of leptin-mediated actions in the infarcted heart. *Cardiovasc. Res.* **89**:9–11.

Dobaczewski M, Gonzalez-Quesada C, Frangogiannis NG. 2010. The extracellular matrix as a modulator of the inflammatory and reparative response following myocardial infarction. *J. Mol. Cell. Cardiol.* **48**:504–11.

Dobaczewski M, de Haan JJ, Frangogiannis NG. 2012. The extracellular matrix modulates fibroblast phenotype and function in the infarcted myocardium. *J. Cardiovasc. Transl. Res.* **5**:837–47.

Engelmayr GC, Cheng M, Bettinger CJ, Borenstein JT, Langer R, Freed LE. 2008. Accordion-like honeycombs for tissue engineering of cardiac anisotropy. *Nat. Mater.* **7**:1003–10.

Falanga V. 2005. Wound healing and its impairment in the diabetic foot. *Lancet* **366**:1736–43.

Fedak PWM, Bai L, Turnbull J, Ngu J, Narine K, Duff HJ. 2012. Cell therapy limits myofibroblast differentiation and structural cardiac remodeling: basic fibroblast growth factor-mediated paracrine mechanism. *Circ. Heart Fail.* **5**:349–56.

Ferguson MWJ, O'Kane S. 2004. Scar-free healing: from embryonic mechanisms to adult therapeutic intervention. *Philos. Trans. R. Soc. Lond. B. Biol. Sci.* **359**:839–50.

Fomovsky GM, Macadangdang JR, Ailawadi G, Holmes JW. 2011. Model-based design of mechanical therapies for myocardial infarction. *J. Cardiovasc. Transl. Res.* **4**:82–91.

Forbes SJ, Russo FP, Rey V, Burra P, Rugge M, Wright N a., Alison MR. 2004. A significant proportion of myofibroblasts are of bone marrow origin in human liver fibrosis☆. *Gastroenterology* **126**:955–963.

Fowlkes V, Clark J, Fix C, Law BA, Morales MO, Qiao X, Ako-Asare K, Goldsmith JG, Carver W, Murray DB, Goldsmith EC. 2013. Type II diabetes promotes a myofibroblast phenotype in cardiac fibroblasts. *Life Sci.* **92**:669–76.

Frangogiannis NG. 2008. The immune system and cardiac repair. *Pharmacol. Res.* **58**:88–111.

Frangogiannis N, Michael LH, Entman ML. 2000. Myofibroblasts in reperfused myocardial infarcts express the embryonic form of smooth muscle myosin heavy chain (SMemb). *Cardiovasc. Res.* **48**:89–100.

Frangogiannis NG. 2012. Regulation of the inflammatory response in cardiac repair. *Circ. Res.* **110**:159–73.

Frangogiannis NG, Lindsey ML, Michael LH, Youker KA, Bressler RB, Mendoza LH, Spengler RN, Smith CW, Entman ML. 1998. Resident cardiac mast cells degranulate and release preformed TNF-alpha, initiating the cytokine cascade in experimental canine myocardial ischemia/reperfusion. *Circulation* **98**:699–710.

Frangogiannis NG, Smith CW, Entman ML. 2002. The inflammatory response in myocardial infarction. *Cardiovasc. Res.* **53**:31–47.

Franke WW, Schmid E, Osborn M, Weber K. 1979. Intermediate-sized filaments of human endothelial cells. *J. Cell Biol.* **81**:570–80.

Frantz S, Bauersachs J, Ertl G. 2009. Post-infarct remodelling: contribution of wound healing and inflammation. *Cardiovasc. Res.* **81**:474–81.

Freed DH, Cunnington RH, Dangerfield AL, Sutton JS, Dixon IMC. 2005. Emerging evidence for the role of cardiotrophin-1 in cardiac repair in the infarcted heart. *Cardiovasc. Res.* **65**:782–92.

Freyman TM, Yannas I V, Yokoo R, Gibson LJ. 2002. Fibroblast contractile force is independent of the stiffness which resists the contraction. *Exp. Cell Res.* **272**:153–62.

Gabbiani G. 1996. The cellular derivation and the life span of the myofibroblast. *Pathol. Res. Pract.* **192**:708–11.

Gabbiani G, Hirschel BJ, Ryan GB, Statkov PR, Majno G. 1972. Granulation tissue as a contractile organ. A study of structure and function. *J. Exp. Med.* **135**:719–734.

Gabbiani G, Ryan GB, Majno G. 1971. Presence of modified fibroblasts in granulation tissue and their possible role in wound contraction. *Experientia* **27**:549–550.

Gabbiani G. 1993. Modulation of fibroblastic cytoskeletal features during wound healing and fibrosis. *Bolletino di Zool.* **60**:399–401.

Galzie Z, Kinsella a R, Smith J a. 1997. Fibroblast growth factors and their receptors. *Biochem. Cell Biol.* **75**:669–85.

Gaudet C, Marganski WA, Kim S, Brown CT, Gunderia V, Dembo M, Wong JY. 2003. Influence of Type I Collagen Surface Density on Fibroblast Spreading ,. *Biophys. J.* **85**.

Gavaghan D, Garny A, Maini PK, Kohl P. 2006. Mathematical models in physiology. *Philos. Trans. A. Math. Phys. Eng. Sci.* **364**:1099–106.

Geris L, Gerisch A, Schugart RC. 2010. Mathematical modeling in wound healing, bone regeneration and tissue engineering. *Acta Biotheor.* **58**:355–67.

Goldthwaite, Charles A. J. 2006. Mending a Broken Heart: stem cells and cardiac repair. http://stemcells.nih.gov/staticresources/info/scireport/PDFs/H. Chapter 6.pdf.

Graw F, Leitner T, Ribeiro RM. 2012. Agent-based and phylogenetic analyses reveal how HIV-1 moves between risk groups: injecting drug users sustain the heterosexual epidemic in Latvia. *Epidemics* **4**:104–16.

Groh a, Wagner M. 2011. Biased three-dimensional cell migration and collagen matrix modification. *Math. Biosci.* **231**:105–19.

Guilbert T, Odin C, Le Grand Y, Gailhouste L, Turlin B, Ezan F, Désille Y, Baffet G, Guyader D. 2010. A robust collagen scoring method for human liver fibrosis by second harmonic microscopy. *Opt. Express* **18**:25794–807.

Hao MM, Bornstein JC, Young HM. 2013. Development of myenteric cholinergic neurons in ChAT-Cre;R26R-YFP mice. *J. Comp. Neurol.* **521**:3358–70.

Herzog E, Gu A, Kohmoto T, Burkhoff D, Hochman JS. 1998. Early activation of metalloproteinases after experimental myocardial infarction occurs in infarct and non-infarct zones. *Cardiovasc. Pathol.* **7**:307–312.

Hilgemann DW, Noble D. 1987. Excitation-contraction coupling and extracellular calcium transients in rabbit atrium: reconstruction of basic cellular mechanisms. *Proc. R. Soc. Lond. B. Biol. Sci.* **230**:163–205.

Hinz B, Celetta G, Tomasek JJ, Gabbiani G, Chaponnier C. 2001. Alpha-smooth muscle actin expression upregulates fibroblast contractile activity. *Mol. Biol. Cell* **12**:2730–41.

Hinz B. 2007. Formation and function of the myofibroblast during tissue repair. *J. Invest. Dermatol.* **127**:526–37.

Hinz B. 2010. The myofibroblast: paradigm for a mechanically active cell. *J. Biomech.* **43**:146–55.

Hinz B, Gabbiani G. 2003. Mechanisms of force generation and transmission by myofibroblasts. *Curr. Opin. Biotechnol.* **14**:538–546.

Hinz B, Phan SH, Thannickal VJ, Galli A, Bochaton-Piallat M-L, Gabbiani G. 2007. The myofibroblast: one function, multiple origins. *Am. J. Pathol.* **170**:1807–16.

Holley RW, Kiernan JA. 1968. “Contact inhibition” of cell division in 3T3 cells. *Proc. Natl. Acad. Sci. U. S. A.* **60**:300–4.

Holmes JW, Nuñez JA, Covell JW. 1997. Functional implications of myocardial scar structure. *Am. J. Physiol.* **272**:H2123–30.

Holt DJ, Chamberlain LM, Grainger DW. 2010. Cell-cell signaling in co-cultures of macrophages and fibroblasts. *Biomaterials* **31**:9382–94.

Howard EW, Crider BJ, Updike DL, Bullen EC, Parks EE, Haaksma CJ, Sherry DM, Tomasek JJ. 2012. MMP-2 expression by fibroblasts is suppressed by the myofibroblast phenotype. *Exp. Cell Res.* **318**:1542–53.

Hudson MP, Armstrong PW, Ruzyllo W, Brum J, Cusmano L, Krzeski P, Lyon R, Quinones M, Theroux P, Sydlowski D, Kim HE, Garcia MJ, Jaber W a, Weaver WD. 2006. Effects of selective matrix metalloproteinase inhibitor (PG-116800) to prevent ventricular remodeling after myocardial infarction: results of the PREMIER (Prevention of Myocardial Infarction Early Remodeling) trial. *J. Am. Coll. Cardiol.* **48**:15–20.

Hunter PJ, McCulloch a D, ter Keurs HE. 1998. Modelling the mechanical properties of cardiac muscle. *Prog. Biophys. Mol. Biol.* **69**:289–331.

Husse B, Briest W, Homagk L, Isenberg G, Gekle M. 2007. Cyclical mechanical stretch modulates expression of collagen I and collagen III by PKC and tyrosine kinase in cardiac fibroblasts. *Am. J. Physiol. Regul. Integr. Comp. Physiol.* **293**:R1898–907.

Ignotz R a, Massagué J. 1986. Transforming growth factor-beta stimulates the expression of fibronectin and collagen and their incorporation into the extracellular matrix. *J. Biol. Chem.* **261**:4337–45.

Ikeuchi M, Tsutsui H, Shiomi T, Matsusaka H, Matsushima S, Wen J, Kubota T, Takeshita A. 2004. Inhibition of TGF-beta signaling exacerbates early cardiac dysfunction but prevents late remodeling after infarction. *Cardiovasc. Res.* **64**:526–35.

Inman GJ, As FJN, Callahan JF, Harling JD, Gaster LM, Reith AD, Laping NJ, Hill CS. 2002. SB-431542 Is a Potent and Specific Inhibitor of Transforming Growth Factor- beta Superfamily Type I Activin Receptor-Like Kinase (ALK) Receptors ALK4, ALK5, and ALK7. *Mol. Pharmacol.* **62**:65–74.

Jacobs M, Staufenberger S, Gergs U, Meuter K, Brandstätter K, Hafner M, Ertl G, Schorb W. 1999. Tumor necrosis factor-alpha at acute myocardial infarction in rats and effects on cardiac fibroblasts. *J. Mol. Cell. Cardiol.* **31**:1949–59.

Javierre E, Vermolen FJ, Vuik C, van der Zwaag S. 2009. A mathematical analysis of physiological and morphological aspects of wound closure. *J. Math. Biol.* **59**:605–30.

Jiang Z-S, Padua RR, Ju H, Doble BW, Jin Y, Hao J, Cattini P a, Dixon IMC, Kardami E. 2002. Acute protection of ischemic heart by FGF-2: involvement of FGF-2 receptors and protein kinase C. *Am. J. Physiol. Heart Circ. Physiol.* **282**:H1071–80.

Jin Y-F, Han H-C, Berger J, Dai Q, Lindsey ML. 2011. Combining experimental and mathematical modeling to reveal mechanisms of macrophage-dependent left ventricular remodeling. *BMC Syst. Biol.* **5**:60.

Johnson J, Nowicki MO, Lee CH, Chiocca EA, Viapiano MS, Lawler SE, Lannutti JJ. 2009. Quantitative analysis of complex glioma cell migration on electrospun polycaprolactone using time-lapse microscopy. *Tissue Eng. Part C. Methods* **15**:531–40.

De Jong S, van Veen T a B, de Bakker JMT, van Rijen HVM. 2012. Monitoring cardiac fibrosis: a technical challenge. *Neth. Heart J.* **20**:44–8.

Jugdutt BI. 2003. Ventricular remodeling after infarction and the extracellular collagen matrix: when is enough enough? *Circulation* **108**:1395–403.

Jugdutt BI, Amy RWM. 1986. Healing after myocardial infarction in the dog: Changes in infarct hydroxyproline and topography. *J. Am. Coll. Cardiol.* **7**:91–102.

Jugdutt BI, Schwarz-Michorowski BL, Khan MI. 1992. Effect of long-term captopril therapy on left ventricular remodeling and function during healing of canine myocardial infarction. *J. Am. Coll. Cardiol.* **19**:713–721.

Kaftan H, Reuther L, Miehe B, Hosemann W, Beule A. 2012. Inhibition of fibroblast growth factor receptor 1: influence on tympanic membrane wound healing in rats. *Eur. Arch. Otorhinolaryngol.* **269**:87–92.

Kanekar S, Hirozanne T, Terracio L, Borg TK. 1998. Cardiac Fibroblasts. *Cardiovasc. Pathol.* **7**:127–133.

Kapuscinski J. 1995. DAPI: a DNA-specific fluorescent probe. *Biotech. Histochem.* **70**:220–33.

Katz AM. 2001. Structure of the Heart, Myocardial Cells, and Biological Membranes. In: . *Physiol. Hear.*, pp. 1–23.

Katz MG, Fargnoli AS, Tomasulo CE, Pritchette LA, Bridges CR. 2011. Model-specific selection of molecular targets for heart failure gene therapy. *J. Gene Med.* **13**:573–86.

Kenneth Mallory G, White PD, Salcedo-Salgar J. 1939. The speed of healing of myocardial infarction. *Am. Heart J.* **18**:647–671.

Khouw IM, van Wachem PB, Plantinga J a, Vujaskovic Z, Wissink MJ, de Leij LF, van Luyn MJ. 1999. TGF-beta and bFGF affect the differentiation of proliferating porcine fibroblasts into myofibroblasts in vitro. *Biomaterials* **20**:1815–22.

Kolk MV V, Meyberg D, Deuse T, Tang-Quan KR, Robbins RC, Reichenspurner H, Schrepfer S. 2009. LAD-ligation: a murine model of myocardial infarction. *J. Vis. Exp.*4–6.

Krenning G, Zeisberg E, Kalluri R. 2010. The Origin of Fibroblasts and Mechanism of Cardiac Fibrosis. *J Cell Physiol* **225**:631–637.

Kuruvilla L, Kartha CC. 2009. Treatment with TNF-alpha or bacterial lipopolysaccharide attenuates endocardial endothelial cell-mediated stimulation of cardiac fibroblasts. *J. Biomed. Sci.* **16**:21.

Kuwahara F. 2002. Transforming Growth Factor-beta Function Blocking Prevents Myocardial Fibrosis and Diastolic Dysfunction in Pressure-Overloaded Rats. *Circulation* **106**:130–135.

Kwabi-Addo B, Ozen M, Ittmann M. 2004. The role of fibroblast growth factors and their receptors in prostate cancer. *Endocr. Relat. Cancer* **11**:709–24.

Lakowicz JR. 2006. Principles of fluorescence spectroscopy. *Princ. Fluoresc. Spectrosc.*

Laping NJ, Grygielko E, Mathur a, Butter S, Bomberger J, Tweed C, Martin W, Fornwald J, Lehr R, Harling J, Gaster L, Callahan JF, Olson B a. 2002. Inhibition of transforming growth factor (TGF)-beta1-induced extracellular matrix with a novel inhibitor of the TGF-beta type I receptor kinase activity: SB-431542. *Mol. Pharmacol.* **62**:58–64.

Lareu RR, Zeugolis DI, Abu-Rub M, Pandit A, Raghunath M. 2010. Essential modification of the Sircol Collagen Assay for the accurate quantification of collagen content in complex protein solutions. *Acta Biomater.* **6**:3146–51.

Leask A. 2010. Potential therapeutic targets for cardiac fibrosis: TGFbeta, angiotensin, endothelin, CCN2, and PDGF, partners in fibroblast activation. *Circ. Res.* **106**:1675–80.

Lee J, Smith NP. 2012. The multi-scale modelling of coronary blood flow. *Ann. Biomed. Eng.* **40**:2399–413.

Lekien F, Marsden J. 2005. Tricubic interpolation in three dimensions. *Int. J. Numer. Methods Eng.* **63**:455–471.

Li RK, Jia ZQ, Weisel RD, Merante F, Mickle D a. 1999. Smooth muscle cell transplantation into myocardial scar tissue improves heart function. *J. Mol. Cell. Cardiol.* **31**:513–22.

Lian R, Chen Y, Xu Z, Zhang X. 2010. Soluble transforming growth factor-beta1 receptor II might inhibit transforming growth factor-beta-induced myofibroblast differentiation and improve ischemic cardiac function after myocardial infarction in rats. *Coron. Artery Dis.* **21**:369–77.

Liang C-C, Park AY, Guan J-L. 2007. In vitro scratch assay: a convenient and inexpensive method for analysis of cell migration in vitro. *Nat. Protoc.* **2**:329–33.

Lindsey ML, Gannon J, Aikawa M, Schoen FJ, Rabkin E, Lopresti-Morrow L, Crawford J, Black S, Libby P, Mitchell PG, Lee RT. 2002. Selective matrix metalloproteinase inhibition reduces left ventricular remodeling but does not inhibit angiogenesis after myocardial infarction. *Circulation* **105**:753–8.

Litwin SE, Litwin CM, Raya TE, Warner a L, Goldman S. 1991. Contractility and stiffness of noninfarcted myocardium after coronary ligation in rats. Effects of chronic angiotensin converting enzyme inhibition. *Circulation* **83**:1028–37.

Liu H, Shao Y, Qin W, Runyan RB, Xu M, Ma Z, Borg TK, Markwald R, Gao BZ. 2013. Myosin filament assembly onto myofibrils in live neonatal cardiomyocytes observed by TPEF-SHG microscopy. *Cardiovasc. Res.* **97**:262–70.

Lodge-Patch I. 1951. The ageing of cardiac infarcts, and its influence on cardiac rupture. *Br. Heart J.* **13**:37–42.

Loftis MJ, Sexton D, Carver W. 2003. Effects of collagen density on cardiac fibroblast behavior and gene expression. *J. Cell. Physiol.* **196**:504–11.

Macchiarelli G, Ohtani O, Nottola S a, Stallone T, Camboni a, Prado IM, Motta PM. 2002. A micro-anatomical model of the distribution of myocardial endomysial collagen. *Histol. Histopathol.* **17**:699–706.

Mark C, Deurs B, Petersen OW. 1990. Regulation of vimentin expression in cultured human mammary epithelial cells. *Differentiation* **43**:146–156.

Masur SK, Conors RJ, Cheung JK, Antohi S. 1999. Matrix adhesion characteristics of corneal myofibroblasts. *Invest. Ophthalmol. Vis. Sci.* **40**:904–10.

Masur S, Dewal H, Dinh T, Erenburg I, Petridou S. 1996. Myofibroblasts differentiate from fibroblasts when plated at low density. *Proc. Natl. Acad. Sci.* **93**:4219–4223.

Matsumura S, Iwanaga S, Mochizuki S, Okamoto H, Ogawa S, Okada Y. 2005. Targeted deletion or pharmacological inhibition of MMP-2 prevents cardiac rupture after myocardial infarction in mice. *J. Clin. Invest.* **115**:599–609.

Matsuo a, Watanabe a, Takahashi T, Futamura M, Mori S, Sugiyama Y, Takahashi Y, Saji S. 2001. A simple method for classification of cell death by use of thin layer collagen gel for the detection of apoptosis and/or necrosis after cancer chemotherapy. *Jpn. J. Cancer Res.* **92**:813–9.

McDougall S, Dallon J, Sherratt J, Maini P. 2006. Fibroblast migration and collagen deposition during dermal wound healing: mathematical modelling and clinical implications. *Philos. Trans. A. Math. Phys. Eng. Sci.* **364**:1385–405.

Mega Y, Robitaille M, Zareian R, McLean J, Ruberti J, DiMarzio C. 2012. Quantification of lamellar orientation in corneal collagen using second harmonic generation images. *Opt. Lett.* **37**:3312–4.

Menke NB, Cain JW, Reynolds A, Chan DM, Segal R a, Witten TM, Bonchev DG, Diegelmann RF, Ward KR. 2009. An in silico approach to the analysis of acute wound healing. *Wound Repair Regen.* **18**:105–13.

Menon SN, Flegg J a, McCue SW, Schugart RC, Dawson R a, McElwain DLS. 2012. Modelling the interaction of keratinocytes and fibroblasts during normal and abnormal wound healing processes. *Proc. Biol. Sci.* **279**:3329–38.

Mewhort HEM, Turnbull JD, Meijndert HC, Ngu JMC, Fedak PWM. 2014. Epicardial infarct repair with basic fibroblast growth factor-enhanced CorMatrix-ECM biomaterial attenuates postischemic cardiac remodeling. *J. Thorac. Cardiovasc. Surg.* **147**:1650–9.

Misao J, Hayakawa Y, Ohno M, Kato S, Fujiwara T, Fujiwara H. 1996. Expression of bcl-2 protein, an inhibitor of apoptosis, and Bax, an accelerator of apoptosis, in ventricular myocytes of human hearts with myocardial infarction. *Circulation* **94**:1506–12.

Mitchell MD, Laird RE, Brown RD, Long CS. 2007. IL-1beta stimulates rat cardiac fibroblast migration via MAP kinase pathways. *Am. J. Physiol. Heart Circ. Physiol.* **292**:H1139–47.

Mohammadi M, McMahon G, Sun L, Tang C, Hirth P, Yeh B, Hubbard S, Schlessinger J. 1997. Structures of the tyrosine kinase domain of fibroblast growth factor receptor in complex with inhibitors. *Science (80-.).* **276**:955–960.

Moon C, Krawczyk M, Ahn D, Ahmet I, Paik D, Lakatta EG, Talan MI. 2003. Erythropoietin reduces myocardial infarction and left ventricular functional decline after coronary artery ligation in rats. *Proc. Natl. Acad. Sci. U. S. A.* **100**:11612–7.

Moore GE, Fellow L. 1998. Cramming More Components onto Integrated Circuits. *Proc. IEEE* **86**:82–85.

Mostaço-Guidolin LB, Ko AC-T, Wang F, Xiang B, Hewko M, Tian G, Major A, Shiomi M, Sowa MG. 2013. Collagen morphology and texture analysis: from statistics to classification. *Sci. Rep.* **3**:2190.

Muinonen-Martin AJ, Veltman DM, Kalna G, Insall RH. 2010. An improved chamber for direct visualisation of chemotaxis. *PLoS One* **5**:e15309.

Mukherjee R, Brinsa TA, Dowdy KB, Scott AA, Baskin JM, Deschamps AM, Lowry AS, Escobar GP, Lucas DG, Yarbrough WM, Zile MR, Spinale FG. 2003. Myocardial Infarct Expansion and Matrix Metalloproteinase Inhibition. *Circulation* **107**:618–625.

Murakami M, Elfenbein A, Simons M. 2008. Non-canonical fibroblast growth factor signalling in angiogenesis. *Cardiovasc. Res.* **78**:223–31.

Murphy KE, Hall CL, Maini PK, McCue SW, McElwain DLS. 2012a. A fibrocontractive mechanochemical model of dermal wound closure incorporating realistic growth factor kinetics. *Bull. Math. Biol.* **74**:1143–70.

Murphy KE, McCue SW, McElwain DLS. 2012b. Clinical strategies for the alleviation of contractures from a predictive mathematical model of dermal repair. *Wound Repair Regen.*1–9.

Murphy-ullrich JE. 2001. Matricellular proteins The de-adhesive activity of matricellular proteins : is intermediate cell adhesion an adaptive state ? *J. Clin. Invest.* **107**:785–790.

Muzard J, Sarda-Mantel L, Loyau S, Meulemans A, Louedec L, Bantsimba-Malanda C, Hervatin F, Marchal-Somme J, Michel JB, Le Guludec D, Billiald P, Jandrot-Perrus M. 2009. Non-invasive molecular imaging of fibrosis using a collagen-targeted peptidomimetic of the platelet collagen receptor glycoprotein VI. *PLoS One* **4**:e5585.

Nahrendorf M, Pittet MJ, Swirski FK. 2010. Monocytes: protagonists of infarct inflammation and repair after myocardial infarction. *Circulation* **121**:2437–45.

Newell AJ, Griffin LD. 2011. Natural Image Character Recognition Using Oriented Basic Image Features. In: . *2011 Int. Conf. Digit. Image Comput. Tech. Appl.* IEEE, pp. 191–196.

Nickerson DP, Smith NP, Hunter PJ. 2001. A model of cardiac cellular electromechanics. *Philos. Trans. R. Soc. A Math. Phys. Eng. Sci.* **359**:1159–1172.

Van Nieuwenhoven F a, Turner N a. 2013. The role of cardiac fibroblasts in the transition from inflammation to fibrosis following myocardial infarction. *Vascul. Pharmacol.* **58**:182–8.

Nijland F, Kamp O, Verhorst PMJ, de Voogt WG, Bosch HG, Visser C a. 2002. Myocardial viability: impact on left ventricular dilatation after acute myocardial infarction. *Heart* **87**:17–22.

Noble D. 1960. Cardiac action and pacemaker potentials based on the Hodgkin-Huxley equations. *Nature* **188**:495–497.

Noble D, Varghese a, Kohl P, Noble P. 1998. Improved guinea-pig ventricular cell model incorporating a diadic space, IKr and IKs, and length- and tension-dependent processes. *Can. J. Cardiol.* **14**:123–34.

Noble D. 2002. The rise of computational biology. *Nat. Rev. Mol. Cell Biol.* **3**:459–63.

Noble PJ, Noble D. 2000. Reconstruction of the cellular mechanisms of cardiac arrhythmias triggered by early after-depolarizations. *Japanese J. Electrocardiol.* **20**:15–19.

Noorlander ML, Melis P, Jonker a., Noorden CJF V. 2002. A Quantitative Method to Determine the Orientation of Collagen Fibers in the Dermis. *J. Histochem. Cytochem.* **50**:1469–1474.

Nwaneshiudu A, Kuschal C, Sakamoto FH, Anderson RR, Schwarzenberger K, Young RC. 2012. Introduction to confocal microscopy. *J. Invest. Dermatol.* **132**:e3.

Odell ID, Cook D. 2013. Immunofluorescence techniques. *J. Invest. Dermatol.* **133**:e4.

Okada H, Takemura G, Kosai K, Li Y, Takahashi T, Esaki M, Yuge K, Miyata S, Maruyama R, Mikami A, Minatoguchi S, Fujiwara T, Fujiwara H. 2005. Postinfarction gene therapy against transforming growth factor-beta signal modulates infarct tissue dynamics and attenuates left ventricular remodeling and heart failure. *Circulation* **111**:2430–7.

Opie LH, Commerford PJ, Gersh BJ, Pfeffer MA. 2006. Controversies in ventricular remodelling. *Lancet* **367**:356–67.

Osborne JM, Walter a, Kershaw SK, Mirams GR, Fletcher a G, Pathmanathan P, Gavaghan D, Jensen OE, Maini PK, Byrne HM. 2010. A hybrid approach to multi-scale modelling of cancer. *Philos. Trans. A. Math. Phys. Eng. Sci.* **368**:5013–28.

Pagès G, Lenormand P, L'Allemain G, Chambard JC, Meloche S, Pouysségur J. 1993. Mitogen-activated protein kinases p42mapk and p44mapk are required for fibroblast proliferation. *Proc. Natl. Acad. Sci. U. S. A.* **90**:8319–23.

Palecek SP, Loftus JC, Ginsberg MH, Lauffenburger DA, Horwitz AF. 1997. Integrin-ligand binding properties govern cell migration speed through cell-substratum adhesiveness. *Nature* **385**:537–40.

Palmen M, Daemen MJ a P, De Windt LJ, Willems J, Dassen WRM, Heeneman S, Zimmermann R, Van Bilsen M, Doevendans P a. 2004. Fibroblast growth factor-1 improves cardiac functional recovery and enhances cell survival after ischemia and reperfusion: a fibroblast growth factor receptor, protein kinase C, and tyrosine kinase-dependent mechanism. *J. Am. Coll. Cardiol.* **44**:1113–23.

Panchuk-Voloshina N, Haugland RP, Bishop-Stewart J, Bhalgat MK, Millard PJ, Mao F, Leung WY. 1999. Alexa dyes, a series of new fluorescent dyes that yield exceptionally bright, photostable conjugates. *J. Histochem. Cytochem.* **47**:1179–88.

Pásek M, Simurda J, Christé G. 2006. The functional role of cardiac T-tubules explored in a model of rat ventricular myocytes. *Philos. Trans. A. Math. Phys. Eng. Sci.* **364**:1187–206.

Pataridis S, Eckhardt A, Mikulikova K, Sedlakova P, Miksik I. 2009. Determination and Quantification of Collagen Types in Tissues Using HPLC-MS/MS. *Curr. Anal. Chem.* **5**:316–323.

Pelouch V, Dixon IM, Sethi R, Dhalla NS. 1993. Alteration of collagenous protein profile in congestive heart failure secondary to myocardial infarction. *Mol. Cell. Biochem.* **129**:121–31.

Petroll M, Ma L, Jester J. 2003. Direct correlation of collagen matrix deformation with focal adhesion dynamics in living corneal fibroblasts. *J. Cell Sci.* **116**:1481–1491.

Petrov V, Fagard R, Lijnen P. 2002. Stimulation of Collagen Production by Transforming Growth Factor-beta1 During Differentiation of Cardiac Fibroblasts to Myofibroblasts. *Hypertension* **39**:258–263.

Phatharajaree W, Phrommintikul A, Chattipakorn N. 2007. Matrix metalloproteinases and myocardial infarction. *Can. J. Cardiol.* **23**:727–33.

Pijnappels D a, Schalij MJ, Ramkisoensing A a, van Tuyn J, de Vries A a F, van der Laarse A, Ypey DL, Atsma DE. 2008. Forced alignment of mesenchymal stem cells undergoing cardiomyogenic differentiation affects functional integration with cardiomyocyte cultures. *Circ. Res.* **103**:167–76.

Pillai MS, Sapna S, Shivakumar K. 2011. p38 MAPK regulates G1-S transition in hypoxic cardiac fibroblasts. *Int. J. Biochem. Cell Biol.* **43**:919–27.

Plotnikov S V, Millard AC, Campagnola PJ, Mohler W a. 2006. Characterization of the myosin-based source for second-harmonic generation from muscle sarcomeres. *Biophys. J.* **90**:693–703.

Pogson M, Smallwood R, Qwarnstrom E, Holcombe M. 2006. Formal agent-based modelling of intracellular chemical interactions. *Biosystems.* **85**:37–45.

Porter KE, Turner N a. 2009. Cardiac fibroblasts: at the heart of myocardial remodeling. *Pharmacol. Ther.* **123**:255–78.

Porter S. 2007. The role of the fibroblast in wound contraction and healing. *WOUNDS UK* **3**:33–40.

Poss KD, Shen J, Nechiporuk a, McMahon G, Thisse B, Thisse C, Keating MT. 2000. Roles for Fgf signaling during zebrafish fin regeneration. *Dev. Biol.* **222**:347–58.

Pratt SC, Sumpter DJT, Mallon EB, Franks NR. 2005. An agent-based model of collective nest choice by the ant Temnothorax albipennis. *Anim. Behav.* **70**:1023–1036.

Przyklenk K, Connelly CM, McLaughlin RJ, Kloner R a, Apstein CS. 1987. Effect of myocyte necrosis on strength, strain, and stiffness of isolated myocardial strips. *Am. Heart J.* **114**:1349–59.

Ramirez-Montagut T, Blachere NE, Sviderskaya E V, Bennett DC, Rettig WJ, Garin-Chesa P, Houghton AN. 2004. FAPalpha, a surface peptidase expressed during wound healing, is a tumor suppressor. *Oncogene* **23**:5435–46.

Ren G, Michael LH, Entman ML, Frangogiannis NG. 2002. Morphological characteristics of the microvasculature in healing myocardial infarcts. *J. Histochem. Cytochem.* **50**:71–9.

Rettig W, Garin-Chesa P, Healey J, Su S. 1993. Regulation and heteromeric structure of the fibroblast activation protein in normal and transformed cells of mesenchymal and neuroectodermal origin. *Cancer Res.* **53**:3327–3335.

Revenko I, Sommer F, Minh DT, Garrone R, Franc JM. 1994. Atomic force microscopy study of the collagen fibre structure. *Biol. Cell* **80**:67–9.

Reznikov N, Almany-Magal R, Shahar R, Weiner S. 2013. Three-dimensional imaging of collagen fibril organization in rat circumferential lamellar bone using a dual beam electron microscope reveals ordered and disordered sub-lamellar structures. *Bone* **52**:676–83.

Rich L, Whittaker P. 2005. Collagen and picrosirius red staining: a polarized light assessment of fibrillar hue and spatial distribution. *Braz J Morphol Sci* **22**:97–104.

Rohde LE, Ducharme A, Arroyo LH, Aikawa M, Sukhova GH, Lopez-Anaya A, McClure KF, Mitchell PG, Libby P, Lee RT. 1999. Matrix metalloproteinase inhibition attenuates early left ventricular enlargement after experimental myocardial infarction in mice. *Circulation* **99**:3063–70.

Rouillard AD, Holmes JW. 2012. Mechanical regulation of fibroblast migration and collagen remodelling in healing myocardial infarcts. *J. Physiol.* **590**:4585–602.

Rouillard AD, Holmes JW. 2014. Coupled agent-based and finite-element models for predicting scar structure following myocardial infarction. *Prog. Biophys. Mol. Biol.*1–9.

Du Roure O, Saez A, Buguin A, Austin RH, Chavrier P, Silberzan P, Siberzan P, Ladoux B. 2005. Force mapping in epithelial cell migration. *Proc. Natl. Acad. Sci. U. S. A.* **102**:2390–5.

Sato M, Muragaki Y, Saika S, Roberts AB, Ooshima A. 2003. Targeted disruption of TGF- β 1 / Smad3 signaling protects against renal tubulointerstitial fibrosis induced by unilateral ureteral obstruction. *J. Clin. Invest.* **112**:1486–1494.

Schiller M, Javelaud D, Mauviel A. 2004. TGF-beta-induced SMAD signaling and gene regulation: consequences for extracellular matrix remodeling and wound healing. *J. Dermatol. Sci.* **35**:83–92.

Schlüter DK, Ramis-Conde I, Chaplain M a J. 2012. Computational modeling of single-cell migration: the leading role of extracellular matrix fibers. *Biophys. J.* **103**:1141–51.

Schneider M, Kostin S, Strøm CC, Aplin M, Lyngbaek S, Theilade J, Grigorian M, Andersen CB, Lukanidin E, Lerche Hansen J, Sheikh SP. 2007. S100A4 is upregulated in injured myocardium and promotes growth and survival of cardiac myocytes. *Cardiovasc. Res.* **75**:40–50.

See EY-S, Toh SL, Goh JCH. 2008. Technique to accurately quantify collagen content in hyperconfluent cell culture. *J. Mol. Histol.* **39**:643–7.

Segovia-Juarez JL, Ganguli S, Kirschner D. 2004. Identifying control mechanisms of granuloma formation during M. tuberculosis infection using an agent-based model. *J. Theor. Biol.* **231**:357–76.

Shah M, Foreman DM, Ferguson MW. 1994. Neutralising antibody to TGF-beta 1,2 reduces cutaneous scarring in adult rodents. *J. Cell Sci.* **107 (Pt 5**:1137–57.

Sherratt JA, Dallon JC. 2002. Theoretical models of wound healing: past successes and future challenges. *C. R. Biol.* **325**:557–64.

Shinde A V, Frangogiannis NG. 2014. Fibroblasts in myocardial infarction: a role in inflammation and repair. *J. Mol. Cell. Cardiol.* **70**:74–82.

Shivakumar K, Sollott S, M S, Sapna S, Ziman B, Wang S, Lakatta E. 2008. Paracrine effects of hypoxic fibroblast-derived factors on the MPT-ROS threshold and viability of adult rat cardiac myocytes. *Am J Physiol Hear. Circ Physiol*:2653–2658.

Siwik D a, Pagano PJ, Colucci WS. 2001. Oxidative stress regulates collagen synthesis and matrix metalloproteinase activity in cardiac fibroblasts. *Am. J. Physiol. Cell Physiol.* **280**:C53–60.

Smart N, Bollini S, Dubé KN, Vieira JM, Zhou B, Davidson S, Yellon D, Riegler J, Price AN, Lythgoe MF, Pu WT, Riley PR. 2011. De novo cardiomyocytes from within the activated adult heart after injury. *Nature* **474**:640–4.

Smith NP, Pullan AJ, Hunter PJ. 2002. An Anatomically Based Model of Transient Coronary Blood Flow in the Heart. *SIAM J. Appl. Math.* **62**:990–1018.

Souders C a, Bowers SLK, Baudino T a. 2009. Cardiac fibroblast: the renaissance cell. *Circ. Res.* **105**:1164–76.

Squires CE, Escobar GP, Payne JF, Leonardi R a, Goshorn DK, Sheats NJ, Mains IM, Mingoia JT, Flack EC, Lindsey ML. 2005. Altered fibroblast function following myocardial infarction. *J. Mol. Cell. Cardiol.* **39**:699–707.

Strijkers GJ, Bouts A, Blankesteijn WM, Peeters THJM, Vilanova A, van Prooijen MC, Sanders HMHF, Heijman E, Nicolay K. 2009. Diffusion tensor imaging of left ventricular remodeling in response to myocardial infarction in the mouse. *NMR Biomed.* **22**:182–90.

Strutz F, Okada H, Lo CW, Danoff T, Carone RL, Tomaszewski JE, Neilson EG. 1995. Identification and characterization of a fibroblast marker: FSP1. *J. Cell Biol.* **130**:393–405.

Sun S, Wise J, Cho M. 2004. Human fibroblast migration in three-dimensional collagen gel in response to noninvasive electrical stimulus. I. Characterization of induced three-dimensional cell movement. *Tissue Eng.* **10**:1548–57.

Sun Y, Weber KT. 1996. Angiotensin converting enzyme and myofibroblasts during tissue repair in the rat heart. *J. Mol. Cell. Cardiol.* **28**:851–8.

Sun Y, Weber KT. 2000. Infarct scar: a dynamic tissue. *Cardiovasc. Res.* **46**:250–6.

Sun Y, Zhang JQ, Zhang J, Lamparter S. 2000. Cardiac remodeling by fibrous tissue after infarction in rats. *J. Lab. Clin. Med.* **135**:316–23.

Sun Y, Kiani MF, Postlethwaite AE, Weber KT. 2002. Infarct scar as living tissue. *Basic Res. Cardiol.* **97**:343–7.

Sundquist T, Moravec R, Niles A, O'Brien M, Riss T. 2006. Timing your apoptosis assays. *Promega, Cell Notes*:18–21.

Takemura G, Ohno M, Hayakawa Y, Misao J, Kanoh M, Ohno a., Uno Y, Minatoguchi S, Fujiwara T, Fujiwara H. 1998. Role of Apoptosis in the Disappearance of Infiltrated and Proliferated Interstitial Cells After Myocardial Infarction. *Circ. Res.* **82**:1130–1138.

Tamamori M, Ito H, Hiroe M, Marumo F, Hata RI. 1997. Stimulation of collagen synthesis in rat cardiac fibroblasts by exposure to hypoxic culture conditions and suppression of the effect by natriuretic peptides. *Cell Biol. Int.* **21**:175–80.

Tan S, Zhang Y, Connelly K, Gilbert R, Kelly D. 2010. Targeted inhibition of activin receptor-like kinase 5 signaling attenuates cardiac dysfunction following myocardial infarction. *Am J Physiol Hear. Circ Physiol* **298**:1415–1425.

Tasaki A, Yamanaka N, Kubo M, Matsumoto K, Kuroki H, Nakamura K, Nakahara C, Onishi H, Kuga H, Baba E, Tanaka M, Morisaki T, Katano M. 2004. Three-dimensional two-

layer collagen matrix gel culture model for evaluating complex biological functions of monocyte-derived dendritic cells. *J. Immunol. Methods* **287**:79–90.

Taylor P, Olsen L, Maini PK, Sherratt JA, Marchant B. 1998. Journal of Theoretical Medicine : An Simple modelling of extracellular matrix alignment in dermal wound healing I . cell flux induced alignment Simple Modelling of Extracellular Matrix Alignment in Dermal Wound Healing I . Cell Flux Induced Alignment. *Flux*:37–41.

Thampatty BP, Wang JH-C. 2007. A new approach to study fibroblast migration. *Cell Motil. Cytoskeleton* **64**:1–5.

Thum T, Gross C, Fiedler J, Fischer T, Kissler S, Bussen M, Galuppo P, Just S, Rottbauer W, Frantz S, Castoldi M, Soutschek J, Koteliansky V, Rosenwald A, Basson MA, Licht JD, Pena JTR, Rouhanifard SH, Muckenthaler MU, Tuschl T, Martin GR, Bauersachs J, Engelhardt S. 2008. MicroRNA-21 contributes to myocardial disease by stimulating MAP kinase signalling in fibroblasts. *Nature* **456**:980–4.

Tomasek JJ, Gabbiani G, Hinz B, Chaponnier C, Brown R a. 2002. Myofibroblasts and mechano-regulation of connective tissue remodelling. *Nat. Rev. Mol. Cell Biol.* **3**:349–63.

Tomasek JJ, Vaughan MB, Kropp BP, Gabbiani G, Martin MD, Haaksma CJ, Hinz B. Contraction of myofibroblasts in granulation tissue is dependent on Rho/Rho kinase/myosin light chain phosphatase activity. *Wound Repair Regen.* **14**:313–20.

Townsend N, Wickramasinghe K, Bhatnagar P, Smolina K, Nichols M, Leal J, Luengo-Fernandez R, Rayner M. 2012. Coronary heart disease statistics 2012 edition. *Br. Hear. Found. London*.

Tranquillo R, Murray J. 1992. Continuum model of fibroblast-driven wound contraction: inflammation-mediation. *J. Theor. Biol.* **158**:135–172.

Trayanova NA. 2011. Whole-heart modeling: applications to cardiac electrophysiology and electromechanics. *Circ. Res.* **108**:113–28.

Turner N a, Porter KE. 2012. Regulation of myocardial matrix metalloproteinase expression and activity by cardiac fibroblasts. *IUBMB Life* **64**:143–50.

Turner N a, Porter KE. 2013. Function and fate of myofibroblasts after myocardial infarction. *Fibrogenesis Tissue Repair* **6**:5.

Turner N, Grose R. 2010. Fibroblast growth factor signalling: from development to cancer. *Nat. Rev. Cancer* **10**:116–129.

Ten Tusscher KHWJ, Noble D, Noble PJ, Panfilov a V. 2004. A model for human ventricular tissue. *Am. J. Physiol. Heart Circ. Physiol.* **286**:H1573–89.

Vandooren J, Geurts N, Martens E, Van den Steen PE, Opdenakker G. 2013. Zymography methods for visualizing hydrolytic enzymes. *Nat. Methods* **10**:211–20.

Vengellur A, LaPres J. 2004. The role of hypoxia inducible factor 1alpha in cobalt chloride induced cell death in mouse embryonic fibroblasts. *Toxicol. Sci.* **82**:638–46.

Venugopal J, Low S, Choon AT, Ramakrishna S. 2008. Interaction of cells and nanofiber scaffolds in tissue engineering. *J. Biomed. Mater. Res. B. Appl. Biomater.* **84**:34–48.

Verhaegen PDHM, Marle J Van, Kuehne A, Schouten HJ, Gaffney E a, Maini PK, Middelkoop E, Zuijlen PPM Van. 2012. Collagen bundle morphometry in skin and scar tissue: a novel distance mapping method provides superior measurements compared to Fourier analysis. *J. Microsc.* **245**:82–9.

Virag J a I, Rolle ML, Reece J, Hardouin S, Feigl EO, Murry CE. 2007. Fibroblast growth factor-2 regulates myocardial infarct repair: effects on cell proliferation, scar contraction, and ventricular function. *Am. J. Pathol.* **171**:1431–40.

Virag JI, Murry CE. 2003. Myofibroblast and endothelial cell proliferation during murine myocardial infarct repair. *Am. J. Pathol.* **163**:2433–40.

Visse R, Nagase H. 2003. Matrix metalloproteinases and tissue inhibitors of metalloproteinases: structure, function, and biochemistry. *Circ. Res.* **92**:827–39.

Volders PG., Willems IEMG, Cleutjens JPM, Arends J-W, Havenith MG, Daemen MJAP. 1993. Interstitial Collagen is Increased in the Non-infarcted Human Myocardium After Myocardial Infarction. *J Mol Cell Cardiol* **25**:1317–1323.

De Vries HJ, Enomoto DN, van Marle J, van Zuijlen PP, Mekkes JR, Bos JD. 2000. Dermal organization in scleroderma: the fast Fourier transform and the laser scatter method objectify fibrosis in nonlesional as well as lesional skin. *Lab. Invest.* **80**:1281–9.

Walker G a, Masters KS, Shah DN, Anseth KS, Leinwand L a. 2004. Valvular myofibroblast activation by transforming growth factor-beta: implications for pathological extracellular matrix remodeling in heart valve disease. *Circ. Res.* **95**:253–60.

Wall ST, Guccione JM, Ratcliffe MB, Sundnes JS. 2012. Electromechanical feedback with reduced cellular connectivity alters electrical activity in an infarct injured left ventricle: a finite element model study. *Am. J. Physiol. Heart Circ. Physiol.* **302**:H206–14.

Weber KT. 1989. Cardiac interstitium in health and disease: the fibrillar collagen network. *J. Am. Coll. Cardiol.* **13**:1637–52.

Weisman HF, Healy B. 1987. Myocardial infarct expansion, infarct extension, and reinfarction: pathophysiologic concepts. *Prog. Cardiovasc. Dis.* **30**:73–110.

Weisman HF, Bush DE, Mannisi J a., Bulkley BH. 1985. Global cardiac remodeling after acute myocardial infarction: a study in the rat model. *J. Am. Coll. Cardiol.* **5**:1355–62.

White HD, Norris RM, Brown M a., Brandt PW, Whitlock RM, Wild CJ. 1987. Left ventricular end-systolic volume as the major determinant of survival after recovery from myocardial infarction. *Circulation* **76**:44–51.

Whittaker P, Boughner DR, Kloner RA. 1989. Analysis of healing after myocardial infarction using polarized light microscopy. *Am. J. Pathol.* **134**:879–93.

Whittaker P, Kloner R a, Boughner DR, Pickering JG. 1994. Quantitative assessment of myocardial collagen with picrosirius red staining and circularly polarized light. *Basic Res. Cardiol.* **89**:397–410.

Willems IE, Havenith MG, De Mey JG, Daemen MJ. 1994. The alpha-smooth muscle actin-positive cells in healing human myocardial scars. *Am. J. Pathol.* **145**:868–75.

Wilson T. 2011. Resolution and optical sectioning in the confocal microscope. *J. Microsc.* **244**:113–21.

Witte MB, Thornton FJ, Kiyama T, Efron DT, Schulz GS, Moldawer LL, Barbul a. 1998. Metalloproteinase inhibitors and wound healing: a novel enhancer of wound strength. *Surgery* **124**:464–70.

Woodcock E a, Matkovich SJ. 2005. Cardiomyocytes structure, function and associated pathologies. *Int. J. Biochem. Cell Biol.* **37**:1746–51.

World Health Organization. 2011. Cardiovascular Diseases Fact Sheet. *Media*:1–4.

Xiao Y, Liu K, Shen J, Xu G, Ye W. 2009. SB-431542 inhibition of scar formation after filtration surgery and its potential mechanism. *Invest. Ophthalmol. Vis. Sci.* **50**:1698–706.

Yang L, Witten TM, Pidaparti RM. 2013. A biomechanical model of wound contraction and scar formation. *J. Theor. Biol.* **332**:228–48.

Yano T, Miura T, Ikeda Y, Matsuda E, Saito K, Miki T, Kobayashi H, Nishino Y, Ohtani S, Shimamoto K. 2005. Intracardiac fibroblasts, but not bone marrow derived cells, are the origin of myofibroblasts in myocardial infarct repair. *Cardiovasc. Pathol.* **14**:241–6.

Yarbrough WM, Mukherjee R, Escobar GP, Mingoia JT, Sample J a, Hendrick JW, Dowdy KB, McLean JE, Lowry AS, O'Neill TP, Spinale FG. 2003. Selective targeting and timing of matrix metalloproteinase inhibition in post-myocardial infarction remodeling. *Circulation* **108**:1753–9.

Zak R. 1974. Development and proliferative capacity of cardiac muscle cells. *Circ. Res.* **35**:suppl II:17–26.

Zhang X, Azhar G, Nagano K, Wei JY. 2001. Differential vulnerability to oxidative stress in rat cardiac myocytes versus fibroblasts. *J. Am. Coll. Cardiol.* **38**:2055–62.

Zhao T, Zhao W, Meng W, Liu C, Chen Y, Sun Y. 2014. Vascular endothelial growth factor-C: its unrevealed role in fibrogenesis. *Am. J. Physiol. Heart Circ. Physiol.* **306**:H789–96.

Zhao W, Lu L, Chen SS, Sun Y. 2004. Temporal and spatial characteristics of apoptosis in the infarcted rat heart. *Biochem. Biophys. Res. Commun.* **325**:605–11.

Zhu X, Sasse J, McAllister D, Lough J. 1996. Evidence that fibroblast growth factors 1 and 4 participate in regulation of cardiogenesis. *Dev. Dyn.* **207**:429–38.

Annexes

A.1 Database organisation

Table 5 Details of the RUNS database table. The first columns (field) details the various fields of the table, while the second column shows the data type used to store said fields

Field	Data type	Description
Run_ID	Number (Auto)	Unique ID for a particular simulation setup
RunDate	Date	Date at which the simulation was performed
GridHeight	Number	Height of the model tissue section
GridWidth	Number	Width of the model tissue section
WoundHeight	Number	Height of the model wounded region
WoundWidth	Number	Width of the model wounded region
WoundShape	Number	Shape of the wounded region (0=circular, 1=rectangular)
InitialCellPopulation	Number	Initial number of fibroblast cells
InitialCellRandomSetup	Yes/No	Initial position configuration of fibroblast cells (yes=uniform and no=random)
Kappa	Number	The maximum ability of cells to reorient the collagen matrix
Avoidance	Yes/No	Inclusion of the avoidance algorithm in the simulation
AvoidanceThresholdDist	Text	The threshold distance for neighbouring cells' affecting the migration of a cell
Polarisation	Text	Dictates the influence of previous motion and collagen matrix
ProandDegCollagen	Yes/No	Ability of cells to produce and degrade collagen
CellShapeInfluence	Number	The shape of the cells' influence (e.g. 4=wedge-shaped)
TimeSteps	Number	The number of model iterations
TimeStepInterval	Text	The time interval between model iterations
ChemotacticGradient	Yes/No	Inclusion of a chemoattractant in the simulation
InterpolationMethod	Number	Interpolation method chosen for simulation (e.g. bilinear)
CellDivision	Yes/No	Inclusion of proliferation in the simulation
DaughterCellBehaviour	Number	Direction of migration of daughter cells' immediately after division (0=lost polarity, 1=repulsion)
DaughterCellSeparation	Number	Distance between daughter cells immediately after division (0=3 μm, 1=10 μm)
Apoptosis	Yes/No	Inclusion of apoptosis in the simulation
FibroblastSpeed	Text	The baseline cell speed for fibroblast cells
Differentiation	Yes/No	Inclusion of differentiation in the simulation
MyofibroblastCellSpeed	Text	The baseline cell speed for myofibroblast cells
MyofibroblastCellSize	Yes/No	Double the area of influence of a myofibroblast cell
MyofibroblastCellInfluence	Yes/No	Double the level of influence of a myofibroblast cell

Table 6 Details of the RESULTS database table. The first columns (field) details the various fields of the table, while the second column shows the data type used to store said fields

Field	Data type	Description
Results_ID	Auto Number	Unique ID for the final results of an individual model simulation
Run_ID	Text	Unique ID for a particular simulation setup
SEED	Number	Seed used to initialise the random number generator
FinalShapeFactor	Number	Number of clusters at the end of the simulation
WoundClosurePer	Text	The percentage wound cellular closure at the end of the simulation
FinalCollagenDensity	Text	The average collagen density at the end of the simulation
NumberFibCells	Number	The number of fibroblast cells at the end of the simulation
NumberMyoCells	Number	The number of myofibroblasts at the end of the simulation

Table 7 Details of the RESULTS_RATES database table. The first columns (field) details the various fields of the table, while the second column shows the data type used to store said fields

Field	Data type	Description
Results_Rates_ID	*Number*	Unique ID for all the results during an individual model simulation
Results_ID	*Text*	Unique ID for the final results of an individual model simulation
TimeStep	*Number*	Each model iteration
WoundCellCoverage	*Text*	The percentage wound cellular closure for each time step
WoundCollagenCoverage	*Text*	Percentage wound collagen coverage for each time step
CurrentShapeFactor	*Number*	Number of clusters for each time step
SelectionShapeFactor	*Number*	Number of clusters within a predefined region within the wound for each time step
CompleteShapeFactor	*Number*	Number of clusters across the whole tissue for each time step
CurrentNumberFibCells	*Number*	Number of fibroblast cells at each time step
CurrentNumberMyoCells	*Number*	Number of myofibroblast cells at each time step
AvgCollagenDensity	*Text*	Average collagen density across the whole tissue at each time step
AvgWoundCollagenDensity	*Text*	Average collagen density in the wounded region at each time step

A.2 3-dimensional cell culture experiments

Cells were cultured in a 3-dimensional (3D) environment. High concentration (8.76 mg ml^{-1}) rat tail collagen I (BD Biosciences, 354249) was neutralised with 1N NaOH in PBS solution to a final concentration of 5 mg ml^{-1} collagen I. All the reagents were kept on ice. The collagen gel was then diluted 2× to a concentration of 2.5 mg ml^{-1}. As the solution thawed, it solidified and set. Gels were formed in a well of an imaging chamber CG 8-well plate (PAA, PAA14220080X). First, 75 µl of the collagen solution was pipetted in the well and allowed to set. Then, 75 µl of the collagen solution was mixed with a cell suspension ($7.45x10^5$ cells ml^{-1}) of β-actin cre and YFP positive primary cardiac fibroblast and pipetted on-top of the other gel and allowed to set.

The imaging chamber was then placed back in a cell culture incubator at 37 °C and 5% CO_2. Cells were imaged by confocal microscopy (Inverted Zeiss LSM 710).